SEPARATION OF CLOSE ISOMERS

BY ENCLATHRATION

by

ALICIA HORNE

B.Sc.(HONS) (University of Cape Town)

Thesis presented to the

UNIVERSITY OF CAPE TOWN

in fulfilment of the degree of

DOCTOR OF PHILOSOPHY

Department of Chemistry
University of Cape Town
Rondebosch
7701
South Africa

August 1997

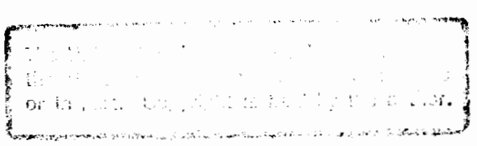

It is by logic that we prove,
but by intuition that we discover.

Jules Henri Poincaré
1854 - 1912

ACKNOWLEDGEMENTS

I wish to express my sincere gratitude to:

Professor Luigi R. Nassimbeni, for his excellent supervision, enthusiasm and good humour.

Professor Mino R. Caira, for his expert advice and guidance.

Dr. Anita Coetzee for data collections.

My colleagues, past and present, in the crystallography long room for assistance and many interesting (both scientific and non-scientific) lunchtime conversations.

My family, especially Victor, for their love, patience and support.

AECI and the Foundation for Research Development for financial assistance.

ABSTRACT

The selective inclusion properties of the host compound 1,1-bis-(4-hydroxyphenyl)cyclohexane were investigated. This host readily forms inclusion compounds with the isomers of phenylenediamine, benzenediol, picoline and lutidine, as well as selected solvents including methanol, ethanol, *i*-propanol, *n*-butanol, ethyl acetate and dioxane. The crystal structures of the complexes formed were elucidated, and comparisons were made between the packing of the complexes, and the intermolecular interactions between the host and guest components of the complexes.

The complexes were characterised using thermal analysis and X-ray powder diffraction. The lattice energies of the complexes were calculated to determine their relative stability. The kinetics of desolvation of the picoline and lutidine inclusion compounds were studied, using isothermal and non-isothermal thermogravimetry. These experiments yielded the kinetic models as well as the activation energies of the desolvation reactions.

Competition experiments were performed to determine which isomers of the compounds mentioned above were enclathrated preferentially by the host, and the observed selectivity was related to differences in complementary between the host and guest components in each complex.

Inclusion compounds were formed between the host and the solid guests (benzenediol and phenylenediamine) by means of solid-solid reactions. The complexes were formed by grinding the two powdered starting components together in a ball mill. The resulting products were analysed by X-ray powder diffractometry. Competition experiments were also performed in the solid state to determine whether the selectivity of the host differed from that observed in solution.

The results of the competition experiments, carried out in solutions and in the solid state, revealed the ability of the host compound, 1,1-bis-(4-hydroxyphenyl)cyclohexane, to separate mixtures of isomers or closely related compounds.

PUBLICATIONS AND CONFERENCES

Parts of this thesis have been published in the following journals:

1. M. R. Caira, A. Horne, L. R. Nassimbeni, K. Okuda and F. Toda, *J. Chem. Soc., Perkin Trans. 2*, 1995, 1063.

2. M. R. Caira, A. Horne, L. R. Nassimbeni and F. Toda, *J. Chem. Soc., Perkin Trans. 2*, in press.

3. M. R. Caira, A. Horne, L. R. Nassimbeni and F. Toda, *J. Materials Chem.*, in press.

4. M. R. Caira, A. Horne, L. R. Nassimbeni and F. Toda, *Supramolecular Chemistry*, submitted.

Parts of this thesis have been presented at the following conferences:

1. AECI Limited: 1994 Postgraduate Research Fellowship Seminar. Johannesburg, South Africa. 6 - 7 October 1994.

2. University of Cape Town Conference on Molecular Recognition and Synthetic Design. Cape Town, South Africa. 3 February 1995.

3. Crystallography of Supramolecular Compounds, International School of Crystallography. Erice, Italy. 1 - 11 June 1995.

4. AECI Limited: 1995 Postgraduate Research Fellowship Seminar. Johannesburg, South Africa. 26 - 27 October 1995.

5. South African Chemical Institute - Young Scientists Meeting. Cape Town, South Africa. 29 November 1995.

6. 33rd Convention of the South African Chemical Institute. Cape Town, South Africa. 29 January 1996 - 2 February 1996.

7. International Union of Crystallography XVII Congress and General Assembly. Seattle, USA. 8 - 17 August 1996.

8. AECI Limited: 1996 Postgraduate Research Fellowship Seminar. Johannesburg, South Africa. 24 - 25 October 1996.

9. University of Cape Town Research Conference - Molecular Design and Recognition. Cape Town, South Africa. 3 - 4 April 1997.

ABBREVIATIONS USED IN THIS THESIS

The inclusion compounds are described by mnemonics which are detailed on the inserted bookmark.

α	extent of reaction
	unsolvated phase of the host compound
	the angle between *b* and *c* unit cell axes
β	heating rate
	the angle between *a* and *c* unit cell axes
γ	the angle between *a* and *b* unit cell axes
BD	benzenediol
D_c	calculated density
D_m	measured density
DSC	differential scanning calorimetry
E	normalised structure factor
E_a	activation energy
F	structure factor
$f(\alpha)$	kinetic rate expression
G	guest compound
GC	gas chromatography
HPLC	high performance liquid chromatography
H	host compound
LUT	lutidine
k	rate constant
PDA	phenylenediamine
PIC	picoline
TG	thermogravimetry
T_{on}	onset temperature
V	cell volume
XRD	X-ray powder diffraction
Z	number of structural units in the unit cell

TABLE OF CONTENTS

APPENDICES

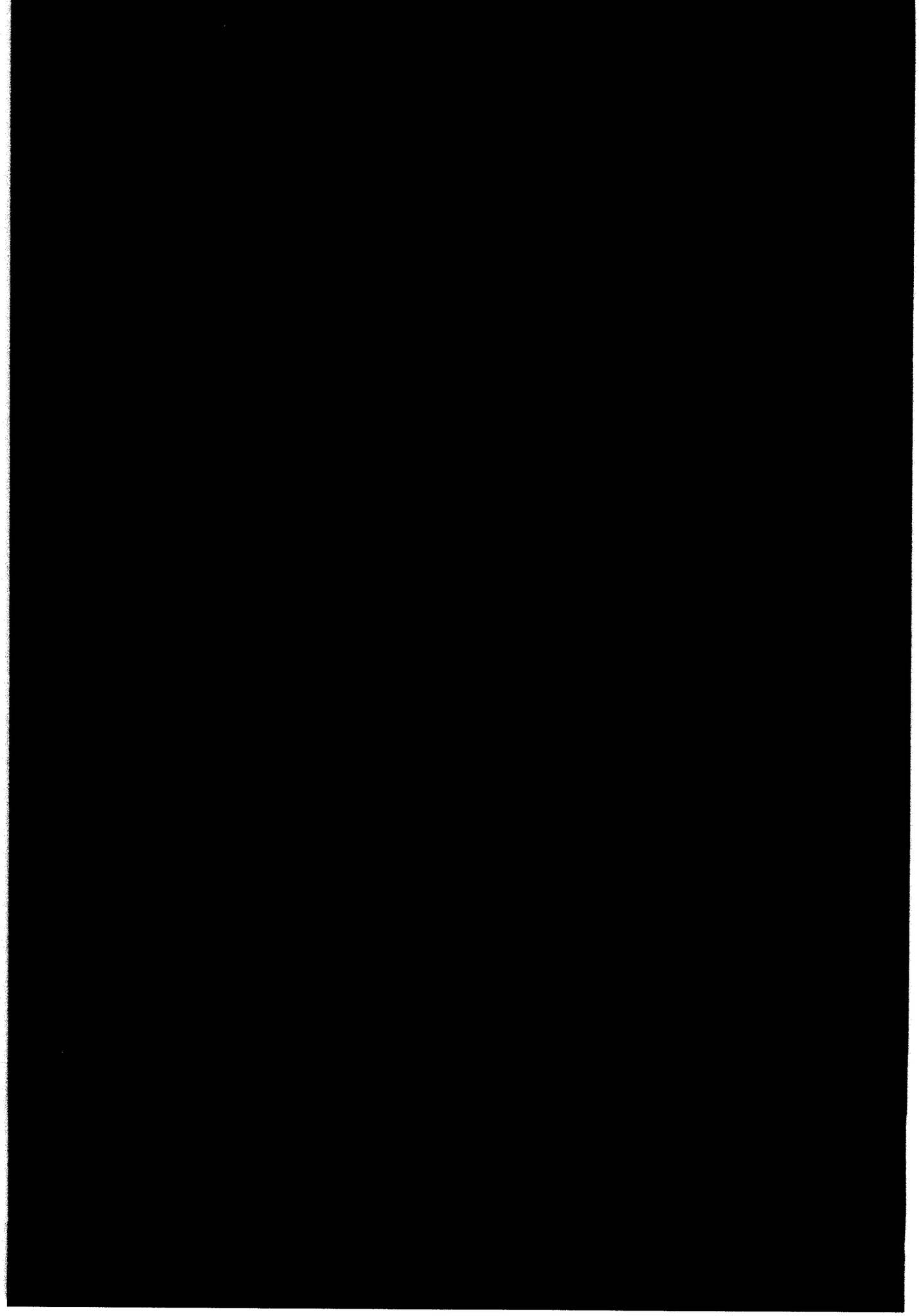

1. INTRODUCTION

1.1 Supramolecular Chemistry

Supramolecular chemistry is the chemistry of the intermolecular bond. It may be defined as "chemistry beyond the molecule", bearing on the organised entities of higher complexity that result from the association of two or more chemical species held together by intermolecular forces.

Jean-Marie Lehn, Nobel Lecture, 1987[1]

A major attraction of supramolecular chemistry is the breadth of scope and the range of perspectives which it offers, since it spans the fields of chemistry, biology and physics[2]. Mother Nature has constructed many supramolecular arrangements in biological systems, and thus this field provides researchers with a great challenge to understand and manipulate these systems.
Atwood[3] has included the following headings, amongst others, under the umbrella of supramolecular chemistry:

- Crystal Engineering
- Molecular Recognition
- Inclusion Compounds
- Macrocycles
- Crown Ethers
- Calixarenes
- Layered Compounds
- Zeolites

The objectives of studies directed in these fields are to create systems which are useful in the areas of catalysis, transport, separation technology and information science[1].

Of particular interest to this study are the topics of *inclusion compounds* and *molecular recognition*, although the extreme diversity of these fields makes any attempt to present a comprehensive discussion of these topics in a single chapter a formidable task. Therefore, only a working knowledge of inclusion compounds, and some of their extensive applications will be presented.

1.2 Inclusion Compounds

The fundamental feature of this type of compound is the fact that a cavity-containing host component incorporates one or several guest components, without covalent bonding. Two distinct categories of inclusion compounds are identified: (1) those where the host component comprises a single molecule, and the guest molecule/s reside completely within the host (e.g. cyclodextrins, calixarenes and cryptands), and (2) those where several host molecules constitute a host framework containing voids in which guest molecules are located. An example of an inclusion compound belonging to each category is illustrated in Figure 1.

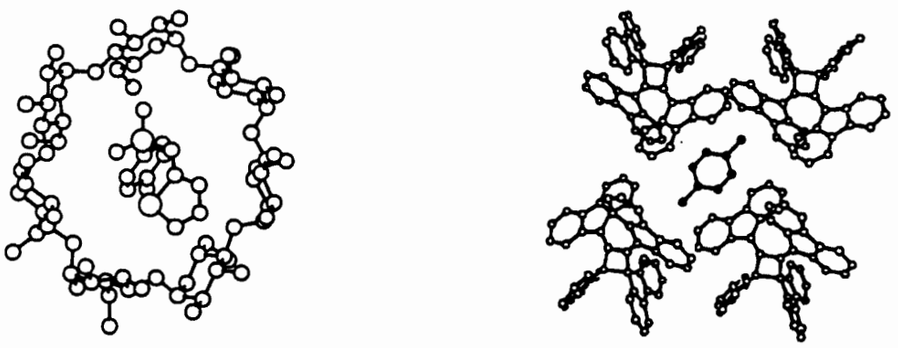

(a) (b)

Figure 1: (a) The drug compound sulfathiazole encapsulated by a single β-cyclodextrin molecule[4], and (b) *p*-Xylene molecule residing in a cavity formed by the packing of four allene dimer host molecules[5].

The majority of inclusion compounds belong to the second category, which may be subdivided into a number of subgroups. The most widely utilised scheme for the division of category (2) is that suggested by Weber[6], which classifies host-guest compounds according to their degree of intermolecular interaction and their topologies.

Inclusion compounds have been known since the beginning of the nineteenth century, when Davy[7] discovered chlorine hydrate, $Cl_2 \bullet 6H_2O$, by bubbling chlorine into water. The most important progress in the understanding of inclusion compounds occurred with the elucidation of the β-quinol•H_2S structure in 1947 by Palin[8] and Powell, and with the important publication by Powell[9] in 1948, entitled 'The structure of molecular compounds' in which he coined the word 'clathrate'. This term has become an accepted part of chemical nomenclature, and even appears in the Oxford English Dictionary[10]:

> *clathrate:* *1. Resembling lattice work; cancellate*
> *2. Chem. of a compound containing molecules of one substance physically enclosed within the structure of another.*

This field of chemistry has undergone tremendous evolution by the end of the twentieth century. Many of these compounds have led to novel applications in research and industry today, and these have been thoroughly reported in books and reviews[1,2,3,11,12,13] on the subject. Most recently, an encompassing set of volumes "Comprehensive Supramolecular Chemistry"[14] has been published, and provides the most up-to-date facts on all aspects of this highly interdisciplinary field.

For example, cyclodextrins (CDs) are increasingly being introduced into industrial processes. In fact, it has been estimated that the annual growth of the total use of cyclodextrins has reached 20 - 30%[15].

Many drugs have undesirable properties since they may display low bioavailabilities, or have unpleasant smells or tastes. In a number of cases, administering a CD•drug inclusion compound instead of the uncomplexed drug provides a solution, since complexation can lead to alteration of the physical and chemical properties of the drug molecule. The cinnarizine•β-CD complex is a representative example. Cinnarizine is widely used orally for the treatment of cerebral diseases. It was found that the dissolution rate, and therefore bioavailability, of cinnarizine was enhanced 30 times by complex formation with CD compared with that of free cinnarizine[16,17].

The food and cosmetic industry has also benefited from cyclodextrin chemistry. Flavour components such as apple, menthol and sage, amongst others, have been included by cyclodextrins and been marketed in complexed form, since the complexes exhibit high stability when they are heated during industrial food processing[15]. A vanillin-glucose compound lost all aroma after 240 days whilst no detectable loss was observed after two years for the vanillin-CD analogue[18].

Calixarene compounds have been known for a long time[19], but their potential in the field of supramolecular chemistry has only recently been recognised[20,21]. In industry, calixarene compounds have applications in pollution control. Wainright[22] has patented a method for the removal of organic compounds, particularly halogenated hydrocarbons, from water using calixarenes. Water supplies are usually chlorinated for the purposes of improving their microbiological quality. However it has been discovered that undesirable side reactions occurred in the water resulting in the formation of compounds with carcinogenic properties, and these have been encountered in water supplies intended for use in the home and in industry. Wainwright discovered that tert-butylcalix[6]arene forms inclusion complexes of relatively high stability with these undesirable compounds, and can therefore be applied as a water purifier, preferably attached to a solid support.

Calixarene inclusion compounds have also found applications as accelerators for cyanoacrylate instant adhesives, which render adhesive capabilities to substrates such as paper, leather and fabric, and several patents[23] have resulted. For example, on addition of a modified calix[4]arene to ethylcyanoacrylate, the fixture time on copy paper can be less than 1 second compared to 60 seconds without additive.

Other classic uses of inclusion compounds include those of molecular storage and stabilisation of guest molecules. Atwood and co-workers[24] have described the novel stabilisation of the highly reactive $[AlMe_2]^+$ cation, of interest with respect to Ziegler-Natta catalysis, within the voids of crown ethers. Also, β-hydroquinone, which displays a double interlocking network structure, has been studied[25] as a method of storage of ^{85}Kr from nuclear power plant off-gases. ^{85}Kr has a half-life of approximately 10 years, and its complexation with hydroquinone results in the formation of a complex which is safe and easy to handle.

Catalysis is a key technology of the chemical industry world-wide and the backbone of most production processes, for bulk chemicals in particular. Therefore catalysis research and industrial catalyst development are strongly dependent upon the immediate needs of the market, and on environmental protection. The wide range of applications of zeolite catalysts[26,27,28] plays an important role in industrial processes, and has led to numerous patents. Toray Industries has built a multipurpose facility for a liquid-phase isomerization process using the zeolite catalyst H-ZSM-5 in a fixed bed in order to produce *m*-chlorotoluene, *m*-dichlorobenzene and 2,6-dichlorotoluene at temperatures of 200 - 400°C[29]. The 2000 t yr^{-1} plant went on stream in 1990[30]. Alkylamines are used as valuable intermediates in the production of insecticides, herbicides and pharmaceuticals. Since 1985, a commercial plant with a capacity of around 40 000 t yr^{-1} has been on stream at NITTO Chemical Industries Co.[30]. This plant uses a process employing the shape-selective zeolite catalyst NaH-MOR to produce mono- and dimethylamine[31].

1.3 Molecular Recognition

Molecular recognition lies at the heart of inclusion chemistry. It depends on the matching of steric and electronic features in different molecules to optimise the number and strengths of intermolecular interactions formed between them[32]. Desiraju[13] has even described intermolecular interactions as *supramolecular glue*, since they are the fundamental causes for the formation and crystallisation of supermolecules. Therefore, an understanding of these interactions is vital. Non-covalent interactions[33] which operate in molecular recognition events include hydrophobic, electrostatic, hydrogen-bonding, metal co-ordination, and charge-transfer phenomena. It has been recognised that these non-covalent interactions often result in the fascinating properties of selective recognition, fast and reversible information transfer, high catalytic activity and chemical conversions in an ecological equilibrium observed in biological systems[34].

In the hierarchy of atomic interactions, the hydrogen bond occupies a special place, falling between chemical bonds and interactions such as van der Waals interactions. Although these are non-bonding interactions, they often have a distinct effect on molecular conformation and crystal close-packing. In inclusion compounds, hydrogen bonds are usually of the type (O,N)-H···(O,N) and have energies[35] in the range 20 - 40 kJ mol^{-1}. Thus these interactions exert a stabilising influence in organic crystals.

It appears that the directing forces of hydrogen bonds are so powerful that many simple organic hydrogen bond donors and acceptors will self-associate in solution and nucleate crystal growth with a predictable hydrogen bond connectivity pattern[36].

In selective binding, guest molecules are geometrically discriminated by the size and shape of the three-dimensional cavity provided by the host molecule, a notion that was enunciated by Emil Fischer in 1894[37] by his "lock-and-key" interpretation of steric fit.

The selective incorporation of the guest molecules into the host framework through hydrogen bonding interactions and favourable van der Waals contacts is a matter of fine tuning. It requires the correct manipulation of the energetic and stereochemical features of the non-covalent, intermolecular forces within a defined molecular architecture. An understanding of these interactions allows scientists to design synthetic systems which mimic those which occur naturally, and also to create systems of academic and industrial value.

1.4 Separation by Enclathration

Separations are at the heart of chemical and process engineering. These separations are generally for the purpose of either producing a product of high purity or maintaining a detrimental element below a fixed concentration level. In general, the traditional separation methods, such as precipitation, reverse osmosis and solvent extraction are established, mature technologies. They are well developed and provide excellent results for the separations where they are applicable. However, these separation procedures have often proven to be inadequate, especially as demands increase for greater product purities and cleaner environments. Conventional separation techniques generally are not species specific. Rather, they depend on the general chemical behaviour shared by many species such as insolubility in water, charge interactions, and adsorption onto media of biological or inorganic origin. Newer separation processes increasingly depend on distinguishing between subtle differences in the molecular structure of the components to be separated - for example, between geometric or chiral isomers.

In 1987, the American National Academy of Sciences[38] evaluated existing separation requirements, and concluded that available techniques were often inadequate to efficiently remove trace amounts of metal ions from large volumes of extremely dilute solutions, or from chemically similar ions. The report emphasised the need for the design of new host reagents capable of interacting selectively with target guest species. In other words, the selectivity should be predetermined and be based on specific molecular interactions. This emphasises the need to understand the basis of such separations at the molecular level.

The lattice inclusion phenomenon has often been reported[39,40,41,42] to bring about successful separations. This technique is easily applicable since molecular recognition rests in the principles of molecular complementarity of host and guest, and is mostly due to a size and shape relationship. This notion is illustrated graphically in Figure 2.

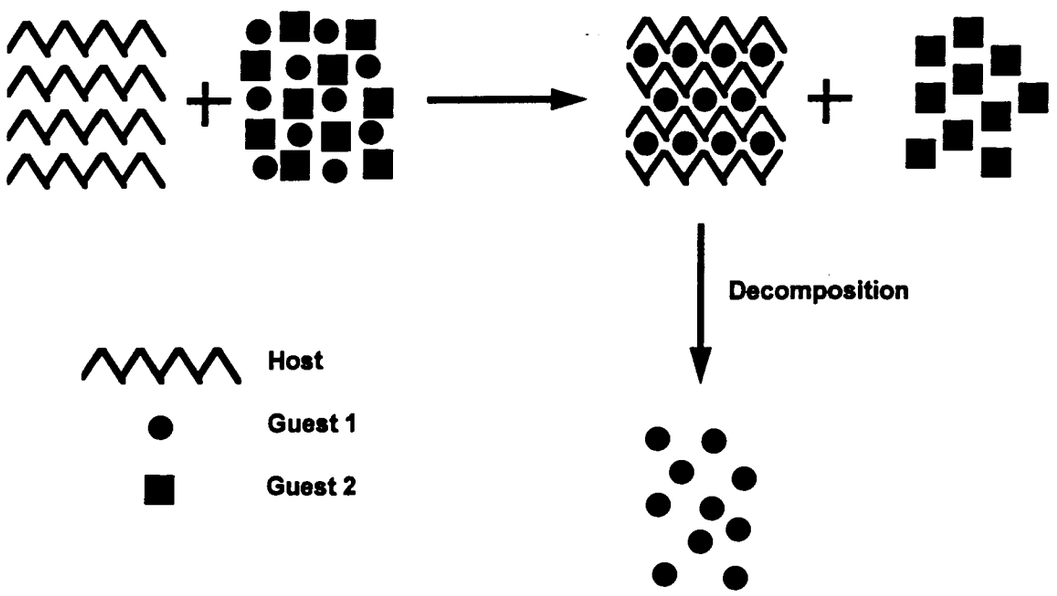

Figure 2: Schematic representation of the process of selective enclathration.

Separations by enclathration essentially follow the same methodology. A suitable host compound is recrystallized from the guest mixture or in the presence of the dissolved guest mixture from an inert solvent. The crystals of the resulting clathrate are filtered, and the included guest compound is released by heating. The uncomplexed guest component may be isolated from the filtrate. The method is never 100% efficient, and therefore often requires several cycles before pure components are obtained. The host compound is not exhausted during the separation process, and may be recovered and recycled.

The crown ethers have shown remarkable use in this field, and the effect of ring size[43] is often observed. Figure 3 shows the logarithms of the complexation constants for two crown ethers, with different ring sizes and numbers of oxygens, plotted against the ionic radii of Na^+, K^+ and Cs^+. One observes "peak selectivity" of crown ether **1** in favour of K^+, while the other two ions are bound significantly less strongly. In the case of crown ether **2**, a less convincing selectivity is observed.

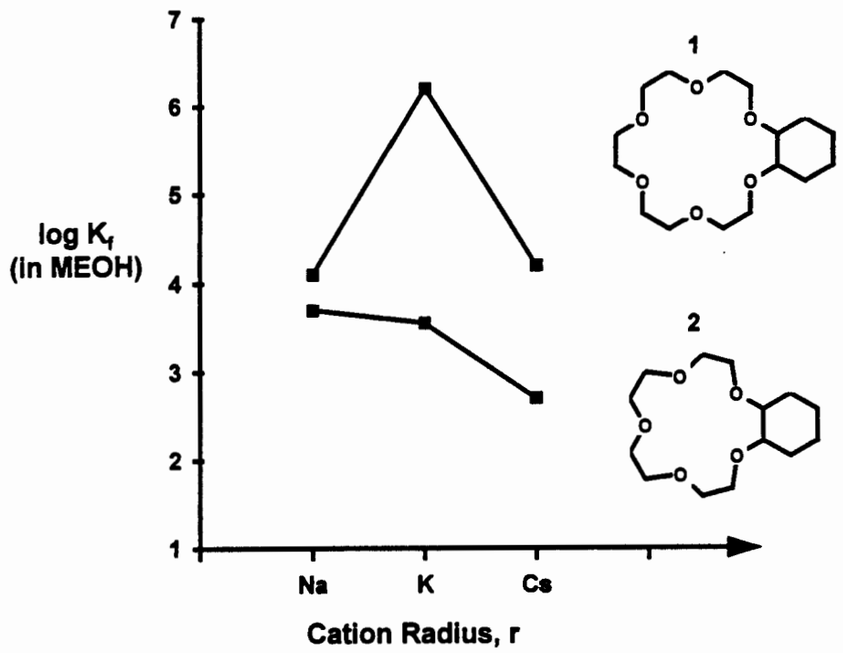

Figure 3: Influence of the ring size on the complexation of crown ethers with cations

This method of metal ion separation is the basis for spectrometric and fluorometric determinations of ion concentrations, and allows the determination of K^+ and Na^+ in blood serum with a simple test strip[44].

One of the most attractive features of calixarenes is their cuplike structure. *p*-tert-Butylcalix[4]arene forms molecular inclusion complexes of well-defined stoichiometry, and its guest-selectivity properties have been investigated[45]. Table 1 reports the results observed during these studies, and shows that for this host compound, benzene is the preferred guest. The results also illustrate the shape-selective discrimination observed between the xylene isomers.

Table 1: Selectivity displayed by *p*-tert-butylcalix[4]arene

Solvent mixture (50/50 v/v)	Ratio of included aromatic
p-Xylene/ m-Xylene	80 / 20
p-Xylene / o-Xylene	100 / 0
p-Xylene / Toluene	90 / 10
p-Xylene / Anisole	75 / 25
Anisole / Toluene	95 / 5
Benzene / Toluene	80 / 20
Benzene / p-Xylene	75 / 25
Benzene / Toluene	90 / 10

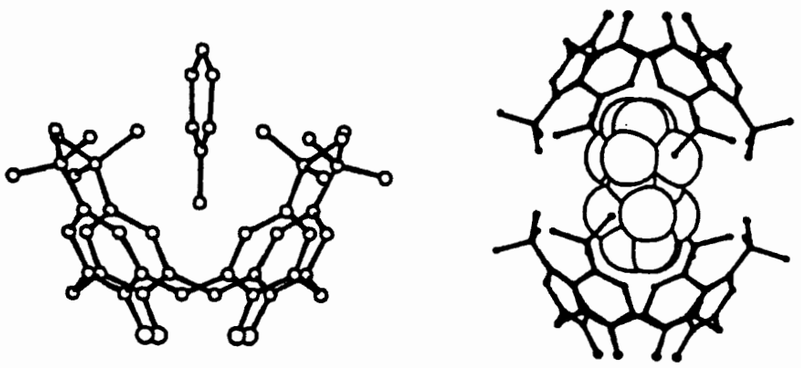

(a) (b)

Figure 4: X-ray crystal structures of the inclusion compounds between *p*-tert-Butylcalix[4]arene and (a) toluene and (b) anisole[45]

In industry, there are numerous examples of separations achieved by urea inclusion compound formation. Urea has been used extensively by the petroleum industry in the dewaxing of certain oil fractions[46], since urea preferentially includes linear above branched hydrocarbons. This is due to the shape and size of the channels, depicted in Figure 5, formed by the packing of the urea host molecules. The channels generally have diameters in the range 5.50 to 5.80 Å[47], and therefore can only accommodate guest compounds of a complementary size.

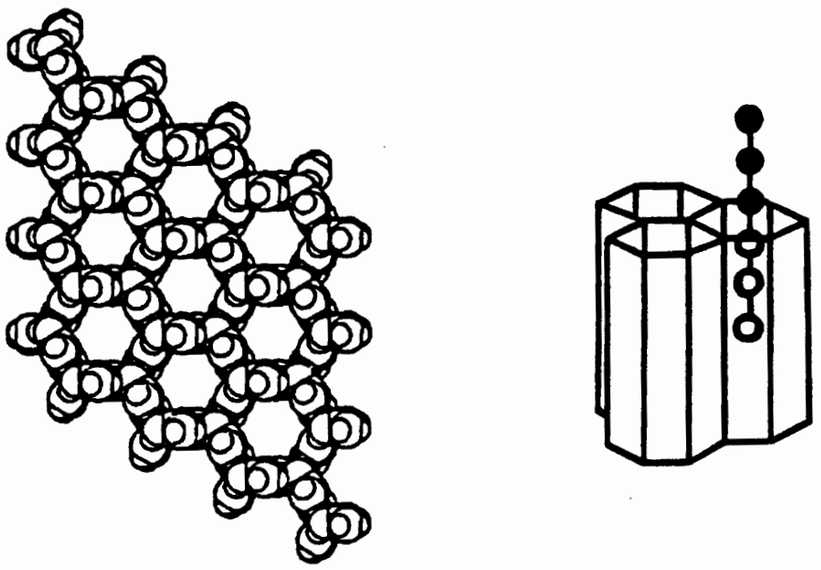

(a) (b)

Figure 5: (a) Representation of the urea host structure viewed along the channel axes, showing van der Waals radii of the urea molecules[48], and (b) schematic view with a guest (n-alkane) included.

Other applications of urea inclusion compounds include the stabilisation of diacyl peroxides and peroxy acids in laundry products, and the use of urea inclusion compounds as solid supports in gas-liquid chromatography[49].

1.5 Chiral Resolution by Enclathration

Stereochemistry, particularly the preparation of optically pure substances is the subject of many contemporary studies[50]. Differences in biological activities, potencies, toxicities, transport mechanisms, and metabolic pathways of stereoisomers and particularly of enantiomers are well established, and often only one member of an enantiomeric mixture is active. The undesired members are effectively impurities, and often represent wasted production. They may also provoke undesirable biological side effects, as witnessed in the thalidomide tragedy.

These factors have driven chemists to research all conceivable ways for the production of chiral materials in enantiopure form for pharmaceutical and agricultural purposes. Methods for obtaining optically active compounds are numerous, yet in the mid-1990's, classical crystallisation methods furnish two-thirds of those optically active marketed drugs which are not derived from natural products.[51]

The study of urea inclusion compounds as a means of resolution has been extensively pursued by Schlenk[52,53], and has given rise to a substantial number of patents[54] (assigned to BASF). Urea has also been found to resolve chiral linear aliphatic molecules such as unbranched hydrocarbons, acids and esters. Early work by Tsoucaris, Green and co-workers[55] has shown that tri-*o*-thymotide (TOT) can effectively separate the enantiomers of compounds like 2-bromobutane.

While the separation of racemates in the case of urea and TOT is achieved by the chiral crystal framework of the host, the optically active cyclodextrins are able to differentiate a chiral guest within their intramolecular cavity. Therefore, a crystal structure is not necessarily needed to form the inclusion compounds, and the guest substances may also be encapsulated in solution.

This particular property allows an application of the cyclodextrins as chiral material for chromatographic racemate resolution[56,57].

Toda has been very successful in resolving racemic mixtures[58,59,60] of a variety of compounds. Most recently[61], he was able to resolve the optically active compound 2,2'-dihydroxy-1,1'-binaphthyl, **1** in Figure 6, into its enantiomers, using an alkyl ammonium salt, **2**. A 1:1 inclusion complex formed between the salt, **2**, and (+)-**1**, and this complex was filtered from the solution. The uncomplexed (–)-**1** remained in the filtrate. The (+)-**1** compound was recovered by recrystallising the complex from a diethyl ether/water solution.

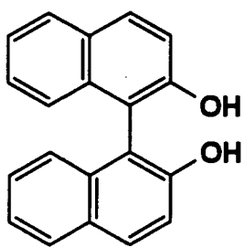

1

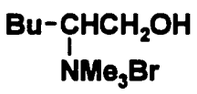

2

Figure 6: **1** : 2,2'-dihydroxy-1,1'-binaphthyl **2** : ammonium salt

The interesting host compound **1**, illustrated in Figure 7, was developed by Weber[62]. Its bulky camphor groups allow facile introduction of chirality from natural sources, without any need for resolution. This host compound includes the aromatic epoxide (S)-(+)-**2** as a 1:1 inclusion compound, but totally excludes the (–)-enantiomer, on crystallisation from solution.

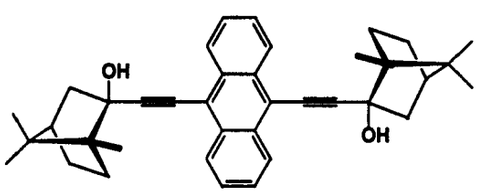

1

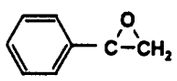

2

Figure 7: **1** : Host compound derived from camphor, **2** : phenyloxirane

1.6 Solid-solid Reactions

Organic solid-solid reactions present promising aspects for chemical synthesis. These reactions are carried out between mixed powders, without the use of a solvent. The possibility of avoiding a toxic, flammable or explosive solvent is highly desirable, as noted by Seebach in a review article on the future of organic chemistry[63]. The applications in industry[64] are highly favourable: hazardous solvents are removed from reaction sequences, and expensive drying procedures of the final products may be avoided.

Much of the pioneering work in this area was carried out by Schmidt and co-workers[65] in the 1960s. More recently, Toda[66] has performed extensive research and found that many traditional organic reactions proceed in the solid state. For example, oxidation reactions[67], reduction reactions[68], coupling reactions[69] and molecular rearrangements[70] were studied, and in many cases were found to be faster and more selective than those in solution. In some solid-solid reactions, the yields of the desired products are greatly enhanced, and thus the production of by-products may be reduced[71,72].

Caira and co-workers[73] have found that co-grinding of sulfadimidine with several aromatic carboxylic acids in the solid state produced 1:1 hydrogen bonded cocrystals which were identical to those obtained from reaction between the components in solution. The kinetics of solid state formation of the cocrystals were measured using X-ray powder diffraction. It was also found that sulfadimidine selectively cocrystallized with 2-aminobenzoic acid when the latter was present in binary mixtures of acids.

1.7 Physical Chemistry of Inclusion Compounds

Solid state chemistry is concerned with the synthesis, structure, properties and applications of solid materials. Two of the principal physical techniques which are used to analyse solid compounds are thermal analysis and diffraction methods. Undoubtedly, the most important and useful technique in solid state chemistry is X-ray diffraction, which has been used extensively for the characterisation of crystalline materials and for the determination of their crystal structures. Neutron diffraction and synchrotron radiation methods are also very important for structural studies, but are much more expensive and are generally used for specialised studies.

The importance of a knowledge of the intermolecular bonding forces that hold molecules together has been alluded to. Single-crystal X-ray analysis of inclusion compounds is a primary source of this type of information, since it provides non-bonded host-guest intermolecular distances and geometries. These parameters reveal the degree of complementarity between the guest molecules and the host framework, and hence the stability of the guest in the inclusion compound.

All crystalline solids have their own characteristic X-ray powder diffraction pattern which may be used as a means of 'fingerprinting'[74]. Powder diffraction has applications which include the study of polymorphism, phase transitions and solid solutions. The most important use of the powder method is in the qualitative identification of crystalline phases or compounds. While most analytical methods yield information about the *elements* or *molecular moieties* present in a sample, powder diffraction is rather unique in that it indicates which *crystalline compounds* or *phases* are present, but gives no direct information about their chemical constitution. Therefore other analytical methods should be employed in conjunction with powder diffraction.

The two main factors which determine the appearance of powder patterns are (a) the size and shape of the unit cell, and (b) the atomic number and position of the various atoms in the cell.

Thermal analysis may be defined as the measurement of physical and chemical properties of materials as a function of temperature. Thermal analysis includes two main techniques, namely *thermogravimetric analysis* (TGA) and *differential scanning calorimetry* (DSC). The principles and applications of these techniques are well-established and have been thoroughly documented[75,76,77] in a number of reviews and books. Thermal analysis has proven to be the most convenient technique to study the stability[76,78,79] of inclusion compounds, and the kinetics of desolvation, since it measures the enthalpy and mass changes which accompany the loss of guest from a complex on heating.

1.8 Kinetics of Decomposition

Kinetic measurements may be of value in industrial processing to determine the most effective and efficient conditions that may be exploited in production so that costs, waste and pollution are minimised[80]. In studying the desolvation reaction of inclusion complexes, the determination of the activation energy of the desolvation event is one of the main aims, since it is an indication of the stability of the inclusion complex.

In solid state reactions, the concepts of concentration and order of reactions generally have no significance, and therefore the rate constant cannot be defined in the same way as for reactions in gases or solutions[81]. Therefore, the concentration terms of rate equations are replaced by parameters representing the progressive changes of area of active interfaces during their advance[82].

Thermogravimetry has been utilised extensively to investigate the thermal stability and thermal decomposition mechanisms of solid complexes[83,84]. The following general thermal decomposition reaction may be written for inclusion compounds, (where H = host, and G = guest):

$$H{\bullet}G_n\,(s) \longrightarrow H(s) + nG(g)$$

During decomposition reactions of this type, gaseous guest compounds, and therefore mass, is lost. This mass loss therefore presents a means of measurement of the extent of decomposition during kinetic studies.

It is assumed that solid state reactions are activated processes[85] and therefore their kinetics are usually described using the Arrhenius equation developed for homogeneous systems:

$$k(T) = A \exp(-E_a/RT)$$

where k is the rate constant, E_a is the activation energy and A the pre-exponential factor. Kinetic equations[86,87,88] have been formulated which express the systematic variation in the extent of chemical change versus time during many solid state reactions. In general, the kinetic equations are expressed in the form, $f(\alpha) = kt$, where α is the fractional extent of reaction (derived from the mass loss due to guest release).

1.9 Diol Host Compounds

Weber[89] describes an efficient host compound as one which has molecular bulkiness, rigidity, 'sticky' groups (e.g. OH) and a degree of symmetry. In order to achieve selectivity, a host molecule must be rigid so as to allow a preorganised binding site which is complementary in size and polarity to a particular guest[90]. Many examples[91,92,93] of excellent host compounds which are diol derivatives with sterically bulky groups are found in the literature.

The diol host compound 1,1-bis(4-hydroxyphenyl)cyclohexane, Figure 8, has proven to be very successful in the scope of molecular separation.

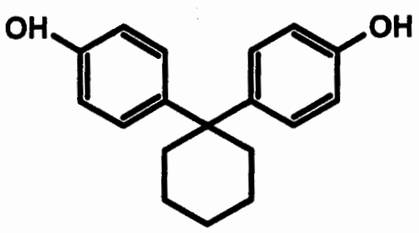

Figure 8: 1,1-bis(4-hydroxyphenyl)cyclohexane

Goldberg and co-workers[94] have studied the selective inclusion capabilities of this host. The study attempted the separation of cresols from a cresol mixture. Cresol isomers are obtained from coal tar, and have important industrial applications. The separation of the *meta* and *para* isomers is of particular interest, since their close boiling points prevent the utilisation of conventional distillation methods [Bp. (*m*-cresol) = 202.0°C, and Bp.(*p*-cresol) = 201.8°C]. Goldberg's study established that the host compound, Figure 8, discriminated between the cresol isomers.

These results were explained by analysing the crystal structures of the complexes formed between the host and each isomer of cresol. The observed

selectivity of the host compound was found to be related to differences in complementarity between the host and guest constituents of each complex, with the complex displaying the higher degree of molecular complementarity being formed preferentially. Manipulation of this phenomenon resulted in the isolation of the individual isomers from a cresol mixture.

1,1-Bis(4-hydroxyphenyl)cyclohexane has also been used to bring about the separation of a mixture of cyclohexanol and cyclohexanone, by means of selective discrimination[95].

Since the host compound 1,1-bis(4-hydroxyphenyl)cyclohexane has proven to discriminate between substituted aromatic compounds, it was employed throughout this study to investigate its potential ability to separate a number of isomer mixtures.

1.10 Guest Compounds

During the course of this study, the separation of a number of commercially important compounds was investigated. These included benzenediols, phenylenediamines, picolines and lutidines. Table 4 lists representative industrial applications of these compounds. Physical properties of the compounds are tabulated in Table 5.

Of these compounds, the total global *p*-benzenediol (hydroquinone) capacity estimated[101] for 1994 was 45,000 - 50,000 tons, while that of *o*-benzenediol (catechol) was approximately 20,000 tons. The global consumption of *m*-benzenediol (resorcinol) reached about 30,000 tons[101], representing a total value of $180 million, and an annual growth rate for the consumption of this compound was estimated at 2 - 4%.

The pyridine bases (picolines and lutidines) were previously isolated from coal tars, but are now mainly produced synthetically. Economic aspects of the volume of pyridine bases produced annually resemble those of speciality markets more than those of commodities, and quantitative information is not available.

Industrial quantities of the phenylenediamines are generally obtained by catalytic hydrogenation of nitroanilines. The American market[96] produces approximately 40,000 tons of the phenylenediamines per annum.

Table 4: Industrial applications of the compounds studied

Compound	Industrial Applications
o-phenylenediamine	manufacture of polybenzimidazoles[96]
m-phenylenediamine	manufacture of polyurethanes, sulphur dyes[97]
p-phenylenediamine	antioxidants, antiozonant[98], dye intermediates[99], reducing agent in colour photography[100], rubbers
o-benzenediol	synthesis of food, pharmaceutical and agrochemical ingredients[101]
m-benzenediol	manufacture of rubber and wood adhesives[101]
p-benzenediol	photographic developers, food antioxidants, water treatment[101]
2-picoline	agrochemicals (nitrapyrin), pharmaceuticals (amprolium)[102]
3-picoline	food additives (niacin), insecticides (chloropyrifos)[102]
4-picoline	manufacture of antituberculosis agent (isoniazid)[102]
2,4-lutidine	organic solvent[102]
3,5-lutidine	organic solvent[102]
2,6-lutidine	antiarteriosclerotic pharmaceuticals (pyridinol carbamate)[102]

Table 5: Physical properties[103] of the compounds studied

Compound	Bp. (°C)[a]	M.p. (°C)[a]	Solubility in H_2O[b,c]	Density (g cm^{-3})[b]
o-phenylenediamine	256	102	v	
m-phenylenediamine	287	63	v	1.139
p-phenylenediamine	267	140	v	
o-benzenediol	245	105	v	1.344
m-benzenediol	280	109	v	1.272
p-benzenediol	285	170	v	1.332
2-picoline	129	-70	v	0.944
3-picoline	144	-18	m	0.967
4-picoline	145	3.6	m	0.955
2,4-lutidine	159	-	v	0.931
2,6-lutidine	146	-6	m	0.923
3,5-lutidine	172	-	p	0.942

a) measured at 760 mm Hg

b) at 20°C

c) Solubility code: m = miscible, p = partly soluble (<10 - 15g / 100g H_2O), v = very soluble (> 25g / 100g H_2O)

In many cases, the various isomers of compounds display profoundly different properties, in particular enantiomers of drugs. Therefore it is often desirable to be able to obtain the isolated isomers in high purity. However, in some cases extreme difficulty is experienced in separating the isomers, especially if the compounds display similar physical properties such as solubility and boiling points. The difficulties experienced by chemical companies in separating these isomers are usually reflected in the prices of the end-products. For example, *meta*- and *para*-cresol are difficult to separate due to their very similar boiling points, and therefore are usually supplied as a mixture. The most recent pricing analysis for bulk quantities of these compounds reveals that one ton of a 85% mixture of *m*- and *p*- cresol (the remaining 15% constituting xylenols and tar acids) costs $915. On removing the impurities to obtain a 99% mixture, the price increases to $1 300 per ton. On separating this mixture into pure *m*- and *p*-cresol components, the price increases dramatically to $3 000 per ton for each compound.

These facts indicate that finding a simple and inexpensive procedure to separate compounds of this nature would be of economic benefit.

1.11 Aims and Objectives

This study attempts the separation of some industrially important regioisomers employing the technique of enclathration. The discriminating properties of the compound 1,1-bis(4-hydroxyphenyl)cyclohexane were studied.

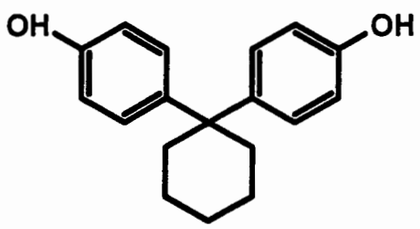

Figure 9: 1,1-bis(4-hydroxyphenyl)cyclohexane

The regioisomers on which separation studies were performed were the phenylenediamines, the benzenediols, the picolines and the lutidines, illustrated in Figure 10.

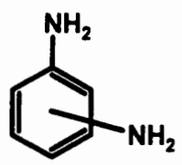

phenylenediamines

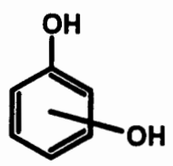

benzenediols

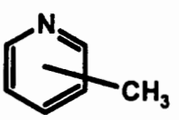

picolines

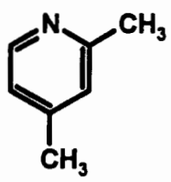

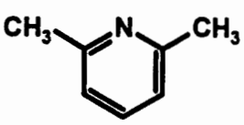

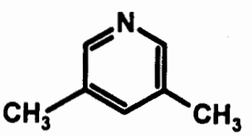

lutidines

Figure 10: Regioisomers studied

The separation of closely related compounds was also attempted. These compounds were the following alcohols: methanol, ethanol, *i*-propanol and *n*-butanol.

Inclusion complexes were formed between the host and each of the guest compounds concerned. The structures of these complexes were elucidated, whenever possible, and studied with regard to the intermolecular interactions between the host and guest components, as well as stability of the inclusion complex.

Where applicable, solid-solid reactions were carried out to determine whether complexation between the host and guest compounds occurred in the solid state, and also to determine the complexation selectivity of the host in the solid state.

Kinetic experiments were performed on the inclusion complexes containing volatile guests, to determine the activation energies of desolvation of the guest compounds from the host framework. In this manner, the relative stabilities of the complexes could be compared.

Competition experiments were performed on each system of compounds to determine the selective behaviour of the host compound. The observed selectivity was related to differences in topological complementarity between the constituents of the inclusion compounds formed. Competition experiments were performed on systems containing two, three and four guest compounds concurrently.

1 J. -M. Lehn, *Angew. Chem., Int. Ed. Engl.* (Nobel lecture), **27**, 1988, 89.

2 J. -M. Lehn, in *Frontiers in Supramolecular Organic Chemistry and Photochemistry*, H. -J. Schneider and H. Dürr (eds.), VCH, Weinheim, 1991.

3 J. L. Atwood, in *Crystallography of Supramolecular Compounds, NATO ASI Series C: Mathematical and Physical Sciences*, Vol. 480, G. Tsoucaris, J. L. Atwood and J. Lipkowski (eds.), Kluwer Academic Publishers, Dordrecht, 1996.

4 M. R. Caira, V. J. Griffith, L. R. Nassimbeni and M. C. B. van Oudtshoorn, *J. Incl. Phenom.*, **17**, 1994, 187.

5 E. Weber, W. Scheiter, I. Goldberg, G. Will and H. -J. Dasting, *J. Incl. Phenom.*, **10**, 1991, 267.

6 E. Weber, *Top. Curr. Chem.*, **140**, 1987, 17.

7 H. Davy, *Philos. Trans. R. Soc. Lond.*, **101**, 1811, 155.

8 D. E. Palin and H. M. Powell, *J. Chem. Soc.*, 1947, 208.

9 H. M. Powell, *J. Chem. Soc.*, 1948, 61.

10 *The New Shorter Oxford English Dictionary*, L. Brown (ed.), Clarendon Press, Oxford, 1993.

11 *Inclusion Compounds*, Vol. 1 to 5, J. L. Atwood, J. E. D. Davies and D. D. MacNicol, Oxford University Press, Oxford, 1991.

12 C. D. Gutsche, *Calixarenes, Monographs in Supramolecular Chemistry*, J. F. Stoddart (ed.), Royal Society of Chemistry, Cambridge, 1989.

13 G. R. Desiraju, in *Comprehensive Supramolecular Chemistry*, Vol. 6, J. L. Atwood, D. D. MacNicol and F. Vögtle (eds.), Pergamon Press, 1996.

14 *Comprehensive Supramolecular Chemistry*, Vol. 1 to 10, J. L. Atwood, D. D. MacNicol and F. Vögtle (eds.), Pergamon Press, 1996.

15 H. Hashimoto, in *Comprehensive Supramolecular Chemistry*, Vol. 3, J. L. Atwood, D. D. MacNicol and F. Vögtle (eds.), Pergamon Press, 1996.

16 F. Hirayama, M. Kurihara, Y. Horiuchi, T. Utsuki, K. Uekama and M. Yamasaki, *Int. J. Pharm.*, **49**, 1989, 163.

17 K. Uekama, H. Arima, T. Irie, K. Matsubara and T. Kuriki, *J. Pharm. Pharmacol.*, **41**, 1989, 874.

18 J. Szejtli, L. Szente and E. Banky-Elod, *Acta. Chim. Acad. Sci. Hung.*, **101**, 1979, 27.

19 A. Zinke and E. Ziegler, *Ber.*, **77**, 1944, 264.

20 C. D. Gutsche, R. Muthukrishnan and K. H. No, *Tetrahedron Letters*, 1979, 2213.

21 G. D. Andreetti, R. Ungaro and A. Pochini, *J. Chem. Soc., Chem. Commun.*, 1979, 1005.

22 K. P. Wainwright, PCT Int. Appl. WO 8908092, 1989.

23 (a) S. J. Harris, UK Patent Appl. GB 2 200 909, 1988.
(b) S. J. Harris and M. MacManus, Eur. Patent Appl. EP 279521.

24 S. G. Bott, A. Alvanipour, S. D. Morley, D. A. Atwood, C. M. Means, A. W. Coleman and J. L. Atwood, *Angew. Chem., Int. Ed. Engl.*, **26**, 1987, 485.

25 H. Shimojima, Y. Nakayama, K. Matsumoto and H. Hyodo, in *Proceedings of the 3rd International Conference on Peaceful Uses of Atomic Energy*, Vol. 14, Geneva, 1964, 314.

26 P. B. Venuto, *Microporous Mater.*, **2**, 1994, 297.

27 W. F. Hölderich and H. van Bekkum, *Stud. Surf. Sci. Catal.*, **58**, 1991, 631.

28 E. Perot and M. Guisnet, *J. Mol. Catal.*, **61**, 1990, 173.

29 S. Okazaka and H. Jouhouji, *Bull. Chem. Soc. Jpn.*, **59**, 1986, 1931.

30 M. Misono and N. Nojiri, *Appl. Catal. A*, **64**, 1990, 1.

31 K. Segawa and H. Tachibana, in *Proceedings of the 10th International Conference on Catalysis, Budapest, 1992*, L. Guczi (ed), Elsevier, Amsterdam, 1993.

32 K. Biradha, C. V. K. Sharma, K. Panneerselvam, L. Shimoni, H. L. Carrell, D. E. Zacharias and G. R. Desiraju, *J. Chem. Soc., Chem. Commun.*, 1993, 1473.

33 Y. Murakami, J. Kikuchi, Y. Hisaeda and T. Ohno, in *Frontiers in Supramolecular Organic Chemistry and Photochemistry*, H. -J. Schneider and H. Dürr (eds.), VCH Publishers, Weinheim, 1991.

34 F. Diederich, in *Frontiers in Supramolecular Organic Chemistry and Photochemistry*, H. -J. Schneider and H. Dürr (eds.), VCH Publishers, Weinheim, 1991.

35 G. R. Desiraju, *Acc. Chem. Res.*, **24**, 1991, 290.

36 G. A. Jeffrey and W. Saenger, *Hydrogen Bonding in Biological Structures*, Springer, Berlin, 1991.

37 E. Fischer, *Ber. Dtsch. Chem. Ges.*, **27**, 1894, 2985.

38 G. J. King (ed.), *Separation and Purification - National Academy of Sciences*, Washington DC, 1987.

39 F. Toda, *Top. Curr. Chem.*, **140**, 1987, 43.

40 W. J. McDowell, *Sep. Sci. Technol.*, **23**, 1988, 1251.

41 R. M. Izatt, J. S. Bradshaw, R. L. Bruening, B. J. Tarbet and M. L. Bruening,in *Comprehensive Supramolecular Chemistry*, Vol. 10, J. L. Atwood, J. E. Davies, D. D. MacNicol and F. Vögtle (eds.), Elsevier, 1996.

42 A. Collet, in *Comprehensive Supramolecular Chemistry*, Vol. 10, J. L. Atwood, J. E. Davies, D. D. MacNicol and F. Vögtle (eds.), Elsevier, 1996.

43 R. M. Izatt, J. S. Bradshaw, S. A. Nielsen, J. D. Lamb, J. J. Christensen and D. Sen, *Chem. Rev.*, **85**, 1985, 271.

44 (a) H. Sumiyoshi, K. Nakahara and K. Ueno, *Talanta*, **24**, 1977, 763.
(b) M. Takagi, H. Nakamura, Y. Sanui and K. Ueno, *Anal. Chim. Acta.*, **126**, 1981, 185.
(c) A. Sanz-Medel, D. B. Gomis and J. R. G. Alvarez, *Talanta*, **28**, 1981, 425.

45 R. Ungaro and A. Pochini, in *Frontiers in Supramolecular Organic Chemistry and Photochemistry,* H-. J. Schneider and H. Dürr (eds.), VCH Publishers, Weinheim, 1991.

46 B. Aurousseau and D. Bauchart, *J. Am. Oil Chem. Soc.*, **7**, 1980, 125.

47 A. R. George and K. D. M. Harris, *J. Mol. Graphics*, **13**, 1995, 138.

48 M. D. Hollingsworth and K. D. M. Harris, in *Comprehensive Supramolecular Chemistry*, Vol. 6, J. L. Atwood, D. D. MacNicol and F. Vögtle (eds.), Pergamon Press, 1996.

49 D. Sybilska and E. Smolková-Keulemansová, in *Inclusion Compounds*, Vol. 3, J. L. Atwood, J. E. D. Davies and D. D. MacNicol (eds.), Academic Press, London, 1984, 173.

50 E. L. Eliel and S. H. Wilen, *Stereochemistry of Carbon Compounds*, Wiley, New York, 1994.

51 H. J. Roth, A. Kleeman and T. Beisswenger, *Pharmaceutical Chemistry*, Vol. 1, Ellis Horwood, Chichester, 1988.

52 W. Schlenk, Jr., *Angew. Chem.*, **72**, 1960, 845.

53 W. Schlenk, Jr., *Liebigs Ann. Chem.*, 1973, 1145.

54 For example, W. Schlenk (to BASF A. -G.), German patent 1,080,557 (1958). *Chem. Abstr.*, 1962, **56**, 2334g. German Patent, 1,074,583 (1960). *Chem. Abstr.*, 1961, **55**, 13318c.

55 G. Tsoucaris, in *Organic Solid State Chemistry*, G. R. Desiraju (ed.), Elsevier, Amsterdam, 1987, 207.

56 B. Tsadon, L. Decsei and M. Szilasi, *J. Chromatogr.*, **270**, 1983, 127.

57 T. Koscielski, D Sybilska and J. Jurczak, *J. Chromatogr.*, **280**, 1983, 131.

58 F. Toda, K. Tanaka and H. Ueda, *Tetrahedron Lett.*, **22**, 1981, 4669.

59 F. Toda and K. Tanaka, *Chem. Lett.*, 1986, 1905.

60 F. Toda and H. Miyamoto, *Chem. Lett.*, 1995, 809.

61 F. Toda and K. Tanaka, *Chem. Commun.*, 1997, 1087.

62 P.P. Korkas, E. Weber, M. Czugler and G. Náray-Szabó, *J. Chem. Soc., Chem. Commun.*, 1995, 2229.

63 D. Seebach, *Angew. Chem.*, **102**, 1990, 1363.

64 F. Toda, J. Okada and K. Mori, *Angew. Chem., Int. Ed. Engl.*, **27**, 1988, 859.

65 G. M. J. Schmidt, *Pure and Applied Chemistry*, **27**, 1971, 647.

66 F. Toda, in *Reactivity in Molecular Crystals*, Y. Ohashi (ed.), VCH, Weinheim, 1993.

67 F. Toda, M. Yagi and K. Kiyoshige, *J. Chem. Soc., Chem. Commun.*, 1988, 958.

68 F. Toda, and K.Mori, *J. Chem. Soc., Chem. Commun.*, 1989, 1245.

69 F. Toda, K. Tanaka and S. Iwata; *J. Org. Chem.*, **54**, 1989, 3007.

70 F. Toda and Y. Tokumaru, *Chem. Lett.*, 1990, 987.

71 F. Toda, M. Yagi and K. Kiyoshige, *J. Chem. Soc., Chem. Commun.*, 1988, 958.

72 F.Toda, K. Tanaka and S. Iwata, *J. Org. Chem.*, **54,** 1989, 3007.

73 M. R. Caira, L. R. Nassimbeni and A. F. Wildervanck, *J. Chem. Soc., Perkin Trans. 2*, 1995, 2213.

74 A. R. West, *Solid State Chemistry and its Applications*, Wiley, Chichester, 1984.

75 P. J. Haines, *Thermal Methods of Analysis*, Chapman and Hall, London, 1995.

76 M. E. Brown, *Introduction to Thermal Analysis - Techniques and Applications*, Chapman and Hall, London, 1988.

77 K. J. Laidler, *Chemical Kinetics*, McGraw-Hill, New York, 1965.

78 E. L. Charsley and S. B. Warrington (eds.), *Thermal Analysis - Techniques and Applications*, Royal Society of Chemistry, London, 1992.

79 W. W. M. Wendlandt, *Thermal Analysis*, 3rd ed., Wiley, New York, 1986.

80 A. K. Galwey and M. E. Brown, *Thermochim. Acta*, **269**, 1995, 1.

81 W. Gomes, *Nature*, **192**, 1961, 866.

82 A. K. Galwey, *J. Thermal Anal.*, **41**, 1994, 267.

83 A. Reisman and J.Karlak, *J. Am. Chem. Soc.*, **80**, 1958, 6500.

84 W. W. Wendlandt, *Anal. Chim. Acta*, **27**, 1962, 309.

85 J. M. Criado and A. Ortega, *Thermochim. Acta*, **239**, 1994, 1.

86 W. E. Garner (ed.), *Chemistry of the Solid State*, Butterworth, London, 1955.

87 M. E. Brown, D. Dollimore and A. K. Galwey, *Comprehensive Chemical Kinetics*, Vol. 22, Elsevier, Amsterdam, 1980.

88 D. A. Young, *Decomposition of Solids*, Pergamon, Oxford, 1966.

89 E. Weber, in *Comprehensive Supramolecular Chemistry*, Vol. 6, J. L. Atwood, D. D. MacNicol and F. Vögtle (eds.), Pergamon Press, 1996.

90 D. J. Cram, *Angew. Chem., Int. Ed. Engl.*, **27**, 1988, 1009.

91 F. Toda, in *Comprehensive Supramolecular Chemistry*, Vol. 6, J. L. Atwood, J. E. Davies, D. D. MacNicol and F. Vögtle (eds.), Elsevier, 1996.

92 E. Weber, K. Skobridis, A. Wierig, L. R. Nassimbeni and L. Johnson, *J. Chem. Soc., Perkin Trans. 2*, 1992, 2123.

93 E. Weber, N. Dörpinghaus and I. Csöregh, *J. Chem. Soc., Perkin Trans. 2*, 1990, 2167.

94 I. Goldberg, Z. Stein, K. Tanaka and F. Toda, *J. Incl. Phenom.*, **6**, 1988, 15.

95 I. Goldberg, Z. Stein, A. Kai and F. Toda, *Chem. Lett.*, 1987, 1617.

96 R. W. Layer, in *Encyclopedia of Chemical Technology*, 4th Edition, Vol. 2, Wiley, New York, 1995.

97 K. Venkataraman, *The Chemistry of Synthetic Dyes*, Vol. 2, Academic Press, New York, 1952.

98 R. P. Lattimer, E. R. Hooser, R. W. Layer and C. K. Rhee, *Rubber Chem. Technol.*, **56**, 1983, 431.

99 K. H. Saunders, *The Aromatic Diazo-compounds and Their Technical Applications*, Edward Arnold & Co., London, 1949.

100 P. Glafkides, *Photographic Chemistry*, Vol. 2, Fountain Press, London, 1960.

101 L. Krumenacker, M. Constantini, P. Pontal and J. Sentenac, in *Encyclopedia of Chemical Technology*, 4th Edition, Vol. 13, Wiley, New York, 1995.

102 E. F. V. Scriven, J. E. Toomey, Jr., R. Murugan, in *Encyclopedia of Chemical Technology*, 4th Edition, Vol. 20, Wiley, New York, 1995.

103 A. J. Gordon and R. A. Ford, *The Chemist's Companion, A Handbook of Practical Data, Techniques and References*, Wiley, New York, 1972.

2. EXPERIMENTAL

2.1 HOST COMPOUND

The host compound 1,1-bis(4-hydroxyphenyl)cyclohexane (hereafter abbreviated to **H**) was supplied by Professor Fumio Toda from Ehime University, Japan. The compound was also synthesised by the author, following the procedure described by McGreal *et. al*[1].

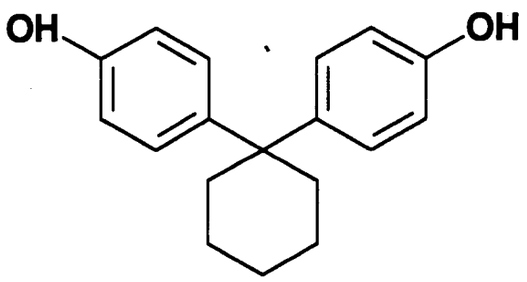

Figure 1: 1,1-bis(4-hydroxyphenyl)cyclohexane (**H**)

Methodology:

A mixture of 160g glacial acetic acid (96%) and 150g H_2SO_4(conc.) was prepared and cooled to 15°C. 2mL Dimethylsulphate was added to the mixture. A separate mixture of phenol (352g, 3.75mol) dissolved in cyclohexanone (73.6g, 0.75mol) was prepared. This solution was added dropwise, while stirring, to the first solution over a period of 30 minutes. The resulting mixture was cooled to 17°C, and was stirred for a further 30 minutes. The crystalline reaction product was obtained from this solution, and was purified by washing with water and then with a solution of sodium acetate. Excess, unreacted phenol was removed from the product by repeated heating of the product in water, followed by recrystallisation from toluene. The product was dried *in vacuo* at 120°C for two hours to remove any included solvent of recrystallisation. Purity of the product was confirmed by nuclear magnetic resonance (nmr) and C, H, N micro-analysis[1]. The product had a melting point

in the range 183 - 185°C, as determined by differential scanning calorimetry (DSC). The melting point quoted by McGreal[1] was 184°C.

2.2 GUEST COMPOUNDS

The solid guest compounds - the benzenediols and phenylenediamines - were recrystallised from chloroform and dried *in vacuo*. Complete desolvation and purity was confirmed by differential scanning calorimetry (DSC) and thermal gravimetry (TG). The liquid guest compounds, the picolines and lutidines, were distilled and stored over dried molecular sieves. The common solvents included by the host were also stored over dried molecular sieves.

2.3 CRYSTAL GROWTH

The inclusion compounds formed with the host, **H**, are listed in Table 1.

2.3.1 Solid Guest Compounds

Stoichiometric quantities of **H** and the solid guests were dissolved in a minimum amount of hot ethyl acetate. The solutions were forced through 0.5μm Teflon Millex-LCR filters to remove dust and debris, thereby reducing the number of nucleation sites. The solutions were kept in glass vials and were covered with perforated parafilm. They were allowed to evaporate over a period of 3 to 5 days at room temperature, until suitable single crystals formed.

2.3.2 Liquid Guest Compounds

Crystals of the inclusion compounds formed between **H** and the liquid guests were obtained by dissolving the host directly into an excess of the heated guests. These solutions were filtered using 0.5μm Teflon Millex-LCR filters and the usual crystallisation techniques of slow evaporation and cooling were employed. In the case of the **2PIC**, **DIOXW** and **EAW** complexes, water was not deliberately added, but rather was included from the atmosphere.

Another method of complex formation employed was that of fast stirring. In this technique, the host was dissolved in the liquid guests, and the solutions were stirred continuously for 1 to 2 days until fine microcrystalline samples of the inclusion compounds were obtained.

Table 1: Inclusion compounds formed with **H**.

Guest	**Host:Guest Ratio**	**Code Name of Complex**
o-phenylenediamine	1:1	**OPDA**
m-phenylenediamine	1:1	**MPDA***
p-phenylenediamine	1:½	**PPDA**
o-benzenediol	1:1	**OBD**
m-benzenediol	1:1	**MBD***
p-benzenediol	1:½	**PBD**
2-picoline / water	1:1:1	**2PIC**
3-picoline	1:1	**3PIC**
4-picoline	1:1	**4PIC**
2,4-lutidine	1:1	**24LUT**
2,6-lutidine	1:1	**26LUT***
3,5-lutidine	1:1	**35LUT**
methanol	1:1	**MEOH**
ethanol	1:1	**ETOH**
i-propanol	1:1	**PROH**
n-butanol	1:1	**BUOH**
1,4-dioxane / water	1:½:1	**DIOXW**
ethyl acetate / water	1:½:1	**EAW**

* Single crystals of these complexes could not be obtained, and therefore their structures were not determined by X-ray analysis.

2.4 MICROANALYSIS

A Fisons EA1108 CHNS-O Elemental Analyser was used to analyse crystals of the inclusion complexes formed for carbon, hydrogen and nitrogen content, in order to determine the host:guest ratios in the complexes. The samples were not dried under vacuum, to avoid risk of guest loss. The analyses were carried out in duplicate, with an expected reproducibility of 0.3% for carbon and nitrogen, and 0.2% for hydrogen. Microanalysis was performed only on those complexes of the solid guest compounds, since thermal gravimetry was employed to determined the host:guest ratios in those complexes with liquid guest compounds.

Hydrogen, carbon and nitrogen contents were calculated for different host:guest ratios, and were compared to the results obtained by microanalysis. Table 2 lists the calculated C, H, N and O content for inclusion compounds with common host:guest ratios. The table illustrates that the difference between the values for complexes of different host:guest ratios far exceeds the error of microanalyses results, thus this experimental technique is applicable to determine the host:guest ratio in these particular inclusion complexes.

Table 2: Calculated C, H, N and O contents for possible inclusion complexes between **H** and the solid guest compounds.

	Host:guest ratio	**%C**	**%H**	**%N**	**%O***
H • ½ phenylenediamine	1:½	78.2	7.4	4.3	10.1
H • 1 phenylenediamine	1:1	76.6	7.4	7.4	8.6
H • 2 phenylenediamine	1:2	74.4	7.4	11.6	6.6
H • ½ benzenediol	1:½	78.0	7.1	-	14.9
H • 1 benzenediol	1:1	76.2	6.9	-	16.9
H • 2 benzenediol	1:2	73.8	6.6	-	19.6

* Obtained by difference

2.5 DENSITY MEASUREMENT

When crystals of inclusion compounds were sufficiently stable, densities were measured by the flotation method. Good quality, single crystals were blotted dry on filter paper. The crystals were suspended in mixtures of aqueous potassium iodide and distilled water. The densities of these KI solutions were measured using a Paar DMA35 digital density meter.

2.6 THERMAL ANALYSIS

Thermogravimetric (TG) and Differential Scanning Calorimetric (DSC) analyses have proven to be convenient techniques for the study of the thermal stability of inclusion compounds.

TG experiments measure the weight loss of a sample as a function of temperature, when the sample is heated at a constant rate. These experiments were performed using a Perkin Elmer PC7 system. The TG thermocouple and balance were calibrated using built-in procedures for furnace and weight calibration. Two-point standard temperature calibration was performed by measuring the Curie points of Alumel (163 °C) and Nickel (354 °C).

DSC experiments measure the enthalpy changes which occur when desolvation or phase transformations occur in inclusion complexes, and were usually performed in collaboration with a TG experiment. The temperature of onset, T_{on}, of the guest release event is an indication of the stability of the inclusion complex. The DSC analyser was calibrated by measuring the apparent melt points of indium and zinc and correcting these to the known values of 156.4 °C and 419.5 °C. Calibration of heat flow was achieved using the enthalpy of melting for indium (28.5 J g^{-1}).
All DSC and TG analyses were carried out at heating rates of 10 °C min^{-1} using dry nitrogen purge gas at a flow rate of 40 mL min^{-1}. Samples were in the mass range 1 - 8 mg, and were blotted dry and lightly crushed before analysis.

Samples were placed in open platinum pans for TG runs, and in closed, vented aluminium pans for DSC runs. Baseline corrections were applied to the DSC curves. Programmed temperature runs were typically in the range 30 - 200 °C, unless stated otherwise.

Isothermal TG experiments were performed to obtain kinetic data. These experiments were performed under the same general conditions as before, but the samples were rapidly heated to the required temperature, which was then maintained until guest desorption was complete.

Both TG and DSC experiments are dependent on sample preparation and experimental conditions. Particle size and heating rates can have a significant influence on the onset temperatures of thermal events[2]. Attempts should be made to keep the geometries of the DSC calorimeters and the rate of flow of purge gas constant. Therefore care was taken to prepare all the samples in as reproducible a manner as possible, particularly with respect to particle size.

2.7 HOT STAGE MICROSCOPY

Hot stage microscopy was carried out in an attempt to correlate the physical appearance of samples with the thermal events observed in the thermal analysis experiments. Crystals were subjected to heating on a Linkam TH600 hot stage mounted on a Nikon microscope. The temperature was controlled by a Linkam CO600 temperature controller, and a camera was mounted on the microscope to photograph thermal events. The crystals were immersed in silicone oil, an inert medium, to observe the desolvation of guest by the evolution of gas bubbles into the medium.

2.8 KINETICS OF DECOMPOSITION

2.8.1 Isothermal Methods

The theory of the kinetics of decomposition of solids is well established and has been reviewed by Brown[3]. Series of isothermal TG experiments were performed on powdered samples. These were carried out over selected temperature ranges, usually lower than the onset temperatures for desolvation of the inclusion complexes, so that desolvation occurs over a time of approximately 4 to 8 hours. Data obtained from these experiments were reduced to extent of reaction, α, versus time curves, and were fitted to various kinetic equations until appropriate models were determined. The kinetic equations which apply to solid state reactions are listed in Table 3.

2.8.2 Non-isothermal methods

Flynn and Wall[4] have described a method to determine kinetic parameters, and this was employed as an alternative to the isothermal method. This method is less laborious and time consuming, although a degree of accuracy is often lost. However, precautions can be taken to ensure consistent particle size distribution of the solid inclusion compound. Samples are subjected to a number of TG experiments over the same temperature range, with each run performed at a different heating rate. The rate of decomposition is given by

$d\alpha/dT = (A/\beta)\, f(\alpha) \exp(-E_a/RT)$

where α is the extent of reaction, T is the absolute temperature, A is the pre-exponential factor of the Arrhenius equation, β is the constant heating rate, E_a is the activation energy and $f(\alpha)$ is a function of the extent of reaction (weight loss). log β is plotted against T^{-1}, at selected extents of decomposition, and the activation energy is determined from the slope.

Table 3: Solid state rate expressions

	$f(\alpha) = kt$	$g(\alpha) = 1/k(d\alpha/dt)$
Acceleratory		
P1 power law	$\alpha^{1/n}$	$n(\alpha)^{(n-1)/n}$
E1 exponential law	$ln\ \alpha$	α
Sigmoidal		
A2 Avrami-Erofe'ev	$[-ln(1-\alpha)]^{1/2}$	$2(1-\alpha)[-ln(1-\alpha)]^{1/2}$
A3 Avrami-Erofe'ev	$[-ln(1-\alpha)]^{1/3}$	$3(1-\alpha)[-ln(1-\alpha)]^{2/3}$
A4 Avrami-Erofe'ev	$[-ln(1-\alpha)]^{1/4}$	$4(1-\alpha)[-ln(1-\alpha)]^{3/4}$
B1 Prout-Tompkins	$ln[\alpha/(1-\alpha)]$	$\alpha(1-\alpha)$
Deceleratory		
Geometrical models:		
R2 contracting area	$1-(1-\alpha)^{1/2}$	$2(1-\alpha)^{1/2}$
R3 contracting sphere	$1-(1-\alpha)^{1/3}$	$3(1-\alpha)^{2/3}$
Diffusion controlled models:		
D1 one-dimensional	α^2	$1/2\alpha$
D2 two-dimensional	$(1-\alpha)ln(1-\alpha)+\alpha$	$[-ln(1-\alpha)]^{-1}$
D3 three-dimensional	$[1-(1-\alpha)^{1/3}]^2$	$3(1-\alpha)^{2/3} / 2[(1-\alpha)^{1/3}]$
D4 Ginstling-Brounshtein	$[1-2\alpha/3)-(1-\alpha)^{2/3}$	$3 / 2[1-\alpha)^{-1/3} - 1]$
'order' of reaction		
F1 first order	$-ln(1-\alpha)$	$1-\alpha$
F2 second order	$1/(1-\alpha)$	$(1-\alpha)^2$
F3 third order	$[1/(1-\alpha)]^2$	$(1-\alpha)^3$
Fn n-th order	$[1/(1-\alpha)]^n$	$(1-\alpha)^n$

2.9 COMPETITION EXPERIMENTS

Competition experiments were performed to determine the complexation selectivity of the host for the various isomers of a compound. Competition experiments were also performed to determine the selective complexation of the host with the alcohols methanol, ethanol, *i*-propanol and *n*-butanol.

The experiments were performed in water suspensions for the solid guest systems (phenylenediamines and benzenediols), and by crystallisation from solution for the liquid guest systems (picolines, lutidines and alcohols).

2.9.1 Water Suspension

Mixtures of the solid guests in mole fractions varying from 0 to 1 in steps of 0.1 were dissolved in distilled water. The host, **H**, which is insoluble in water, was added to each solution. The total guest concentration in each solution was always in a 20:1 excess over the host, **H**, so that an excess of even the lesser guest was always maintained with respect to **H**. The suspensions were shaken for 1 hour during which time complexation occurred. The solid inclusion compounds so formed were filtered and dissolved in ethyl acetate. The relative amounts of guests in the inclusion compounds were determined by either GC or HPLC analyses.

2.9.2 Crystallisation

As before, a series of mixtures of the liquid guests was made up with mole fractions of each guest varying from 0 to 1 in steps of 0.1. **H** was dissolved directly into these mixtures. Guest volumes were chosen so that an excess of the lesser guest was always maintained with respect to **H**. The solutions were allowed to evaporate slowly at room temperature over a period of 3 to 5 days, until crystals of the inclusion complexes appeared. Guest ratios in the mother liquor were checked by GC to ensure that no significant evaporation of the lower boiling component had occurred.

In the picoline and lutidine competition experiments, crystals of the inclusion complexes formed were dissolved in ethyl acetate, and the relative amounts of the guests included in each instance were determined by GC analysis.

In the alcohol competition experiments, crystals of the inclusion complexes formed were removed from the mother liquor solutions and blotted dry on filter paper. The crystals were placed in air tight glass vials with silicone seals incorporated into the screw-on lids. The vials were heated to 150°C on a hot plate to induce desolvation of the inclusion compounds. On air-cooling of the vials, the vapours of alcohol guest condensed on the sides of the vials, and these drops were used for GC analyses.

2.10 GAS CHROMATOGRAPHY (GC)

The relative amounts of the phenylenediamines and lutidines included during the competition experiments were analysed by GC using a Carlo Erba Fractovap 4200 instrument equipped with a BP255 capillary column (0.25 mm diameter, 25 m length) and a Spectra-Physics SP4290 integrator.

For the analyses involving picolines, a Varian 3300 instrument with a Supelcowax 10 column (0.2 mm diameter, 30 m length) and a Varian 4290 integrator was used.

For the GC analyses of the alcohols, a Philips PYE Unicam Series 304 chromatograph equipped with a 10% OV101 on Chromosorp column (1m) was used. This apparatus was linked to a Waters 746 Data Module integrator.

2.11 HIGH PERFORMANCE LIQUID CHROMATOGRAPHY (HPLC)

The relative amounts of the isomers of benzenediol included during the competition experiments were determined by HPLC using a Waters 510 pump and Series 440 Absorbance detector. The column used was a Prodigy 5μ C8 (4.6 mm diameter, 150 mm length).

2.15 CRYSTAL STRUCTURE ANALYSIS

Single crystals of suitable size (typically 0.2 - 0.5 mm in all dimensions) and quality were selected for diffractometry experiments. Stable crystals were mounted directly onto glass fibres, but the less stable crystals were mounted in 0.3 mm or 0.5 mm Lindemann capillary tubes which were flame-sealed. The glass fibres or Lindemann tubes were then mounted in brass pins before insertion into the diffraction goniometer head. A photograph of a crystal mounted in a Lindemann capillary is shown in Figure 2.

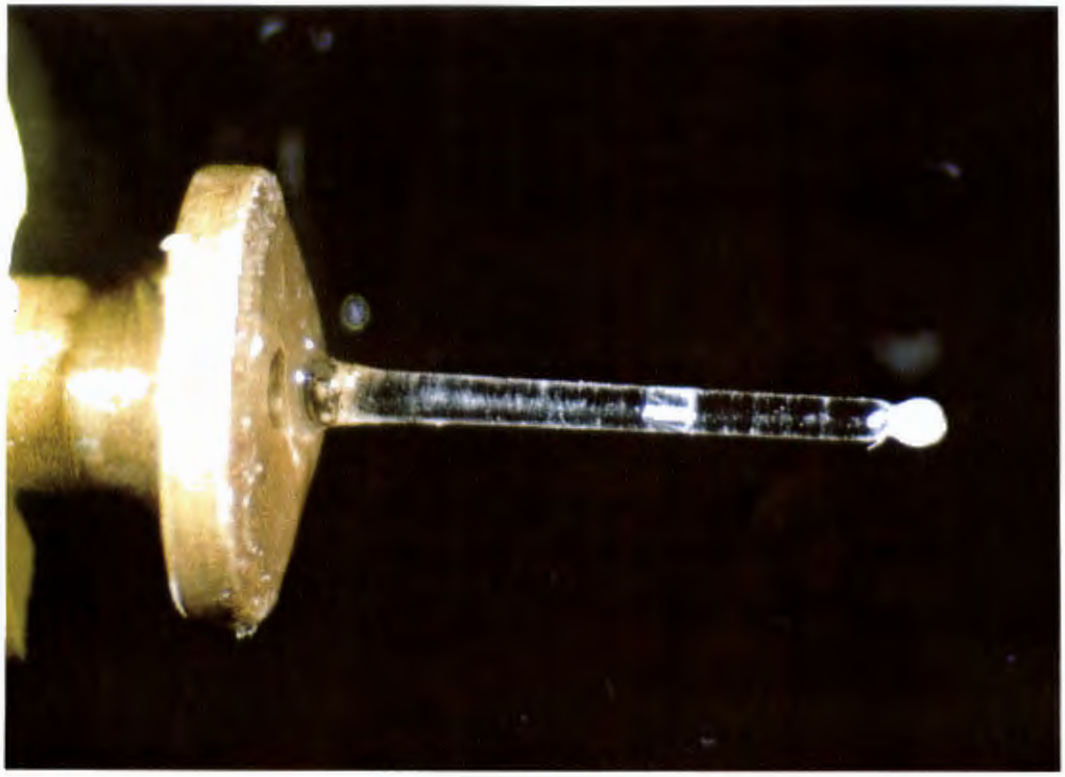

Figure 2: Photograph of a crystal of **BUOH** mounted in a Lindemann capillary.

Preliminary cell parameters and space group symmetry were determined from oscillation and Weissenberg photographs taken on a Stoë goniometer using Ni-filtered Cu-K_α radiation (λ = 1.5418 Å).

Accurate cell parameters were obtained by least-squares analysis of the setting angles of 24 reflections collected in the θ range 16 - 17° and centred on the diffractometer. Data were collected on an Enraf-Nonius CAD4 diffractometer at room temperature using Mo-K_α radiation (λ = 0.7107 Å) and the ω-2θ scan mode with a final acceptance limit of 20σ at 20° min^{-1} and a maximum scan time of 40s. The vertical aperture length was fixed at 4 mm, the aperture width at (1.12 + 1.05 tan θ)mm and the scan width at ω = (x + 0.35 tan θ)°, with x = 0.80 or 0.85. During each data collection, three reference reflections were monitored periodically to check crystal stability. Data were corrected for Lorentz-polarisation effects. Absorption corrections were not applied as values of μR_{min} and μR_{max} (where R_{max} and R_{min} are one-half the largest and smallest crystal dimensions respectively) were between 0 and 0.1 for all crystal fragments used and thus values of A* indicated are 1.00[5], over the whole θ range collected.

2.16 COMPUTATION

2.16.1 Structure solution and refinement

Structure solutions and final refinements were performed on a remote MicroVAX 3100-90 mainframe computer running VMS-5.5. Structures were solved by direct methods using the program SHELX-86[6]. Equivalent reflections were merged and those with $I < 2\sigma(I)$ were suppressed. Subsequent refinement by full-matrix least-squares were performed using the program SHELXL-93[7], in which structures were refined against F^2. To determine the accuracy of the calculated structure model, critical examination of the results was performed. The agreement between observed structure factors (F_o) and calculated structure factors (F_c) is expressed by the residual index, R_1:

$$R_1 = \frac{\sum \| F_o | - | F_c \|}{\sum | F_o |}$$

Refinement against F^2 leads to R indices which are larger than those based on F. Therefore the R-factor based on F values as well as that based on F^2, wR_2, will be quoted.

$$wR2 = \left[\frac{\sum w(F_o^2 - F_c^2)^2}{\sum w(F_o^2)^2}\right]^{\frac{1}{2}}$$

A weighting scheme (w) was refined for each structure, where:

$$w = 1/\left[\sigma^2(F_o^2) + (aP)^2 + bP\right]$$

$$P = [\max(0, F_o^2) + 2F_c^2]/3$$

and a and b were refined for each structure. The Goodness of Fit (S) is based on F^2:

$$S = \left[\sum (w(F_o^2 - F_c^2)^2)/(n-p)\right]^{\frac{1}{2}}$$

where n is the number of reflections and p is the total number of parameters refined. The program examines the analysis of variance and prints a warning that an extinction parameter, x, should be refined if S is significantly higher than unity. When necessary an extinction parameter, x, was refined by least-squares, where F_c is multiplied by:

$$[(1 + 0.001 \times X \times F_c^2 \times \lambda^3) / \sin(2\theta)]^{-\frac{1}{4}}.$$

The expression is empirical and covers both primary and secondary extinction.

Packing factors, defined as the volume of the cell divided by the number of non-hydrogen atoms in the cell, were calculated for all the structures solved. Molecular and packing diagrams were produced using the IBM PC version of PLUTO[8]. The program MOLMAP[9] was used to plot "slices" through the unit cell in order to determine the shape of guest cavities or channels formed by host molecules.

The Cambridge Structural Database[10] was used to search, retrieve and analyse crystallographic data of previously solved crystal structures.

2.16.2 Calculated XRD traces

X-ray powder diffraction patterns were calculated for inclusion complexes using the program LAZY PULVERIX[11] performed on a personal computer in the DOS environment. Space group data, refined unit cell parameter, atomic co-ordinates and thermal parameters obtained from the structure solutions were used as input for the program.

2.17 POTENTIAL ENERGY STUDIES

The potential energy environment of guest molecules in the host structural environment was studied using empirical atom pair potentials. The program HEENY[12] was used to calculate intermolecular non-bonded interactions. HEENY is a modified version of EENY[13] and calculates atom-pair potentials using van der Waals energy of the form

$$U(r) = a\exp(-br)/r^d - c/r^6$$

where *r* is the distance in Å between any pair of atoms and *a*, *b*, *c* and *d* are coefficients calculated by Giglio *et al.*[14] and reviewed by Pertsin and Kitaigorodskii[15] to yield U(r) in kcal mol^{-1}. In addition, hydrogen bonding potentials have been incorporated into the calculations. A simplified version of that used by Vedani and Dunitz[16] was employed, using the potential

$$U_{hb} = \left[\left(A/R^{16}\right) - \left(C/R^{10}\right)\right]\cos^2\theta$$

where U_{hb} is the energy associated with the hydrogen bond, R the distance between the hydrogen atom and the acceptor, θ the angle donor-H···acceptor

and the constants A and C are related to the well-depth U_{min} and the equilibrium distance R_o by $A = -5R_o^{12}U_{min}$ and $C = -6R_o^{10}U_{min}$.

A mixing scheme was introduced to allow the full non-bonded potential U_{norm} to take effect as θ deviates from the ideal angle of 180° such that

$$U_{total} = U_{hb} + \left(1 - \cos^2\theta\right)U_{norm}$$

1 M. E. McGreal, V. Niederl and J. B. Niederl, *J. Am. Chem. Soc.*, **61**, 1939, 345.

2 W. W. M. Wendlandt, *Thermal Analysis*, Wiley, New York, 1964.

3 M. E. Brown, *Introduction to Thermal Analysis*, Chapman & Hall, London, 1988.

4 J. H. Flynn and L. A. Wall, *Polym. Lett.*, **4**, 1966, 323.

5 *International Tables for Crystallography, Vol. C*, A. J. C. Wilson (ed.), Kluwer Academic Publishers, Dodrecht, 1992, 523.

6 G. M. Sheldrick, SHELXS-86, *Crystallographic Computing 3*, G. M. Sheldrick, C. Kruger and R. Goddard (eds.), Oxford University Press, 1985.

7 G. M. Sheldrick, *SHELXL-93: Programme for Crystal Structure Determination*, unpublished work.

8 W. D. S. Motherwell, *PLUTO89, Program for plotting molecular and crystal structures*, University of Cambridge, England, 1989.

9 L. J. Barbour, *Clathration by Diol Hosts: Thermodynamics and Structure*, PhD Thesis, University of Cape Town, 1994.

10 Cambridge Structural Database & Cambridge Structural Database System, Version 5.11, April 1996, Cambridge Crystallographic Data Centre, University Chemical Laboratory, Cambridge, England.

11 K. Yvon, W. Jeitschko and E. Parthe, *J. Appl. Cryst.*, **10**, 1977, 73.

12 C. F. Marais, *HEENY - Modification of EENY to allow H-bonding calculations*, University of Cape Town,1990.

13 W. D. S. Motherwell, *EENY Potential Energy Program*, Cambridge University, England, 1973.

14 E. Giglio, *Nature*, **222**, 1969, 339.

15 A. J. Pertsin and A. I. Kitaigorodskii, *The Atom-atom Potential Method, Chemical Physics 43*, Springer, Berlin, 1987.

16 A. Vedani and J. D. Dunitz, *J. Amer. Chem. Soc.*, **107**, 1985, 7653.

3. INCLUSION OF PHENYLENEDIAMINE GUESTS

The inclusion compounds formed between the host compound, **H**, and the isomers of phenylenediamine will be discussed in this chapter. The thermal behaviour of the complexes was analysed, as well as their preferential formation during competition experiments. The competition experiments were performed to determine whether the observed selectivity upon complexation with the host compound is related to the structural complementarity between the host and guest components in the complexes formed.
Single crystals of the complexes **OPDA** and **PPDA** were grown and their structures will be reported. However, several attempts to obtain single crystals of the inclusion complex between **H** and *m*-PDA were unsuccessful, and therefore the structure of this complex cannot be reported.

Preliminary X-ray photography was used to determine the unit cell parameters, crystal systems and space groups of the complexes **OPDA** and **PPDA**. Crystallographic experimental and refinement details are provided in Table 1. Final atomic co-ordinates, temperature factors, tables of bond lengths and bond angles are contained in Appendix 3, and tables of observed and calculated structure factors are listed in Appendix 4.

Table 1: Crystal data, experimental and refinement parameters for **OPDA** and **PPDA**

	OPDA	**PPDA**
Molecular formula	$C_{18}H_{20}O_2 \bullet C_6H_8N_2$	$C_{18}H_{20}O_2 \bullet ½C_6H_8N_2$
M_r /g.mol^{-1}	376.48	322.41
Space Group	C2/c	$P2_1/c$
a /Å	21.080(2)	6.362(2)
b /Å	6.202(8)	26.610(3)
c /Å	32.132(2)	10.509(2)
β /°	101.88(6)	106.77(2)
V /Å^3	4110.9(7)	1703.4(6)
Z	8	4
D_c /g.cm^{-3}	1.22	1.26
D_m /g.cm^{-3}	1.22(3)	1.25(5)
μ(Mo-Kα) /cm^{-1}	0.77	0.80
F(000)	1616	692
Crystal size /mm	0.4 x 0.5 x 0.5	0.3 x 0.2 x 0.3
Range scanned θ /°	1 - 25	1 - 25
Range of indices	*h*: ±24; *k*: 0, 7; *l*: 0, 38	*h*: ±7; *k*: 0, 31; *l*: 0, 12
Crystal decay /%	7.0	3.0
No. reflections collected	4049	3254
No. reflections observed ($I_{rel} > 2\sigma(I_{rel})$)	2722	2091
No. parameters	279	236
R_1	0.0483	0.0406
wR_2	0.1337	0.1021
S	1.015	0.850
Δρ excursions /eÅ^{-3}	0.250; -0.242	0.161; -0.202

3.1 OPDA

3.1.1 Structure Solution

Stable single crystals of the inclusion complex **OPDA** were obtained. C, H, N micro-analysis indicated the host:guest ratio in **OPDA** to be 1:1 (*exptl*: %C=76.4(2), %H=7.2(2), %N=7.3(1) ; *calc*: %C=76.6, %H=7.4, %N=7.4)[1]. Preliminary oscillation and Weissenberg photography revealed *2/m* Laue symmetry, indicating a monoclinic structure. The X-ray data collection exhibited the following non-extinction reflection conditions:

hkl : $h + k = 2n$

*h*0*l* : $l = 2n$; ($h = 2n$)

0*k*0 : (k=2n)

These correspond to the possible space groups C2/c or Cc. The $|E^2-1|$ values obtained after the first direct methods run implied centrosymmetric statistics. Thus the space group was identified to be C2/c, and this choice was confirmed by the successful refinement of the structure.

The numbering scheme used for the host, **H**, in all the structure solutions in this thesis is shown in Figure 1.

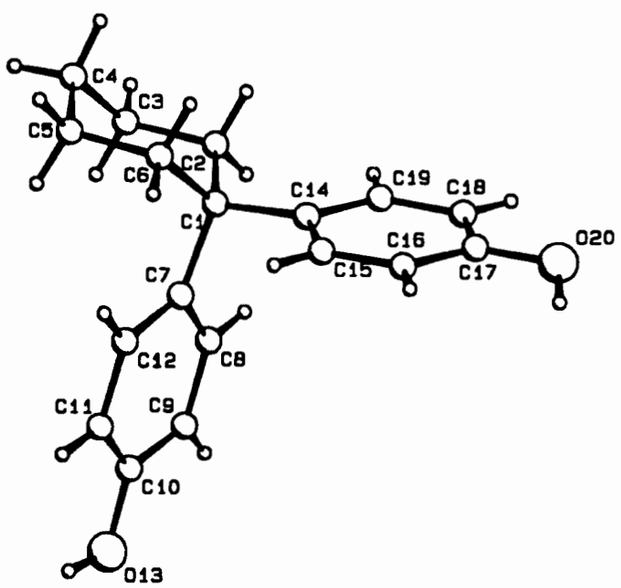

Figure 1: Numbering scheme of **H**

The numbering scheme used for *o*-phenylenediamine is shown in Figure 2.

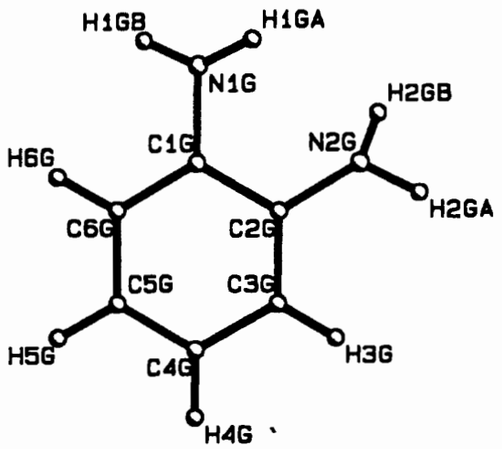

Figure 2: Numbering of *o*-phenylenediamine used during the structure solution of **OPDA**

The positions of the non-hydrogen atoms of both the host and guest molecules in **OPDA** were obtained by direct methods. There are eight host molecules and eight guest molecules in the unit cell. No crystallographic symmetry is imposed on either host or guest molecule. Refinement was carried out with the non-hydrogen atoms of both the host and guest treated anisotropically. The hydrogen atoms of the host and guest were all independently located in difference electron density maps, but in the final model, the aromatic and methylenic hydrogens were geometrically constrained [*d*(C-H) = 1.00Å] and assigned common isotropic temperature factors. The hydroxyl and amine hydrogens were independently located in difference electron density maps. The hydroxyl hydrogens were refined with simple bond length constraints relating O-H distances versus O-O distances[2]. The guest amino hydrogens were refined with geometrical constraints relating the N-H to N-O distances[2]. The amine hydrogens of NG2 displayed high thermal motion and were thus also constrained about the C-N-H angles by assuming the nitrogen to be sp^2 hybridised. The amine hydrogens were fixed at a distance of 2.08Å from CG2.

The structure refined successfully to R_1 = 0.0479. Bond lengths and bond angles of the host and guest molecules in this structure were all in acceptable ranges[3]. The host conformation data obtained from all the structure solutions in this thesis will be discussed in more detail in Chapter 8.

3.1.2 Structure Analysis

The packing diagram of **OPDA** viewed down [010] is shown in Figure 3. Adjacent host molecules hydrogen bond through their hydroxyl groups, and form ribbons which run parallel to [100]. Adjacent ribbons are interlinked by the arrangement of the cyclohexyl rings of the host molecules. The cyclohexyl rings of one ribbon conveniently fit between the cyclohexyl rings of the next ribbon. These double-ribbon structures interact with one another in the *c* direction through hydrogen bonding interactions with the guest molecules. This packing arrangement is similar to that observed between this host and phenol and the isomers of cresol in a study by Goldberg *et al.*[4].

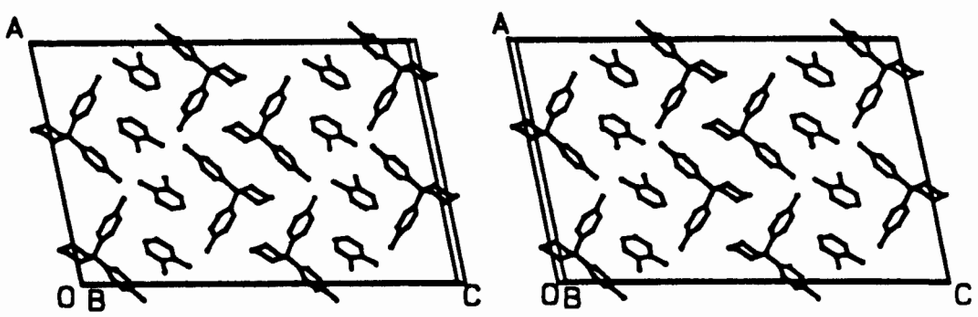

Figure 3: Stereo view of the packing of **OPDA** down [010]

Figure 4 is a MOLMAP plot viewed down [100]. This figure illustrates the shapes of the channels formed by the packing of the host molecules, and the fit of the guest molecules in these channels. The host framework is represented by the hatched area, and the guest atoms are depicted with van der Waals radii. The channels run parallel to *b*, and are relatively unconstricted. The

channels have circular cross sections, with diameters of approximately 6Å. The packing factor for this structure was found to be 18.36 $Å^3$ / non hydrogen atom.

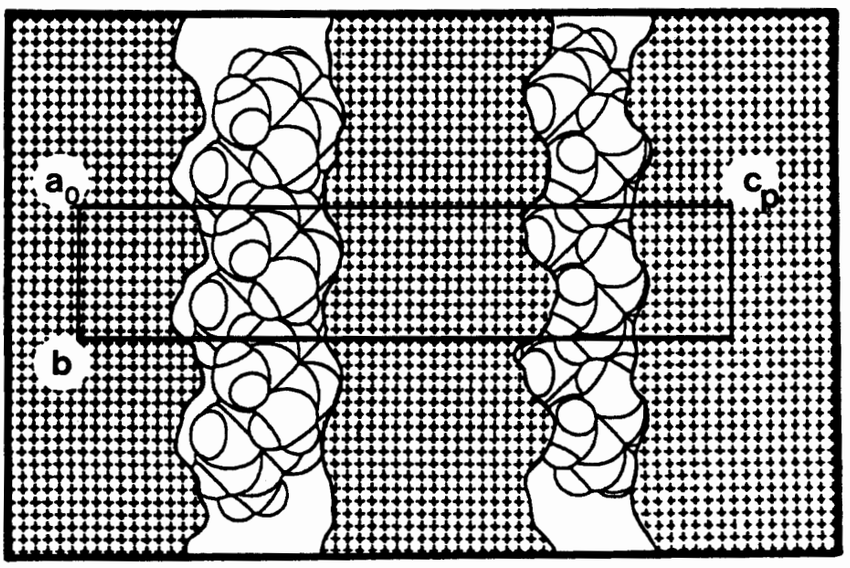

Figure 4: MOLMAP plot of **OPDA** viewed down [100], and sectioned at x = 0.2

Adjacent host molecules are hydrogen bonded to each other through their hydroxyl groups. Each host molecule is also hydrogen bonded to a guest molecule, and therefore each guest molecule is hydrogen bonded to the host structure twice - once from below and once from above. This arrangement utilises the dual capacity for hydrogen bonding of both amine and hydroxyl groups, since these groups act as both proton donors and proton acceptors. Details of the hydrogen bonding interactions in **OPDA** are listed in Table 2.

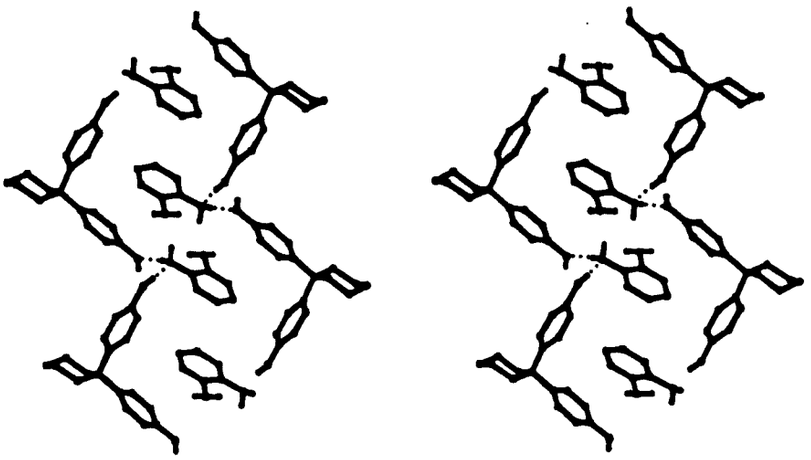

(a) viewed down [010]

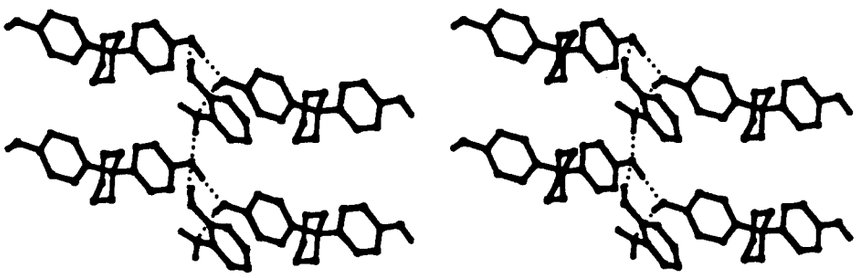

(b) viewed down [100]

Figure 5: Hydrogen bonding scheme of **OPDA**

Table 2: Details of hydrogen bonding in **OPDA**.

Donor	Acceptor	D-H /Å*	D···A /Å*	D-H···A /°*
O13	N1G	0.96(2)	2.677(3)	173(3)
N1G	O20[a]	0.94(3)	2.989(4)	164(3)
O20	O13[b]	0.97(3)	2.675(4)	170(3)

Symmetry code : *(a) x+½ , y+½ , z ; (b) x-½ , y+½ , z*

* **D** = Donor ; **A** = Acceptor

3.1.3 Thermal Analysis

The TG and DSC traces for **OPDA** are illustrated in Figure 6. No distinct features representing guest loss are observed, only the endotherm of melting at T_{on} = 162.5°C. This temperature of melting is between the melting temperatures of the host and *o*-BD guest compounds alone (i.e. 184°C and 103°C respectively). A possible explanation for this single endotherm could be that the guest is released from the crystal at ±160°C, and that **H** dissolves in the hot molten guest, thereby resulting in destruction of the host framework. A crystal of **OPDA** was heated on a hot stage, and physical changes to the crystal on heating were observed. No distinct guest release and host melt events were observed, and the crystal merely degraded to a liquid at 162°C.

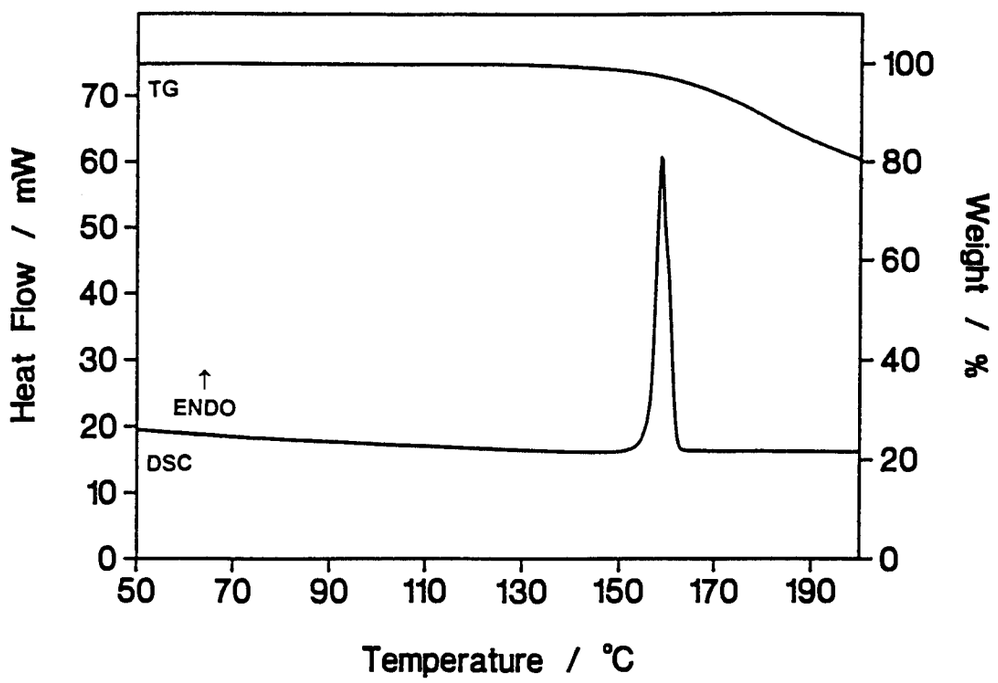

Figure 6: TG and DSC traces of **OPDA**

3.2 PPDA

3.2.1 Structure Solution

The host:guest ratio in this complex was found to be 1:½ by C, H, N micro-analysis (*exptl*: %C=77.9(2), %H=7.2(2), %N=4.1(1) ; *calc*: %C=78.2, %H=7.4, %N=4.3)[1]. Oscillation and Weissenberg photography revealed *2/m* Laue symmetry, indicating a monoclinic structure. The following conditions limiting possible reflections were also observed:

hkl : none

h0l : *l*=2n

0*k*0 : *k*=2n

and thus the space group $P2_1/c$ was assigned for **PPDA**. The unit cell contains four host molecules, located at general positions, and two *p*-PDA guest molecules, located on centres of inversion at Wyckoff position *c*. Due to the centrosymmetrical nature of the guest molecule, it could easily accommodate being positioned on a centre of inversion. The atomic numbering of *p*-phenylenediamine used is illustrated in Figure 7.

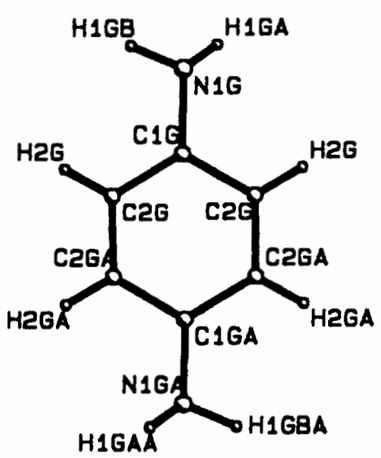

Figure 7: Numbering of *p*-phenylenediamine used during structure solution of **PPDA**

The positions of the non-hydrogen atoms of the host molecule were obtained by direct methods, while the positions of the non-hydrogen atoms of the guest were located in the difference electron density maps upon subsequent refinement. Refinement was carried out with the non-hydrogen atoms of both the host and guest treated anisotropically. The hydrogen atoms of the host and guest were all independently located in difference electron density maps, but in the final model the aromatic and methylenic hydrogens were geometrically constrained [*d*(C-H) = 1.00Å] and assigned common isotropic temperature factors. The hydroxyl and amine hydrogens were independently located in difference electron density maps, and were refined with simple bond length constraints relating O-H distances versus O--O distances, and N-H distances versus N--O distances[1]. All bond lengths and angles of the host and guest molecules were in acceptable ranges for structures of this type, and the structure refined successfully to R_1 = 0.0406.

3.2.2 Structure Analysis

Packing diagrams of **PPDA** are illustrated in Figures 8 and 9, viewed down [100] and down [001] respectively. As before, the host molecules pack to form double ribbons, in this case running parallel to *c*.

The channels formed by the host structure are significantly constricted, and may almost be regarded as pockets. Figure 10 illustrates the channel topography. The channels run parallel to *a*, and have approximately circular cross sections which have diameters of ~1Å across in their narrowest regions, and ~6Å across their widest regions. The packing factor for this structure was calculated to be 17.75 $Å^3$ / non-hydrogen atom.

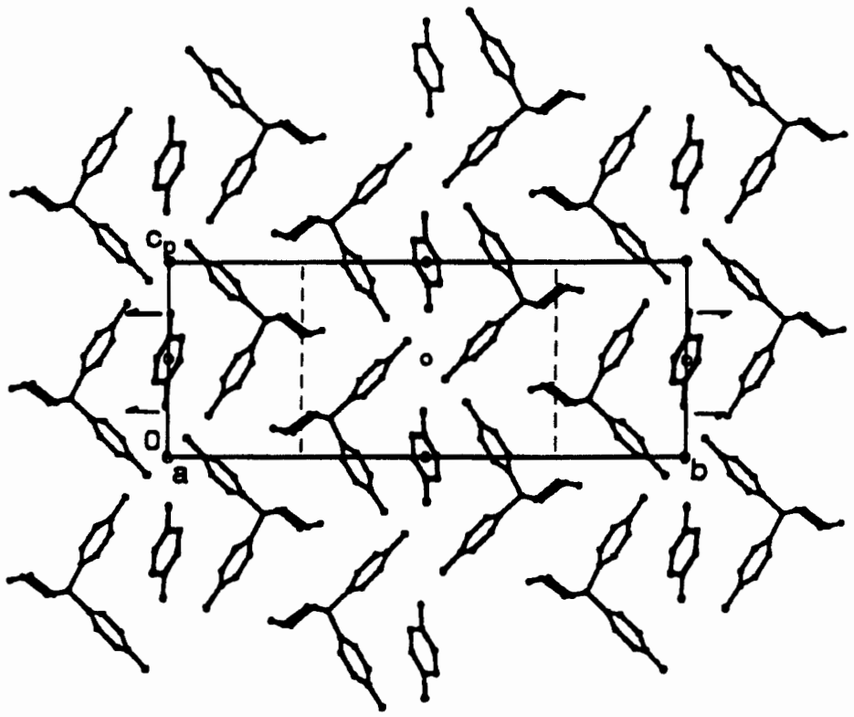

Figure 8: Packing diagram of **PPDA** viewed down [100]

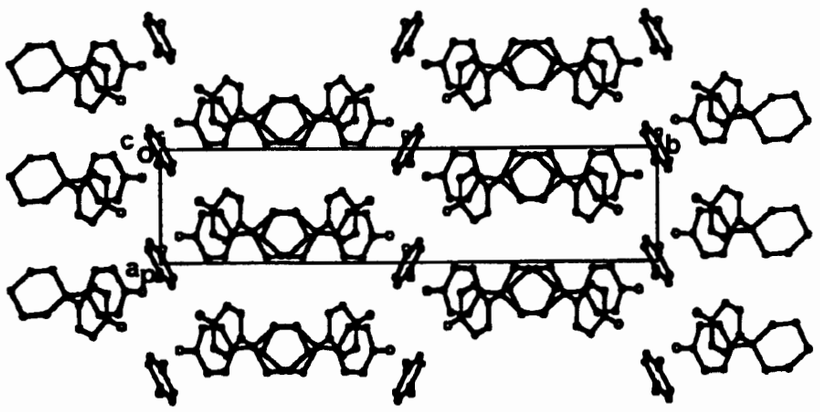

Figure 9: Packing of **PPDA** viewed down [001]

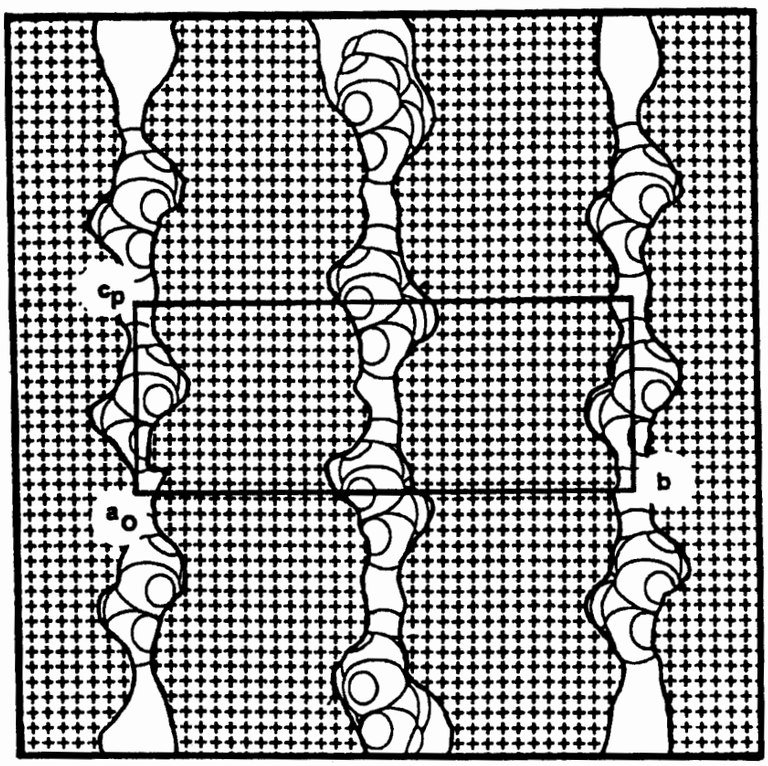

Figure 10: MOLMAP plot of **PPDA** viewed down [100], sectioned at x =0.

The hydrogen bonding scheme is represented graphically in Figure 11. The host–host interactions are similar to those observed in **OPDA**. Each amine group of the guest molecules is hydrogen bonded to two host molecules, thereby utilising its dual hydrogen bonding capacity. Thus each *p*-PDA molecule is hydrogen bonded to the host structure four times. Details of the unique hydrogen bonds are listed in Table 3.

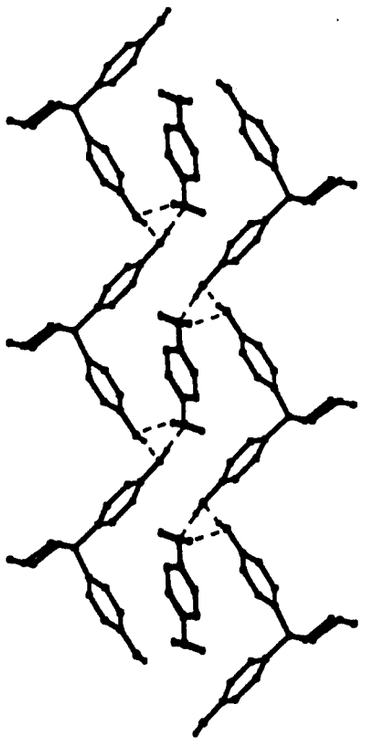

Figure 11: Hydrogen bonding scheme of **PPDA**

Table 3: Details of hydrogen bonding in **PPDA**.

Donor	Acceptor	D-H /Å*	D--A /Å*	D-H--A /°
O20	N1G[a]	0.98(3)	2.742(3)	167(3)
N1G	O13[b]	0.96(2)	3.144(3)	151(2)
O13	O20[c]	0.94(3)	2.799(3)	168(3)

Symmetry code: *(a) -x , 1-y , 1-z (b) 1-x , 1-y , 2-z (c) x , y , z+1*

* **D** = Donor ; **A** = Acceptor

3.2.3 Thermal Analysis

The stability of the structure of **PPDA** is indicated by the thermal analytical results. The TG and DSC traces do not indicate a separate guest release step, and it is assumed that the guest is released only on destruction of the host framework due to melting, at T_{on} = 194.8°C. A sharp endotherm is observed in the DSC trace at this temperature. Hostage microscopy did not reveal any physical changes to a crystal of **PPDA** besides the degradation of the crystal due to melting at 195°C.

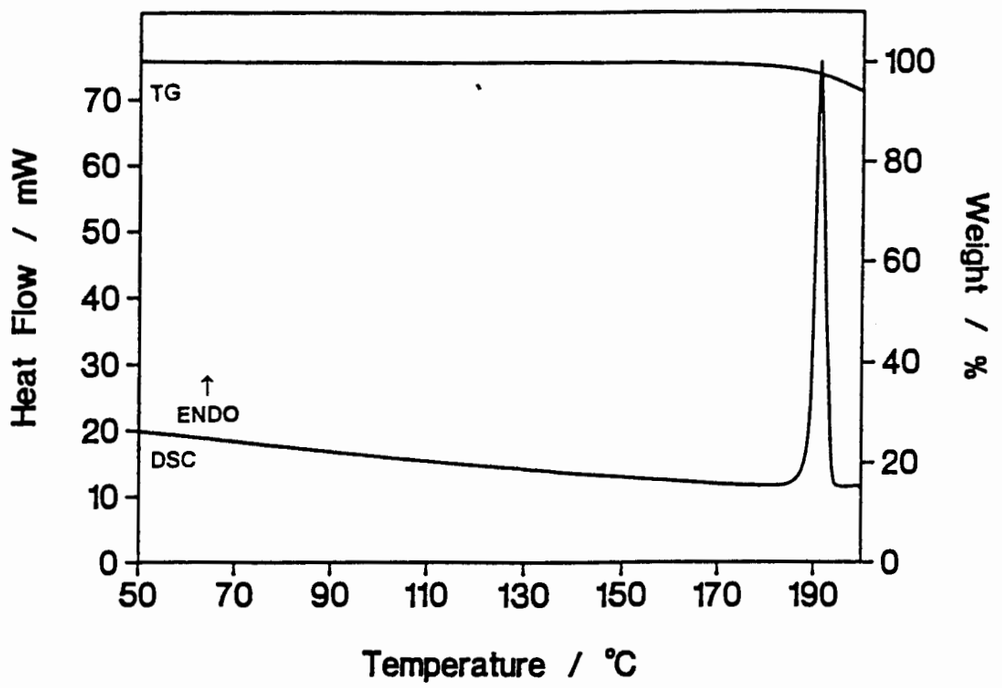

Figure 12: TG and DSC traces of **PPDA**

3.3 POTENTIAL ENERGY CALCULATIONS

Using the methods described in Chapter 2, the potential lattice energies of the complexes **OPDA** and **PPDA** were calculated with the program HEENY. In each case, an unique host and guest molecule was chosen. All the host–host, host–guest and guest–guest interactions experienced by these two molecules to all other molecules in the structure, within a radius of 10 Å, were summed. The results of the calculations are tabulated in Table 4.

Table 4: Results of the lattice energy calculations

	OPDA	**PPDA**
	E /kJ mol^{-1}	E /kJ mol^{-1}
H–H	-193.6	-174.3
H–G	-15.9	-75.3
G–G	-26.3	-15.7
TOTAL:	-235.8	-265.3

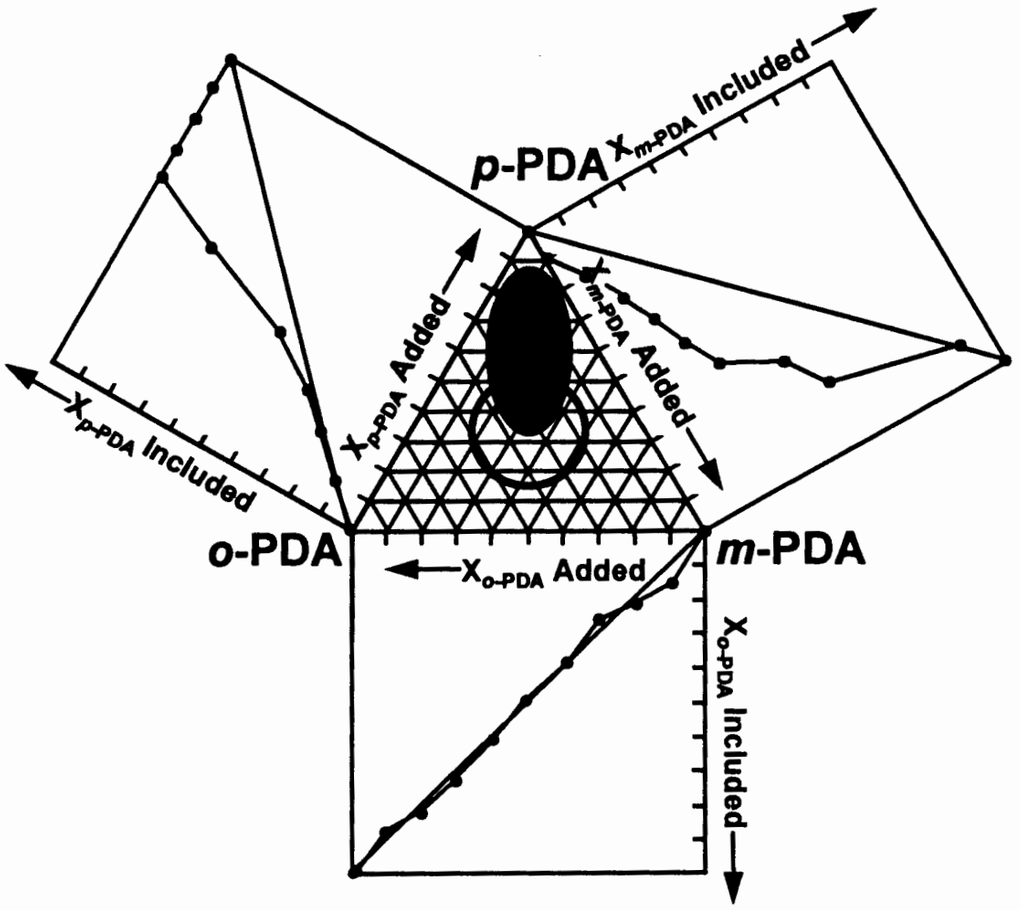

Figure 13: Competition experiments conducted between the host, **H**, and the isomers of phenylenediamine

By virtue of the 'migration' of the circle towards the vertex of the triangle representing *p*-phenylenediamine, it is apparent that there is a general selectivity in favour of *p*-phenylenediamine when all three isomers are initially present. In the 3-component competition experiments, no selectivity is observed between *o*-PDA and *m*-PDA. This would have been indicated by a horizontal shift of the circle away from the least favoured isomer.

Therefore the host compound shows preferential complexation selectivity with the isomers of phenylenediamine in the following order:

p-PDA > *o*-PDA ≅ *m*-PDA.

3.5 SOLID STATE INCLUSION

Stoichiometric quantities of **H** and the isomers of phenylenediamine were co-ground and the products analysed by XRD. This method of complex preparation yielded inclusion complexes between the host and each isomer of phenylenediamine. Each ground product had a unique trace which was not the trace of any starting materials.

An example is shown in Figure 14 for the complex formed between **H** and *m*-phenylenediamine by solid-solid reaction. On grinding a 1:1 stoichiometric amount of these two compounds together, a new XRD trace was observed - confirming that a complex does indeed form between **H** and *m*-phenylenediamine[5]. The product has a melting point of T_{on} = 156.5°C, which lies between the melting points of *m*-PDA (62°C) and **H** (184°C).

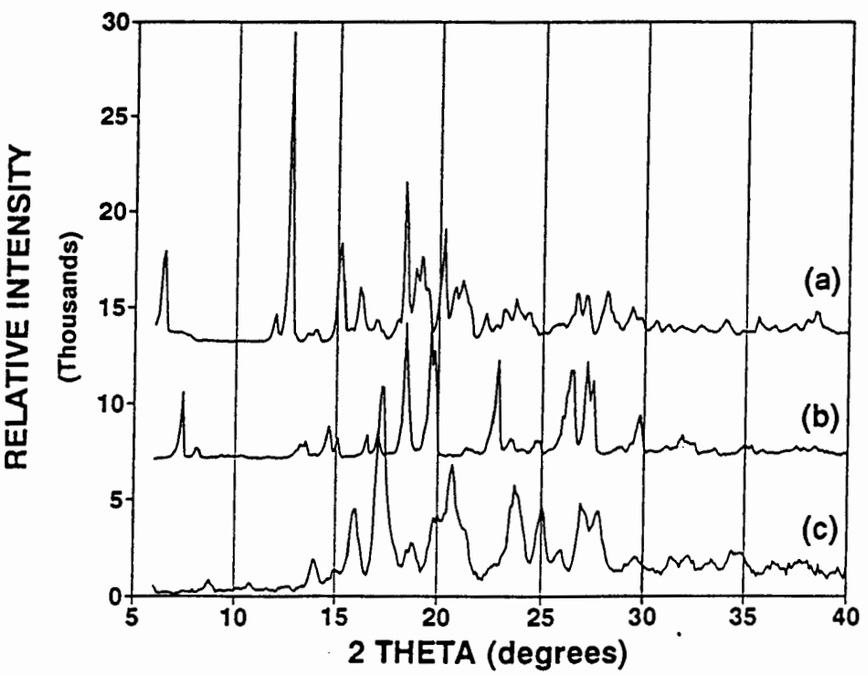

Figure 14: Experimental XRD traces of (a) **H** alone, (b) *m*-PDA alone, and (c) **H** and *m*-PDA co-ground product

When stoichiometric quantities of *o*-PDA and **H** were ground for 15 minutes, the XRD trace of the resulting co-ground product, illustrated in Figure 15, was the same as that calculated for **OPDA** crystals grown from solution. The melting temperature of the co-ground product was also the same as that of the **OPDA** complex (T_{melt} = 162.5°C).

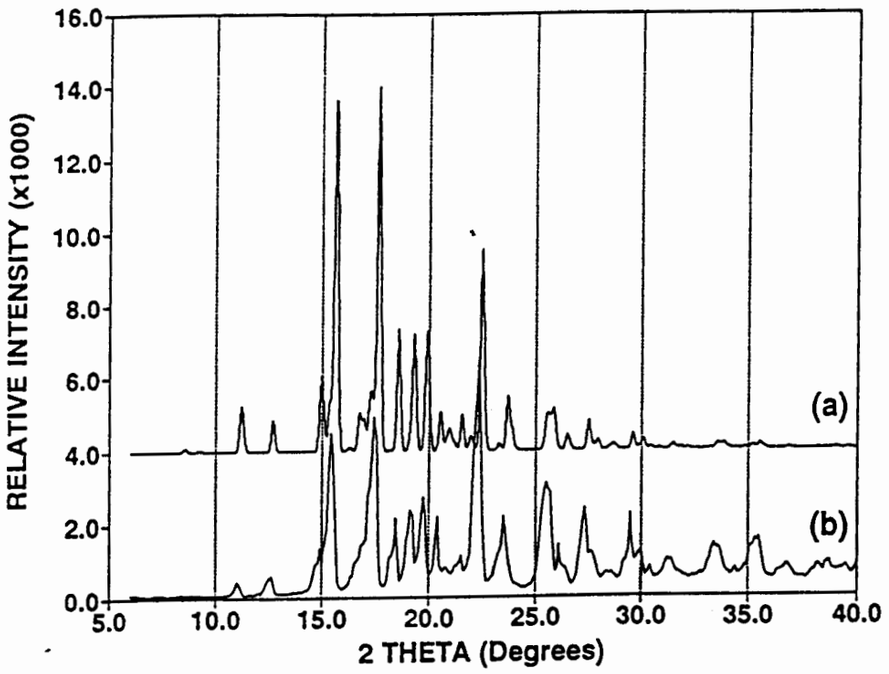

Figure 15: (a) Calculated XRD trace for **OPDA** (using the program LAZY PULVERIX), and (b) experimental XRD trace of *o*-PDA co-ground with **H**

On grinding stoichiometric quantities of *p*-PDA and **H** together, the co-ground product was identical to **PPDA** grown from solution. The experimental XRD trace of the product was the same as that calculated for **PPDA** in relative intensities and peak positions, and the melting temperature of the co-ground product was also 194.8°C.

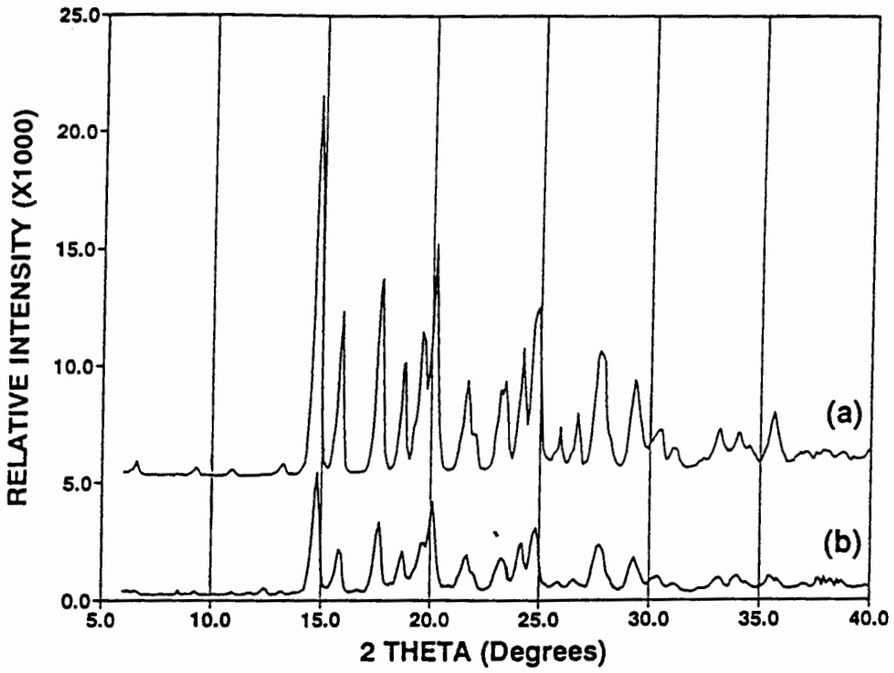

Figure 16: (a) Calculated XRD trace for **PPDA**, and (b) experimental XRD trace of the co-ground product of *p*-PDA and **H**

On examination of the XRD trace of the co-ground product of *m*-PDA and **H**, it was observed that the trace was significantly different from those calculated for **OPDA** and **PPDA**, and therefore the complex formed between *m*-PDA and **H** has a different structure from those discussed in this chapter.

3.6 SOLID STATE COMPETITION

Stoichiometric quantities of **H** and different combinations of the three isomers of phenylenediamine were co-ground. The resulting powdered products were analysed by XRD.

3.6.1 2-Component

The XRD trace of the powdered product resulting when **H**, *o*-PDA and *p*-PDA are co-ground was predominately the same as the trace of **PPDA**, with a few identifying peaks of uncomplexed *o*-PDA being observed. Thus, **H** preferentially complexed with *p*-PDA in the solid state, while *o*-PDA remained uncomplexed.

In a similar manner it was determined that *p*-PDA was included preferentially above *m*-PDA during the solid state experiments, and that *o*-PDA was favoured above *m*-PDA.

3.6.2 3-Component

p-PDA was the favoured isomer in a three component competition in the solid state The XRD trace of the product obtained when **H** was co-ground with stoichiometric amounts of all 3 isomers simultaneously was predominantly that of the **PPDA** complex. Peaks identifying uncomplexed *o*- and *m*-PDA were also observed.

The selectivity of the host for complexation with the isomers of phenylenediamine in the solid state therefore followed a similar trend to that observed in water suspension experiments, i.e. *p*-PDA > *o*-PDA ≥ *m*-PDA.

3.7 DISCUSSION

The structures of the inclusion complexes **OPDA** and **PPDA** have been solved and analysed. The general host packing is similar in both structures, although the host-guest interactions differ significantly. In **OPDA,** each guest molecule is stabilised in the structure by forming two hydrogen bonds to the host framework. In **PPDA**, four stabilising hydrogen bonds are formed per guest molecule. The stabilising energy contribution, calculated with HEENY, of the more extensive hydrogen bonding in **PPDA** was found to be ~20kJ mol^{-1} more than that found in the **OPDA** structure.

Channels are formed by the packing of the host molecules in each structure, although the geometries of the channels are different. In **OPDA**, the channels have large dimensions, and are unconstricted. In **PPDA**, the channels are severely restricted and are only approximately 1Å in diameter at their narrowest parts. The channels in **PPDA** thus provide a significant physical barrier to the desorption of the guest molecules from the structure. The *p*-phenylenediamine molecules therefore have to overcome a this barrier in addition to the breaking of more hydrogen bonds in order to escape the host lattice.

The packing factor for **PPDA** is 17,75 $Å^3$ / non-hydrogen atom and for **OPDA** is 18.36 $Å^3$ / non-hydrogen atom. This factor indicates that **PPDA** has a more tightly packed, stable structure[6], again implying a higher barrier to the destruction of the lattice by desorption of the *p*-PDA guest molecules.

The thermal analysis results confirm the structural results. The higher stability of the **PPDA** complex is indicated by the fact that **PPDA** has a melting point which is 30°C higher than that of **OPDA**. Therefore more energy is required to break the bonds in the **PPDA** crystals.

The inclusion complexes were also formed by co-grinding of the host and guest compounds. The ground products have the same structure as those formed in solution, since they have similar XRD traces and melting points. The formation

of the complexes in the solid state is highly favourable, since complexation is brought about in approximately 15 minutes, and the often difficult task of crystallisation is eliminated.

Competitions experiments were performed in water suspensions and in the solid state to determine whether the observed selectivity of complexation was related to differences in the complementarity between the host and guest constituents. The experiments showed that the preferred selectivity of the host, **H**, in both suspension and in the solid state, followed the trend:
p-PDA > *o*-PDA ≅ *m*-PDA.
The preferential complexation with *p*-PDA is not surprising, since the resulting complex is more stable than that formed between the host and *o*-PDA. Unfortunately a comparison cannot be made with the **H**•*m*-PDA complex structure.

1 Refer to Chapter 2, section 2.4

2 I. Olovsson and P. Jönsson, *The Hydrogen Bond - Structure and Spectroscopy*, P. Schuster, G. Zundel and C. Sarderfy (eds.), North-Holland Publishing Company, USA, 1975.

3 F. H. Allen, O. Kennard, D. G. Watson, L. Brammer, A. G. Orpen and R. Taylor, *J. Chem. Soc., Perkin Trans. 2*, 1987, S1-S19.

4 I. Goldberg, Z. Stein, K. Tanaka and F.Toda, *J. Incl. Phenom.*, **6**, 1988, 15.

5 A. R. West, *Solid State Chemistry and its Applications*, Wiley, Chichester, 1984.

6 A. I. Kitaigorodsky, *Molecular Crystals and Molecules*, Academic Press, New York, 1973.

4. INCLUSION OF BENZENEDIOL GUESTS

The structures of the inclusion compounds formed between the host, **H**, and *o*-benzenediol and *p*-benzenediol, **OBD** and **PBD** respectively, were solved and analysed. Many attempts to obtain single crystals of the inclusion complex between **H** and *m*-benzenediol were unsuccessful, and therefore the structure of this complex cannot be reported. The thermal behaviour of the three complexes was studied, as well as their preferential formation during competition experiments. The observed selectivity of the host upon complexation will be discussed in terms of the structural differences between the complexes formed.

Table 1 lists details of crystallographic experimental and refinement parameters for **OBD** and **PBD**. The unit cell parameters, crystal systems and space groups of the complexes were determined by X-ray photography. Final atomic co-ordinates, temperature factors, tables of bond lengths and bond angles are contained in Appendix 3, and tables of observed and calculated structure factors are listed in Appendix 4.

No. parameters	[illegible]	[illegible]
R_1	0.0424	0.0423
wR_2	0.1126	0.1097
S	1.046	1.028
$\Delta\rho$ excursions /e Å^{-3}	0.160 ; -0.226	0.194 ; -0.228

4.1 OBD

4.1.1 Structure Solution

OBD crystallises in the triclinic crystal system, the possible space groups being P1 and P $\bar{1}$. The centrosymmetric space group, P $\bar{1}$, was indicated by $|E^2-1|$ values in the range 0.849 to 1.071 for the zonal reflections 0*kl*, *h*0*l*, *hk*0 and the remainder of the reflections, and this choice was confirmed by successful refinement of the structure.

The atomic numbering used for the host compound is as before (Chapter 3), while the numbering scheme used for *o*-benzenediol is given in Figure 1.

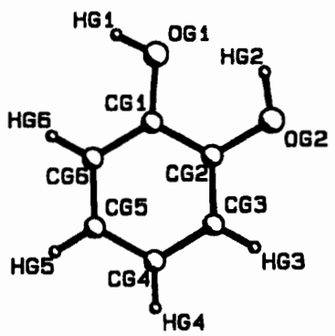

Figure 1: Atomic numbering of *o*-benzenediol

Direct methods calculations yielded the positions of the non-hydrogen atoms of both the host and guest molecules. C, H, N micro-analysis indicated that the host:guest ratio in **OBD** was 1:1 (*exptl*: %C = 75.9(1), %H = 7.0(1); *calc*: %C = 76.2, %H = 6.9)[1]. Both the host and guest molecules are located at general positions in the cell, and Z = 2. Refinement was carried out with all the non-hydrogen atoms treated anisotropically. The hydrogen atoms of the host and guest were all independently located in difference electron density maps, but in the final model the aromatic and methylenic hydrogens were geometrically constrained [*d*(C-H) = 1.00Å] and assigned common isotropic temperature factors. The hydroxyl hydrogens of both host and guest molecules were independently located in difference electron density maps, and were refined

with a simple bond length constraint relating O-H distances versus O--O distances[2], and with independent temperature factors. The structure refined successfully to R_1 = 0.0424.

4.1.2 Structure Analysis

The molecular parameters of the host and guest molecules are all in acceptable ranges for structures of this type[3]. The host conformation will be discussed further in Chapter 8.

Packing diagrams of **OBD** down [100] and [010] are shown in Figures 2 and 3. Layers of host pack end-to-end, forming ribbons parallel to [010]. The continuous chains of host formed in this manner are cross-linked to each other through the guest molecules by hydrogen bonding. The interlinked arrangement of the host ribbons is stabilised by weak van der Waals forces. It is characterised by the convenient steric fit of the cyclohexyl rings of the host molecules in adjacent layers.

Channels running parallel to *a* are formed by the packing motif of the host, and are depicted in Figure 4. This is a MOLMAP plot in which the guest molecules are depicted with van der Waals radii. The channels are relatively unconstricted, and have cross sections which are approximately circular, with diameters of ± 5.3 Å . The packing factor for this structure was calculated to be 17.4 $Å^3$ / non-hydrogen atom.

All the hydroxyl groups are both proton donors and proton acceptors in various hydrogen bonds, and therefore utilise the dual capacity of hydroxyl groups for hydrogen bonding. Each O(13)--O(20) site on the host framework interacts with two guest molecules: one from above and one from below. Correspondingly, each guest molecule interacts with two host ribbons, donating a proton to one chain, and accepting a proton from the other chain. The intermolecular

interactions in **OBD** are illustrated graphically in Figure 5, while the geometric details are listed in Table 2.

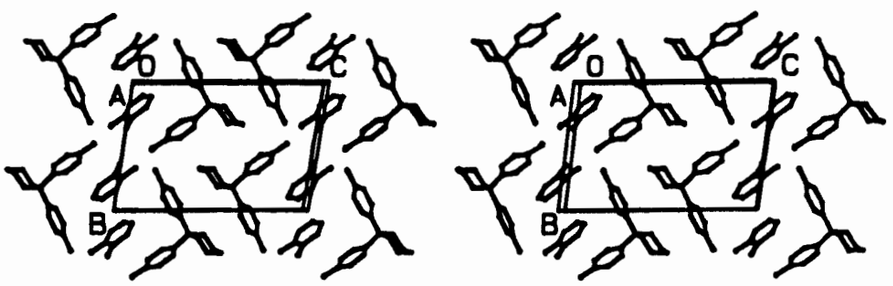

Figure 2: Stereo view of the packing of **OBD** down [100]

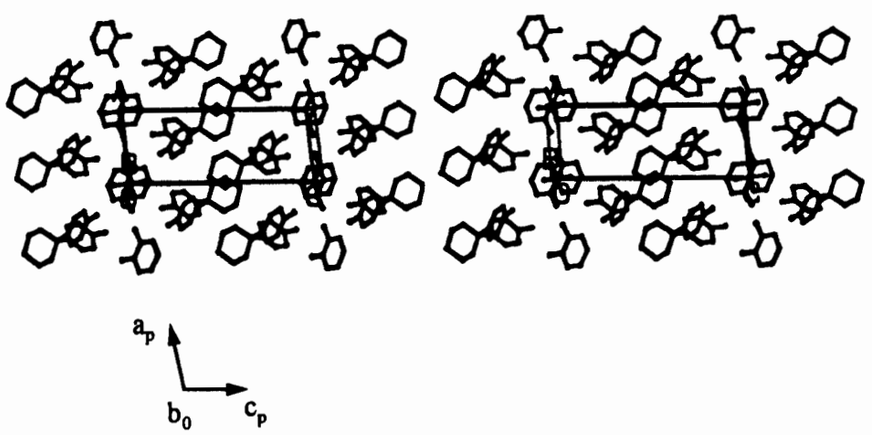

Figure 3: Stereo view of the packing of **OBD** down [010]

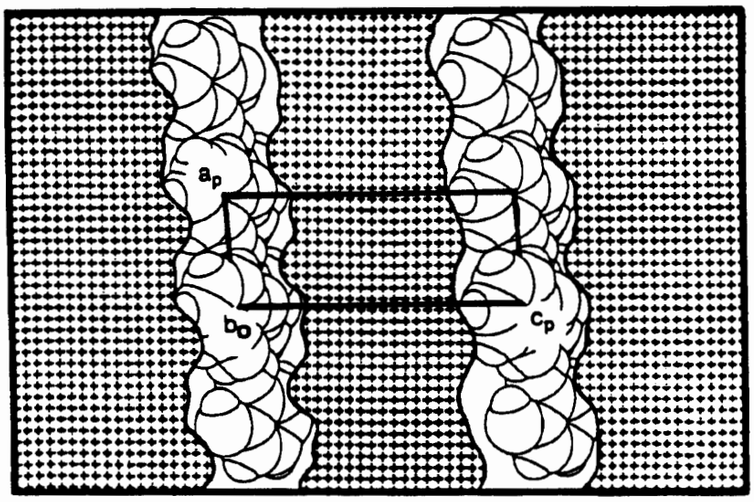

Figure 4: MOLMAP plot of **OBD** down [010] sectioned at y = 0. The host structure is represented by the hatched area, while the guest molecules are depicted with van der Waals radii.

Table 2: Details of hydrogen bonding details in **OBD**.

Donor	Acceptor	D-H /Å*	D–A /Å*	D-H–A /°*
O13	OG2[a]	0.98(2)	2.697(3)	175(2)
OG1	O20	0.98(2)	2.899(2)	156(2)
OG2	O20[b]	0.97(2)	2.814(2)	156(2)
O20	O13[c]	0.97(2)	2.711(3)	174(2)

Symmetry code: *(a) -x, -y, -z (b) -x+1, -y+1, -z (c) x, y+1, z*

** (**D** = Donor ; **A** = Acceptor)*

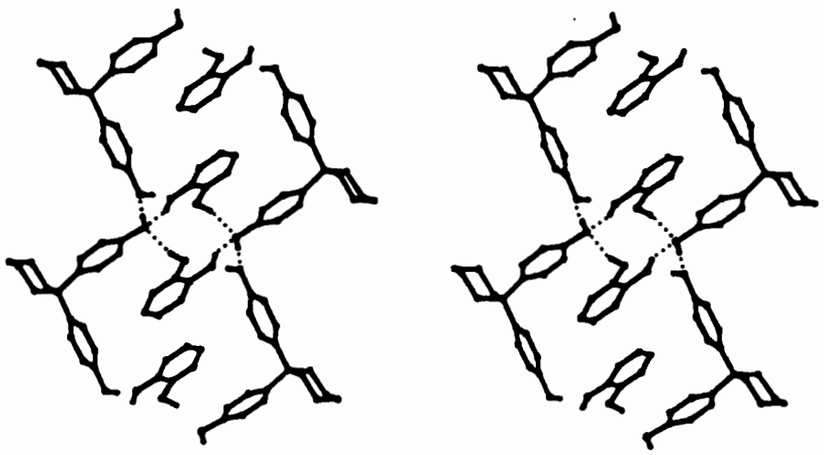

(a) Viewed down [100]

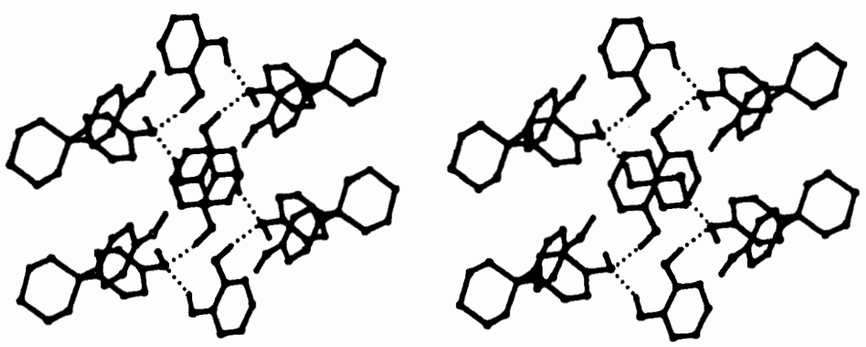

(b) Viewed down [010]

Figure 5: Hydrogen bonding scheme of **OBD**

4.1.3 Thermal Analysis

The TG and DSC traces for **OBD** are shown in Figure 6. Only one endotherm is observed in the DSC trace at T_{on} = 146.9°C. This temperature is between the melting temperatures of the host compound and *o*-benzenediol (i.e. 184°C and 102°C respectively). It is hypothesised that the single endotherm occurs at the temperature of guest release, which is accompanied by dissolving of the host in the hot guest. Thus no separate endotherm is observed for the degradation of the desolvated host. This is confirmed by viewing the thermal degradation of a crystal of **OBD** undergoing heating on the hot stage. The only event observed was that of the crystal melting at 147°C.

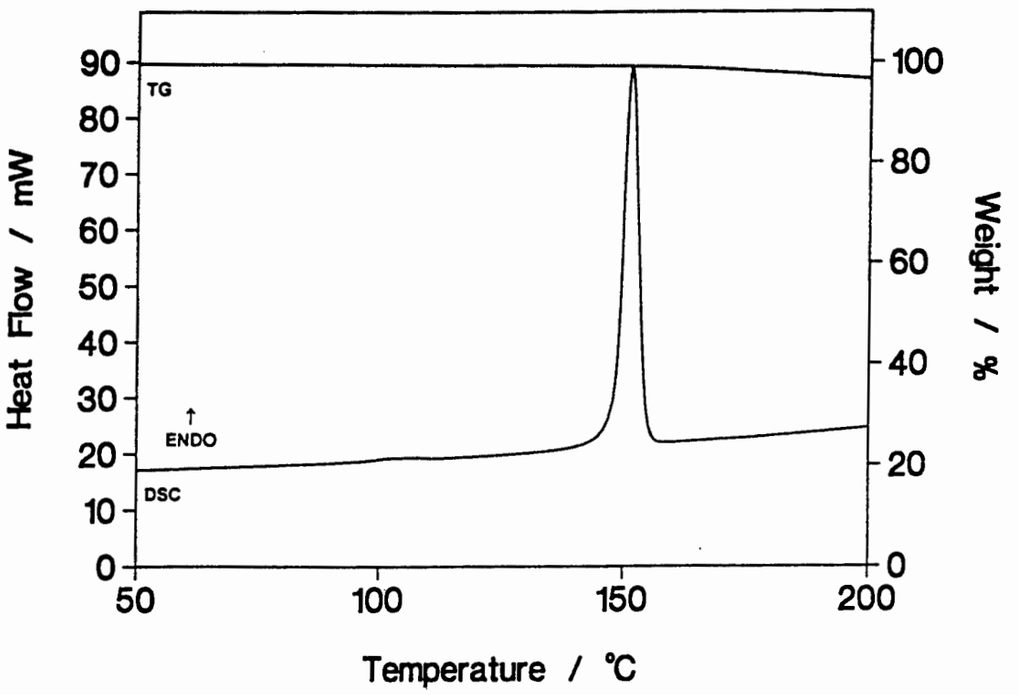

Figure 6: TG and DSC traces of **OBD**

4.2 PBD

4.2.1 Structure Solution

Preliminary X-ray photography indicated that the diffraction pattern of **PBD** possesses *2/m* Laue symmetry and thus belongs to the monoclinic crystal system. The following conditions limiting possible reflections were observed:

hkl : $h + k = 2n$

h0l : $l = 2n$; ($h = 2n$)

0*k*0 : ($k = 2n$)

The two possible space groups corresponding to these conditions are Cc and C2/c. The centrosymmetric space group C2/c was chosen based on the observed $|E^2-1|$ statistics after the first direct methods run, and this choice was vindicated by the successful refinement of the structure.

C, H, N micro-analysis indicated the host:guest ratio in **PBD** to be 1:½ (*exptl*: %C = 77.9(1), %H = 7.3(1); *calc*: %C = 78.0, %H = 7.1)[1]. The unit cell contains eight host molecules and four guest molecules. The host molecules are located at general positions, while the guest molecules are located on diads at Wyckoff position *e*. The atomic numbering used for the guest *p*-benzenediol molecule is shown in Figure 7.

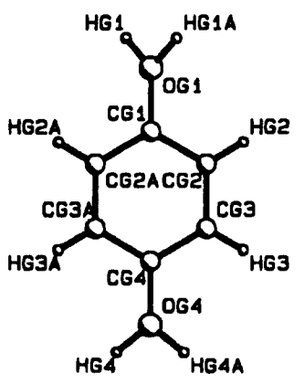

Figure 7: Numbering of *p*-benzenediol used during the structure solution of **PBD**

The positions of the non-hydrogen atoms of both the host and guest molecules were obtained by direct methods. These atoms were refined anisotropically. Thermal motion in the a^* direction for OG4 was found to be relatively high (U_{11} = 0.21Å^2), while being acceptable in the b^* and c^* directions (U_{22} = 0.03Å^2, and U_{33} = 0.05Å^2). This oxygen is locked into position in the *yz*-plane by hydrogen bonding, and therefore vibrates more freely in the a^* direction. The hydrogen atoms of the host were all independently located in difference electron density maps, but in the final model the aromatic and methylenic hydrogens were geometrically constrained [*d*(C-H) = 1.00Å] and assigned common isotropic temperature factors. Since the oxygen atoms of the guest hydroxyl moieties are located on diads, their hydrogens are required to be disordered across the diad. These hydrogen atoms were therefore modelled with half site occupancy factors. The demands of host-guest hydrogen bonding also required the host hydroxyl hydrogen atoms to be disordered over two sites. The two hydrogen positions for each host hydroxyl group were located in the difference maps. The host hydroxyl hydrogens were each modelled at half site occupancy factors, and were refined with independent temperature factors. The structure refined successfully to R_1 = 0.0423.

4.2.2 Structure Analysis

The molecular parameters of the host and guest molecules were acceptable for these types of structures[3]. The packing observed in **PBD** is illustrated in Figures 8 and 9, viewed along [010] and [001] respectively.

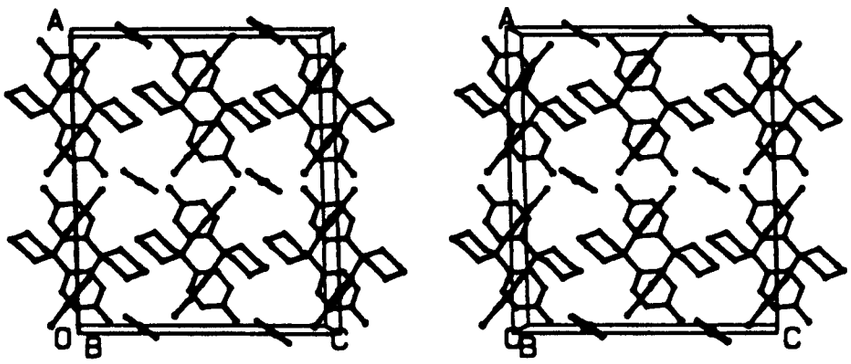

Figure 8: Stereo view of the packing of **PBD** down [010]

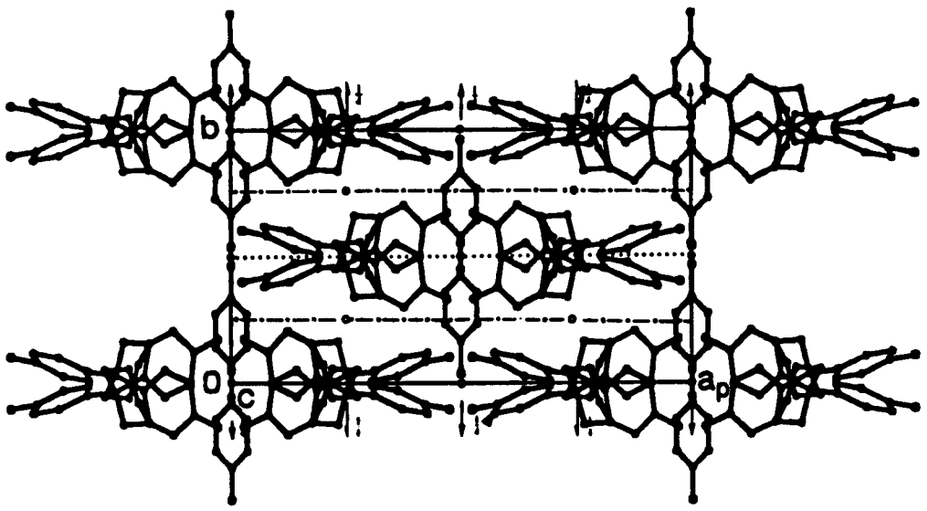

Figure 9: Packing diagram of **PBD** viewed down [001]

The guest molecules are located in cavities formed by the packing of the host. These centres of these cavities are located at (0,¼,¼) and (½,¼,¾), and at (0,¾, ¾) and (½,¾,¼). Figure 10 is a MOLMAP plot viewed down [010], illustrating the positioning of the pockets. The pockets are ellipsoid in shape, with approximate dimensions of 9 x 5.5 x 4.5 Å. The packing factor for this structure was calculated to be 17.75 $Å^3$ / non-hydrogen atom.

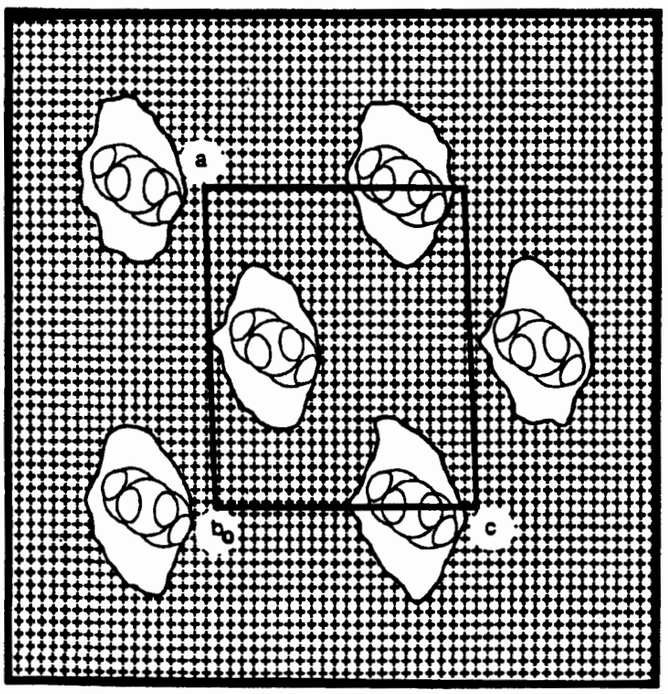

Figure 10: MOLMAP plot of **PBD** viewed down [010], sectioned at y = 0.25

Layers of host molecules form parallel to the *ac* plane. Host molecules within a layer are linked to one another through hydrogen bonding. Each layer formed in this manner is linked to the adjacent parallel layer through their interactions with the *p*-benzenediol guest molecules. These interactions occur along direction of the *b*-axis. Figure 11 is a schematic diagram which illustrates the hydrogen bonding interactions in **PBD**. The positions of the guest hydroxyl hydrogens across the diads propagate the positions of the host hydroxyl

hydrogens. This "flip-flop" arrangement[4] of the hydrogen atoms results in two possible hydrogen bonding schemes, which are both illustrated in Figure 11. Details of the intermolecular interactions are given in Table 3. A model of a representative portion of the crystal structure was constructed in order to understand the intermolecular interactions in **PBD**. A photograph of this model is shown in Figure 12.

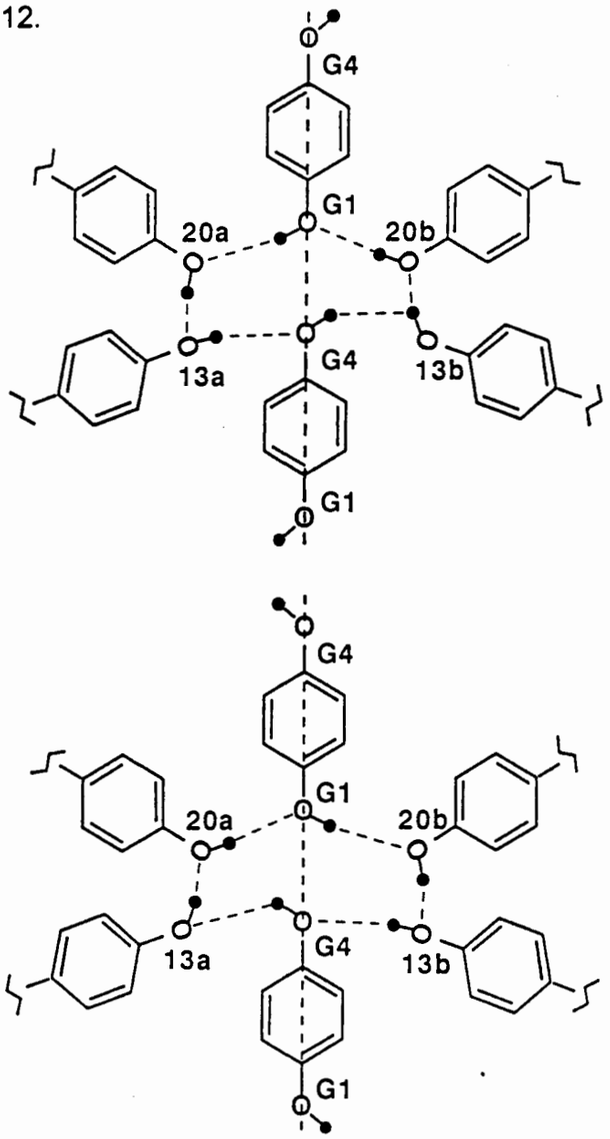

Figure 11: The two hydrogen bonding schemes observed in **PBD** due to the 'flip-flop' arrangements of the hydroxyl hydrogens. The vertical dotted line represents the diad which passes through the guest molecules.

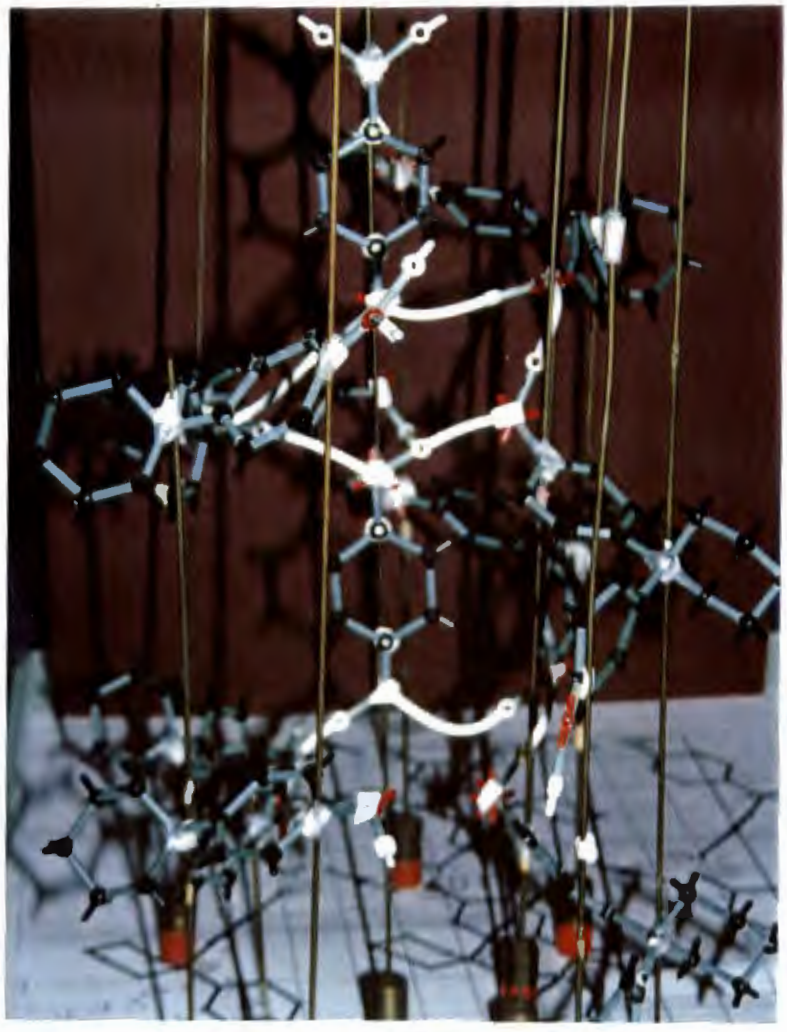

Figure 12: Photograph of the model constructed to represent the structure of **PBD**

Table 3: Geometric details of hydrogen bonding in **PBD**.

Donor	Acceptor	D-H /Å*	D···A /Å*	D-H···A /°*
OG1	O20[a]	0.98(2)	2.721(2)	172(3)
OG4	O13[b]	0.98(2)	2.649(3)	169(2)
O13	O20[c]	0.93(5)	2.671(3)	167(5)

Symmetry code: *(a) -x+1, y, -z+½ (b) x-½, y+½, z (c) x+½, y+½, z*

* (**D** = Donor ; **A** = Acceptor)

4.2.3 Thermal Analysis

The TG and DSC traces of **PBD**, Figure 13, do not show a separate guest release step, and it is assumed that the guest is released only on destruction of the host framework due to melting at T_{on} = 194.7°C. Hot stage microscopy confirmed these results, and the only thermal event observed was that of melting.

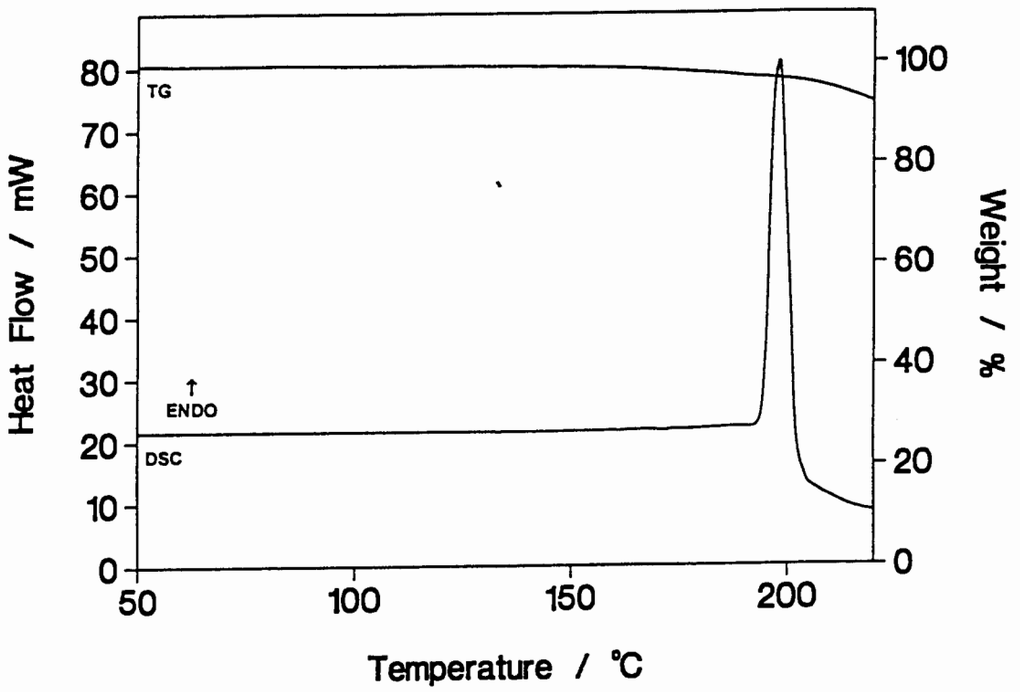

Figure 13: TG and DSC traces of **PBD**

4.3 POTENTIAL ENERGY CALCULATIONS

The lattice energies of **OBD** and **PBD** were calculated using the program HEENY, and following the procedure described in Chapter 2. Due regard was given to the fact that the guests in **PBD** lie on a diad and that the hydroxyl groups were disordered. The results are given in Table 4.

Table 4: Results of the lattice potential energy calculations

	OBD	**PBD**
	E /kJ mol^{-1}	E /kJ mol^{-1}
H···H	-140.4	-177.1
H···G	-68.1	-83.5
G···G	-41.0	-2.2
TOTAL:	-249.5	-262.8

These calculations could not be performed for the complex between **H** and *m*-BD due to the absence of structural data. However, it will be seen in section 4.5 of this chapter that a complex does indeed form between the host and *m*-BD, and that it is isomorphous with **OBD**. Therefore the lattice energy of this complex is likely to be very similar to that of **OBD**.

4.4 COMPETITION EXPERIMENTS

The results of the competition experiments are illustrated in Figure 14, and details are listed in Appendix 1.

Each graph on the edges of the triangle represents a 2-component competition, and shows the mole ratio of the guests in the initial solutions versus that included by the host. The central triangular region represents the competition experiments where mixtures of all three isomers of benzenediol were present.

For the benzenediol system, the competition experiments were performed in water suspensions (described in Chapter 2).

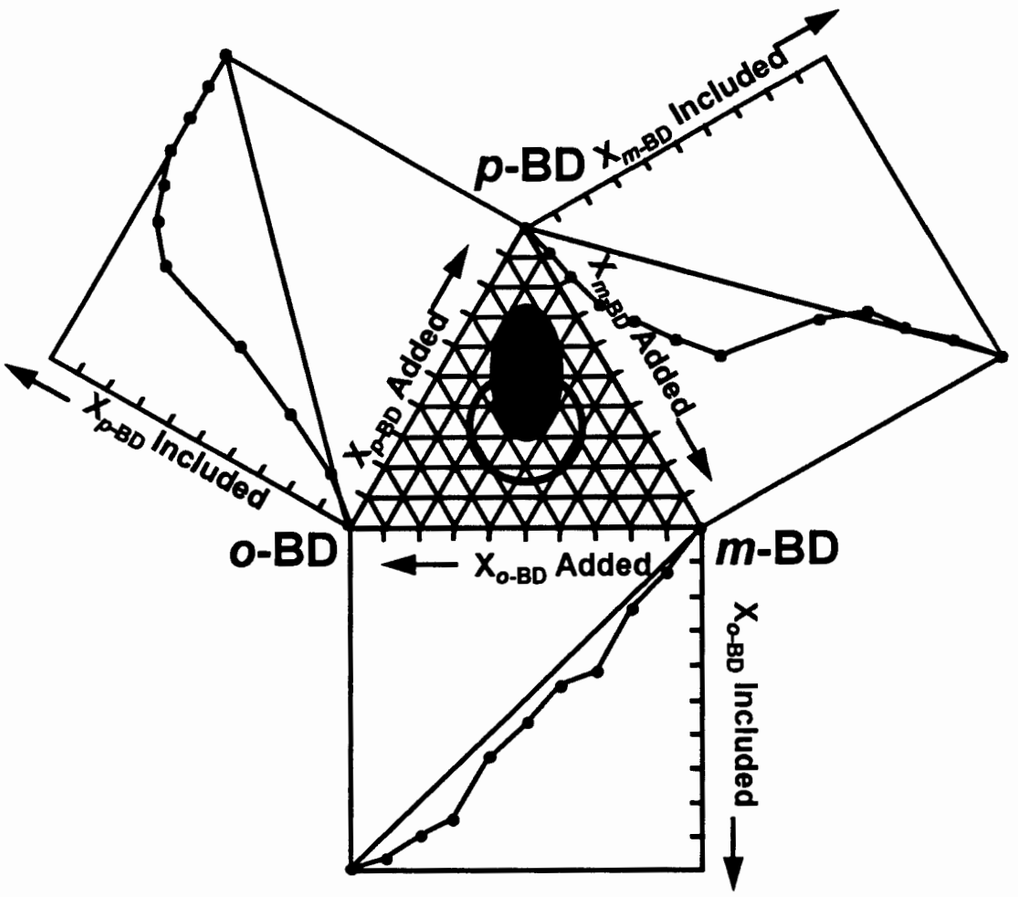

Figure 14: Results of the competition experiments performed on the benzenediol system

4.4.1 2-Component

In the *o*-BD/*p*-BD competition, the preferential inclusion of *p*-BD was already observed in those solutions where it was only present in small concentrations. In the solutions originally containing more than 50% *p*-BD, this isomer was almost exclusively included by the host.

In the competition between *o*-BD and *m*-BD, a slight preference of *o*-BD was observed, but the selectivity was poor. The relative amounts of each isomer included by the host upon complexation was approximately the same as the concentrations of the starting isomer solutions.

In the competition between *m*-BD and *p*-BD, preferential complexation between the host and *p*-BD was observed when p-BD was present in the starting solutions in concentrations greater than 35%, while no discrimination was observed in the solutions containing less than 35% *p*-BD.

4.4.2 3-Component

The migration of the circle representing the initial mixture concentrations towards the *p*-BD vertex of the triangle confirms that *p*-BD is favoured by the host in competition experiments conducted simultaneously with the three isomers of benzenediol. In this experiment, no selectivity was observed between *o*-BD and *m*-BD, since the circle had not migrated horizontally.

4.5 SOLID STATE INCLUSION

Stoichiometric quantities of **H** and each isomer of benzenediol were co-ground, and the products were analysed by XRD, to determine whether complexation had occurred.

When grinding **H** and *p*-BD together, an inclusion complex was not formed. The XRD trace of the resulting co-ground powder was simply the sum of the individual components' traces. Complexation could not be invoked by heating the powdered starting reagents to 60°C, followed by immediate grinding. Figure 15 illustrates the XRD trace of the co-ground product of **H** and *p*-BD versus that of the complex **PBD**, which was obtained by recrystallisation of a solution containing **H** and *p*-BD.

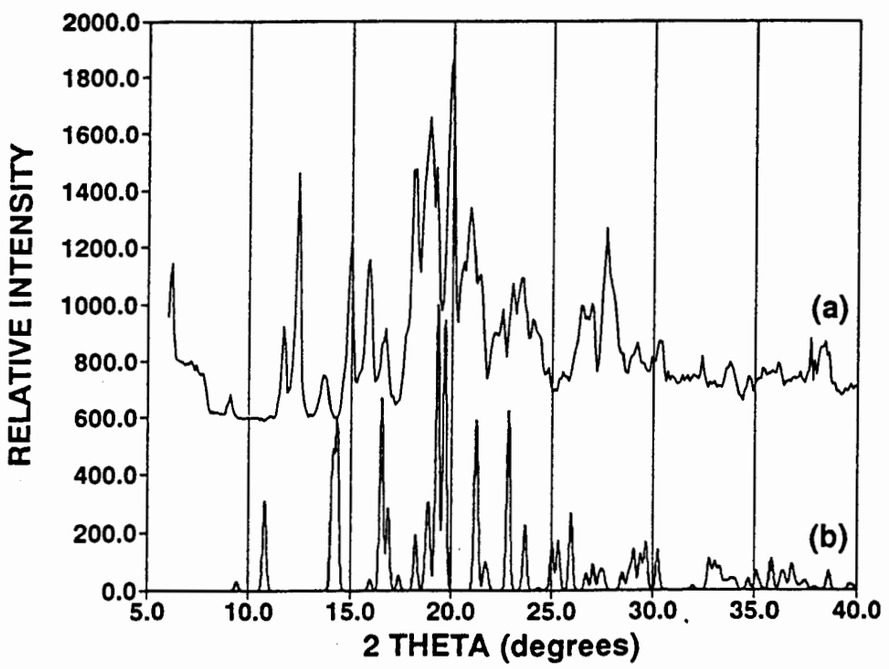

Figure 15: (a) Experimental XRD trace of the co-ground product of *p*-BD and **H**, and (b) calculated XRD trace of **PBD**. These two traces are different, and therefore the two powders do not have the same structure.

o-BD formed a complex with **H** by solid-solid reaction, and this complex had a XRD trace which matched that of **OBD** grown from solution in peak positions and intensities. It also had the same melting point (146.2°C) as **OBD**. Thus the co-ground product is identical to **OBD**. Figure 16 compares the experimental XRD trace of the ground product with that of **OBD**. The match is satisfactory in that all the main peaks in the observed X-ray spectrum are found in the calculated spectrum.

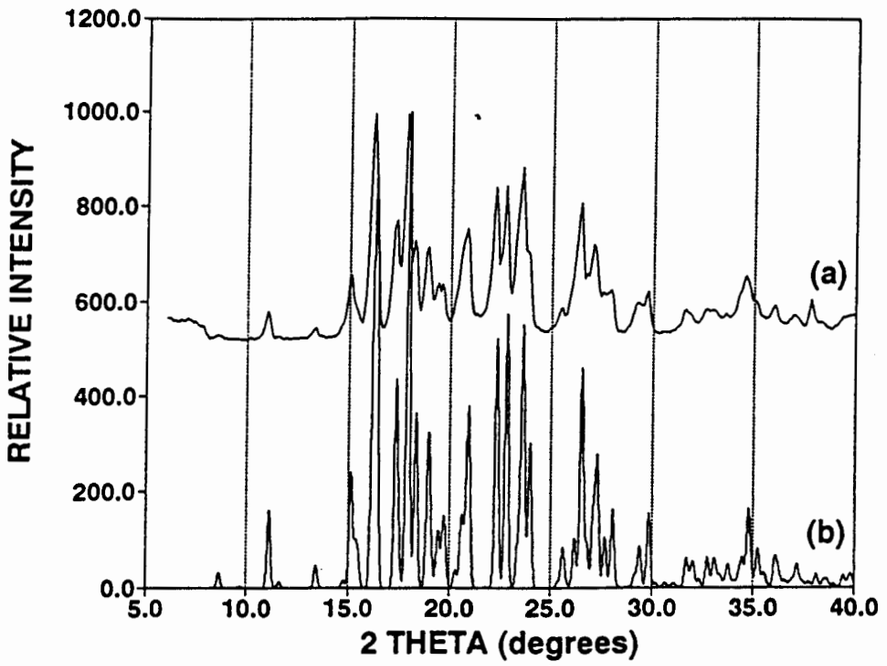

Figure 16: (a) Experimental XRD trace of the co-ground product of **H** and *o*-BD , and (b) the calculated XRD trace of the complex **OBD** obtained by recrystallisation methods.

m-BD formed a complex with **H** in the solid state, since the XRD trace of the co-ground product of these two compounds was not the sum of the traces of the uncomplexed compounds. The complex formed between **H** and *m*-BD was found to be isomorphous to that of **OBD**, since it displayed an identical XRD trace, shown in Figure 17.

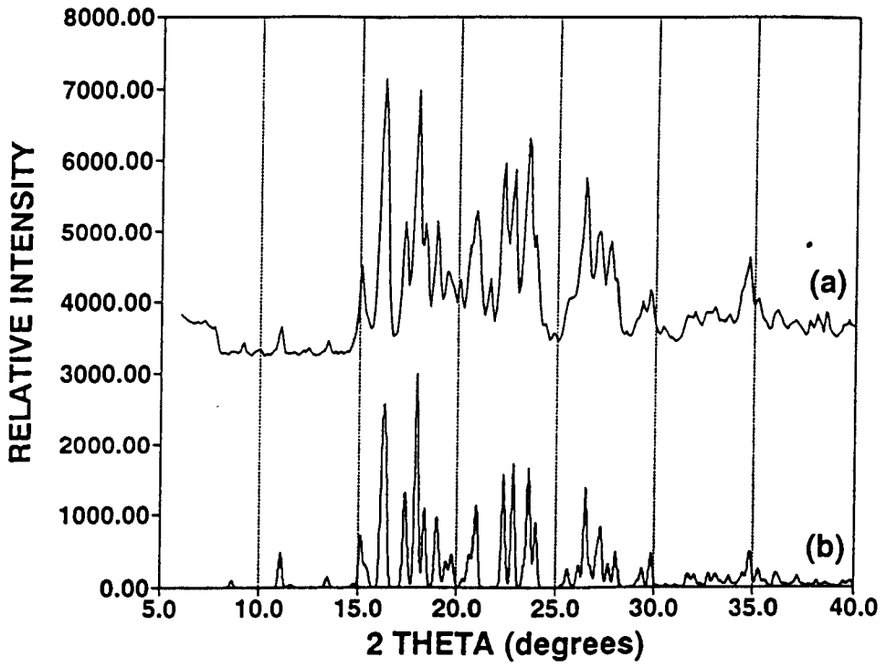

Figure 17: (a) Experimental XRD trace of the co-ground product of *m*-BD and **H**, and (b) calculated XRD trace of **OBD** (calculated using the program LAZY PULVERIX)

Kálmán[5] has discussed the issue of isomorphism, and has determined that molecular associates such as clathrates often display isomorphic tendencies. If two clathrates have similar host structures, and merely contain different guest molecules in their voids, then depending on the interactions between the different guest molecules, the crystal pairs may exhibit varying degrees of isostructurality.

Attempts were made to obtain a possible crystal structure for the complex formed between the host and *m*-benzenediol. This was achieved by exchanging the *o*-benzenediol molecules in the complex **OBD** with *m*-benzenediol molecules.

This approach was justified, since the **OBD** and **MBD** complexes are isostructural and therefore their host frameworks must be almost identical.
An idealised molecule of *m*-benzenediol was placed in the host framework obtained from the structure solution of **OBD**. The atomic numbering scheme used for the *m*-benzenediol molecule is shown in Figure 18. The hydroxyl hydrogen atoms of *m*-BD were omitted from the model, since rotation about the C1G-O1G and C3G-O3G bonds gives the hydroxyl hydrogens a degree of freedom and therefore prevents the accurate determination of the hydrogen positions.

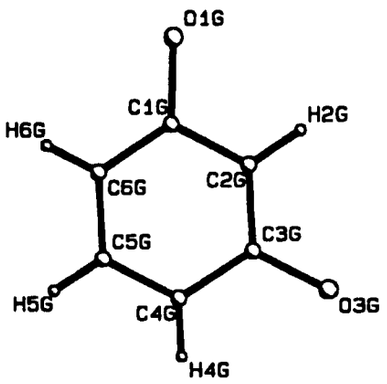

Figure 18: Atomic numbering scheme used for the *m*-BD molecule during calculation of the **MBD** structure

The program HEENY[6] was used to minimise the position of the guest molecule in the host framework. The host molecules were retained in the fixed positions derived from the **OBD** structure. The *m*-benzenediol molecule was initially positioned as in the **OBD** structure. The molecule was then rotated about three orthogonal axes and the resulting energy was mapped. Three unique minima were found. The structures corresponding to each minimum was allowed to refine by least squares to the lowest energy position. Only one of these three structures yielded sensible O···O contacts. This structure had a global minimum energy of -254.1kJ mol^{-1}.

The XRD trace of the idealised structure was calculated using the program LAZY PULVERIX, and was compared to the calculated XRD trace of the co-ground product of *m*-BD and **H**. Figure 19 illustrates the good agreement obtained between the two traces.

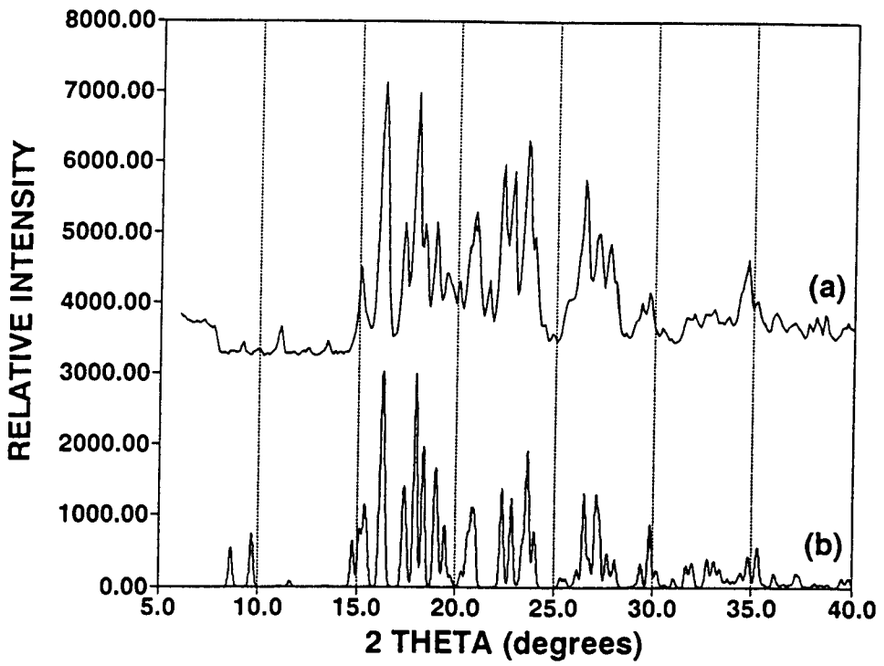

Figure 19: (a) Experimental XRD trace of the co-ground product of **H** and *m*-BD, and (b) calculated XRD trace of the proposed **MBD** complex structure

The contribution made by the guest molecules to the XRD trace of the complex was calculated using the program LAZY PULVERIX. This was achieved by omitting the host molecules from the structure, and calculating the trace using the guest co-ordinates only. The resulting XRD trace is shown in Figure 20(a). Similarly, the contribution made by the host molecules to the XRD trace of the complex was calculated, and is illustrated in Figure 20(b). A large peak at 2θ = 11.6° is observed in both the host trace and the guest trace. However, the

intensity of this peak is very low in the XRD trace of the complex. The peak at $2\theta = 11.6°$ is due to the scattering from the (*002*) plane. The F_{calc} value for the (*002*) reflection for the host alone is -68.48, while that for the guest alone is +77.34. These two values are of similar magnitude, but are out of phase. Therefore their addition results in a very small peak, as observed in the XRD trace of the complex.

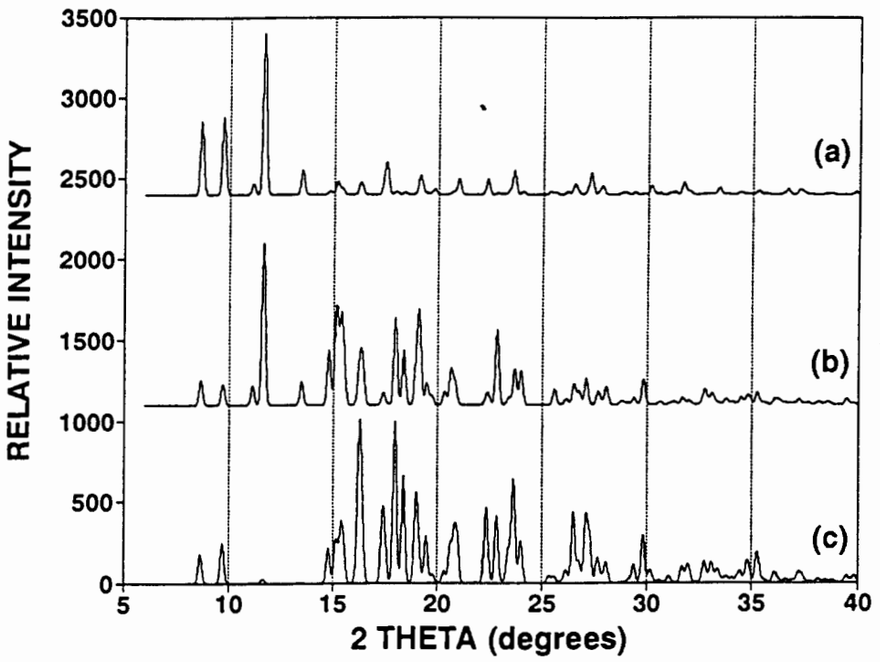

Figure 20: (a) Calculated XRD trace of the *m*-BD molecule in the **MBD** complex, (b) the calculated XRD trace of the host framework in **MBD**, and (c) the calculated XRD trace of the MBD complex

Figure 21 is a packing diagram of the calculated structure of **MBD** viewed down [100]

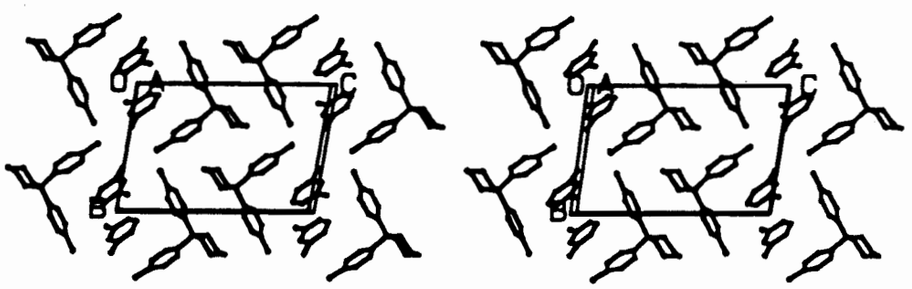

Figure 21: Stereo view of the packing of the proposed **MBD** complex, down [100]

A possible hydrogen bonding scheme for **MBD** was determined by considering the O⋯O contacts in the structure. Table 4 lists the O⋯O contacts which are in the range 2.5 Å to 3.4 Å. Since the hydrogen atoms of the *m*-benzenediol molecule were not included during the calculation of the structure, hydrogen bond angles could not be determined. However, these hydrogen positions were calculated by placing the hydrogen atoms 0.98Å from the parent oxygen atom, so that the O(donor)-H⋯O(acceptor) angles were 180°. The hydrogen bonding scheme which results from the consideration of these close contacts is illustrated in Figure 22.

Adjacent host molecules hydrogen bond to each other via their hydroxyl group. Each O(host)⋯O(host) hydrogen bonding site is hydrogen bonded to two guest molecules: one from above and one from below, when viewing the structure down [100]. Guest molecules which are related by translation along [100] are also hydrogen bonded to each other.

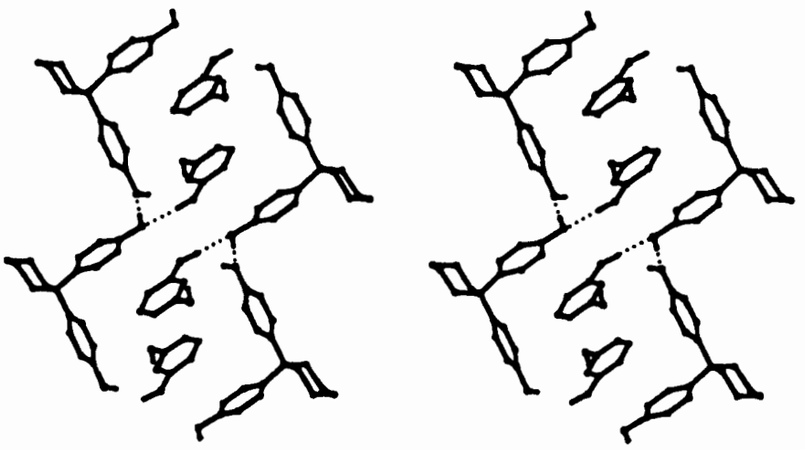

(a) viewed down [100]

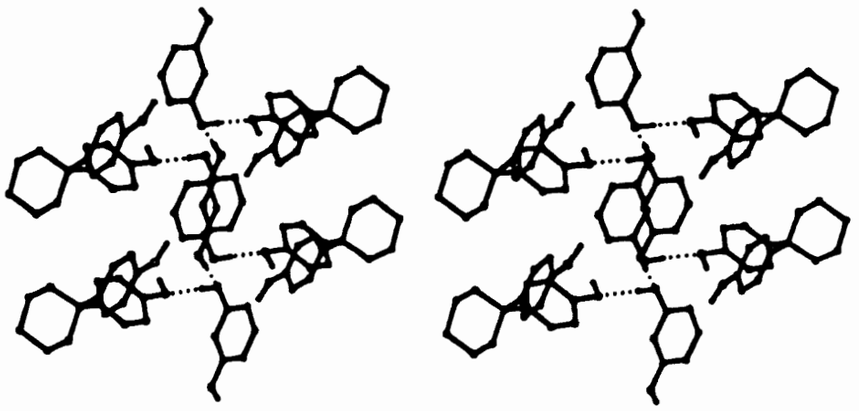

(b) viewed down [010]

Figure 22: Hydrogen bonding scheme in the derived **MBD** complex

Table 4: Possible hydrogen bonds in the calculated **MBD** structure.

Interatomic Contact	O-O /Å
O13-O20[a]	2.7108
O13-O1G[b]	3.3778
O13-O3G[c]	3.1395
O20-O1G[d]	3.0583
O1G-O1G[d]	3.3935
O1G-O3G[e]	2.8255

Symmetry code: *(a) x, y-1, z (b) -x+1, -y, -z (c) -x, -y, -z (d) -x+1, -y+1, -z (e) x+1, y, z*

The lattice energy of the derived **MBD** structure was calculated using the program HEENY, and a value of -254.1 kJ mol^{-1} was obtained. This value is slightly lower than the value of -249.5 kJ mol^{-1} obtained for the **OBD** complex. This is possibly due to the fact that ideal hydrogen positions were inserted into the **MBD** structure for hydrogen bond formation. HEENY takes the O-H-O angle into account, and assigns a lower energy to those hydrogen bonding interactions where the angle is close to 180°.

4.6 SOLID STATE COMPETITION

Stoichiometric quantities of **H** and combinations of the three isomers of benzenediol were co-ground, and analysed by XRD.

4.6.1 2-Component

The XRD trace of the powder resulting from the co-grinding of stoichiometric quantities of **H**, *o*-BD and *p*-BD was predominately the same as the trace of **OBD**, with a few identifying peaks of uncomplexed *p*-BD being observed. Thus, **H** selectively included *o*-BD rather than *p*-BD in the solid state.

Stoichiometric quantities of **H**, *o*-BD and *m*-BD were ground together. Since the traces of the complexes formed between **H** and *o*- and *m*-BD were identical, it was not possible to determine which complex had formed in the solid state. However, since the complexes formed were isomorphous and therefore of similar stability, one would not expect there to be any selectivity between *o*-BD and *m*-BD. This notion was supported by the presence of unique peaks of both of the uncomplexed isomers in the XRD trace. Therefore neither one of the isomers was exclusively complexed by the host.

When competing *p*-BD and *m*-BD in the solid state, the host displayed preferential complexation with *m*-BD. The XRD trace contained peaks identifying the **H**•*m*-BD complex and peaks identifying uncomplexed *p*-BD.

4.6.2 3-Component

The XRD trace of the co-ground product of **H** and the three isomers of benzenediol was similar to that of the **OBD** and **MBD** complexes. However, since these complexes were isomorphous, it was not possible to determine which was formed preferentially, although one would expect there to be no selectivity between *o*- and *m*-BD. In this experiment, *p*-BD remained uncomplexed, as before.

4.7 DISCUSSION

The structures of the inclusion complexes **OBD** and **PBD** have been elucidated. These two structures have different packing motifs and intermolecular interactions. The host:guest ratio in **OBD** is 1:1, while in **PBD** it is 1:½. An important point to note is that in **PBD** four hydrogen bonds per guest molecule to the host framework are formed, while in **OBD** there are three. An indication of the higher stability of **PBD** is in the shape of the voids in the host framework. In **PBD** the guests are 'locked' into the complex by being located in cavities. These cavities provide a very high physical barrier to the release of the guest. In **OBD** the guest molecules are located in channels which provide much lower physical barriers to guest release. The lattice energy calculations also indicate that the complex **PBD** is more stable since its energy is ~15 kJ mol^{-1} lower than that of **OBD**. The thermal stabilities of the two complexes show that in **OBD** the structure collapses due to guest release at 146°C, while in **PBD** this event only occurs at 194°C. This difference of ~50°C is significant.

Inclusion complexes between the host and *o*-BD and *m*-BD were also formed by solid-solid reactions. The inclusion compounds formed in this manner have the same structure as **OBD** formed in solution, since they have identical XRD traces. Complexation between the host, **H**, and *p*-BD does not occur in the solid state. The mechanism of the solid-solid reaction is not well understood, but may well involve an initial attack on the host surface by guest vapour, followed by interdiffusion of the host and guest molecules. At room temperature the vapour pressure of *p*-BD is 0.04Pa, and is approximately one tenth that of *m*-BD (0.3Pa), and one-hundredth that of *o*-BD (5Pa). It is therefore suggested that the relatively low vapour pressure of *p*-BD may be the primary factor for the failure of the **H**-*p*-BD reaction in the solid state.

The preferential selectivity of the host for complexation with the isomers of benzenediol was determined by water suspension competition experiments.

The order of selectivity was: *p*-BD > *o*-BD ≅ *m*-BD. No significant selectivity was observed between *o*-BD and *m*-BD since they form nearly isomorphous complexes with the host compound, and therefore have similar stabilities. On comparison of the calculated lattice energies of the **OBD** structure and the calculated **MBD** structure, the energy of **MBD** was ~5 kJ mol^{-1} lower than **OBD**. The slightly lower energy of **MBD** is possibly due to the fact that the hydroxyl hydrogen atoms of the *m*-BD molecule were placed at ideal positions, which increases the stabilising influence of hydrogen bonds in the crystal structure.

In the solid-solid competition experiments, the following selectivity order was displayed by the host: *o*-BD ≅ *m*-BD > *p*-BD. This is the reverse of the selectivity order when complexation was brought about by crystallisation from solutions. This is a very interesting result, since it not only demonstrates the effectiveness of the inclusion phenomenon for separating isomers, but also demonstrates that in some systems the method of preparation of the complexes is of utmost importance.

1 Refer to Chapter 2, Section 2.4

2 I. Olovsson and P. Jönsson, *The Hydrogen Bond - Structure and Spectroscopy*, P. Schuster, G. Zundel and C. Sarderfy (eds.), North-Holland Publishing Company, USA, 1975.

3 F. H. Allen, O. Kennard, D. G. Watson, L. Brammer, A. G. Orpen and R. Taylor, *J. Chem. Soc., Perkin Trans.* 2, 1987, S1-S19.

4. B. Hingerty, B. Klar, G. L. Hardgrove, C.H. Betzel and W. Saenger, *J. Biomol. Struct. Dyn.*, **2**, 1984, 249.

5. A. Kálmán, L. Partikanyi and G. Argay, *Acta Crystallogr.*, **B49**, 1993, 1039.

6 Refer to Chapter 2, Section 2.17

5. INCLUSION OF PICOLINE GUESTS

In this chapter, the inclusion compounds between the host and the isomers of picoline are examined. The structures, thermal behaviour and preferential formation during competition experiments of the inclusion compounds **2PIC**, **3PIC** and **4PIC** will be discussed in this chapter. The observed selectivity upon complexation with the host, **H**, will be related to the structural features of the complexes formed, and kinetic parameters of the desolvation of guest from the complexes will be discussed.

Crystallographic experimental and refinement details for the complexes are provided in Table 1. Final atomic co-ordinates, temperature factors, tables of bond lengths and bond angles are contained in Appendix 3. Tables of observed and calculated structure factors are listed in Appendix 4.

Table 1: Crystal data, experimental and refinement parameters.

	3PIC	4PIC	2PIC
Molecular formula	$C_{18}H_{20}O_2 \bullet C_6H_7N$	$C_{18}H_{20}O_2 \bullet C_6H_7N$	$C_{18}H_{20}O_2 \bullet H_2O \bullet C_6H_7N$
M_r /g mol^{-1}	361.47	361.47	379.49
Space group	$P2_1/c$	$P2_12_12_1$	$P\bar{1}$
a /Å	10.684(3)	10.649(5)	6.319(2)
b /Å	11.712(2)	11.885(2)	10.880(2)
c /Å	32.021(4)	31.872(6)	15.94(1)
α /°	90	90	83.08(5)
β /°	93.39(2)	90	89.79(5)
γ /°	90	90	77.30(2)
V /Å^3	3999.8(1)	4033.8(2)	1061.0(1)
Z	8	8	2
D_c /g cm^{-3}	1.20	1.19	1.19
D_m /g cm^{-3}	1.18(5)	1.16(4)	1.16(6)
μ(Mo-K_α) /cm^{-1}	0.75	0.75	0.77
F(000)	1552	1552	408
Crystal size /mm	0.4 x 0.4 x 0.34	0.4 x 0.4 x 0.4	0.3 x 0.35 x 0.5
Range scanned, θ /°	1 - 25	1 - 25	1 - 25
Range of indices	*h*:±12;*k*:0,13;*l*:0,38	*h*:-12,6;*k*:±14; *l*: 0,37	*h*: ±7; k: ±12; *l*: 0,18
No. reflections collected	7152	12411	3878
No. reflections observed	7016	8346	3729
No. parameters	533	513	220
R_1	0.0477	0.0409	0.1621*
wR_2	0.1134	0.1030	0.4773
S	1.047	0.968	1.200
$\Delta\rho$ excursions /e Å^3	0.201; -0.264	0.154; -0.249	1.110 ; -0.675*

* The structure solution of **2PIC** was not highly satisfactory. This will be discussed further in section *5.3.1.*

5.1 3PIC

5.1.1 Structure Solution

TG experiments indicated that the host:guest ratio in the complex **3PIC** was 1:1. The X-ray diffraction pattern of **3PIC** displays *2/m* Laue symmetry, and therefore belongs to the monoclinic crystal system. Based on the reflection conditions:

hkl : none

*h*0*l* : $l = 2n$

0*k*0 : $k = 2n$

(00*l* : $l = 2n$),

the space group $P2_1/c$ was assigned. With Z = 8, no crystallographic symmetry is imposed on either host or guest molecules. There are eight host molecules and eight guest molecules in the unit cell, with two each in the asymmetric unit. The general atomic numbering scheme used for the *3*-picoline guest molecules is illustrated in Figure 1. The two crystallographically independent host and guest molecules were assigned the suffixes "A" and "B".

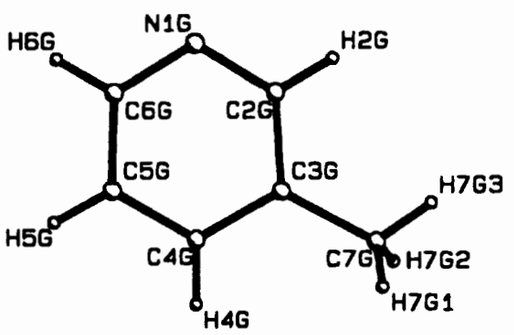

Figure 1: Atomic numbering of the *3*-picoline molecule

The positions of the non-hydrogen atoms of both the host and guest molecules were located by direct methods. The positions of the nitrogen atoms in the guest molecules were ambiguous since there was not a significant difference in

electron density between the six peaks representing the guest rings. Thus all the guest atoms were entered as carbon atoms at first. The nitrogen atoms were recognised in subsequent runs on examination of their distances to the hydroxyl oxygens of the host molecules. The temperature factors of these atoms were also higher than the other atoms, but became acceptable on changing the assignment of the relevant atoms from carbons to nitrogens. Refinement was carried out with the non-hydrogen atoms of both the host and guest molecules treated anisotropically. The hydrogen atoms of the host and guest molecules were all independently located in difference electron density maps, but in the final model, the aromatic, methylenic and methyl hydrogens were geometrically constrained [*d*(C-H) = 1.00Å] and assigned common isotropic temperature factors. The host hydroxyl hydrogens were independently located in difference electron density maps, and were refined with simple bond length constraints relating O-H distances versus O⋯O distances[1]. The final R factor refined to R_f = 0.0477.

5.1.2 Structure Analysis

The bond lengths and angles of both the host and guest molecules were in acceptable ranges for structures of this kind[2].

The packing of **3PIC** is illustrated as projections viewed along [100] and [010] in Figures 2 and 3. The host molecules are linked end-to-end via hydrogen bonding, and in this manner form double ribbon motifs running parallel to *a*. A given pair of host ribbons is related by a two-fold screw axis. This packing of the host molecules results in the formation of channels which run parallel to [010]. The guest molecules are located in these channels. The topologies of the channels are illustrated in Figure 4. The channels have circular cross sections with diameters of ~2Å across their narrowest parts, and ~6Å at their widest parts. The packing factor for **3PIC** was calculated to be 18.52 $Å^3$ / non-hydrogen atom.

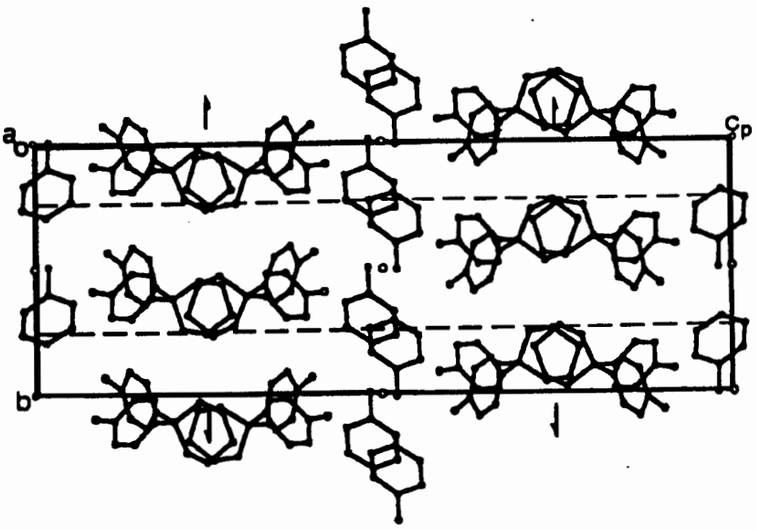

Figure 2: A projection down [100] showing the crystal packing in **3PIC**

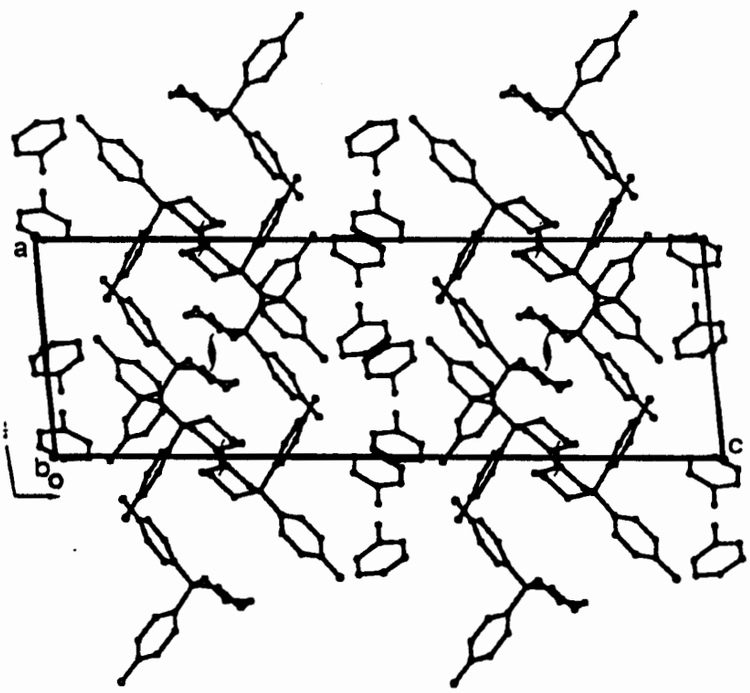

Figure 3: A projection down [010] showing the crystal packing in **3PIC**

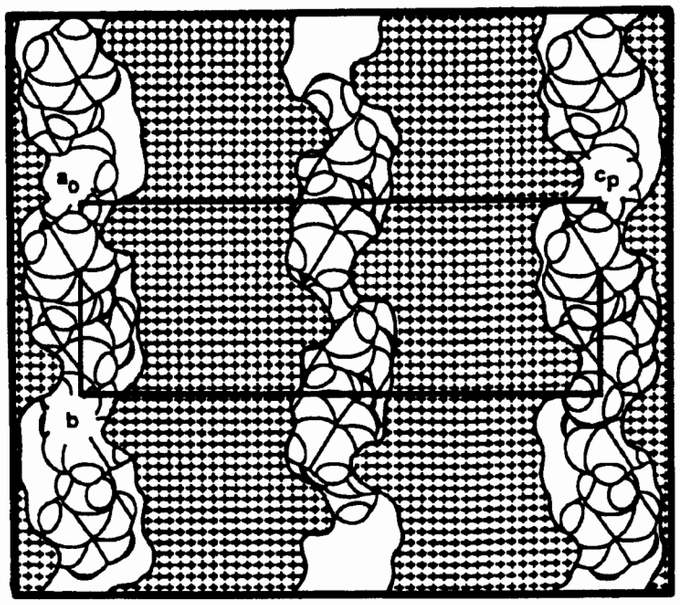

Figure 4: MOLMAP plot of **3PIC** viewed down [100] at the section x = 0. The host structure is represented by the hatched area, and the guest molecules are depicted with van der Waals radii.

As observed in all other structures with this host, adjacent host molecules hydrogen bond to each other via their hydroxyl groups. In this manner, the ribbons of host parallel to [100] are formed. Each guest molecule is hydrogen bonded once to the host structure. The hydrogen bonding scheme in **3PIC** is represented in Figure 5, and geometric details are presented in Table 2.

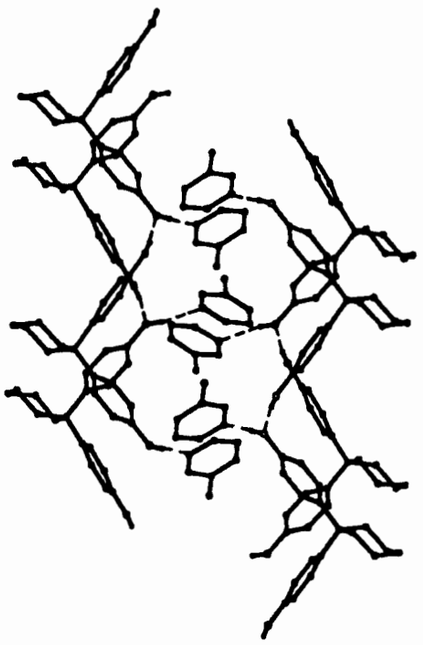

Figure 5: Hydrogen bonding scheme in **3PIC**. The guest nitrogen atoms are shaded for clarity.

Table 2: Details of hydrogen bonding in **3PIC**.

Donor	Acceptor	D-H /Å*	D–A /Å*	D-H–A /°*
O20A	N1GA[a]	0.96(3)	2.664(3)	172(3)
O13B	N1GB[b]	0.98(3)	2.647(3)	168(3)
O13A	O20A[c]	0.93(3)	2.733(3)	171(3)
O20B	O13B[d]	0.94(4)	2.735(3)	171(4)

Symmetry code: *(a) -x+1,-y+1,-z (b) -x,-y+1,-z (c) x-1, y, z (d) x+1, y, z*

* **D** = Donor ; **A** = Acceptor

5.1.3 Thermal Analysis

The TG and DSC traces for **3PIC** are illustrated in Figure 6. A sharp endotherm is observed in the DSC trace at T_{on} = 146.2°C , which represents the desorption of the *3*-picoline guest molecules from the host framework. This corresponds to an observed mass loss of 25.4% in the TG trace (calculated mass loss for H:G = 1:1 is 25.8%). A separate endotherm representing the melt of the host in the DSC trace is not observed. A possible explanation for this could be that the host dissolves in the hot guest during the desolvation process. This behaviour was in fact observed during hot stage microscopy.

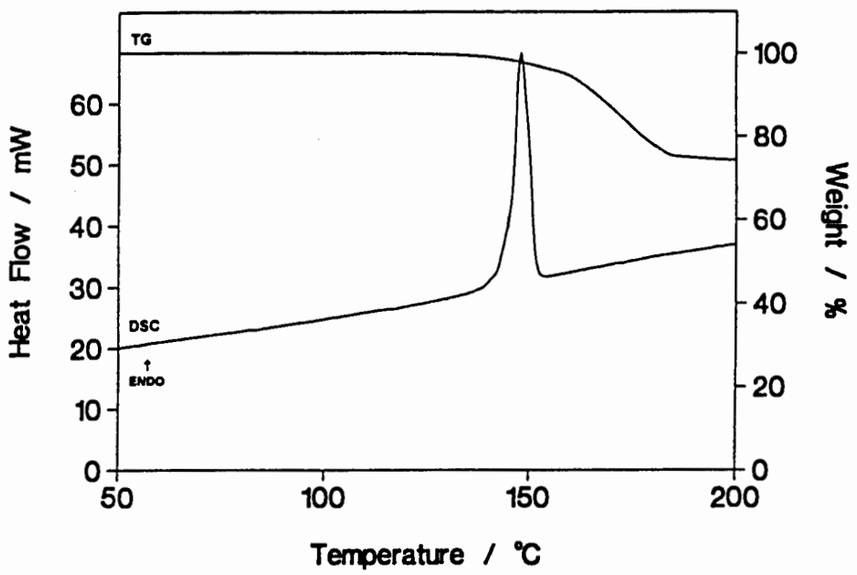

Figure 6: TG and DSC traces of **3PIC**

5.1.3.1 Hot Stage Microscopy

Crystals of **3PIC** were placed on the hot stage microscope, under a drop of silicone oil, and heated. A series of photographs depicting the physical changes occurring in **3PIC** upon heating in the range 20°C to 200°C is illustrated in Figure 7. The temperatures at which the changes were observed were often higher than those observed in the thermal analysis of the samples. This is mainly due to the different geometries of the hot stage and DSC apparatus. Another contributing factor is particle size differences. Powdered samples (10 - 200μm) were used during DSC measurements, while large crystals (with dimension between 0.2 and 0,.5 mm) were used during hot stage microscopy.

(a) Crystals of **3PIC**, in silicone oil at 20°C (light source from below)

(b) At 122°C, the crystals become slightly opaque, indicating the commencement of the guest loss reaction

(c) At 154°C, the desolvated crystals begin to dissolve in the desolvated 3-picoline.

(d) By 156°C, the crystals are almost completely dissolved.

Figure 7: Microscope photographs of a **3PIC** crystal undergoing heating (27X enlarged)

5.1.3.2 Desolvation: Non-isothermal Methods

A number of TG experiments were performed on samples of **3PIC**. These samples were microcrystalline, and were obtained by stirring a solution of the host in the guest until crystallisation occurred. All of the TG runs were performed over the temperature range 50° to 200°C, but had heating rates in the range 1° to 20°C min^{-1}. The mass loss versus temperature data obtained from these traces were reduced to -log β versus 1/T curves, shown in Figure 9, and were analysed for various stages of the decomposition ranging from 6.25% to 21.87%. The slopes of these curves yielded values for the activation energy of desolvation in the range 76(4) kJ mol^{-1} to 81(2) kJ mol^{-1}.

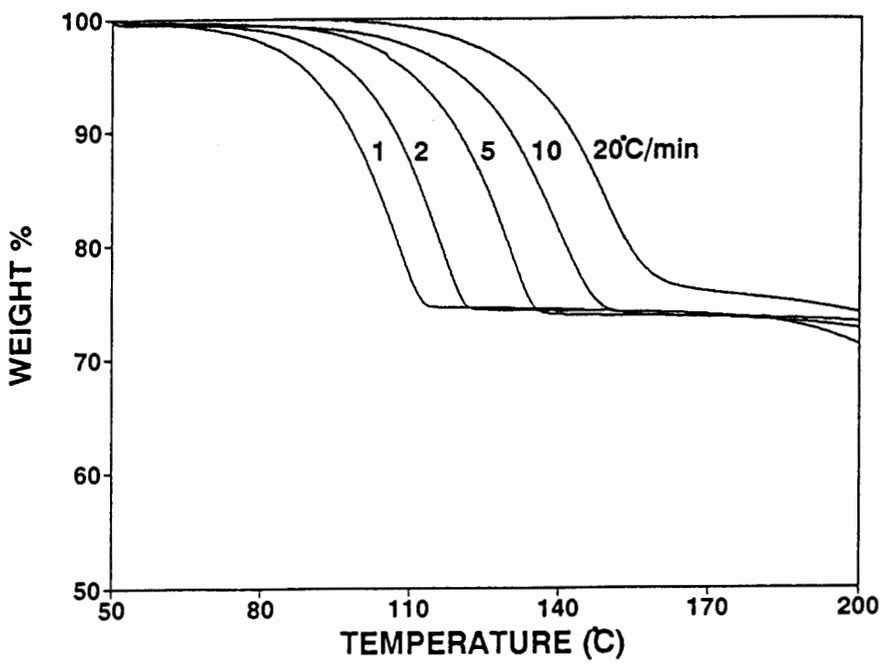

Figure 8: TG runs performed on **3PIC** over the range 50 to 200°C at heating rates of 1, 2, 5, 10 and 20°C min^{-1}

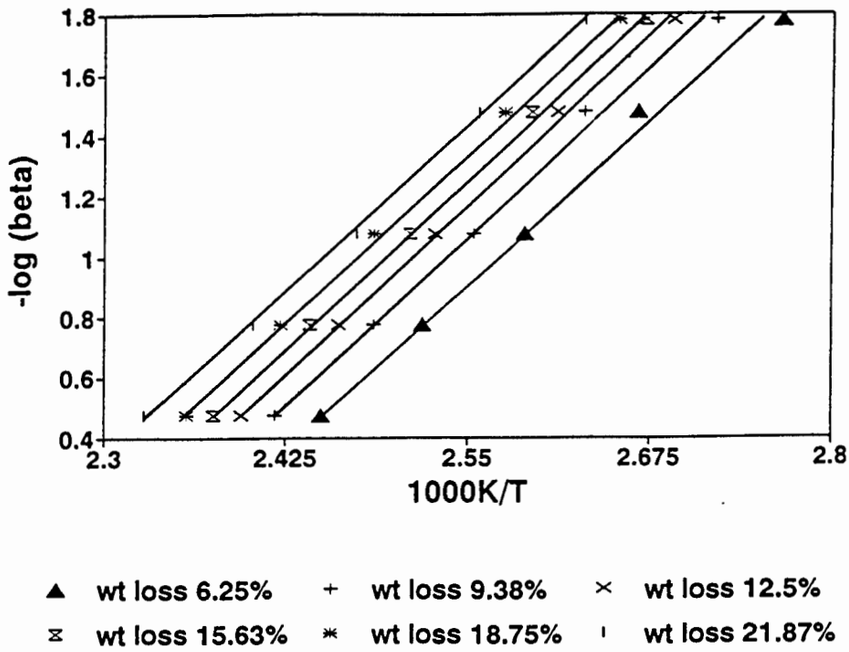

Figure 9: -log β versus 1/T curves for **3PIC**

The results obtained from this experiment are very satisfactory, since they display a high degree of consistency. The lines in Figure 9 do not deviate significantly from linearity, and their slopes are approximately equal. This means that the activation energy for the desolvation reaction is independent of temperature, and therefore the activation energies calculated from these slopes lie in a very small range. This behaviour is an indication that the desolvation reaction proceeds as a single-step reaction[3,4].

5.1.4 Desolvation: Isothermal Kinetics

Samples of **3PIC**, obtained by fast stirring methods, were subjected to a series of isothermal TG experiments in the temperature range 73° - 87°C, at intervals of 2 - 3°C. The resulting α versus time curves, of which one example is illustrated in Figure 10, were analysed and found to best fit the deceleratory contracting area model R2: $kt = 1-(1-\alpha)^{\frac{1}{2}}$, over the α range 0.05 to 0.95. The resulting Arrhenius plot is shown in Figure 11, the slope of which yielded an activation energy of 87(4) kJ mol^{-1} .

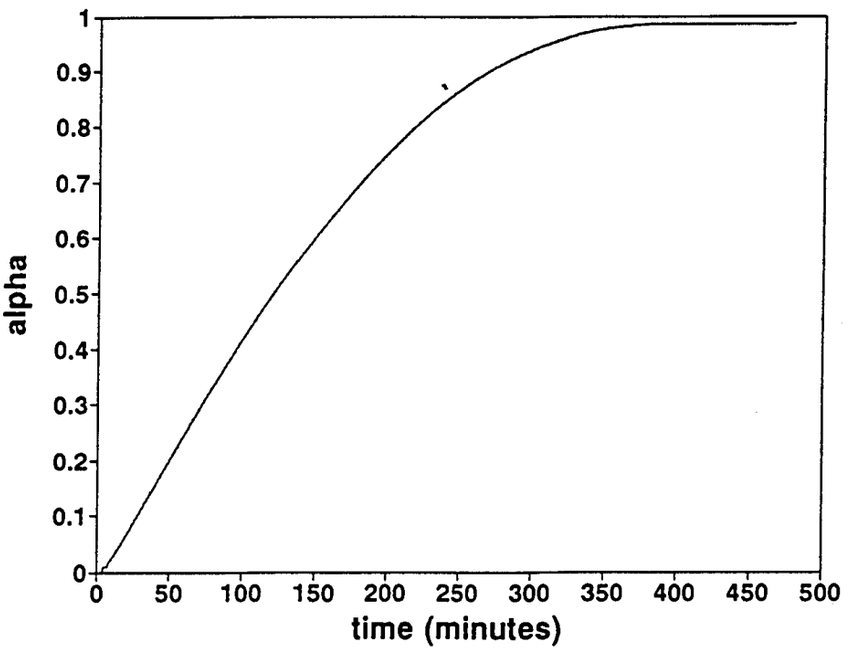

Figure 10: α versus time curve for the desolvation of **3PIC** at 77°C

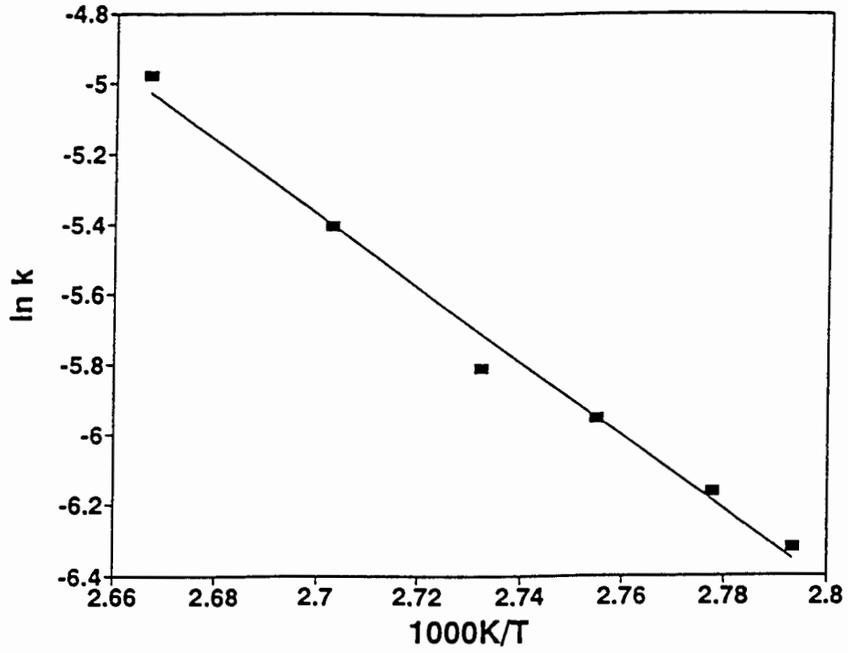

Figure 11: Plot of ln k versus 1/T for **3PIC**

It is well-known that different methods of preparation of inclusion compounds may lead to a variety of structures with inconsistent host:guest ratios[5]. The microcrystalline samples of **3PIC** used during the thermal analyses were obtained by fast stirring methods, and were therefore examined to ensure that they had the same crystal structure as that of the larger single crystals grown from solution. This was confirmed by XRD analysis. Figure 12(a) shows the XRD trace of the microcrystalline sample grown by fast stirring in comparison to the XRD trace for **3PIC** (Figure 12(c)), calculated using the program LAZY PULVERIX. These patterns match very well both in peak positions and relative intensities, and thus the two samples have the same structure.

Inclusion compounds were also obtained by exposing the powdered, uncomplexed host material to vapours of *3*-picoline, and the resulting sample yields essentially the same XRD pattern as before (Figure 12(b)). Thus inclusion of *3*-picoline from the vapour phase also results in the inclusion compound **3PIC**.

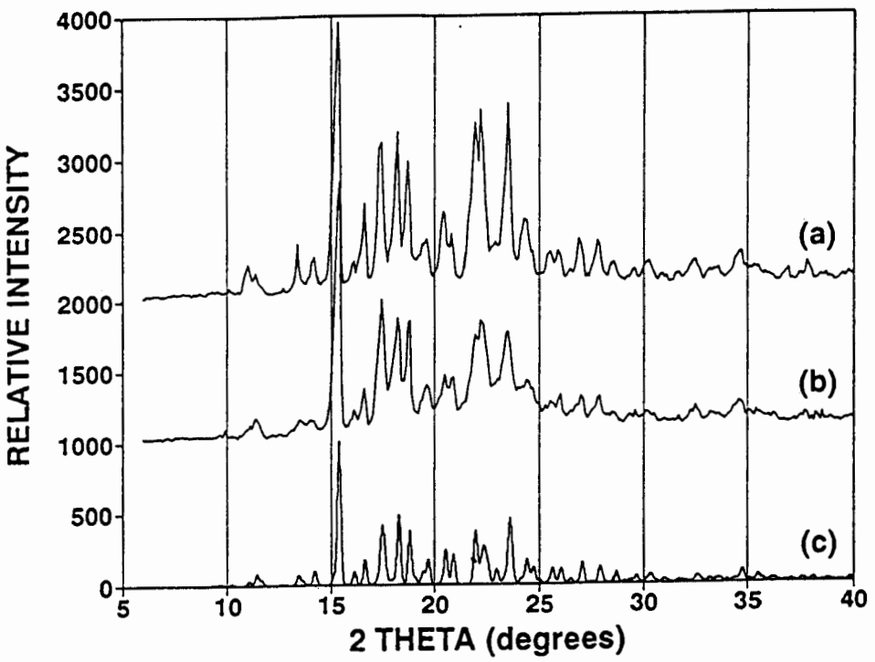

Figure 12: (a) experimental XRD pattern of **H** stirred in *3*-picoline, (b) experimental XRD pattern of **H** exposed to *3*-picoline vapour, and (c) calculated XRD pattern of **3PIC**, obtained using the program LAZY PULVERIX (using the single crystal X-ray data as input)

5.2 4PIC

5.2.1 Structure Solution

X-ray photography revealed *mmm* Laue symmetry, indicating an orthorhombic structure. The following reflection limiting conditions were also observed:

*h*00 : $h = 2n$

0*k*0 : $k = 2n$

00*l* : $l = 2n$

The space group for **4PIC** was therefore unambiguously assigned as $P2_12_12_1$. The asymmetric unit contains two host and two guest molecules, and there are four such units in the cell. The numbering scheme used for the *4*-picoline molecules is shown in Figure 13. The two crystallographically independent host and guest molecules were labelled as shown with the appended suffixes "A" and "B".

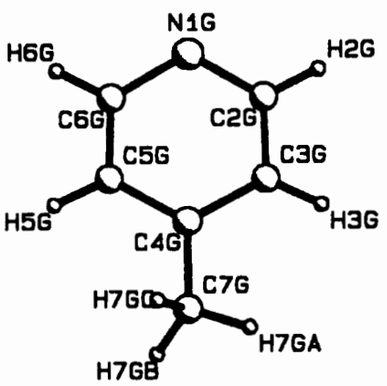

Figure 13: Atomic numbering used for *4*-picoline.

The non-hydrogen atom positions of the host molecules were yielded by direct methods, while the non-hydrogen atoms of the guests were located in difference electron density maps upon subsequent refinement. Refinement was carried out with the non-hydrogen atoms of both the host and guest molecules treated anisotropically. The hydrogen atoms of the host and guest molecules were all independently located in difference electron density maps,

but in the final model the aromatic, methylenic and methyl hydrogens were geometrically constrained [*d*(C-H) = 1.00Å] and assigned common isotropic temperature factors. The hydroxyl hydrogens were independently located in difference electron density maps, and were refined with simple bond length constraints relating O-H distances versus O--O distances[1]. The final R value obtained was R_1 = 0.0409.

5.2.2 Structure Analysis

The packing of **4PIC**, viewed down [100] and [010], is illustrated in Figures 14 and 15. Double-layered ribbons of host molecules are formed, and are held together by hydrogen bonding interactions between the host hydroxyl groups. The arrangement of the ribbons in **4PIC** is subtly different from that observed in **3PIC**. In this case, any two ribbons are displaced by a vector of ½(*a*) relative to one another, in order to accommodate the $P2_12_12_1$ symmetry. Channels are formed by the packing of the host, and these run parallel to *b*. The shapes of the channels, viewed down [100], are illustrated in Figure 16. The channels have approximately circular cross sections, with diameters of 2.5Å at the narrowest portions, and diameters of 6.5Å at the widest portions. The packing factor for **4PIC** was calculated to be 18.67 $Å^3$ / non-hydrogen atom.

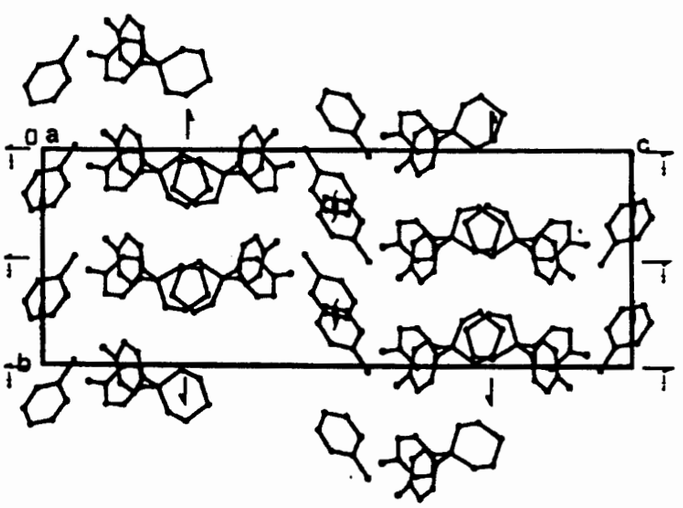

Figure 14: Crystal packing in **4PIC**, viewed down [100]

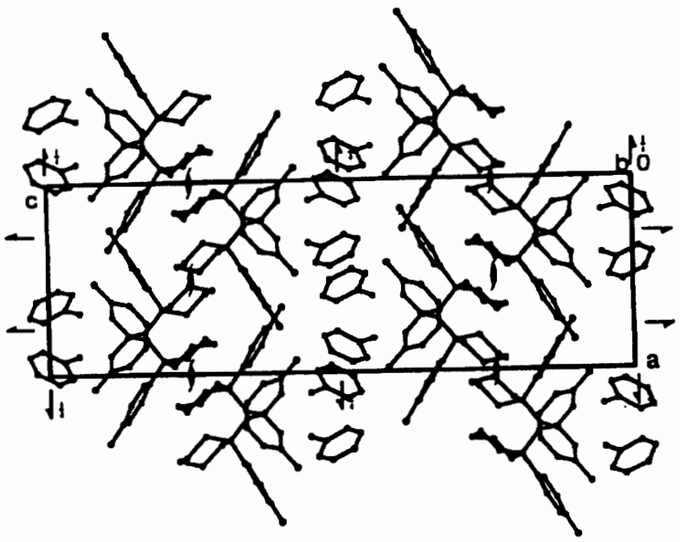

Figure 15: Crystal packing in **4PIC**, viewed down [010]

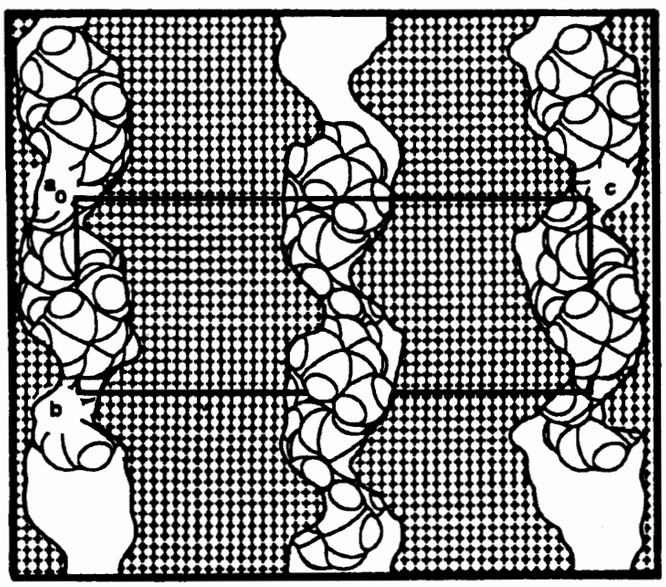

Figure 16: MOLMAP plot of **4PIC** viewed down [100], sectioned at x = 0

The hydrogen bonding scheme in **4PIC** is represented graphically in Figure 17, and details of the interactions are listed in Table 3. Host–host intermolecular interactions result in chains of host molecules running parallel to *a*. Each guest *4*-picoline molecule is stabilised in a channel by one hydrogen bond to a host molecule.

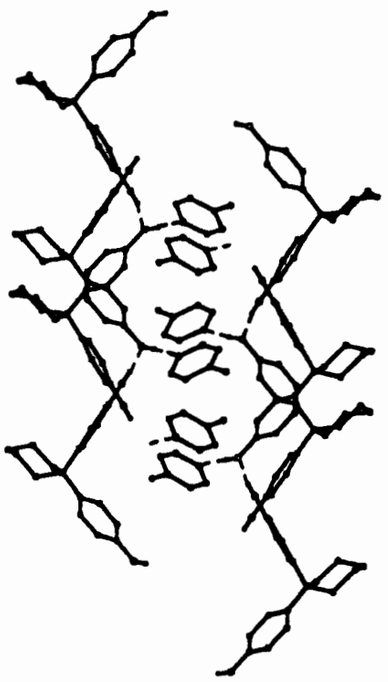

Figure 17: Hydrogen bonding scheme in **4PIC**

Table 3: Details of hydrogen bonding in **4PIC**.

Donor	Acceptor	D-H /Å*	D–A /Å*	D-H–A /°*
O13A	N1GA[a]	0.95(2)	2.676(3)	169(4)
O20B	N1GB[b]	0.97(4)	2.678(3)	174(3)
O20A	O13A[c]	0.94(3)	2.723(3)	169(3)
O13B	O20B[d]	1.00(4)	2.728(3)	169(3)

Symmetry code: *(a) x-½,-y-½,-z (b) x-½,-y+½,-z (c) x-1, y, z*
(d) x+1, y, z

* **D** = Donor ; **A** = Acceptor

5.2.3 Thermal Analysis

The TG and DSC traces for **4PIC** are shown in Figure 18. A sharp endotherm of desolvation at T_{on} = 116.5°C is observed in the DSC trace, with a corresponding mass loss of 25.0% in the TG trace (calculated mass loss for H:G = 1:1 is 25.8%). No melt endotherm is observed for the melting of the desolvated host, since the host dissolved in the hot liquid guest on desorption. Hot stage microscopy confirmed these results.

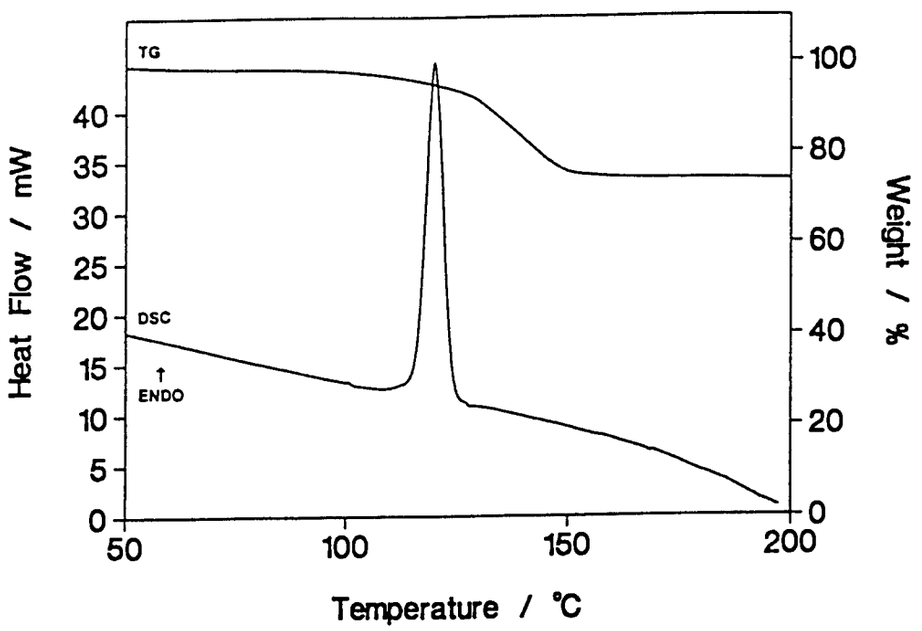

Figure 18: TG and DSC traces for **4PIC**

5.2.3.1 Hot stage microscopy

The visual interpretation of heating supports the thermal analysis, and Figure 19 illustrates the physical changes occurring in a crystal of **4PIC** upon heating. A single crystal of **4PIC** was heated on a hot stage from 25 to 200°C and photographed. Some discrepancies were observed between the temperatures at which changes occurred on the hot stage and the thermal events observed during TG and DSC experiments. These were due to different particle sizes used in the experiments, as well as the fact that the geometries of the instruments are different.

(a) Crystals of **4PIC** at 25°C.

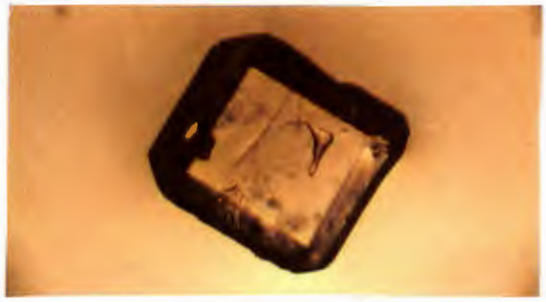

(b) A crystal of **4PIC** at 25°C, with the light source from below.

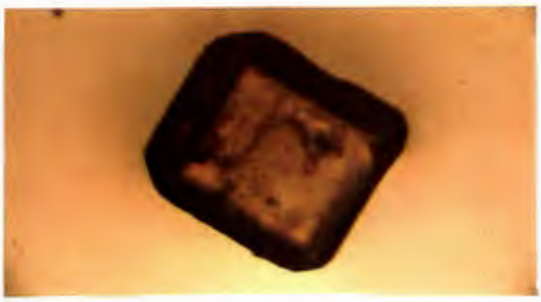

(c) The crystal starts to turn opaque at 103°C, indicating the beginning of desolvation.

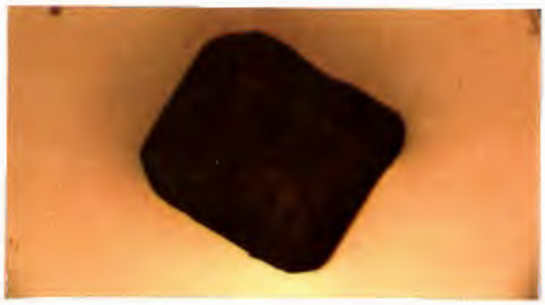

(d) At 111°C, the crystal is almost entirely opaque.

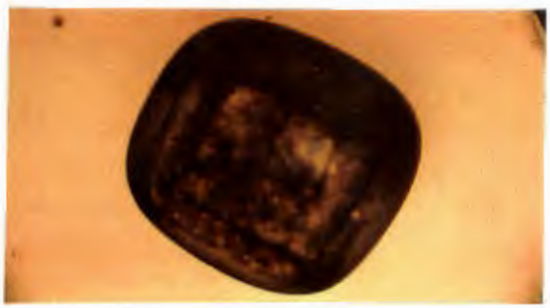

(e) At 123°C, the host compound starts to dissolve in the desolvated guest.

(f) After 30 seconds at 123°C, the crystal has nearly completely dissolved.

Figure 19: Physical changes which occur in crystals of **4PIC** upon heating (40X enlarged)

5.2.4 Desolvation: Non-isothermal Methods

Microcrystalline samples of **4PIC**, obtained by fast stirring methods, were subjected to a number of TG experiments in the range 50° to 200°C, illustrated in Figure 20. The TG runs were performed at heating rates of 1, 2, 5, 10 and 20°C per minute. The mass loss versus temperature data were reduced to -log β versus 1/T curves, Figure 21, and were analysed for various stages of the decomposition ranging from 6.25% to 21.87%. The slopes of these lines were used to calculate activation energies of the desolvation event, and values obtained were in the range 79(1) kJ mol^{-1} to 82(1) kJ mol^{-1}.

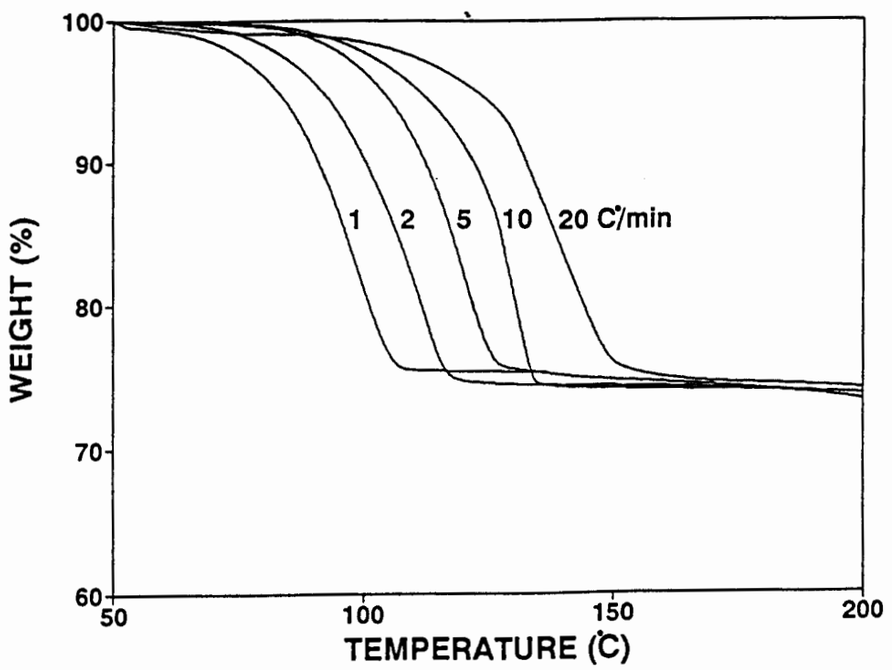

Figure 20: TG runs performed on **4PIC** over the temperature range 50 to 200°C at heating rates of 1, 2, 5, 10 and 20 °C min^{-1}

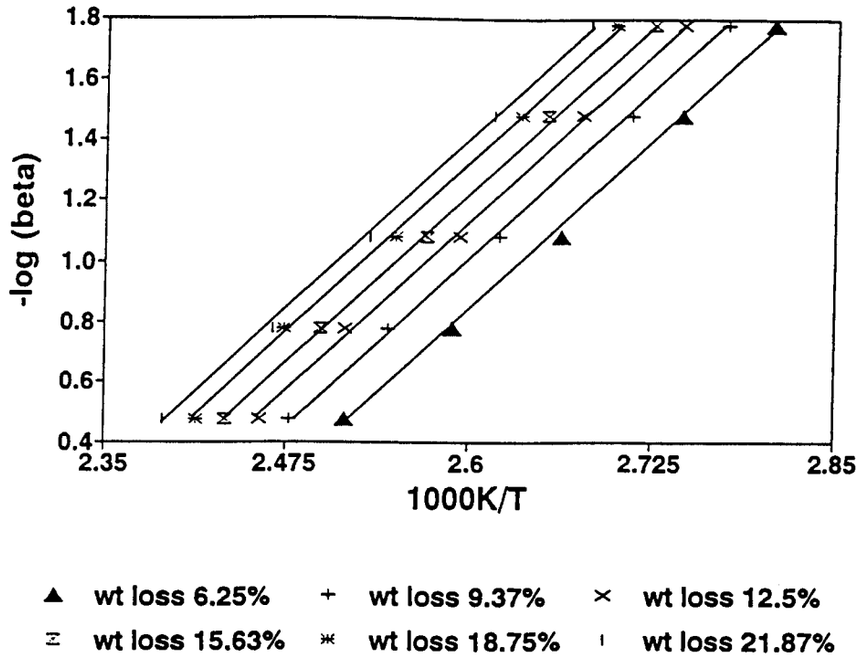

Figure 21: Plots of -log β versus 1/T for **4PIC**

The results obtained by the non-isothermal method are very satisfactory, since the lines in Figure 21 are linear, and very close to parallel. This behaviour results in a reliable estimation of the activation energy, since it is indicative of a simple, single-step desolvation process[3].

5.2.5 Desolvation: Isothermal Kinetics

A series of isothermal TG experiments were carried out on microcrystalline **4PIC** samples, over the temperature range 63°C to 75°C at intervals of 2 or 3°C. The resulting α versus time curves were sigmoidal, and were fitted to the various kinetic models for sigmoidal systems. The R2 (contracting area) model, $kt = 1-(1-\alpha)^{\frac{1}{2}}$, was found to be the best-fitting model. The Arrhenius plot yielded by application of this model is shown in Figure 22. An activation energy of 85(5) kJ mol^{-1} for desolvation of **4PIC** was obtained from the slope of this line.

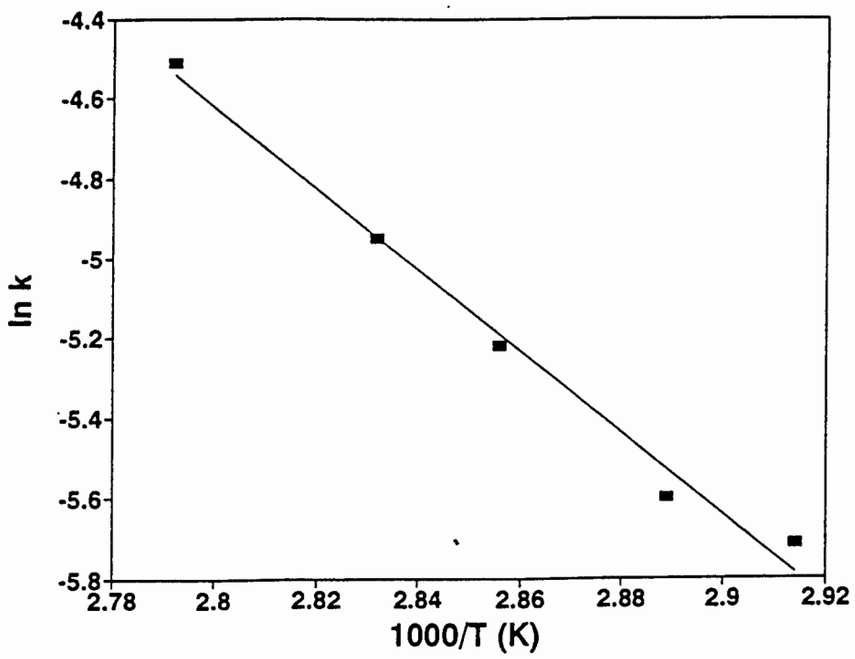

Figure 22: Plot of ln k versus 1/T for **4PIC**

The microcrystalline samples used for thermal analyses were obtained by fast stirring methods, and were examined by XRD to ensure that they had the same structure as the **4PIC** crystals obtained by slow evaporation from solution. Figures 23(a) and 23(c) compares the experimental XRD trace of the microcrystalline sample with the calculated trace of **4PIC**, obtained using the program LAZY PULVERIX. These two traces coincide well in peak position and relative intensities, and thus the two samples are isomorphous.

Exposing the host to vapours of *4*-picoline also yielded the same inclusion compound as that grown from solution. The XRD trace of the product resulting from this experiment is also represented in Figure 23(b), and coincides well with the trace of the **4PIC** complex.

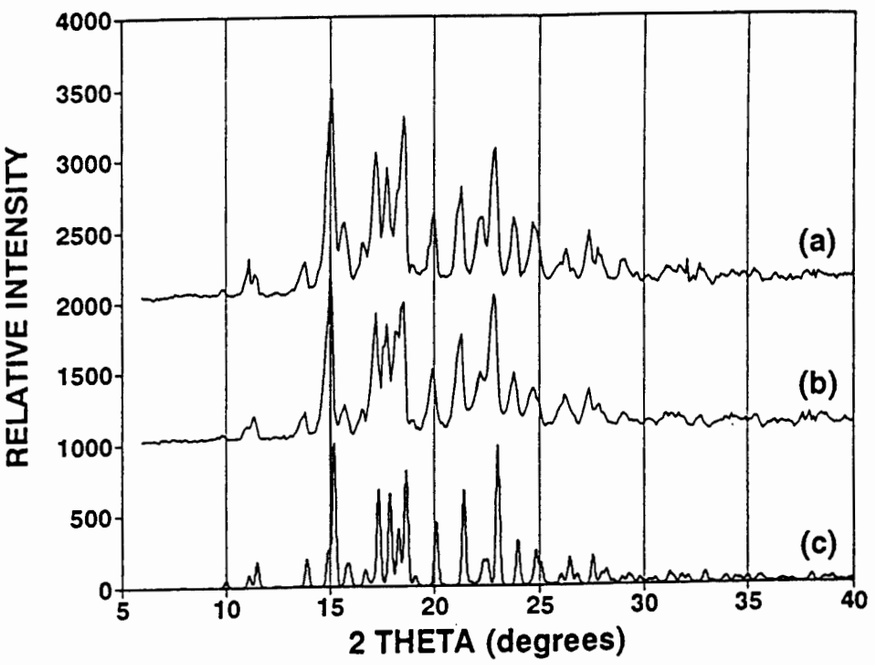

Figure 23: (a) experimental XRD trace of **H** stirred in *4*-picoline, (b) experimental XRD trace of **H** exposed to *4*-picoline vapour, and (c) calculated XRD trace of **4PIC** (calculated using the program LAZY PULVERIX)

5.3 2PIC

It proved to be very difficult to obtain crystals of the inclusion complex formed between the host, **H**, and 2-picoline, and numerous attempts failed. However, crystals of the ternary inclusion complex with **H**, 2-picoline and water (**2PIC**) were obtained, and the structure of this complex will be presented in the next section. The crystals were of low quality and gave a poor diffraction pattern with very weak reflections beyond $\theta = 10°$. The structure solution of **2PIC** is not totally satisfactory, but allows one to draw some conclusions about the overall molecular packing and the relative stability of the complex.

5.3.1 Structure Solution

Preliminary photography indicated that the inclusion complex **2PIC** belonged to the triclinic crystal system, and therefore the possible space groups were P1 and P $\bar{1}$. The centrosymmetric space group P $\bar{1}$ was chosen based on the mean $|E^2-1|$ statistics, which were in the range 0.899 to 1.023 for the zonal reflections 0*kl*, *h*0*l*, *hk*0 and the remainder of the reflections.

TG experiments indicated that the compound **2PIC** was a ternary complex with an **H**:H_2O:2-picoline ratio of 1:1:1. The atomic numbering scheme used for the 2-picoline and water molecule during the structure solution of **2PIC** is given in Figure 24.

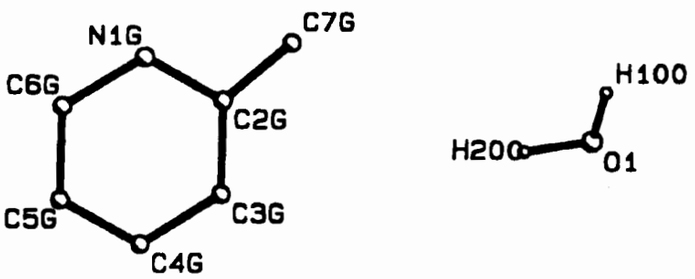

Figure 24: Atomic numbering used for the 2-picoline and H_2O molecules

Direct methods yielded the positions of all the non-hydrogen atoms of the host compound. The position of the water oxygen atom was located in the difference electron density maps upon subsequent refinement. The positions of the host aromatic and methylenic hydrogen atoms were identified from the difference electron density maps, but they were inserted into the model with geometric constraints [*d*(C-H) = 1.00Å], and were assigned common isotropic temperature factors. The host hydroxyl hydrogens and water hydrogens were independently located in the maps, and were refined with simple bond lengths constraints relating O-H distances versus O···O distances[1].

Peaks representing the 2-picoline molecule were located in difference electron density maps, but these yielded a molecule of unsatisfactory geometry. The ring of the 2-picoline molecule was thus geometrically constrained to fit a regular hexagon, and the atoms were assigned a common isotropic temperature factor. U_{eq} for the ring atoms at the end of refinement was 0.12Å^2. The position of the nitrogen atom in the ring was identified by its distance to the oxygen atom of the water molecule. The 2-picoline molecule was refined isotropically, and its hydrogen atoms were omitted from the model. The final R factor for the model was R_1 = 0.162.

5.3.2 Structure Analysis

The packing of **2PIC**, viewed down [100] and [010] is depicted in Figures 25 and 26. The host framework consists of ribbons of host molecules parallel to [100]. Within the ribbons, adjacent host molecules are hydrogen bonded to each other via their hydroxyl groups. Adjacent ribbons interlink by the convenient steric fit of their cyclohexyl moieties, to form double layers.

The positioning of these layers is such that channels form between them in which the guest water and 2-picoline molecules are located. Figure 27 is a MOLMAP plot demonstrating the shapes of the channels down [010], which are relatively unconstricted, and have diameters of 7.6Å across their narrowest parts. The packing factor for **2PIC** was calculated to be 18.94 Å^3 / non-hydrogen atom.

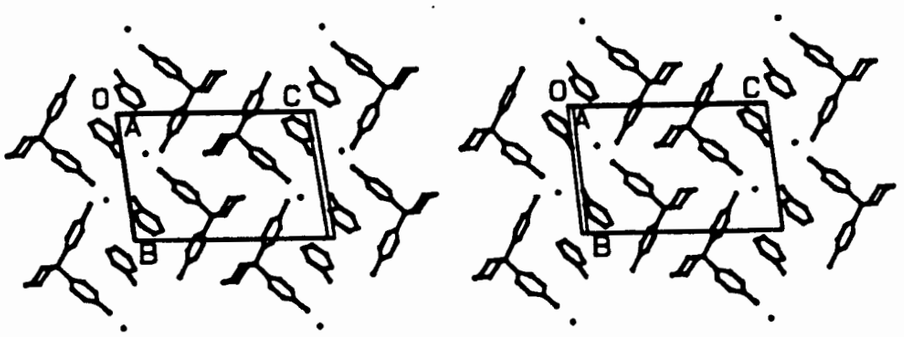

Figure 25: A stereo projection down [100] showing the crystal packing in **2PIC**

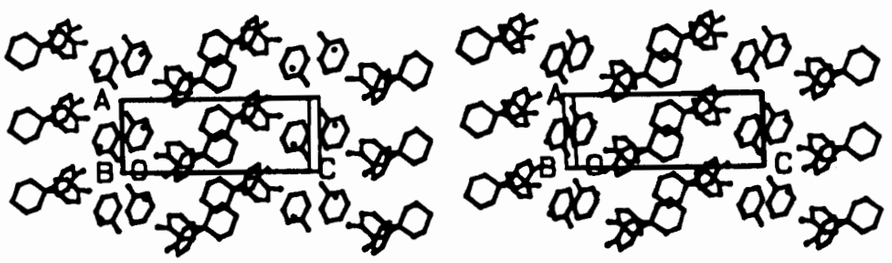

Figure 26: Packing diagram of **2PIC** viewed down [010]

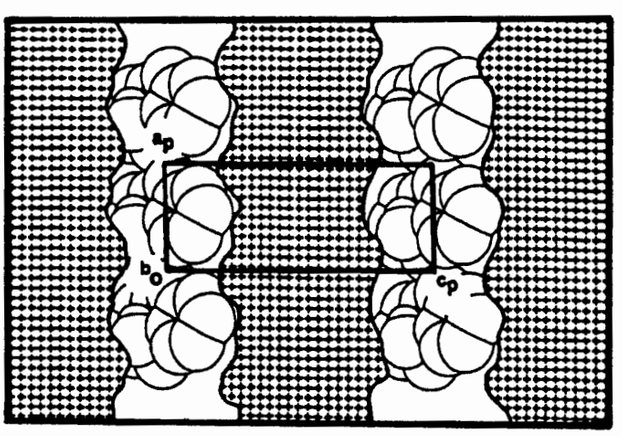

Figure 27: MOLMAP plot of **2PIC** viewed down [010], sectioned at y=0. The channels are relatively wide and unconstricted.

The hydrogen bonding scheme in **2PIC** is illustrated in Figure 28, and geometric details are listed in Table 4. Ribbons of host molecules pack parallel to *a*, by the end-to-end hydrogen bonding of adjacent molecules. Each hydroxyl group involved in a host–host hydrogen bond interacts with a water molecule, which in turn hydrogen bonds to a 2-picoline molecule. Each water molecule in the structure is therefore involved in three hydrogen bonds, twice as a proton donor and once as a proton acceptor. The 2-picoline molecules do not interact directly with the host framework, but are linked to it via water molecules.

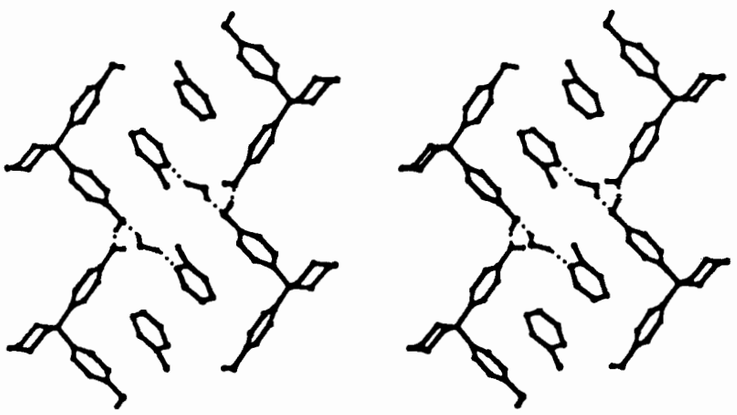

Figure 28: Hydrogen bonding scheme in **2PIC**

Table 4: Details of hydrogen bonding in **2PIC**.

Donor	Acceptor	D-H /Å*	D–A /Å*	D-H–A /°*
O1	O20	0.99(8)	2.77(1)	157(8)
O13	O1[a]	0.98(11)	2.57(1)	169(10)
O20	O13[b]	0.97(9)	2.68(1)	153(8)
O1	N1G[c]	0.99(9)	2.720(9)	138(8)

Symmetry code: *(a) x-1, y+1, z (b) x, y-1, z (c) -x+1,-y+1,-z*

* **D** = Donor ; **A** = Acceptor

5.3.3 Thermal Analysis

The TG and DSC traces for **2PIC** are illustrated in Figure 29. TG confirms the **H**:H_2O:2-picoline ratio in the **2PIC** complex. The TG shows two mass loss steps labelled "A" and "B".

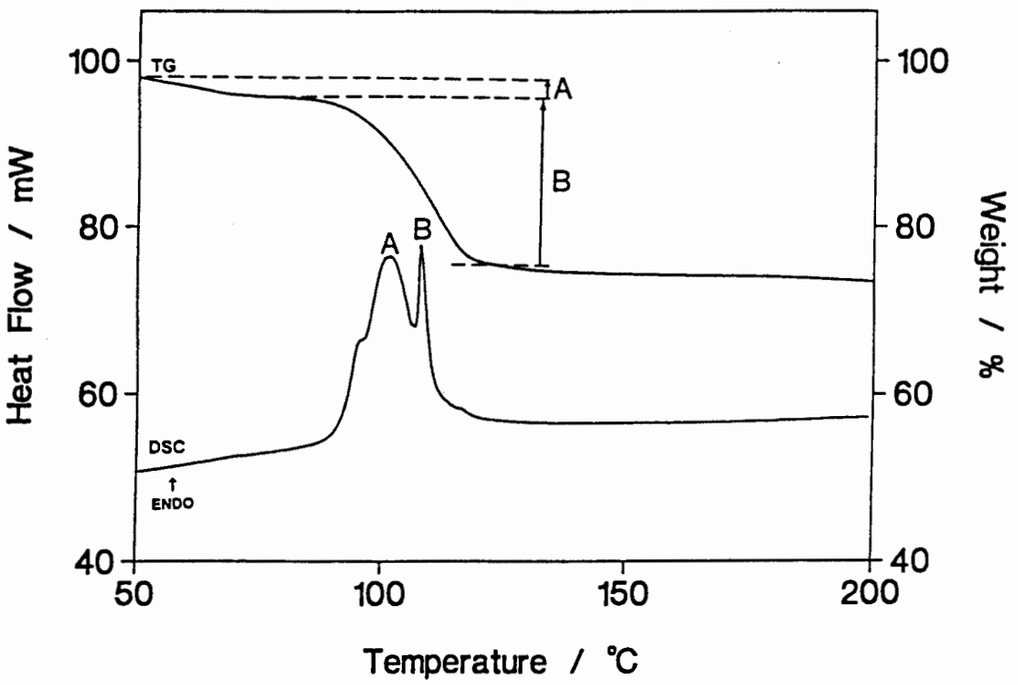

Figure 29: TG and DSC traces for **2PIC**

The experimental mass losses for steps A and B are 4.7% and 24.8% respectively. The calculated mass losses are 4.8% for the loss of water, and 24.5% for the desorption of the picoline from **2PIC**. Two endotherms in the DSC trace at T_{on} = 92.3°C (endotherm A) and T_{on} = 107.2°C (endotherm B), correspond to the desolvation of water and 2-picoline respectively. The desolvated host compound dissolved in the desorbed 2-picoline, and therefore a separate endotherm representing a melt is not observed.

5.3.3.1 Hot Stage Microscopy

Crystals of **2PIC** were covered in silicone oil and heated on a hot stage over the temperature range 20°C to 200°C. Photographs were taken of the changes to the physical appearance of the crystals. These photographs are presented in Figure 30.

At 90°C, the crystals turn opaque due to the commencement of desolvation. Bubbles of desolvated guest vapour are observed in the silicone oil. More bubbles appear as the desolvation reaction proceeds, and these are also observed within the crystal. At 106°C, small crystallites form at the edges of the crystal, until 109°C when the crystal is completely opaque, and begins to dissolve. At 111°C, the crystal has completely dissolved.

Attempts have been made to isolate the two desolvation steps of **2PIC**, and to evaluate their kinetics. However, the two desolvation processes were not easily distinguishable, and therefore could not be studied separately.

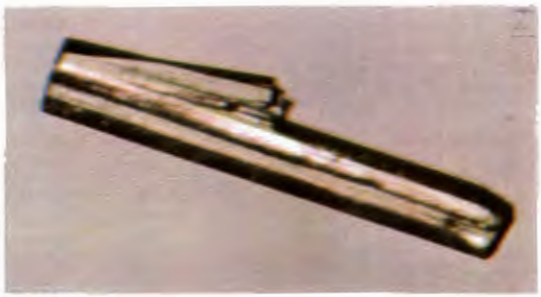

(a) Crystals of **2PIC**, submerged in silicone oil, at 20°C

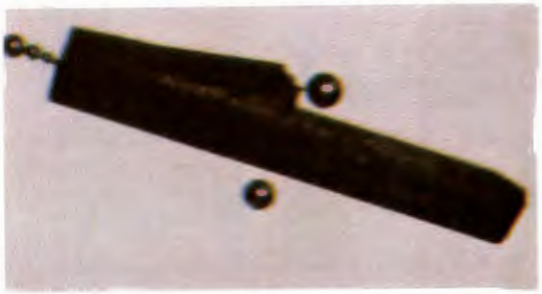

(b) Desolvation commences at 90°C

(c) At 106°C, crystallites appear at the edges of the larger crystals

(d) At 106°C after 1 minute, more crystallites have formed

(e) The crystal begins to dissolve in the desolvated guest at 109°C

(f) The crystal has completely dissolved by 111°C

Figure 30: Hot stage microscope photographs taken while heating crystals of **2PIC**

5.4 POTENTIAL ENERGY CALCULATIONS

Lattice energies of the complexes were calculated using the program HEENY, and the results are listed in Table 5. The procedure followed was as described in Chapter 2.

Table 5: Lattice energy values for the complexes **3PIC, 4PIC** and **2PIC**

	3PIC E /kJ mol^{-1}	**4PIC** E /kJ mol^{-1}	**2PIC** E /kJ mol^{-1}
H--H	-183.9	-171.8	-135.6
H--G (non-hydrogen bonding)	-40.8	-54.6	-37.4*
G--G (non-hydrogen bonding)	-35.5	-33.9	-25.6
TOTAL:	-260.2	-260.3	-198.6

* G = H_2O + 2-picoline

5.5 COMPETITION EXPERIMENTS

2- and 3-Component competition experiments were performed on the picoline system. These competitions were carried out by the recrystallisation of the host from mixtures of the picoline isomers, as described in Chapter 2. The results of these experiments are depicted in Figure 31, while details are listed in Appendix 1.

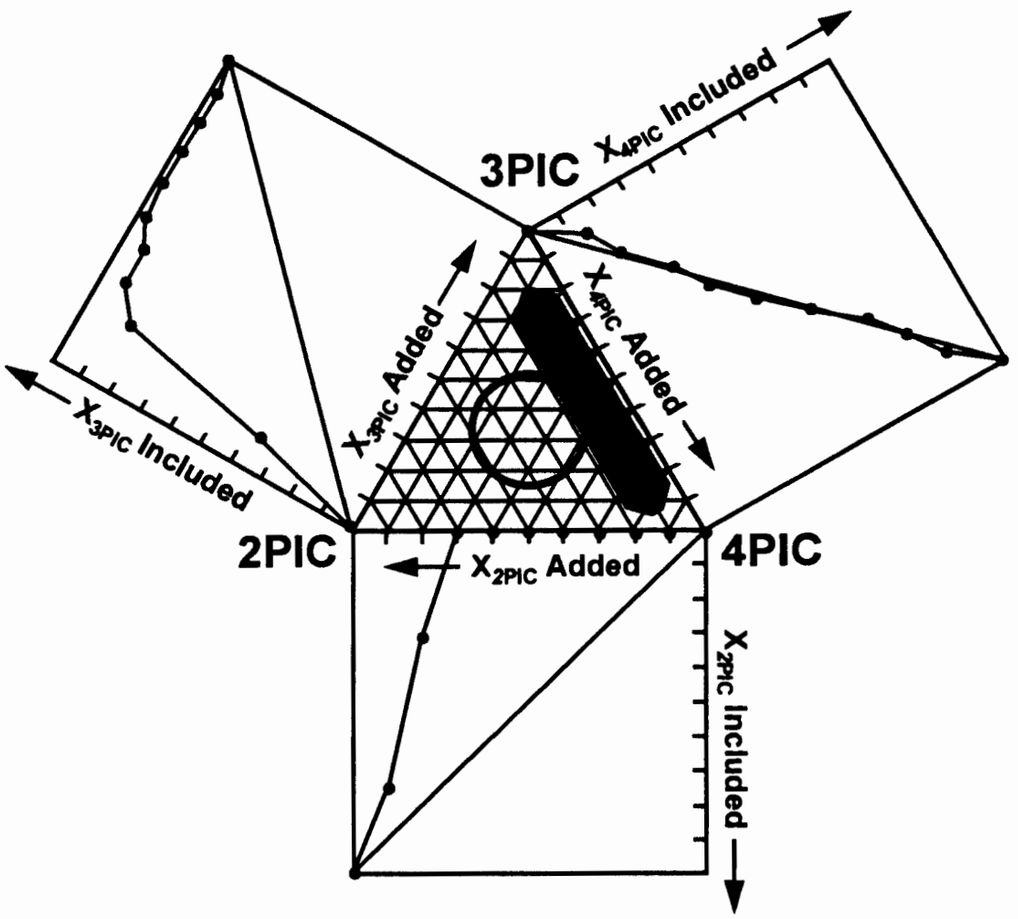

Figure 31: Results of the picoline competition experiments

5.5.1 2-Component

In the 2-picoline/*3*-picoline competition the latter is strongly favoured by the host, **H**. Solutions initially containing more than 20% *3*-picoline result in more than 90% *3*-picoline being complexed.

4-Picoline is also convincingly favoured over *2*-picoline, and solutions containing more than 20% *4*-picoline result in the exclusive complexation of this isomer.

In the *3*-picoline/*4*-picoline experiment no significant selectivity is observed. The ratio of the two isomers complexed by the host in each case was approximately the same as the ratio of the isomers in the original solutions. The resulting selectivity curve therefore approximates the line x = y.

5.5.2 3-Component

The results of the three-component experiment is shown on the equilateral triangle. Points on the circle represent the concentrations of the isomers originally present in the solutions, while points on the shaded area represent the concentrations of the isomers included by the host after recrystallisation.

A migration of the starting circle occurs towards the *3*-picoline / *4*-picoline line, with no particular selectivity occurring for either of these two isomers. The circle moves **away** from the 2-picoline apex, indicating that this isomer is very convincingly disfavoured in this experiment. These results correspond to those obtained from the 2-component competition experiments.

5.6 DISCUSSION

A comparison of the structures of **3PIC** and **4PIC** reveals that they are nearly isomorphous[6], since they have similar cell dimensions and display similar packing motifs. However, the packing arrangements in the two complexes are subtly different. In both cases, the host molecules pack to form double ribbons, but in **4PIC** the ribbons are displaced by a vector of ½(*a*) relative to one another, while in **3PIC** the ribbons are related to each other by a two-fold screw operation.

The relative stabilities of the complexes **3PIC** and **4PIC** were obtained by determining the activation energies for the desolvation reactions which occur on heating the complexes. Both isothermal and non-isothermal methods were employed, and excellent agreement was obtained between these two methods. The kinetic models for desolvation of the two complexes were different, with **4PIC** following the sigmoidal mechanism A, and **3PIC** following the deceleratory contracting area model R2. However, the activation energy for the desolvation of **3PIC** was not significantly different from that obtained for the desolvation of **4PIC**. A possible explanation for this similar stability lies in the fact that in both complexes the guest molecules are located in channels of approximately the same dimensions. Therefore the *3*-picoline and *4*-picoline guest molecules have to overcome a similar physical barrier during the desolvation process. In addition, the guest molecules in each structure have to overcome the stabilising influence of one hydrogen bond each to the host framework in order to escape from the crystals. The calculated lattice energy of each complex also reflects the similar stability of the two complexes, since the energy is approximately -260 kJ mol^{-1} in both cases.

It was therefore not surprising that no preferential selectivity was observed between *3*-picoline and *4*-picoline on complexation with **H**, since the resulting complexes are of similar stability.

The convincing disfavouring of 2-picoline by the host **H** during the competition experiments is supported by the experimental difficulties experienced in obtaining crystals of the resulting complex. A possible deterring factor could be the steric hindrance which the methyl substituent of 2-picoline provides, blocking access to the nitrogen atom for hydrogen bonding directly to the host. The addition of a small water molecule to the complex overcomes this problem, and acts as a linkage between 2-picoline and **H**. A graphical representation of the position of the water molecule between the phenol moiety of a host molecule and a 2-picoline molecule is shown in Figure 32. This diagram illustrates the structural complementarity between the water and 2-picoline molecules.

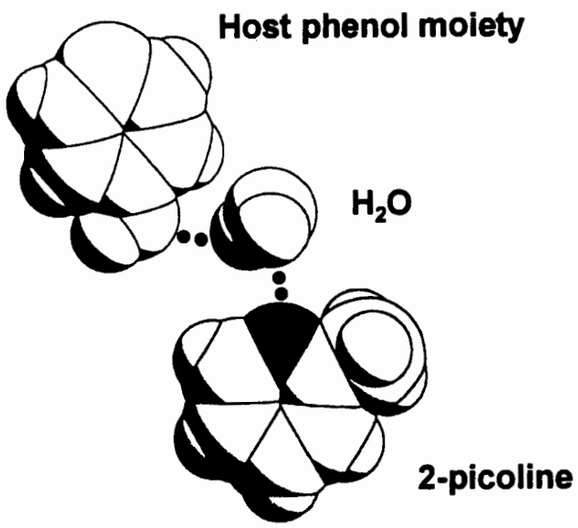

Figure 32: The sterically favourable arrangement of 2-picoline, H_2O and the phenol moiety of the host molecule

The selective complexation of the host with the isomers of picoline follows the trend: **3PIC** ≅ **4PIC** > **2PIC**, and these results support the comments made regarding the relative stability of the complexes. The results obtained during the 3-component competition experiments concur, and show the migration of the starting circle towards the 3-picoline/4-picoline line, with no preference for

either of these two isomers. However, the disfavouring of 2-picoline for complexation with the host is very convincing. The lattice energy of **2PIC** was calculated to be -198 kJ mol^{-1}, which is remarkably lower than that of **3PIC** and **4PIC** (-260 $kJmol^{-1}$ for both complexes). This is indicative of the much lower stability of the **2PIC** complex, and explains why this complex is not formed easily.

1 I. Olovsson and P. Jönsson, *The Hydrogen Bond - Structure and Spectroscopy*, P. Schuster, G. Zundel and C. Sarderfy (eds.), North-Holland Publishing Company, USA, 1975.

2 F. H. Allen, O. Kennard, D. G. Watson, L. Brammer, A. G. Orpen and R. Taylor, *J. Chem. Soc., Perkin Trans.* 2, 1987, S1-S19.

3 S. V. Vyazovkin and A. I. Lesnikovich, *Thermochim. Acta*, **165**, 1990, 273.

4 J. Opfermann and E. Kaisersberger, *Thermochim. Acta,* **203**, 1992, 167.

5 D. Giron, *Thermochim. Acta*, **248**, 1995, 1.

6 A. Kálmán, L. Partikanyi and G. Arkay, *Acta Crystallogr.*, **B49**, 1993, 1039.

6. INCLUSION OF LUTIDINE GUESTS

The interactions between the host compound and the isomers of lutidine were investigated, and will be discussed in this chapter. Single crystals of the inclusion compounds **24LUT** and **35LUT** were obtained, and their structures have been elucidated. The activation energies and the kinetic models of desolvation for these two complexes were determined. Competition experiments were performed to investigate which isomer of lutidine is preferentially enclathrated by the host. Lattice energy calculations explain the results of the competition experiments. Numerous attempts to grow single crystals of the inclusion complex between **H** and *2,6*-lutidine failed, and therefore the structure cannot be reported.

Unit cell parameters and space groups were determined by preliminary X-ray photography. Crystallographic experimental and refinement details for **24LUT** and **35LUT** are provided in Table 1, while final atomic co-ordinates, temperature factors, tables of bond lengths and bond angles are contained in Appendix 3, while tables of observed and calculated structure factors are listed in Appendix 4.

Table 1: Details of crystals, data collections and final refinements

	24LUT	**35LUT**
Molecular formula	$C_{18}H_{20}O_2 \bullet C_7H_9N$	$C_{18}H_{20}O_2 \bullet C_7H_9N$
Molecular weight /g mol^{-1}	375.49	375.49
Space group	$P2_1/n$	$P2_1$
a /Å	7.665(9)	10.509(2)
b /Å	31.361(5)	6.309(2)
c /Å	8.874(2)	16.118(6)
β /°	99.14(1)	96.99(2)
V /Å^3	2106.0(6)	1060.7(5)
Z	4	2
D_c /g cm^{-3}	1.18	1.18
D_m /g cm^{-3}	1.16(2)	1.15(4)
μ (Mo-K_α) /cm^{-1}	0.70	0.74
F(000)	808	404
Crystal size /mm	0.34 x 0.34 x 0.30	0.4 x 0.5 x 0.35
Range scanned, θ /°	1 - 25	1 - 25
Range of indices	*h*: 9,18; *k*: 0,37; *l*: 0,10	*h*: ±12; *k*: 0,7; *l*: 0,19
Crystal decay, /%	-1.9	2.4
No. reflections collected	3937	2136
No. reflections observed ($I > 2\sigma(I_{rel})$)	3696	2059
No. parameters	271	271
R_1	0.0448	0.0365
wR_2	0.1250	0.0885
S	1.046	1.075
Δρ /e Å^{-3}	0.183; -0.242	0.129; -0.198

6.1 24LUT

6.1.1 Structure Solution

The X-ray diffraction pattern of **24LUT** was found to possess *2/m* Laue symmetry and the complex therefore crystallises in the monoclinic system. The space group $P2_1/n$ was assigned after observation of the following reflection conditions :

hkl : none

*h*0*l* : $h+l = 2n$

0*k*0 : $k = 2n$

(*h*00 : $h = 2n$)

(00*l* : $l = 2n$)

$P2_1/n$ is equivalent to the space group $P2_1/c$, but refers to a different cell choice which results in the *c*-glide plane being converted into an *n*-glide plane.

There are four host molecules and four guest molecules in the unit cell of **24LUT**, and thus no crystallographic symmetry is imposed on either host or guest molecule. The numbering scheme used to label the atoms of *2,4*-lutidine is illustrated in Figure 1. The host numbering scheme is as before (illustrated in Chapter 3, Figure 1).

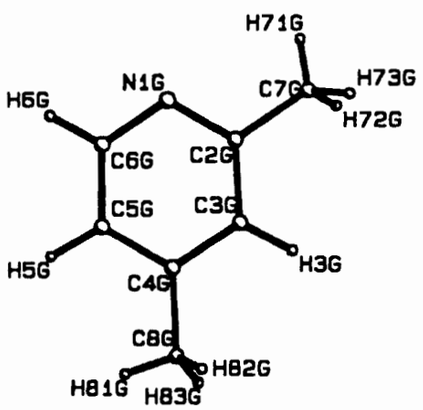

Figure 1: Atomic numbering of *2,4*-lutidine

The non-hydrogen atom positions of both the host and guest molecules were obtained by direct methods. The position of the nitrogen atom of the guest was ambiguous since there was not a convincing difference in the electron density of the peaks representing the lutidine ring. Therefore all guest atom peaks located in the electron density maps were initially entered as carbon atoms. The nitrogen atom was identified by its distance to the oxygen atom of a host hydroxy group, accompanied by the fact that its temperature factor was higher than those of the other atoms of the guest. On changing the atom assignment from carbon to nitrogen, the temperature factor became acceptable. Refinement was carried out with the non-hydrogen atoms of both the host and guest molecules treated anisotropically. The hydrogen atoms of the host and guest were located in difference electron density maps, but in the final model, the aromatic, methylenic and methyl hydrogens were geometrically constrained [d(C-H) = 1.00Å] and assigned common isotropic temperature factors. The host hydroxyl hydrogens were independently located in difference electron density maps, and were refined with a simple bond length constraint relating O-H distances versus O--O distances[1]. The structure refined successfully to R_1 = 0.0448.

6.1.2 Structure Analysis

Bond lengths, bond angles and torsion angles of the host and guest molecules were in acceptable ranges[2]. The host conformation will be discussed in detail in Chapter 8.

Packing diagrams of **24LUT,** viewed along [100] and [001] are illustrated in Figures 2 and 3. The familiar packing of this host is once again observed in this structure. The host molecules pack to form ribbons which run parallel to [001]. Two ribbons are held together by van der Waals forces, and the cyclohexyl moieties of one ring fit between the cyclohexyl moieties of the adjacent ribbon. Double ribbons formed in this manner are separated by ribbons of guest molecules, also parallel to [001]. The shapes of the channels formed in the host framework of the crystal are depicted by a MOLMAP plot in

Figure 4. The channels have approximately circular cross sections with diameters of ~8Å at their widest portions, and ~3Å at their narrowest. The packing factor for this structure was found to be 18.80 $Å^3$ / non-hydrogen atom.

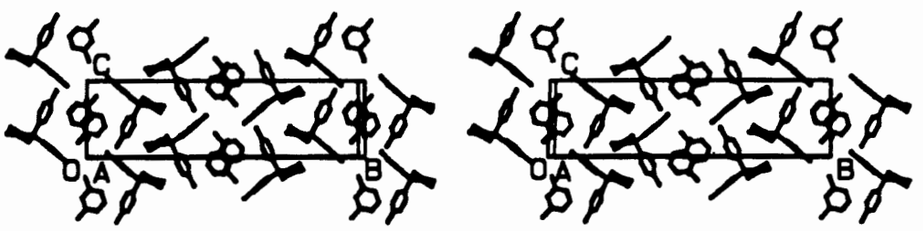

Figure 2: Stereo view of the packing of **24LUT** down [100]

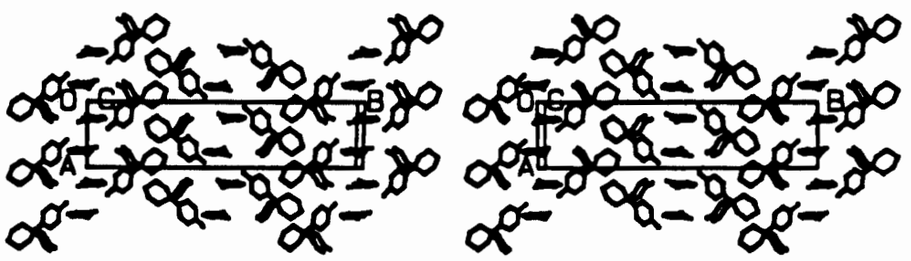

Figure 3: Stereo view of the packing **24LUT** down [001]

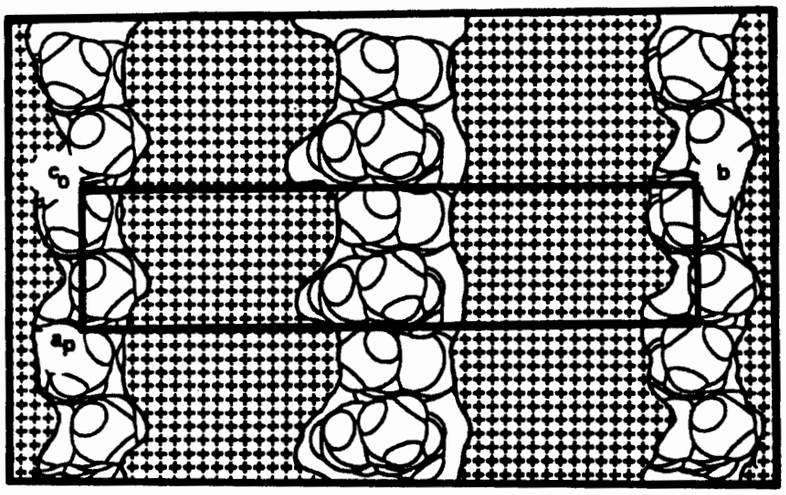

Figure 4: MOLMAP plot of **24LUT** viewed down [001], at the section z = 0.0

Both host–host and host–guest intermolecular interactions occur, and these are illustrated in Figure 5. The host ribbons are formed by adjacent host molecules hydrogen bonding to each other at their hydroxyl sites. Each guest lutidine molecule is hydrogen bonded to the host structure once. Table 2 contains the hydrogen bonding details for **24LUT**.

Stabilising π–π interactions occur between the guest molecules in **24LUT**. The characteristic pattern of a C–C stabilised stack structure, with partial overlap of parallel adjacent molecules is observed between guest molecules in the channels[3]. C–C stack distances between a guest molecule and its nearest neighbouring guest molecule are all in the range 3.574(2) to 4.909(1) Å.

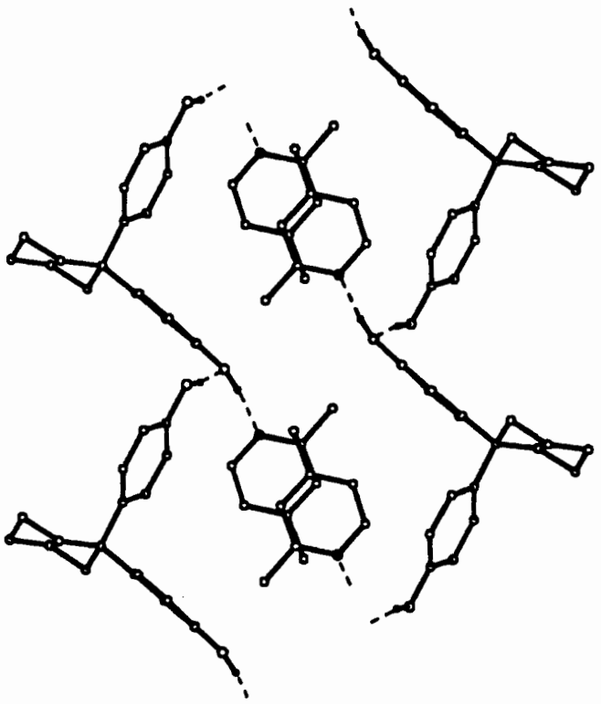

Figure 5: Hydrogen bonding scheme in **24LUT**, viewed down [100]. The guest nitrogen atoms are shaded for clarity.

Table 2: Hydrogen bonding data for **24LUT**.

Donor	Acceptor	D-H /Å*	D–A /Å*	D-H–A /°*
O13	N1G[a]	0.96(4)	2.677(3)	172(3)
O20	O13[b]	0.96(3)	2.743(3)	167(3)

Symmetry code: *(a) x, y, z+1 (b) x-1, y, z-1*

* **D** = Donor ; **A** = Acceptor

6.1.3 Thermal Analysis

The TG and DSC traces for **24LUT** are shown in Figure 6. A mass loss step of 27.5% in the TG trace agrees well with the calculated value of 28.5% for a 1:1 inclusion complex between **H** and *2,4*-lutidine. An endotherm at T_{on} = 125.4°C in the DSC trace corresponds to guest desorption. The host dissolves in the hot guest liquid, and therefore an endotherm for the melt of the host is not observed. A crystal of **24LUT** was heated on a hot stage to correlate the physical changes of the crystals with the thermal events observed in the TG and DSC traces.

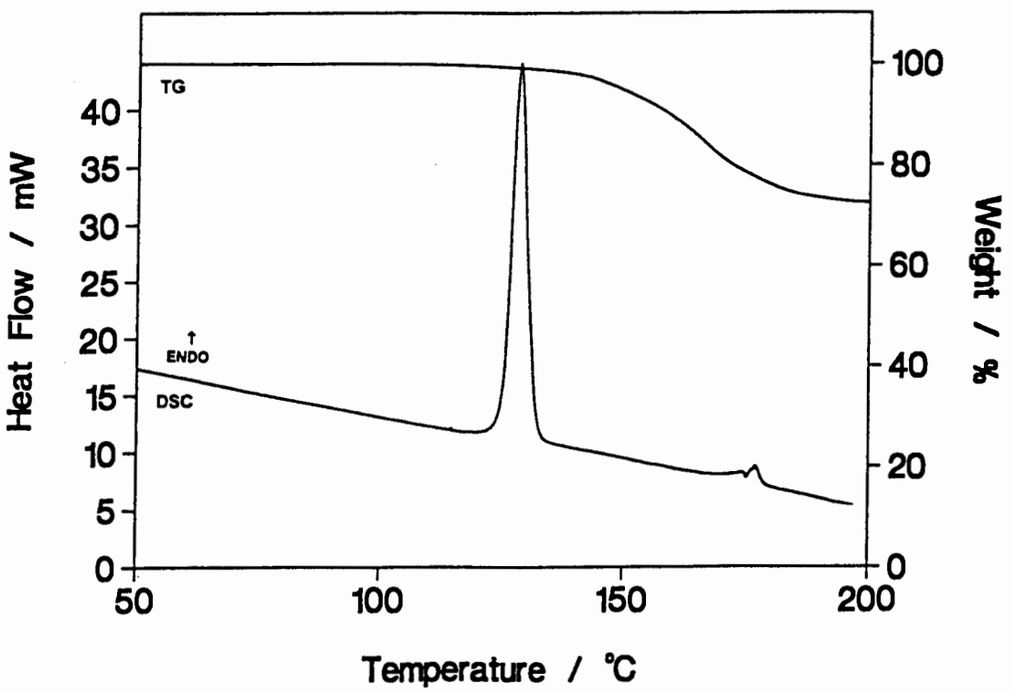

Figure 6: TG and DSC traces for **24LUT**

6.1.3.1 Hot Stage Microscopy

A series of photographs depicting the changes occurring in **24LUT** upon heating in the range 20°C to 200°C is depicted in Figure 7.

(a) A crystal of **24LUT** in silicone oil at 20°C, with the light source from below.

(b) At 108°C, small defects appear in the crystal, indicating the beginning of guest desorption.

(c) At 115°C, desolvation is still in progress, and the crystal starts becoming opaque.

(d) By 125°C, small crystallites form on the edges of the crystal.

(e) At 128°C, many crystallites have formed, and the crystal begins to dissolve.

(f) The crystal dissolves completely in the desorbed *2,4*-lutidine at 129°C.

Figure 7: Photographs of physical changes which occur when heating crystals of **24LUT** (40X enlarged)

6.1.3.2 Desolvation: Non-isothermal Methods

Powdered samples of the complex **24LUT**, obtained by stirring a solution of **H** in *2,4*-lutidine, were subjected to a series of TG experiments. The experiments were all performed over the temperature range 50 to 180°C, but at heating rates of 1, 2, 5, 10 and 20°C min^{-1}. The mass loss versus temperature data were reduced to extent of reaction versus 1/T , and a series of -log β versus 1/T curves were obtained. The slopes of these curves yielded values of activation energy, E_a, for desorption of *2,4*-lutidine in the range 81(4) to 83(5) kJ mol^{-1}. The experimental desorption curves and reduced data curves are represented in Figures 8 and 9 respectively.

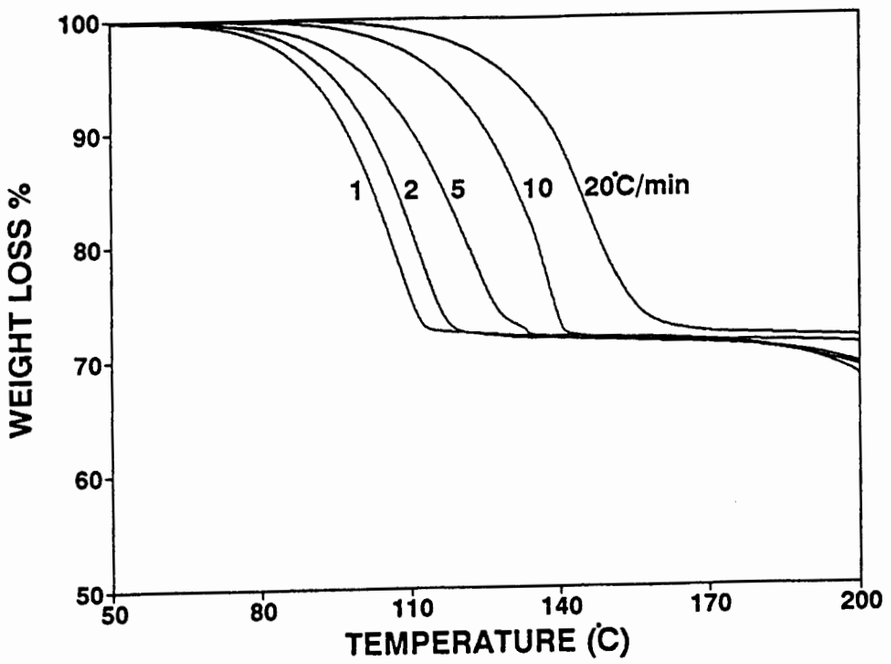

Figure 8: TG curves for desorption of **24LUT** at various heating rates

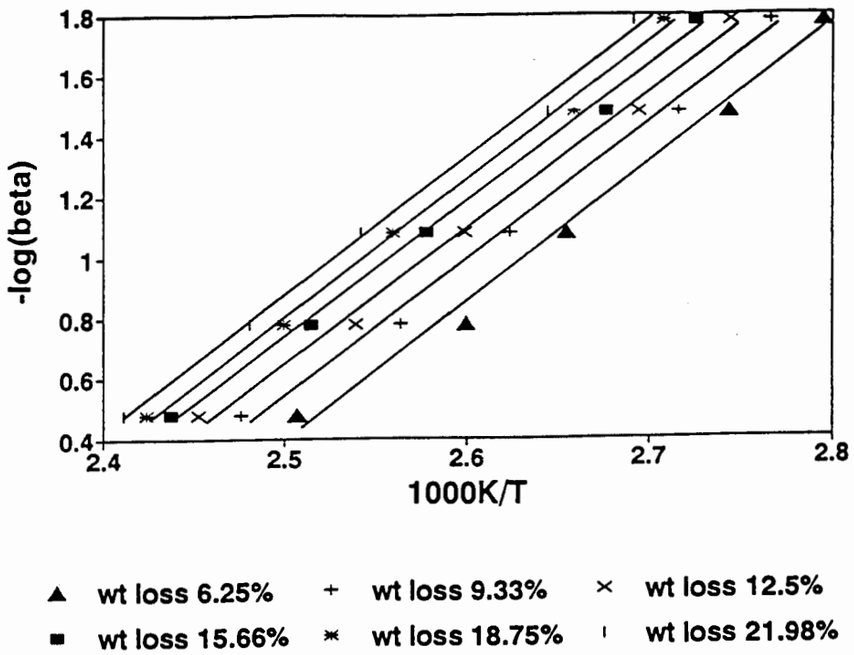

Figure 9: -log β versus 1/T curves for the desorption of **24LUT**

The results obtained from the non-isothermal determination are particularly satisfactory, since they show a high level of consistency. The activation energy values obtained from this experiment fall in a very small range. This is an indication that the desolvation reaction of *2,4*-lutidine from the complex **24LUT** is a single-step reaction[4].

6.1.3.3 Desolvation: Isothermal Kinetics

A series of mass loss versus time curves were obtained for the isothermal desolvation of **24LUT** over a temperature range of 65 to 83°C. These were converted into fractional reaction (α) versus time curves, and were fitted to various kinetic models[5]. The model which most closely approached linearity was deceleratory, namely that for the contracting volume mechanism of a sphere (R3): $kt = 1-(1-\alpha)^{1/3}$. The plot of ln *k* versus 1/T is shown in Figure 10,

and its slope yielded an activation energy of -95(6)kJ mol^{-1} over the α range 0.05 to 0.95.

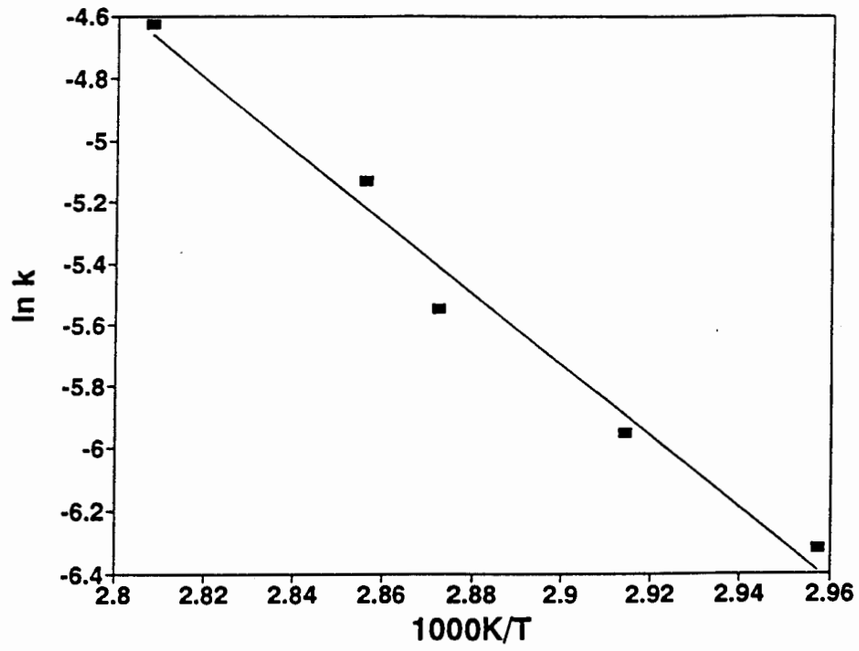

Figure 10: Arrhenius plot for the desolvation of **24LUT**

The microcrystalline samples of **24LUT** used for the thermal analyses were obtained by stirring solutions of the host in *2,4*-lutidine until crystals appeared. XRD experiments were performed on these samples to ensure that the samples had the same structure as the single crystals of **24LUT** grown from solution. Figure 11 contains the XRD trace of a microcrystalline sample and the calculated trace of the **24LUT**. The XRD trace of **24LUT** was calculated with the program LAZY PULVERIX, which uses the atomic co-ordinates and cell dimensions of the structure as input parameters. The two traces match very closely in relative intensities and peak positions, and thus the samples have the same structure.

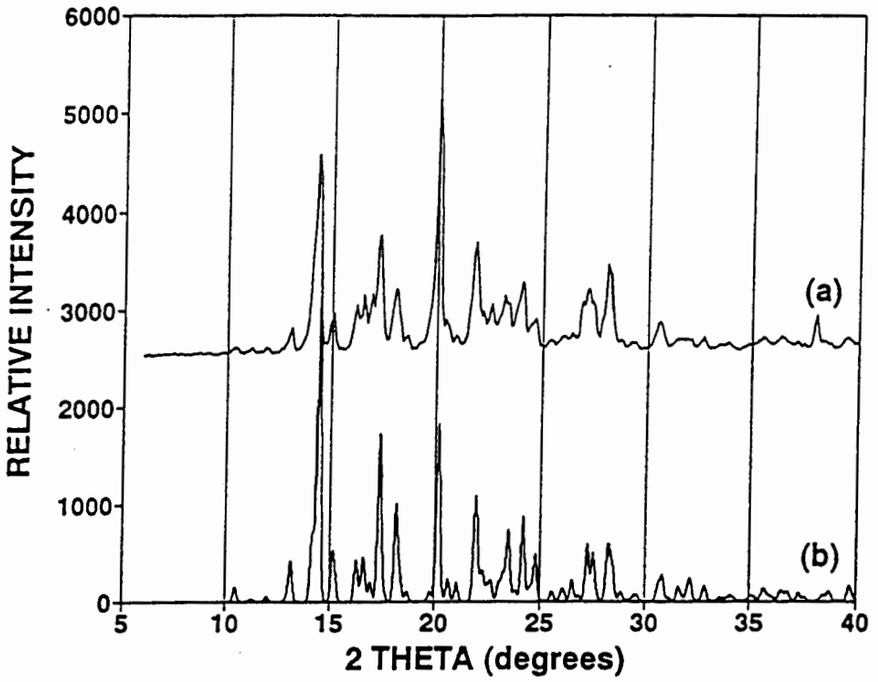

Figure 11: (a) experimental XRD trace for a sample of **H** stirred in a *2,4*-lutidine solution, and (b) the calculated XRD trace for **24LUT** grown from solution.

Exposing the host compound to vapours of *2,4*-lutidine did not result in the formation of the **24LUT** complex obtained from solution. The XRD traces of the products resulting from these two experiments are different, as shown in Figure 12(a) and 12(c). In fact, the XRD trace in 12(a) is the same as that of the uncomplexed host compound (Figure 12(b)). TG experiments confirmed that an inclusion compound had not formed by gaseous guest absorption.

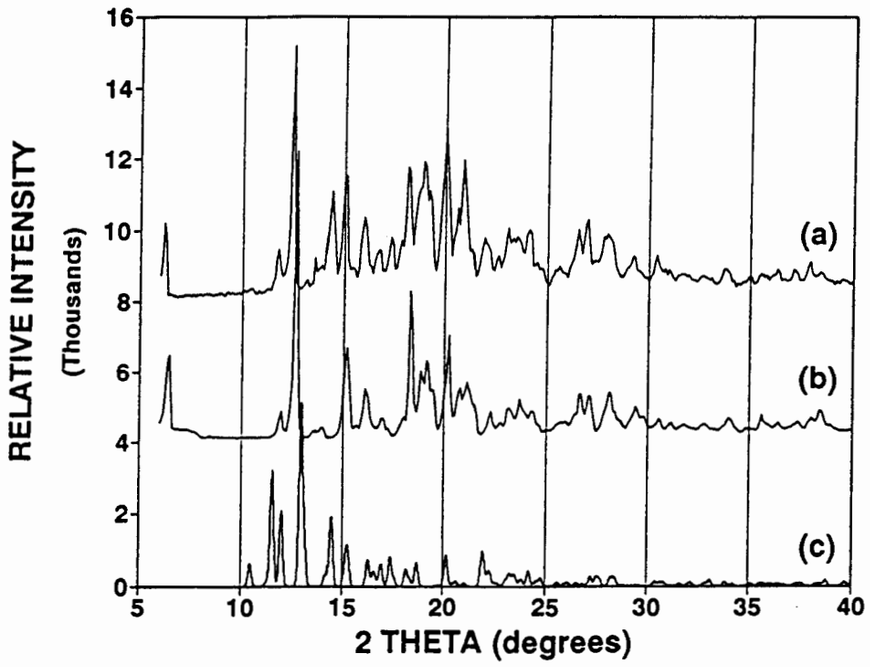

Figure 12: (a) Experimental XRD trace of the host exposed to *2,4*-lutidine vapours, (b) experimental XRD trace of the unsolvated host compound, and (c) calculated XRD trace of **24LUT**, obtained by recrystallisation of **H** from a *2,4*-lutidine solution.

6.2 35LUT

6.2.1 Structure Solution

35LUT crystallised in the monoclinic space group $P2_1$. The following reflection limiting conditions were observed :

hkl : none

h0l : none

0k0 : *k*=2n

The atomic numbering scheme used for *3,5*-lutidine during structure solution is illustrated in Figure 13.

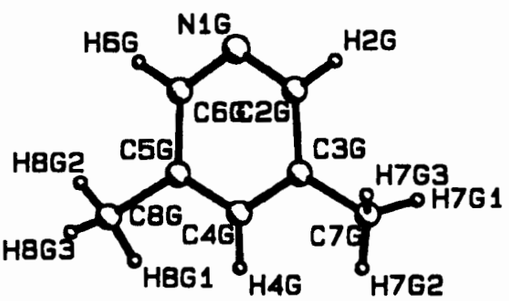

Figure 13: Numbering of *3,5*-lutidine

The unit cell contains two host molecules and two guest molecules, both located at general positions. The positions of the non-hydrogen atoms of both host and guest molecules were obtained from direct methods. In this case, assignment of the guest nitrogen atom was unambiguous. Refinement was carried out with the non-hydrogen atoms of both the host and guest treated anisotropically. The hydrogen atoms of the host and guest molecules were all independently located in difference electron density maps, but the aromatic, methylenic and methyl hydrogens were geometrically constrained [*d*(C-H) = 1.00Å] in the model and assigned common isotropic temperature factors. The hydroxyl hydrogens were independently located in difference electron density maps, and were refined with simple bond length constraints relating O-H

distances versus O-O distances[1]. The structure refined successfully to R_1 = 0.0365.

6.2.2 Structure Analysis

The packing of the structure, viewed along [010] and [100], is shown in Figures 14 and 15. Adjacent host molecules are hydrogen bonded, and form infinite ribbons which run parallel to [100]. Van der Waals interactions occur between adjacent ribbons, and the two ribbons are interlinked by the packing arrangement of their cyclohexyl moieties. Pairs of ribbons are displaced from each other to form constricted channels in which the guest molecules are located. The shapes of the channels in the host structure are depicted in Figure 16. They have circular cross-sections of ~7Å across their widest parts, and ~3Å across their narrowest parts. The packing factor for this structure was calculated to be 18.94 $Å^3$ / non-hydrogen atom.

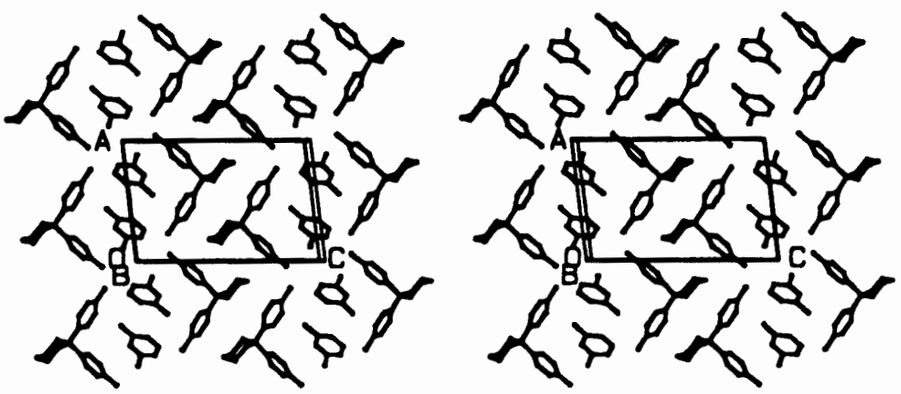

Figure 14: Packing diagram of **35LUT** viewed down [010]

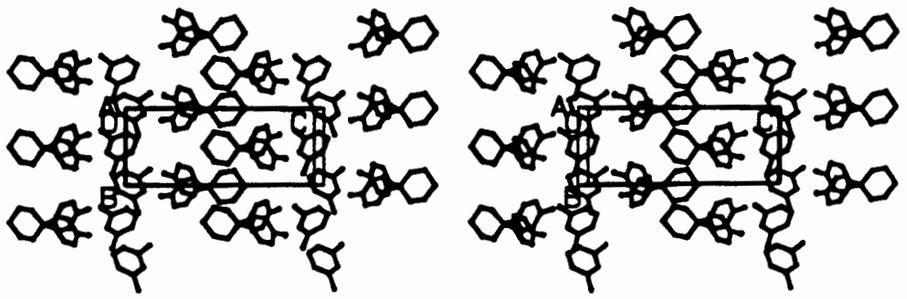

Figure 15: Packing diagram of **35LUT** viewed down [100]

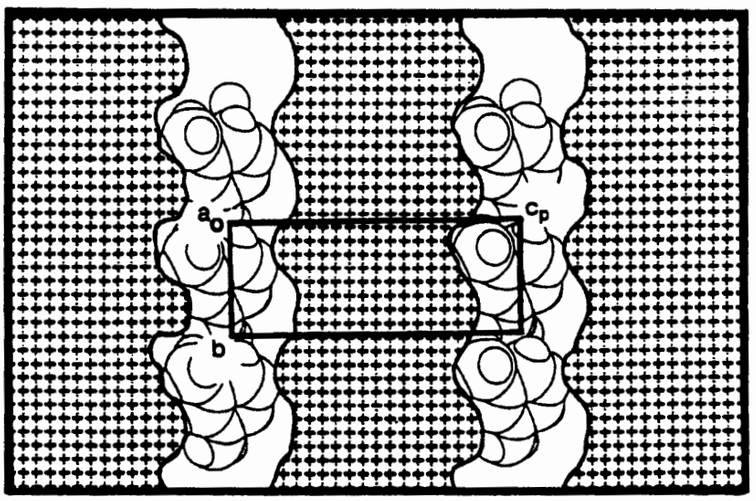

Figure 16: MOLMAP plot of **35LUT**. The host structure is represented by the hatched area, and the guests are represented with van derWaals radii. The cell is viewed down [100], and sectioned at x = 0.0

The hydrogen bonding scheme in **35LUT** is represented graphically in Figure 17, and details are listed in Table 3. Adjacent host molecules interact through their hydroxyl groups. O20 utilises its dual capacity for hydrogen bonding, and acts as both a proton donor and a proton acceptor. Each guest lutidine molecule is hydrogen bonded to the host structure once.

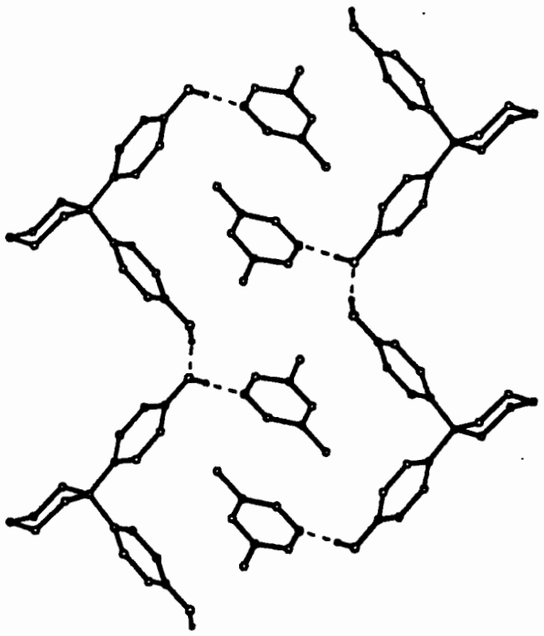

Figure 17: Hydrogen bonding scheme in **35LUT**, viewed down [010]

Table 3: Details of hydrogen bonding data for **35LUT**.

Donor	Acceptor	D-H /Å*	D--A /Å*	D-H--A /°*
O20	N1G	0.94(4)	2.654(4)	170(4)
O13	O20[a]	0.95(4)	2.763(4)	167(3)

Symmetry code: *(a) x+1, y, z*

* **D** = Donor ; **A** = Acceptor

6.2.3 Thermal Analysis

The TG trace of **35LUT** indicates a guest release step corresponding to a mass loss of 28.8% (calc. mass loss for 1:1 complex = 28.5%). A sharp endotherm is observed in the DSC trace at T_{on} = 148.2°C which is due to guest desorption. A separate endotherm for the host melt is not observed, and it is assumed that the host dissolves the hot guest on its desorption.

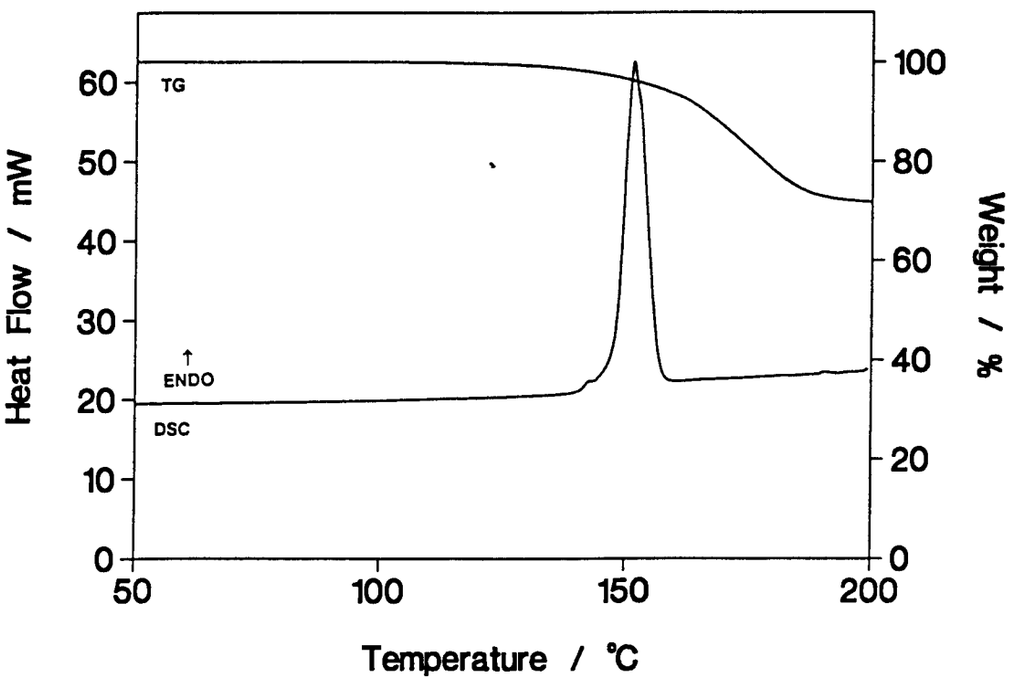

Figure 18: TG and DSC traces for **35LUT**

6.2.3.1 Hot stage microscopy

A crystal of **35LUT** was covered in silicone oil, and heated on a hot stage. The visual interpretation of the degradation of the crystal upon heating is shown in Figure 19.

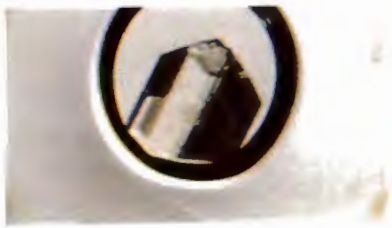

(a) A crystal of **35LUT** , immersed in silicone oil at 20°C.

(b) At 94°C, the appearance of small defects indicate the start of the guest release reaction.

(c) By 128°C, guest release is still in progress, and the crystal starts to become opaque

(d) The crystal is nearly completely opaque by 139°C.

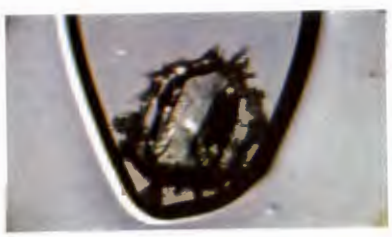

(e) At 140°C, crystallites grow at the edges of the crystal.

(f) By 142°C, the crystal has dissolved in the desorbed *3,5*-lutidine.

Figure 19: Microscope photographs of the thermal events occurring in a crystal of **35LUT** on heating (30X enlarged)

6.2.3.2 Desolvation: Non-isothermal Methods

A series of TG experiments were performed on microcrystalline samples of **35LUT** over the temperature range 50 to 180°C. The desorption experiments were carried out at heating rates of 1, 2, 5, 10 and 20°C min^{-1}, and the mass loss data were reduced to extent of reaction versus 1/T. A series of -log β versus 1/T curves were obtained, and were analysed for various stages of the decomposition ranging from 6.25% to 21.88%. The slopes of these curves yielded values of activation energy, E_a, for the guest release reaction in the range 107(2) to 112(2) kJ mol^{-1}.

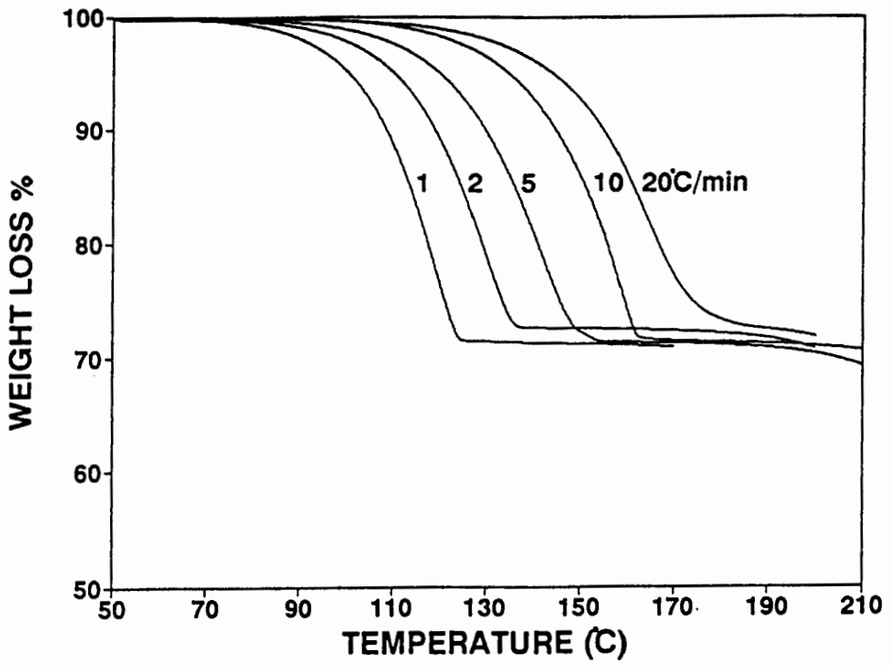

Figure 20: Desorption curves for **35LUT** at heating rates of 1, 2, 5, 10 and 20°C min^{-1}

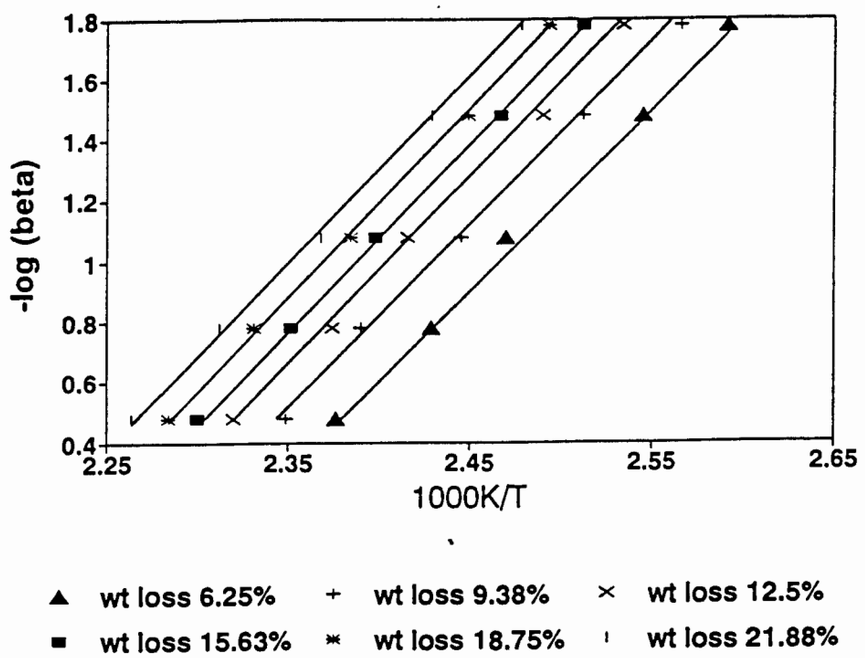

Figure 21: -log β versus 1/T curves for **35LUT**

The results obtained from the non-isothermal determination are highly satisfactory, since they show a high level of consistency. The activation energy values obtained from this experiment fall in a very small range, which indicates that the desolvation reaction of *3,5*-lutidine from the complex **35LUT** is a single-step reaction[4].

6.2.3.3 Desolvation: Isothermal Kinetics

A series of isothermal TG runs were performed on microcrystalline samples of **35LUT** over the temperature range 77 to 95°C. The mass loss versus time data were reduced to extent of reaction, α, versus time curves, and various kinetic models were tested on the data. The deceleratory contracting area kinetic model (R2), where $kt = 1-(1-\alpha)^{\frac{1}{2}}$, was best suited to the data. A graph of *ln k* vs. 1/T yielded an activation energy of 106(4) kJ mol^{-1} over an α range of 0.05 to 0.95.

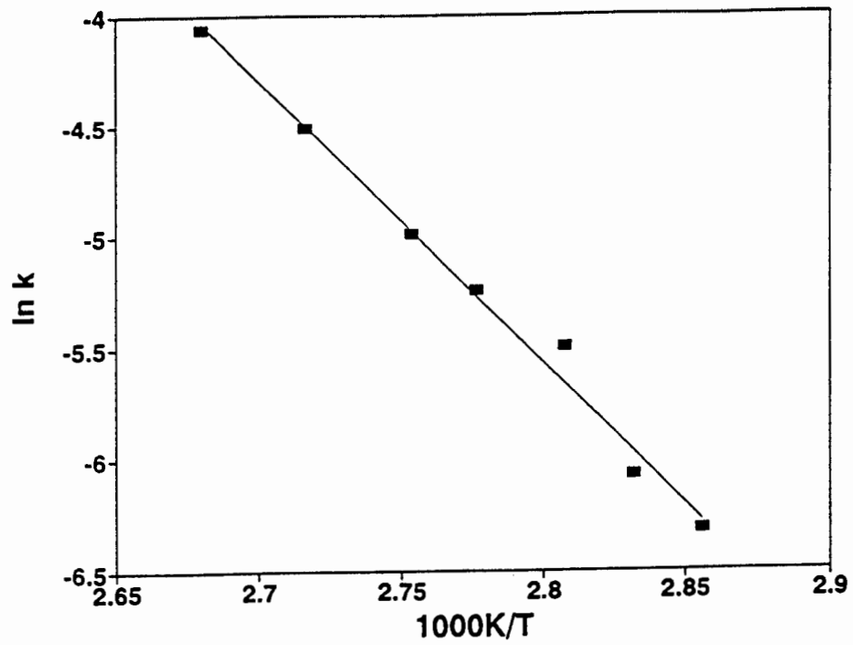

Figure 22: Plot of ln k versus 1/T for **35LUT**

The microcrystalline samples of used in the desolvation experiments, were obtained by stirring the host compound in *3,5*-lutidine, and were examined by XRD. Figure 23 compares the XRD pattern for these samples with that of **35LUT** calculated from the X-ray structure data using the program LAZY PULVERIX. The two traces are identical, and therefore the sample used to obtain kinetic parameters has the same structure as **35LUT**.

The host compound does not include vapours of *3,5*-lutidine to form a complex. The XRD trace of the sample of host exposed to *3,5*-lutidine, Figure 24(a), is very similar to that of the uncomplexed host compound, Figure 24(b). It is not the same as the trace of **35LUT** crystals, Figure 24(c), obtained by slow evaporation methods.

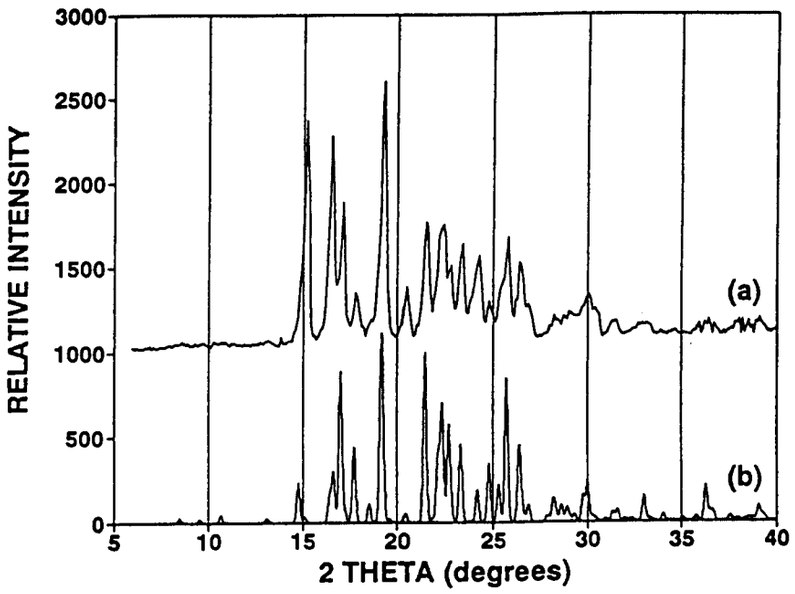

Figure 23: (a) experimental XRD pattern of the microcrystalline samples obtained by stirring **H** in a solution of *3,5*-lutidine, and (b) the calculated XRD trace for **35LUT**

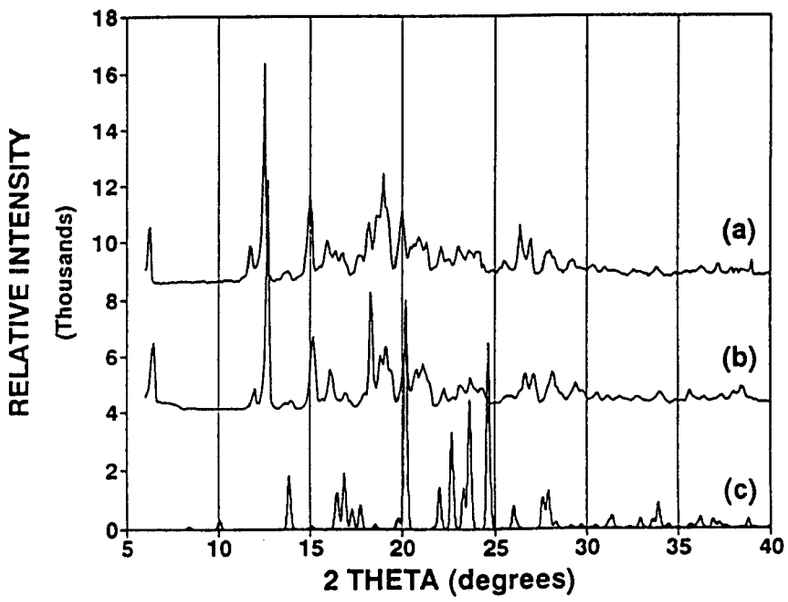

Figure 24: (a) Experimental XRD trace of **H** exposed to *3,5*-lutidine vapours, (b) experimental XRD trace of uncomplexed host compound, and (c) calculated XRD trace of **35LUT** (calculated using the program LAZY PULVERIX)

6.3 POTENTIAL ENERGY CALCULATIONS

The lattice energies of the complexes **24LUT** and **35LUT** were calculated using the program HEENY, and following the procedure described in Chapter 2. The results are presented in Table 4.

Table 4: Results of the lattice potential energy calculations

	24LUT E /kJ mol^{-1}	**35LUT** E /kJ mol^{-1}
H···H	-135.2	-175.4
H···G(non-hydrogen bonding)	-83.1	-86.5
G···G	-52.1	-43.9
TOTAL:	-270.4	-305.8

6.4 COMPETITION EXPERIMENTS

2- and 3-component competition experiments were performed to determine the selectivity of the host compound, **H**, for complexation with the isomers of lutidine. These experiments were performed by dissolving the host in mixtures of the lutidines, and allowing crystals of the inclusion complexes to be formed by slow evaporation. This method was described in detail in Chapter 2.

The results of the competition experiments are represented graphically in Figure 25, and details are presented in Appendix 1.

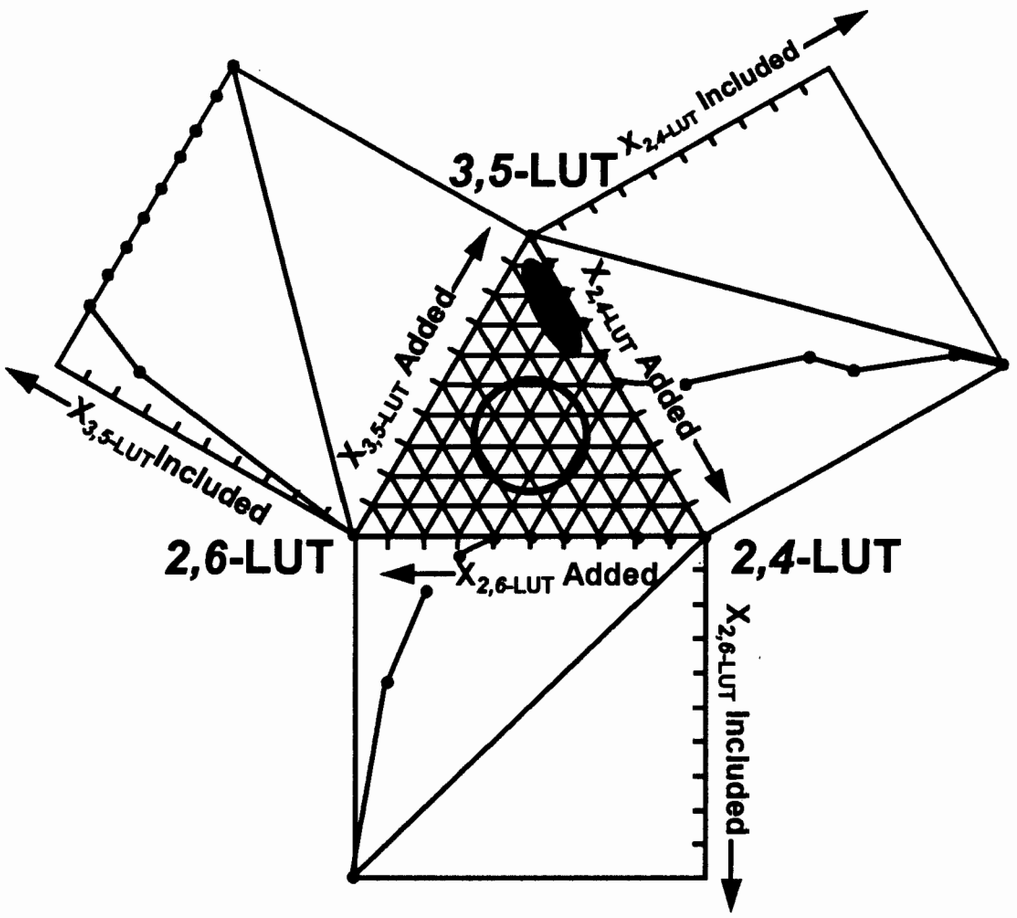

Figure 25: Competition experiment results for the lutidine system

6.4.1 2-Component

In the *3,5*-lutidine/*2,6*-lutidine competition experiment, *3,5*-lutidine was found to be the favoured isomer. This isomer was solely complexed by the host compound in all those mixtures where it was present in concentrations of more than 10%.

The results obtained from the competition between *3,5*-lutidine and *2,4*-lutidine were also convincing. Preferential complexation of the host and *3,5*-lutidine was observed throughout the series of experiments, although *3,5*-lutidine was the *only* isomer complexed in those solutions where it was initially present in concentrations greater than 40%.

In the competition between *2,4*-lutidine and *2,6*-lutidine, *2,4*-lutidine was preferred from concentrations as low as 10%. *2,6*-Lutidine was not complexed at all by **H** in solutions containing more than 30% *2,4*-lutidine.

Thus the selectivity displayed by the host, **H**, for complexation with the isomers of lutidine follows the trend: *3,5*-lut > *2,4*-lut > *2,6*-lut.

6.4.2 3-Component

Similar results were obtained in the 3-component competitions. The circle representing the ratios of the isomers in the starting solutions migrated towards the apex of the triangle representing *3,5*-lutidine. Therefore *3,5*-lutidine is the favoured isomer. A horizontal shift, away from the *2,6*-lutidine vertex, of the circle indicated that *2,6*-lutidine was the least favoured isomer for complexation with **H**.

6.5 DISCUSSION

The structures of **24LUT** and **35LUT** were solved and their crystal structures were analysed. The two structures displayed similar intermolecular interactions. In each case, one hydrogen bond formed between each guest molecule and the host framework. In both structures, the host molecules pack to form constricted channels with diameters of ~7Å at their widest portions, and ~3Å at their narrowest.

The activation energies of the desolvation reactions of both **24LUT** and **35LUT** were obtained by non-isothermal and isothermal methods. There was highly satisfactory agreement between the values obtained using the different methods. For **35LUT**, ~20kJ mol^{-1} more energy was required to bring about desorption of the guest molecules. The relatively higher stability of the **35LUT** complex was also indicated by the calculated lattice energy values. The lattice energy of **35LUT** was found to be ~30kJ mol^{-1} lower than that of **24LUT**.

The difficulty experienced in obtaining crystals of the complex between the host and *2,6*-lutidine is possibly due to the steric hindrance of the methyl substituents. This would hinder the formation of stabilising hydrogen bonds between the hydroxyl groups of the host structure and the nitrogen atoms of the guest molecules. Therefore complexation between **H** and *2,6*-lutidine by means of hydrogen bonding is possibly highly disfavoured. Figure 26 is a schematic diagram of an idealised *2,6*-lutidine molecule, and illustrates the crowding around the nitrogen atom due to the *ortho*-positioned methyl groups.

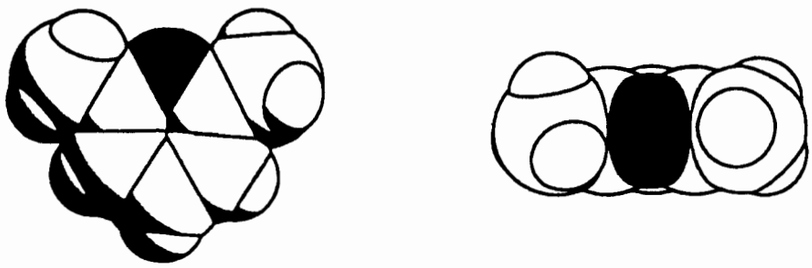

(a) (b)

Figure 26: An idealised *2,6*-lutidine molecule represented with van der Waals radii, and viewed (a) perpedicular to the plane of the aromatic ring, and (b) down the N1-C4 axis. The nitrogen atom is completely shaded for clarity.

The competition experiments were convincing, and showed the following selectivity trend: *3,5*-lut > *2,4*-lut > *2,6*-lut. This result corresponds well with the information regarding the relative stability of the complexes formed. The most stable complex, **35LUT**, is formed preferentially, due to an increased structural complementarity between the host and guest components. The complementarity between *2,6*-lutidine and **H** is highly unsatisfactory, and therefore this isomer is not complexed easily,

1 I. Olovsson and P. Jönsson, *The Hydrogen Bond - Structure and Spectroscopy*, P. Schuster, G. Zundel and C. Sarderfy (eds.), North-Holland Publishing Company, USA, 1975.

2 F. H. Allen, O. Kennard, D. G. Watson, L. Brammer, A. G. Orpen and R. Taylor, *J. Chem. Soc., Perkin Trans.* 2, 1987, S1 - S19.

3 G. R. Desiraju and K. V. Radha Kishan, *J. Am. Chem. Soc.*, **111**, 1989, 4838.

4 J. Opfermann and E. Kaisersberger, *Thermochim. Acta*, **203**, 1992, 167.

5 M.E. Brown, D. Dollimore and A. K. Galwey, *Comprehensive Chemical Kinetics*, C. H. Bamford and C. J. Tipper (eds.), Elsevier, Amsterdam, 1980, vol. 22, 220.

7. INCLUSION OF ALCOHOLS

In this chapter, the structures and thermal behaviour of the inclusion complexes **MEOH**, **ETOH**, **PROH** and **BUOH** will be discussed. These complexes were all formed by dissolving the host directly into the relevant solvents, which were then included. Competition experiments indicated which of the alcohols were included preferentially by the host.

The inclusion complexes formed between the host and the alcohols were not stable, and therefore kinetic parameters for the desolvation of the complexes were not studied.

Preliminary photography determined the unit cell parameters and the crystal systems of the complexes. Crystallographic experimental and refinement details for the four structures are contained in Table 1, while lists of final atomic co-ordinates, temperature factors, tables of bond lengths and bond angles are to be found in Appendix 3. Tables of observed and calculated structure factors are presented in Appendix 4.

Table 1: Crystal data, experimental and refinement parameters.

	MEOH	ETOH
Molecular formula	$C_{18}H_{20}O_2 \bullet CH_4O$	$C_{18}H_{20}O_2 \bullet C_2H_6O$
M_r /g.mol^{-1}	300.38	314.41
Space Group	P $\bar{1}$	P $\bar{1}$
a /Å	6.276(2)	6.293(2)
b /Å	10.895(4)	10.859(2)
c /Å	12.887(8)	13.420(3)
α /°	90.34(5)	84.73(2)
β /°	101.52(5)	77.91(2)
γ /°	102.18(3)	78.96(2)
V /Å^3	842.9(7)	878.8(4)
Z	2	2
D_c /g.cm^{-3}	1.18	1.18.
D_m /g.cm^{-3}	1.16(2)	1.16(3)
μ(Mo-K_α) /cm^{-1}	0.80	0.78
F(000)	324	340
Crystal size /mm	0.35 x 0.35 x 0.25	0.45 x 0.4 x 0.4
Range scanned θ /°	1 - 25	1 - 25
Range of indices	*h*: ±7; *k*: ±12; *l*: 0, 15	*h*: ±7; k: ±12; *l*: 0,15
Crystal decay /%	-5.2%	-7.1%
No. reflections collected	3116	3233
No. reflections observed	2970	3088
No. parameters	219	227
R_1	0.0587	0.0482
wR_2	0.1602	0.1328
$\Delta\rho$ excursions /eÅ^{-3}	0.214 ; -0.311	0.333; -0.177

Table 1, ctd.: Crystal data, experimental and refinement parameters.

	PROH	**BUOH**
Molecular formula	$C_{18}H_{20}O_2 \bullet C_3H_8O$	$C_{18}H_{20}O_2 \bullet C_4H_{10}O$
M_r /g.mol^{-1}	328.43	342.46
Space Group	P $\bar{1}$	P $\bar{1}$
a /Å	6.3207(6)	6.285(8)
b /Å	10.881(2)	10.784(2)
c /Å	14.301(3)	14.789(3)
α /°	86.59(1)	98.14(2)
β /°	79.43(1)	92.24(1)
γ /°	79.51(1)	101.07(1)
V /Å^3	950.4(3)	971.5(3)
Z	2	2
D_c /g.cm^{-3}	1.15	1.17
D_m /g cm^{-3}	1.13(2)	1.15(3)
μ (Mo-Kα) /cm^{-1}	0.75	0.76
F(000)	356	372
Crystal size /mm	0.4 x 0.4 x 0.25	0.4 x 0.35 x 0.35
Range scanned, θ /°	1 - 25	1 - 25
Range of indices	*h*: ±7; *k*: ±12; *l*: 0,16	*h*: ±7; *k*: ±12; *l*: 0,7
Crystal decay /%	-6.54%	-9.13%
No. reflections collected	3483	3563
No. reflections observed	3337	3418
No. parameters	224	236
R	0.0816	0.0891
wR_2	0.2283	0.2398
S	1.019	1.219
$\Delta\rho$ excursions /eÅ^{-3}	0.581 ; -0.337	1.025 ; -0.807

7.1 MEOH

7.1.1 Structure Solution

Preliminary X-ray photography indicated that **MEOH** belonged to the triclinic crystal system, the two possible space groups being P1 and P $\bar{1}$. The centrosymmetric space group P $\bar{1}$ was chosen based on the $|E^2-1|$ values for the zonal and general reflections, which were in the range 0.958 to 1.054. This choice of space group was vindicated by the successful refinement of the structure.

TG experiments confirmed the host:guest ratio in this complex to be 1:1. The atomic numbering scheme used for **H** is as before (see Chapter 3, Figure 1), while that used for the methanol guest molecule is shown in Figure 1.

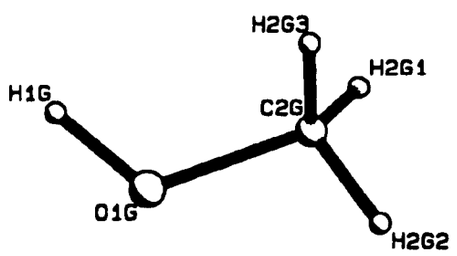

Figure 1: Atomic numbering used for the methanol guest in **MEOH**

The positions of all the host non-hydrogen atoms in the asymmetric unit were obtained from direct methods. One host molecule was placed in a general position in the unit cell, with Z=2. The positions of the methanol carbon and oxygen atoms were located in the difference electron density maps upon subsequent refinement. The oxygen atom of the methanol was placed at the location of the peak with the higher electron density in the map for the guest molecule. The non-hydrogen atoms of both host and guest molecules were treated anisotropically. The host and guest hydrogen atoms were located in the difference maps, but were entered into the model in geometrically constrained positions and refined with common temperature factors for atoms

of the same type. The hydroxyl hydrogens of both host and guest were located in a difference map, and were entered independently and refined with simple bond length constraints according to a function of O-H versus O--O distances[1]. The structure refined successfully to R_1 = 0.0587.

7.1.2 Structure Analysis

Bond lengths and bond angles of the molecules were all in acceptable ranges for structures of this type[2], and will be discussed in more detail in the following chapter. The crystal structure of **MEOH** is similar to that of the structures discussed previously. The crystal packing, viewed down [100] and [010] is shown in Figures 2 and 3. The host molecules pack to form channels parallel to [100] in which the methanol guest molecules are located. These channels are unconstricted, and have approximately circular cross sections of diameter ~4Å. Figure 4 is a MOLMAP plot illustrating the shapes of the channels. The packing factor for **MEOH** was calculated to be 19.15 Å^3 / non-hydrogen atom.

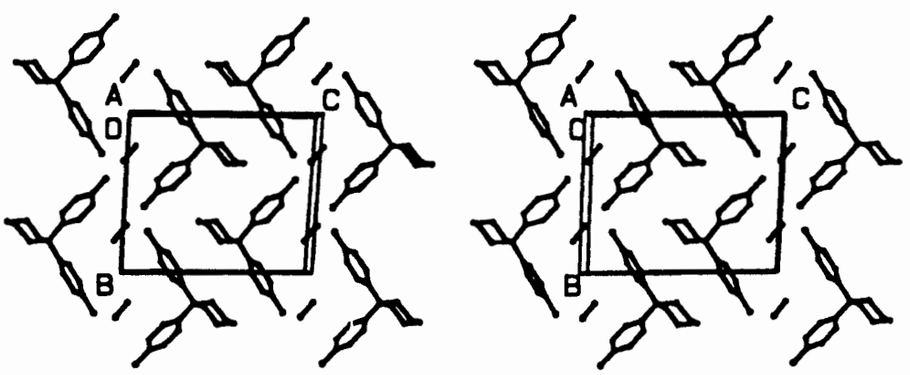

Figure 2: Stereo view of the crystal packing of **MEOH** down [100]

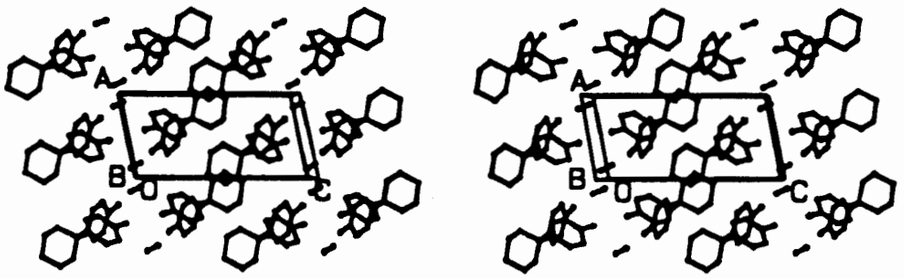

Figure 3: Stereo view down [010] of the crystal packing of **MEOH**

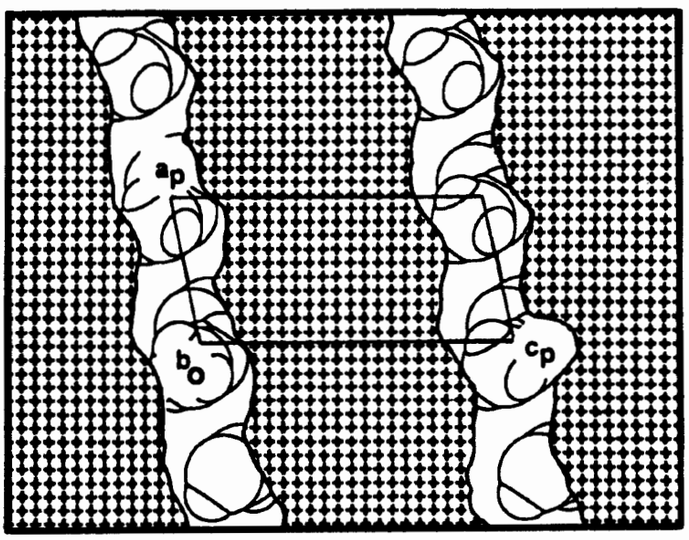

Figure 4: MOLMAP plot of **MEOH** viewed down [010], and sectioned at y = 0. The host structure is represented by the hatched area, and the guest molecules are depicted with van der Waals radii.

The intermolecular interactions which occur in **MEOH** are illustrated in Figures 5(a) and 5(b), while geometric details are listed in Table 2. Adjacent host molecules are linked via their phenolic sites to form hydrogen bonded ribbons parallel to [010]. Each methanol guest molecule hydrogen bonds to two host molecules. The dual capacity of hydroxyl groups for hydrogen bonding is fully utilised, with each hydroxyl oxygen acting both as a proton donor and as a proton acceptor.

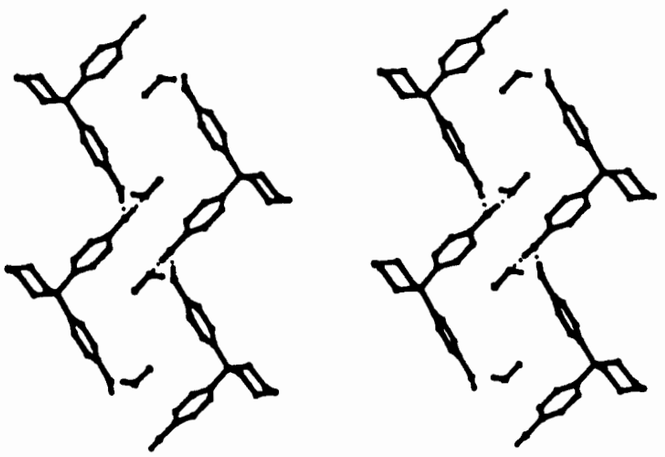

(a) stereo view of **MEOH** down [100]

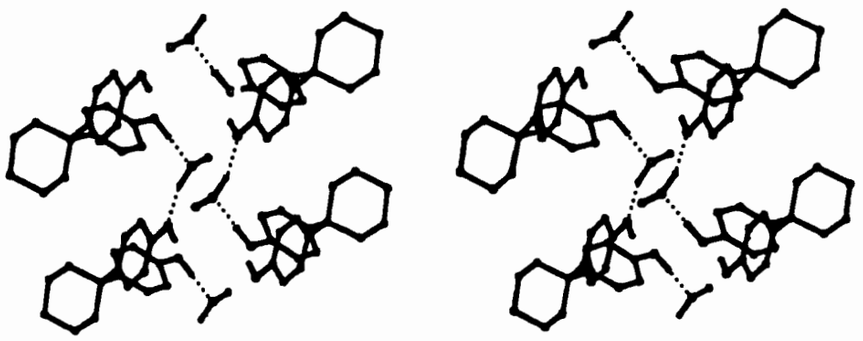

(b) stereo view of **MEOH** down [010]

Figure 5: Hydrogen bonding interactions in **MEOH**. Only the C-O-H atoms of the guest molecule are drawn for clarity.

Table 2: Details of hydrogen bonding in **MEOH**.

Donor	Acceptor	D-H /Å*	D–A /Å*	D-H–A /°*
O1G	O20[a]	0.94(5)	2.664(4)	162(5)
O13	O1G	0.98(7)	2.666(4)	176(6)
O20	O13[b]	1.00(5)	2.672(4)	177(4)

Symmetry code: (a) x+1, y+1, z (b) x, y-1, z

* **D** = Donor ; **A** = Acceptor

7.1.3 Thermal Analysis

7.1.3.1 TG and DSC

TG and DSC experiments were performed on **MEOH**, heating from 30 to 200°C at a rate of 10°C min^{-1}. The results of these experiments are shown in Figure 6. A mass loss of 10.2% for desolvation was observed in the TG trace. The calculated mass loss for a 1:1 complex between **H** and methanol is 10.7%. Three endotherms, labelled A, B and C, were observed in the DSC trace. Endotherm A, at T_{on} = 105.5°C, corresponds to desolvation of the guest. The onset temperatures of endotherms B and C are 183.9°C and 188.4°C respectively. Endotherm B is possibly due to a polymorphic rearrangement of the crystal shortly before it melts at 188.4°C.

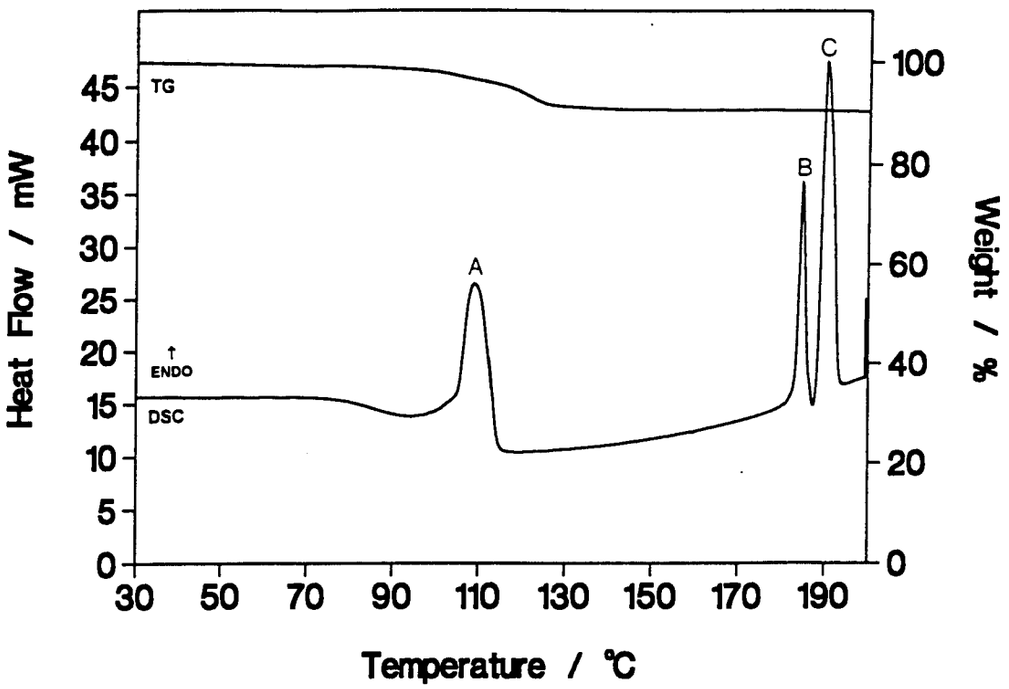

Figure 6: TG and DSC traces for **MEOH**

7.1.3.2 Hot Stage Microscopy

A single crystal of **MEOH** was submerged in a drop of silicone oil, and heated on a hot stage over the temperature range 20 to 200°C. Figure 7 contains photographs of the physical changes to the crystal during heating. The guest desorption reaction begins at 106°C (Figure 7(b)), and is indicated by the appearance of bubbles of the desorbed methanol vapour in the silicone oil. This reaction proceeds until 150°C (Figure 7(e)), at which point no more bubbles appear in the oil, and the crystal is completely opaque. The crystal melted at 192°C.

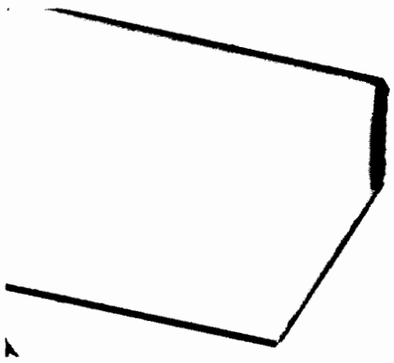

(a) 20°C

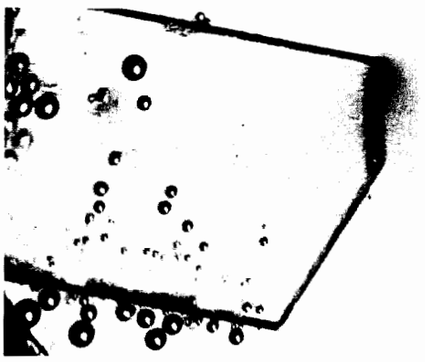

(b) 106°C

(c) 109°C

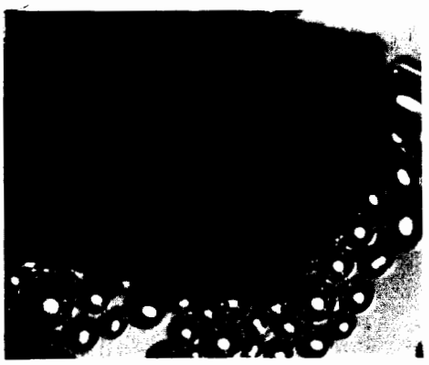

(d) 114°C

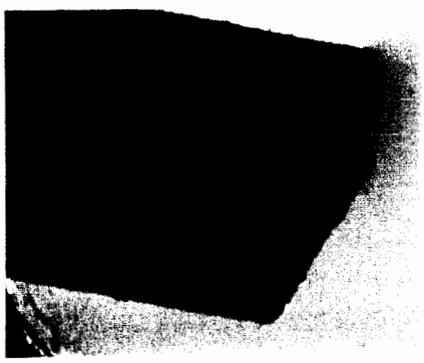

(e) 150°C

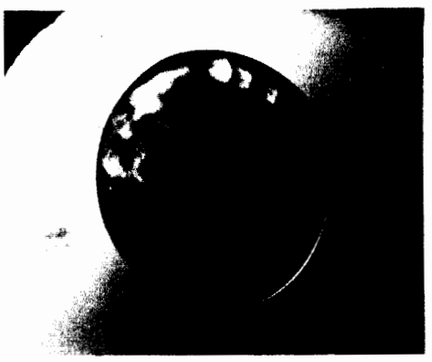

(f) 192°C

Figure 7: Hot stage microscope photographs of **MEOH** (40X enlarged)

The host, **H**, was found to form an inclusion complex with methanol by absorbing it from the vapour phase. A 1:1 complex was indicated by a mass loss of 9.8% (calculated mass loss = 10.7%) obtained from TG analysis. The XRD trace of the complex formed in this manner contained the major peaks observed in the XRD trace of the complex **MEOH** obtained from methanol solutions, and therefore the samples have the same structure. The relative intensities of the peaks did not coincide exactly, and this is attributed to the packing of the sample in the XRD sample holder. The XRD traces are compared in Figure 8.

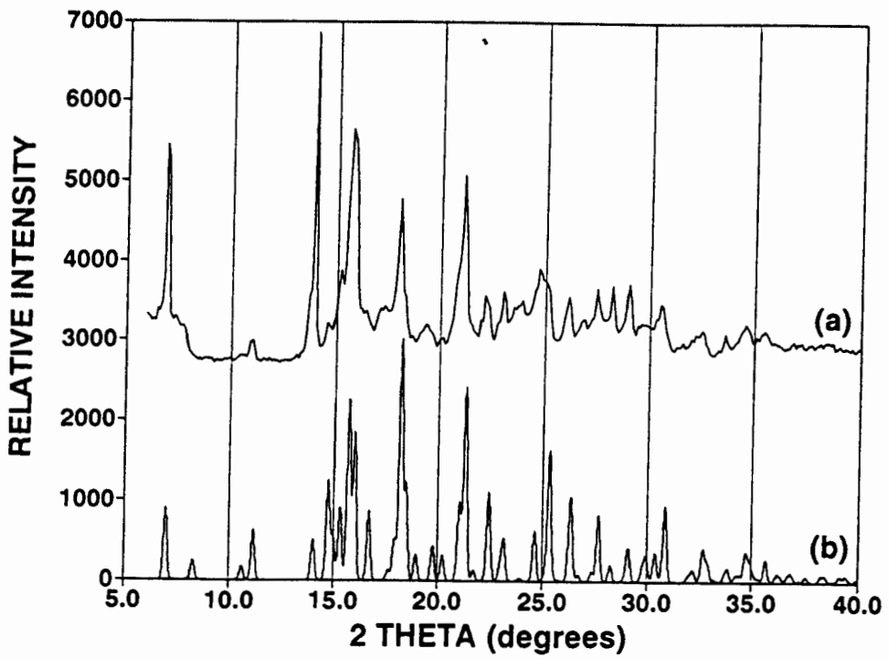

Figure 8: (a) Experimental XRD trace of **H** exposed to methanol vapour, and (b) calculated XRD trace of **MEOH** (calculated using the program LAZY PULVERIX).

7.2 ETOH

7.2.1 Structure Solution

A single crystal of **ETOH** was subjected to X-ray photography to determine its cell dimensions and space group. The space group P $\bar{1}$ was chosen from the two possible triclinic space groups, P1 and P $\bar{1}$, based on the $|E^2-1|$ statistics of zonal and other reflections. The numbering scheme used for ethanol during structure solution of **ETOH** is depicted in Figure 9.

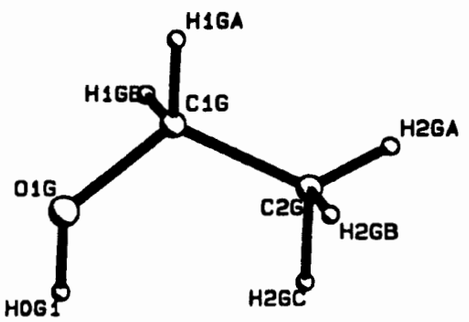

Figure 9: Atomic numbering scheme used for ethanol

TG experiments indicated the host:guest ratio in **ETOH** to be 1:1. Direct methods yielded the positions of all the non-hydrogen host atoms, and these were used for subsequent refinement. The host molecule was placed at a general position in the cell, with Z=2. The positions of the guest non-hydrogen atoms were located in difference electron density maps. The oxygen atom of ethanol was entered at the position of the highest peak in the map representing guest atoms. The non-hydrogen atoms of both the host and guest molecules were treated anisotropically. The hydrogen atoms of **H** and ethanol were located in difference electron density maps, but were geometrically constrained at *d*(C-H) = 1Å in the final model, and similar hydrogen atoms were assigned common isotropic temperature factors. All the hydroxyl hydrogen atoms were located and were entered into the model with independent isotropic

temperature factors. These hydrogen atoms were constrained with simple bond lengths relating O-H distances to O--O distances[1]. The structure refined successfully to R_1 = 0.0482.

7.2.2 Structure Analysis

The crystal packing in **ETOH** is illustrated in Figures 10 and 11, viewed down [100] and [010] respectively. Double ribbons of host molecules pack parallel to [010]. The layers formed in this manner are separated by ribbons of guest molecules. Channels are formed by the packing of the host molecules, and these run parallel to [100]. The channels have circular cross sections with diameters of ~4Å. The channel shapes are depicted in Figure 12. The packing factor for **ETOH** was calculated to be 19.12 Å^3 / non-hydrogen atom.

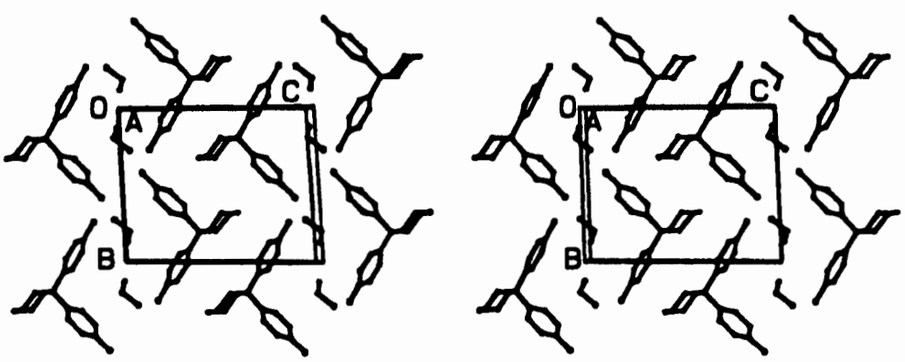

Figure 10: Stereo view of the crystal packing of **ETOH** down [100]

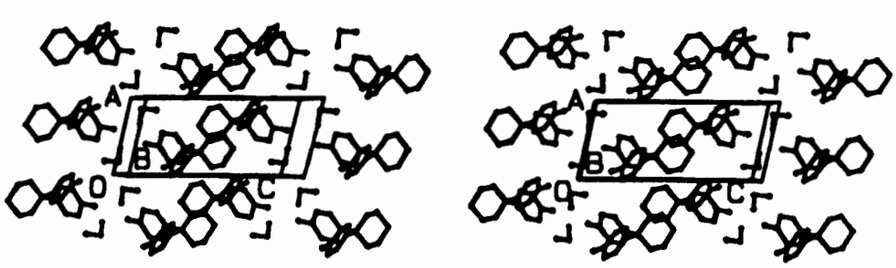

Figure 11: Stereo view of the crystal packing of **ETOH** down [010]

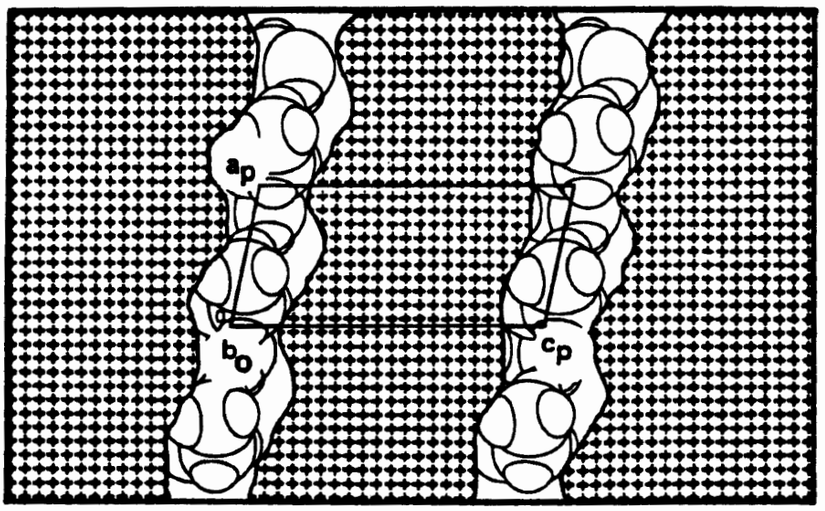

Figure 12: MOLMAP plot of **ETOH** viewed down [010], and sectioned at y = 0

Intermolecular interactions occur between adjacent host molecules via their hydroxyl groups. In addition, each host molecule also hydrogen bonds to a guest ethanol molecule, and in this manner each ethanol guest molecule is hydrogen bonded to the host structure twice. Therefore all hydroxyl oxygen atoms in the structure participate in two hydrogen bonds. The hydrogen bonding scheme in **ETOH** is illustrated in Figure 13, while details of the interactions are given in Table 3.

Table 3: Details of hydrogen bonding in **ETOH**.

Donor	Acceptor	D-H /Å*	D-A /Å*	D-H-A /°*
O13	O1G[a]	0.99(3)	2.583(4)	173(3)
O1G	O20[b]	0.85(3)	2.782(3)	166(3)
O20	O13[c]	0.94(3)	2.706(3)	172(3)

Symmetry code: (a) x-1, y, z (b) x, y+1, z (c) x, y-1, z

* **D** = Donor ; **A** = Acceptor

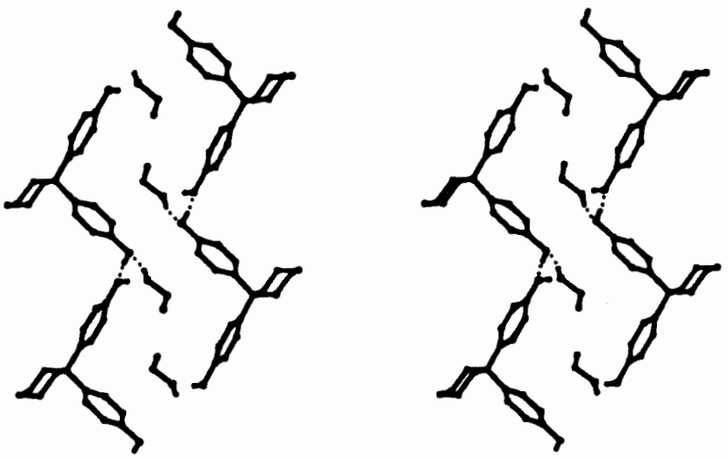

(a) Stereo view of **ETOH** down [100]

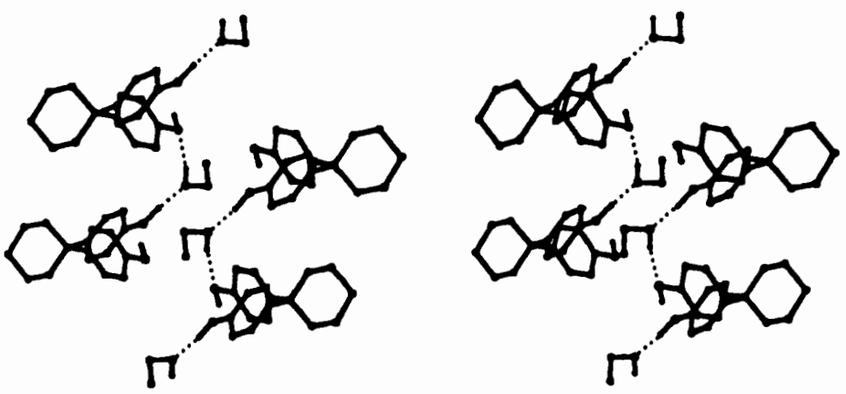

(b) Stereo view of **ETOH** down [010]

Figure 13: Hydrogen bonding interactions in **ETOH**. Only the C-C-O-H atoms of the guest molecule are drawn for clarity.

7.2.3 Thermal Analysis

7.2.3.1 TG and DSC

TG and DSC experiments were performed on **ETOH** over the temperature range 50 to 200°C, and the resulting traces are illustrated in Figure 14. The TG experiment performed on a sample of **ETOH** reveals a mass loss step 14.6%. This is in excellent agreement with the calculated mass loss of 14.6% for a 1:1 complex between the host and ethanol. The DSC trace reflects three endotherms. The onset temperatures for the three endotherms are $T_{on}(A)$ = 97.9°C, $T_{on}(B)$ = 182.8°C and $T_{on}(C)$ = 187.7°C. The diffuse endotherm A corresponds to the desolvation of ethanol, while endotherm B represents a polymorphic rearrangement of the desolvated host compound before its melt (endotherm C).

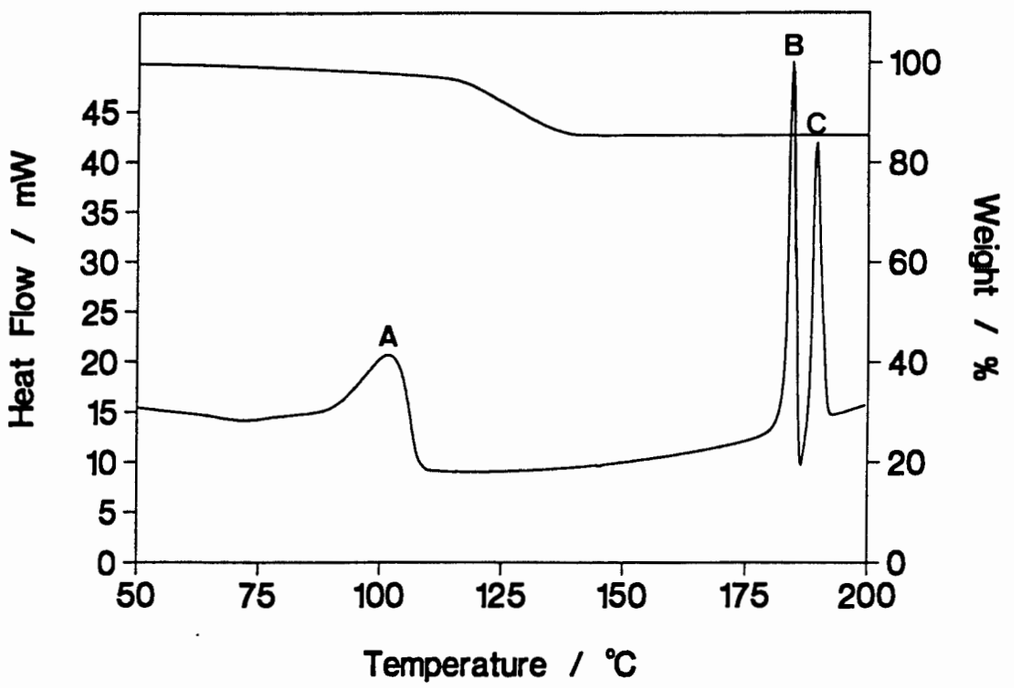

Figure 14: TG and DSC traces of **ETOH**

7.2.3.2 Hot Stage Microscopy

A crystal of **ETOH** was submerged in silicone oil, and heated from 20 to 200°C on a hot stage apparatus. Photographs were taken of all physical changes occurring in the crystal, and these are illustrated in Figure 15. The first signs of the desolvation reaction appeared at 107°C, at which temperature bubbles of vapour were observed in the silicone oil. As guest release proceeded, more bubbles formed in the oil, and the **ETOH** crystal became more opaque. By 150°C, guest desorption was complete, since the crystal was completely opaque, and no more vapour escaped from the crystal. The crystal melted at 190°C.

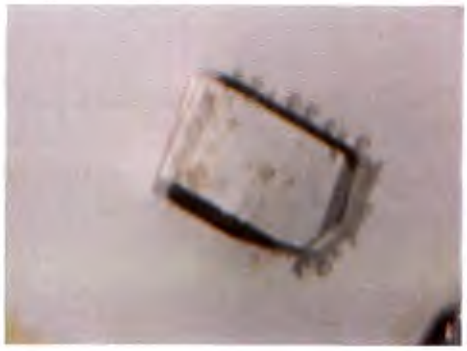

(a) 107°C

(b) 109°C

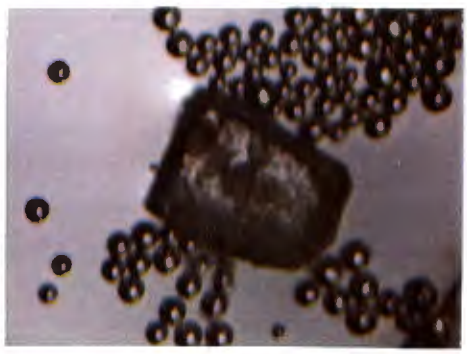

(c) 112°C

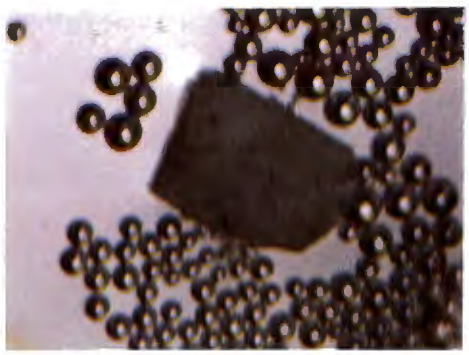

(d) 120°C

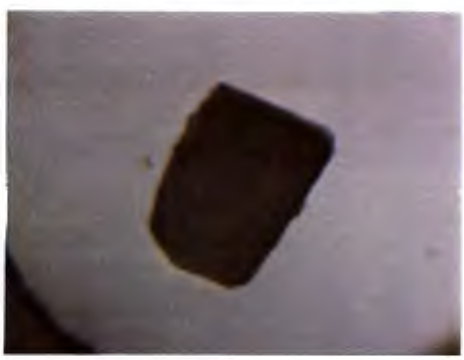

(e) 150°C

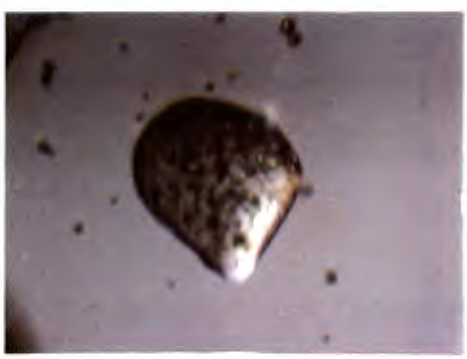

(f) 190°C

Figure 15: Hot stage photographs of **ETOH**, (40X enlarged)

A powdered sample of the host compound was exposed to ethanol vapour, and an inclusion complex was formed. A host:guest ratio of 1:1 was confirmed by a mass loss of 15.2% observed in the TG trace of this complex (calculated mass loss = 14.6%). The XRD trace of the complex was compared to the calculated trace of **ETOH** crystals. The traces are depicted in Figure 16, and show good agreement between peak positions and relative intensities. The complex formed by complexation of ethanol from the vapour phase therefore has the same structure as **ETOH**.

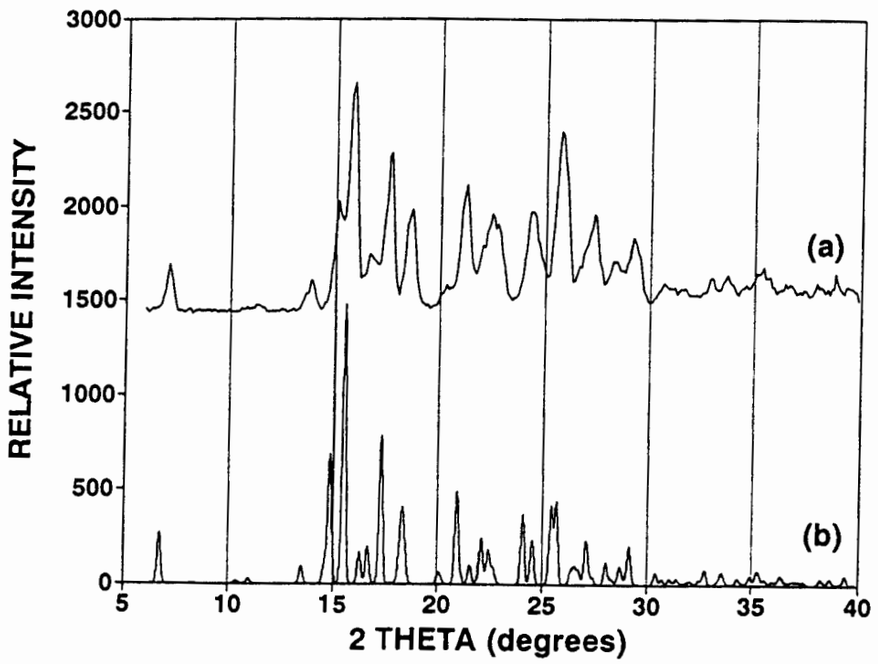

Figure 16: (a) Experimental XRD trace of **H** exposed to ethanol vapour, and (b) calculated XRD trace of **ETOH**

7.3 PROH

7.3.1 Structure Solution

TG analysis confirmed that a 1:1 inclusion complex was formed between **H** and *i*-propanol. Preliminary photography indicated that the inclusion complex **PROH** belonged to the triclinic system. The centrosymmetric space group P $\bar{1}$ was chosen based on the mean $|E^2-1|$ values obtained from direct methods. This choice was confirmed by the successful refinement of the structure. The numbering scheme used for *i*-propanol in **PROH** is shown in Figure 17.

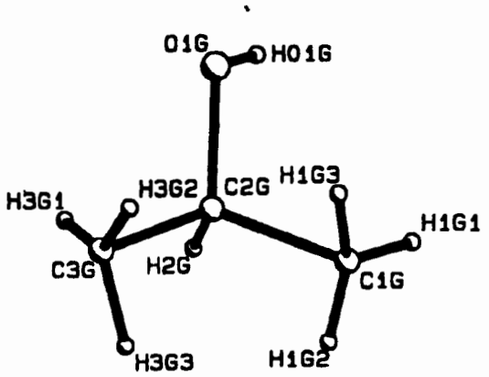

Figure 17: Atomic numbering scheme used for *i*-propanol

Direct methods yielded the positions of the non-hydrogen atoms of both host and guest molecules. These atoms were refined anisotropically. The hydrogen atoms were located in difference electron density maps, but were placed in the final model with geometric constraints and refined with a common isotropic temperature factor for similar groups. The host and guest hydroxyl hydrogens were located in a difference electron density map, and were refined with bond length constraints (relating O-H to O-O distances[1]) and individual temperature factors. The structure refined successfully to R_1 = 0.0816. All bond lengths and angles were in acceptable ranges for structures of this type[2].

7.3.2 Structure Analysis

The crystal packing of **PROH** is viewed down [100] and [010] in Figures 18 and 19 respectively. The familiar double ribbon motif of the host is once again observed, and the ribbons run parallel to [100]. Constricted channels form between these double ribbons, and the guest molecules are located in the channels. The channels have approximately circular cross sections of diameters ~6Å at their widest parts, and ~3.5Å at their narrowest parts. Figure 20 illustrates the channel shapes by representing the host structure as the hatched area, and the guest molecules with van der Waals radii. The packing factor for **PROH** was calculated to be 19.8 $Å^3$ / non-hydrogen atom.

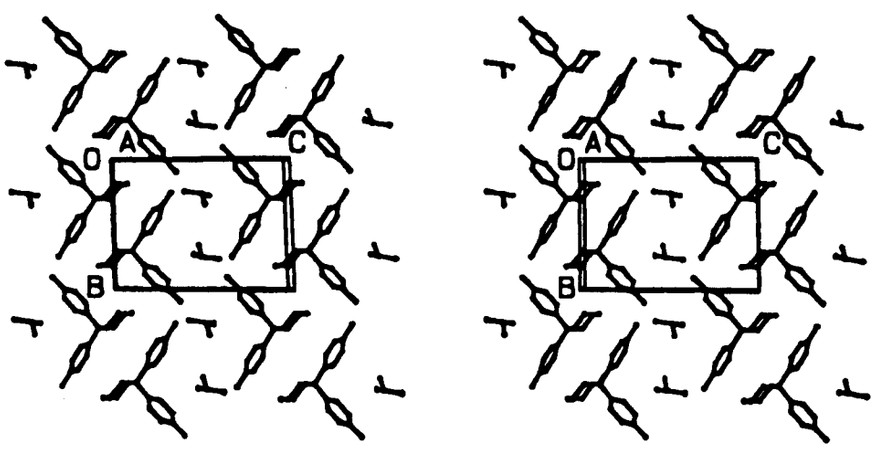

Figure 18: Stereo view of the crystal packing of **PROH** down [100]

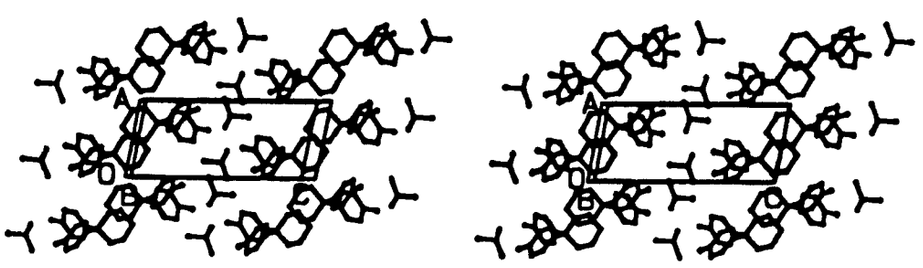

Figure 19: Stereo view of the crystal packing of **PROH** down [010]

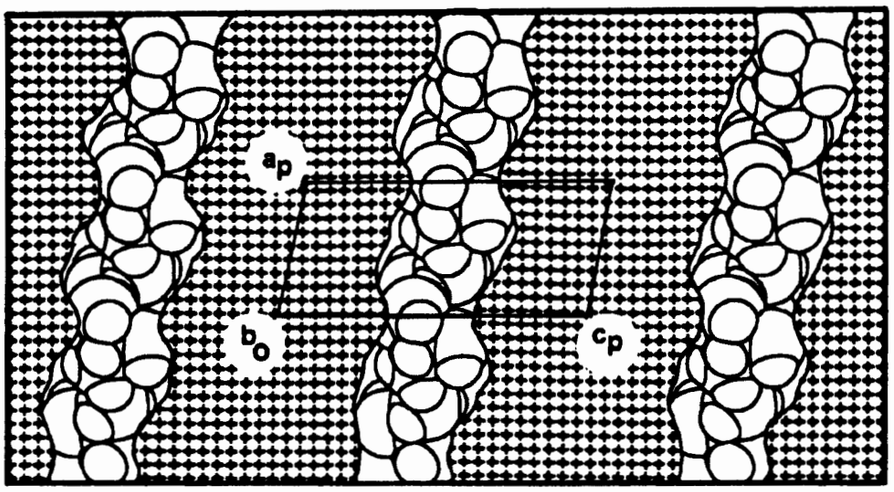

Figure 20: MOLMAP plot of **PROH** viewed down [010], and sectioned at y = 0

Figure 21 is a representation of the hydrogen bonding scheme in **PROH**, and the geometric details of these interactions are listed in Table 4. Each host molecule is involved in a hydrogen bond to the adjacent host molecule, and to a guest *i*-propanol molecule. Therefore each host hydroxyl group is involved in two hydrogen bonds, acting as both a proton acceptor and a proton donor. Each guest *i*-propanol molecule forms hydrogen bonds to two host molecules.

Table 4: Details of hydrogen bonding in **PROH**.

Donor	Acceptor	D-H /Å*	D-A /Å*	D-H-A /°*
O20	O1G[a]	0.96(5)	2.595(5)	156(5)
O1G	O13[b]	0.98(4)	2.735(4)	173(5)
O13	O20[c]	0.94(5)	2.677(4)	172(4)

Symmetry code: (a) -x,-y+1,-z+1 (b) -x+1,-y,-z+1 (c) x, y-1, z

* **D** = Donor ; **A** = Acceptor

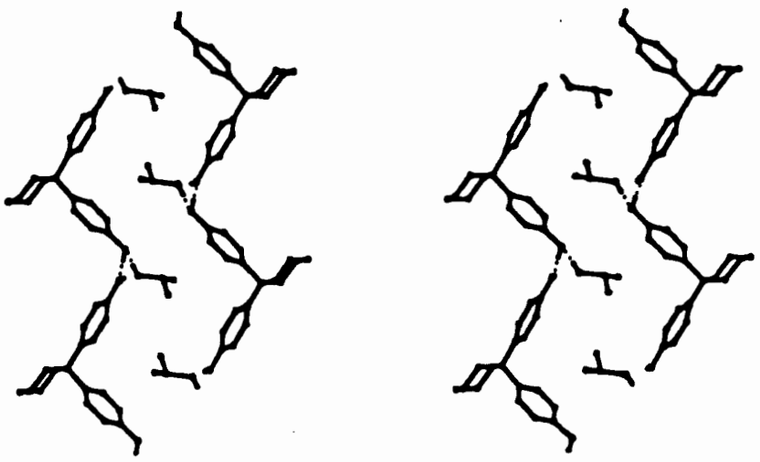

(a) Stereo view of **PROH** down [100]

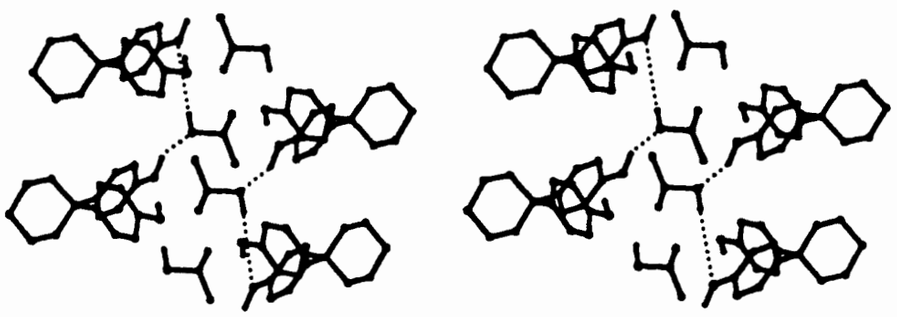

(b) Stereo view of **PROH** down [010]

Figure 21: Intermolecular interactions in **PROH**. Hydrogen atoms have been omitted, except for the hydroxy group hydrogen atoms

7.3.3 Thermal Analysis

7.3.3.1 TG and DSC

TG and DSC experiments were performed on **PROH** over the temperature range 50 to 200°C. The TG trace for **PROH** shows a mass loss step of 18.7% for the desolvation of *i*-propanol, which agrees well with the calculated value of 18.3% for a 1:1 inclusion complex. Three endotherms are observed in the DSC trace, at onset temperatures of 105.2°C, 184.6°C and 189.8°C. Endotherm A corresponds to desorption of the guest, while endotherm B is due to a polymorphic rearrangement of the desolvated host compound before its melt at 189.8°C (endotherm C). The TG and DSC traces for **PROH** are illustrated in Figure 22.

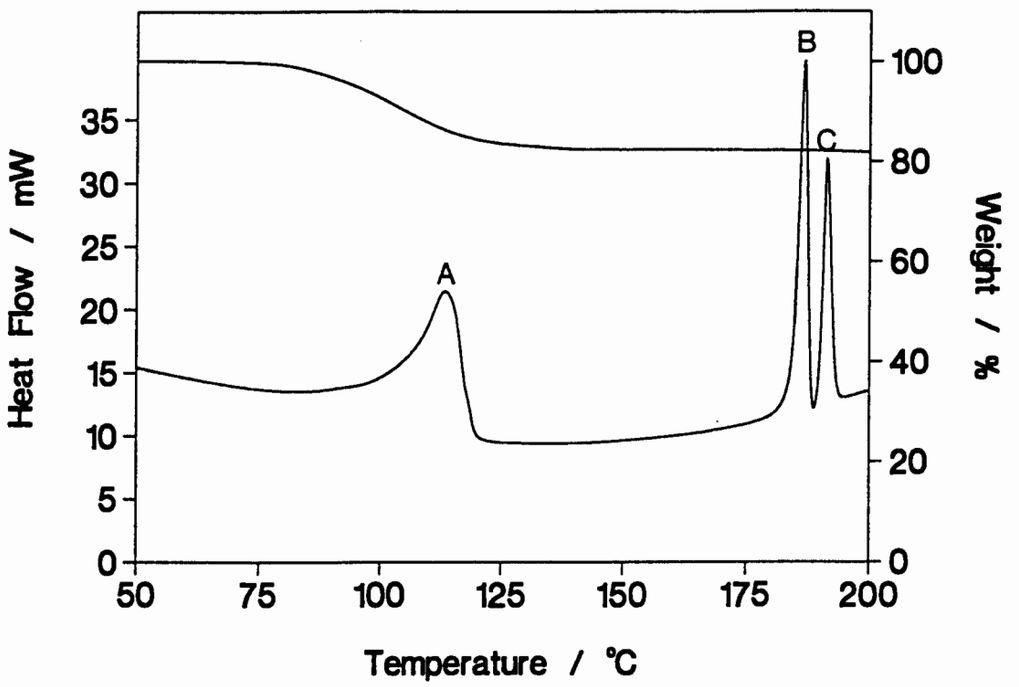

Figure 22: TG and DSC traces of **PROH**

7.3.3.2 Hot Stage Microscopy

A single crystal of **PROH** was covered with a drop of silicone oil, and heated on a hot stage apparatus. Figure 22 is a series of photographs depicting the thermal events occurring in **PROH** on heating from 20 to 200°C.

Small defects appeared in the crystal at 100°C and 116°C, although bubbles of desolvated *i*-propanol only formed in the silicone oil at 120°C. By 146°C, the crystal was completely opaque. The crystal melted at 188°C.

A powdered sample of the host compound was exposed to vapours of *i*-propanol, and an inclusion complex formed. The host:guest ratio in the complex was indicated to be 1:1 by TG analysis (experimental mass loss = 18.3%, calculated mass loss = 18.3%). However, the XRD trace of this complex differs from that of **PROH** crystals obtained from *i*-propanol solutions, and therefore the complexes do not have the same structure[3]. The XRD traces of the complexes formed by the different methods are compared in Figure 23.

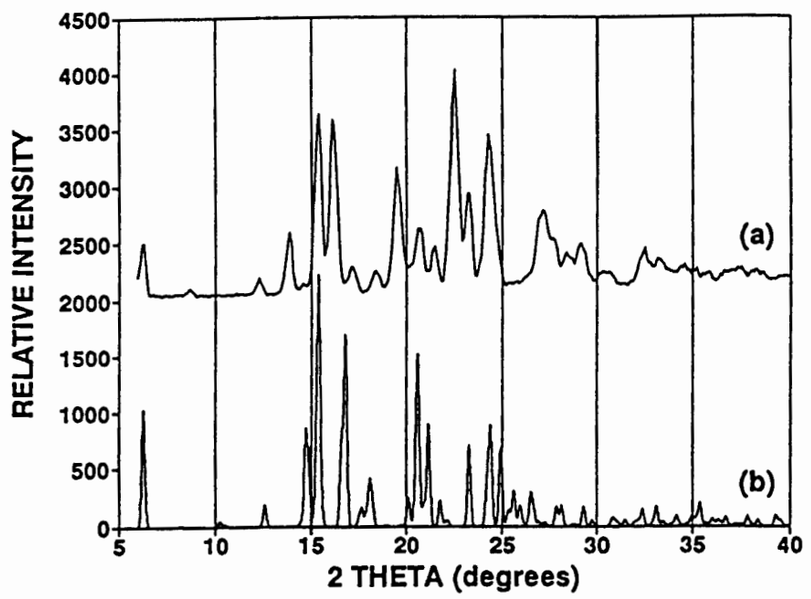

Figure 23: (a) Experimental XRD trace of **H** exposed to *i*-propanol vapour, and (b) the calculated XRD trace of **PROH**

(a) 20°C

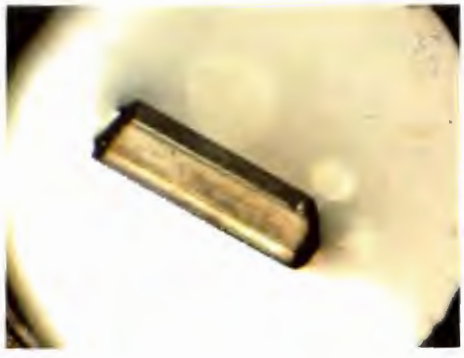

(b) 100°C

(c) 116°C

(d) 120°C

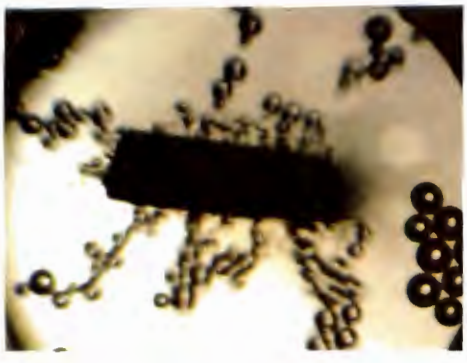

(e) 146°C

(f) 188°C

Figure 22: Hot stage photographs of **PROH** (40X enlarged)

7.4 BUOH

7.4.1 Structure Solution

TG analysis confirmed that the host:guest ratio of the complex formed between **H** and *n*-butanol was 1:1. X-ray photography indicated that **BUOH** belonged to the triclinic crystal system. The centrosymmetric space group P $\bar{1}$ was chosen based on the $|E^2-1|$ values for the zonal and general reflections, which were in the range 0.982 to 1.102. This choice was vindicated by the successful refinement of the structure.

The numbering scheme used for the host molecule is as before (see Chapter 2, Figure 1), while that used for the *n*-butanol guest molecule is shown in Figure 24.

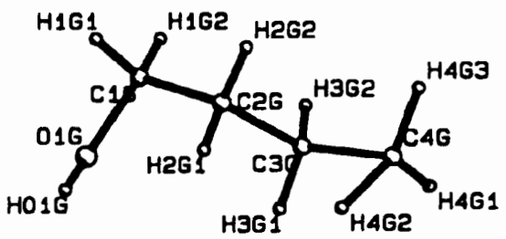

Figure 24: Atomic numbering scheme used for the *n*-butanol guest molecule in **BUOH**

Direct methods yielded the positions of all the host and guest non-hydrogen atoms in the asymmetric unit. Both molecules were placed in general positions in the unit cell (Z=2). The oxygen atom of the *n*-butanol molecule was placed at the location of the peak with the higher electron density in the map for the guest molecule. The non-hydrogen atoms of the host molecule were treated anisotropically. C3G and C4G displayed relatively high thermal motion, and therefore were refined with isotropic temperature factors. O1G, C1G and C2G were treated anisotropically. The host and guest molecules' hydrogen atoms were located in the difference maps, but were entered into the model in

geometrically constrained positions and refined with common temperature factors for atoms of the same type. The hydroxyl hydrogens of both host and guest were located in a difference map, and were entered independently and refined with simple bond length constraints according to a function of O-H versus O–O distances[1]. The structure refined successfully to R_1 = 0.0891.

7.4.2 Structure Analysis

The crystal packing of **BUOH** is viewed down [100] and [010] in Figures 25 and 26 respectively. The host molecules pack to form ribbons which run parallel to [100]. Channels which are slightly constricted form between the host ribbons, and the guest *n*-butanol molecules are located here. The channels run parallel to [100], and have circular cross sections with diameters of ~4Å at their narrowest parts, and ~5.5Å at their widest parts. The shapes of the channels are illustrated by a MOLMAP plot in Figure 27. The guest molecules are represented with van der Waals radii, and the host framework is represented by the hatched area. The packing factor of the **BUOH** structure was calculated to be 19.4 $Å^3$ / non-hydrogen atom.

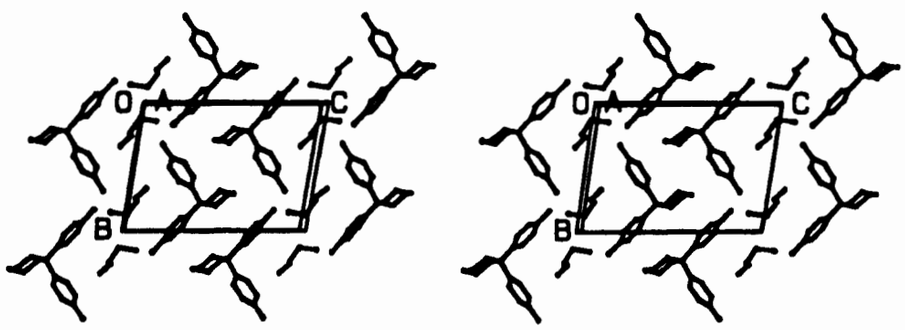

Figure 25: Stereo view of the crystal packing of **BUOH**, down [100]

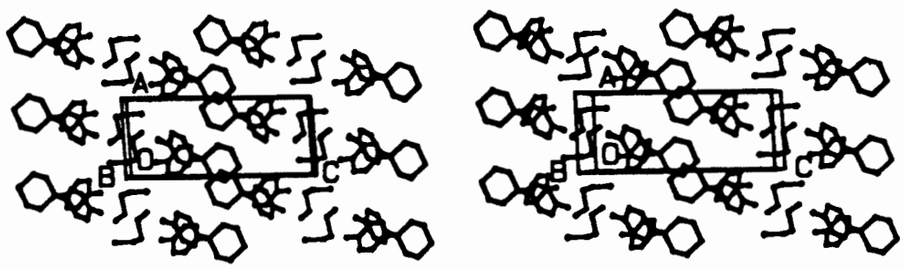

Figure 26: Stereo view of the crystal packing of **BUOH**, down [010]

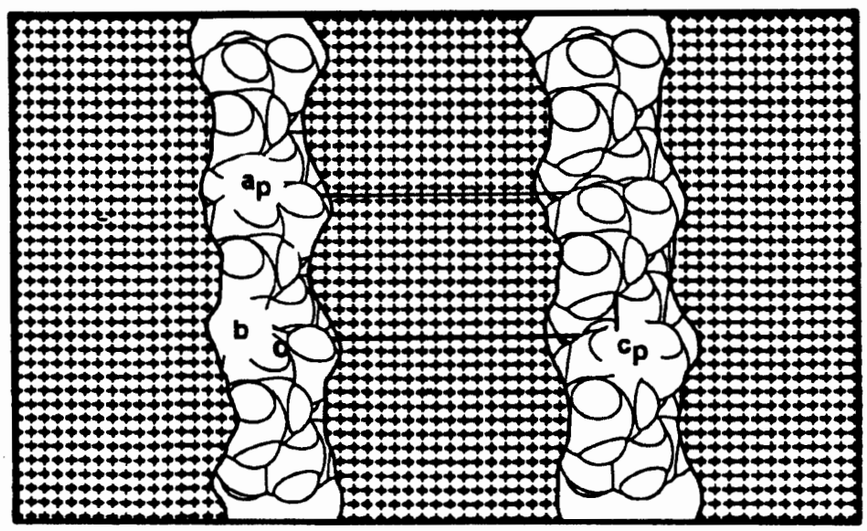

Figure 27: MOLMAP plot of **BUOH** viewed down [010], and sectioned at y = 0

Host molecules which are related to each other by translation along [010] hydrogen bond via their hydroxyl groups. Each host hydroxyl group is also hydrogen bonded to a guest *n*-butanol molecule. Thus every host and guest hydroxyl group acts as both a proton donor and a proton acceptor. Figure 28 illustrates the intermolecular interactions in **BUOH**, while geometric details are listed in Table 5.

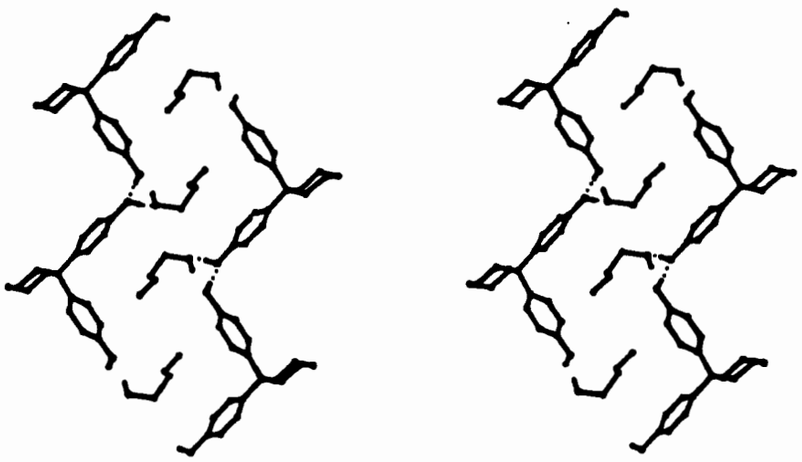

(a) Stereo view of **BUOH** down [100]

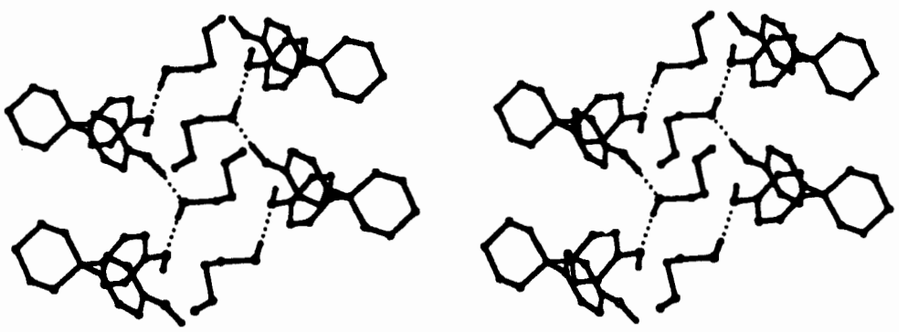

(b) Stereo view of **BUOH** down [010]

Figure 28: Hydrogen bonding in **BUOH**. Hydrogen atoms have been omitted except for the hydroxy group hydrogen atoms.

Table 5: Geometric details of the intermolecular interactions in **BUOH**

Donor	Acceptor	D-H /Å*	D–A /Å*	D-H–A /°*
O13	O1G[a]	1.00(4)	2.626(4)	172(3)
O1G	O20[b]	0.83(3)	2.774(4)	169(4)
O20	O13[c]	0.87(4)	2.708(4)	170(4)

Symmetry code: (a) -x+1, -y+2, -z (b) -x, -y+1, -z (c) x, y-1, z

* **D** = Donor ; **A** = Acceptor

7.4.3 Thermal Analysis

7.4.3.1 TG and DSC

TG and DSC experiments were performed on **BUOH** over the temperature range 50 to 200°C. The resulting traces are illustrated in Figure 29. The TG trace indicates a mass loss step of 21.8%, which is due to guest desorption. The calculated mass loss for a 1:1 inclusion complex is 21.6%. Three endotherms are observed in the DSC trace. These have onset temperatures of $T_{on}(A)$ = 109.2°C, $T_{on}(B)$ = 182.6°C and $T_{on}(C)$ = 187.7°C. Endotherm A represents the desolvation reaction, while endotherm B represents a polymorphic rearrangement of the desolvated host compound shortly before its melt (endotherm C).

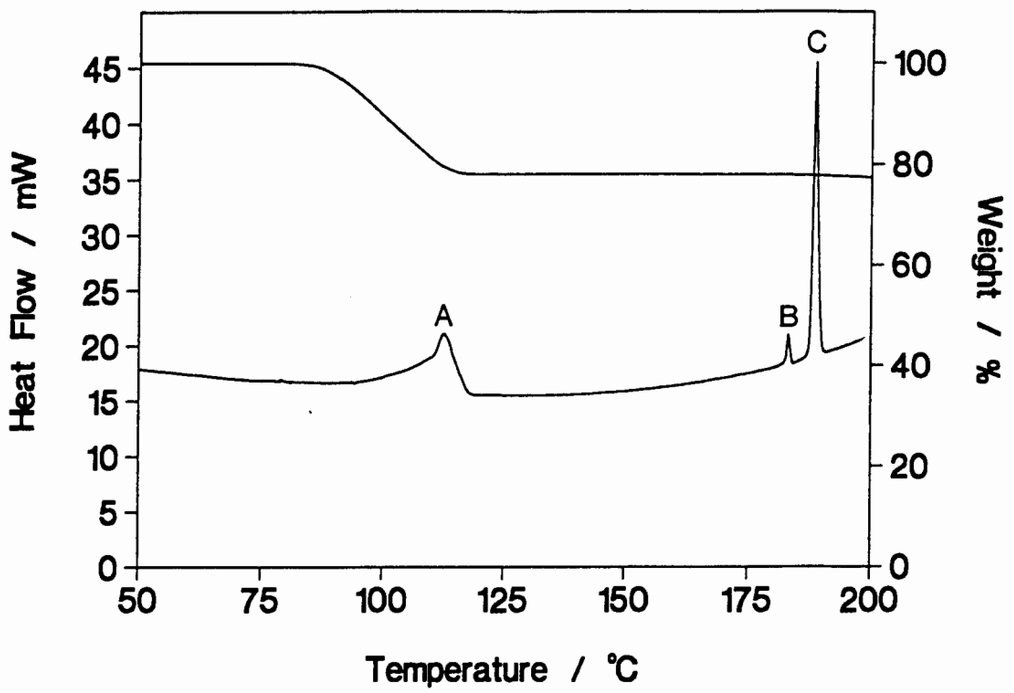

Figure 29: TG and DSC traces of **BUOH**

7.4.3.2 Hot Stage Microscopy

Photographs were taken of the physical changes to a crystal of **BUOH**, while it was subjected to heating on a hot stage apparatus. The crystal was submerged in a drop of silicone oil, and heated over the temperature range 20 to 200°C. The photographs are shown in Figure 30.

At 88°C, a large crack appeared in the crystal, and a few small bubbles of desorbed guest vapour appeared in the silicone oil. By 114°C, many more bubbles appeared in the oil, and the edges of the crystal became opaque. At 121°C, small crystallites formed on the edges of the crystal, and at 130°C, bubbling occurred inside the crystal. The crystal melted at 190°C.

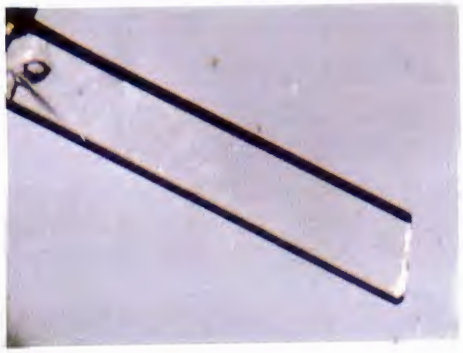

(a) 20°C

(b) 88°C

(c) 99°C

(d) 114°C

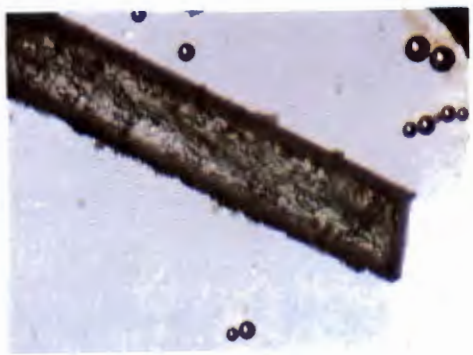

(e) 121°C

(f) 167°C

Figure 30: Hot stage microscope photographs of **BUOH** (40X enlarged)

On exposing the host to vapours of *n*-butanol, an inclusion complex was formed. TG analysis indicated that the host:guest ratio in the complex was not 1:1, since the experimental mass loss due to guest desolvation was 18.3% (calc. mass loss for a 1:1 complex = 21.6%). The XRD trace did not correspond to that of the **BUOH** complex, and therefore the complexes formed by the two different methods do not have the same structure.

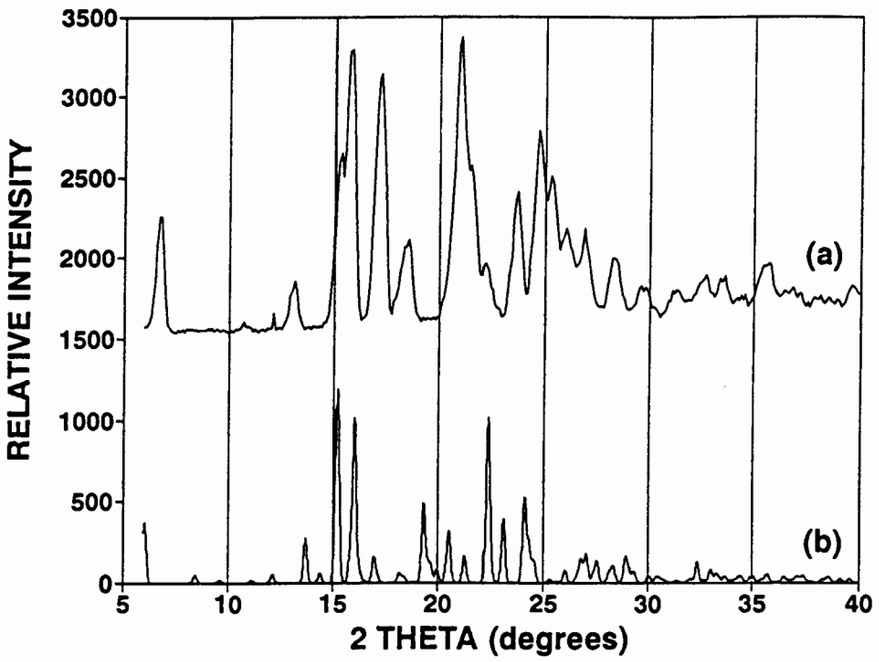

Figure 31: (a) Experimental XRD of the host exposed to n-butanol vapour, and (b) calculated XRD trace of the complex **BUOH**

7.5 POTENTIAL ENERGY CALCULATIONS

The lattice energies of the four structures described in this chapter were calculated using the program HEENY. The results of these calculations are listed in Table 6.

Table 6: Lattice energy calculations.

	MEOH	**ETOH**	**PROH**	**BUOH**
	E / kJ mol^{-1}	E / kJ mol^{-1}	E / kJ mol^{-1}	E / kJ mol^{-1}
H--H	-177.5	-191.1	-183.6	-185.8
H--G	-35.8	-17.8	-71.3	-45.3
G--G	-2.6	-6.3	-13.1	-27.2
TOTAL	-215.9	-215.2	-268.0	-258.3

7.6 COMPETITION EXPERIMENTS

Competition experiments were carried out with the alcohol guests to determine which alcohol is preferentially complexed by the host. These experiments were performed by dissolving the host compound directly into mixtures of the alcohols and allowing crystallisation of the inclusion complexes to occur. Competition experiments were carried out with mixtures of two of the alcohols at a time, and also with all four alcohols simultaneously.

7.6.1 2-Component

In the competition experiments between methanol and ethanol, selectivity of ethanol was observed in those solutions where it was initially present in more than 30% concentration, although the selectivity was not convincing. These results are shown in Figure 32(a).

i-Propanol was found to be preferred above methanol for complexation with the host in those solutions in which *i*-propanol was initially present in concentrations greater than 20% (Figure 32(b)).

Figure 32(c) illustrates that in the competition experiments between methanol and *n*-butanol, *n*-butanol was favoured by the host for complexation, particularly in those solutions initially containing more than 40% *n*-butanol.

The results of the competition experiment between ethanol and *i*-propanol are shown in Figure 33(a). *i*-Propanol was preferentially included by the host in the solutions containing more than 10% *i*-propanol.

Similar results were observed in the competition experiments between ethanol and *n*-butanol (Figure 33(b)), where *n*-butanol was preferred above ethanol by the host in those solutions initially containing more than 10% *n*-butanol.

Figure 33(c) contains the results of the competition experiments carried out between *i*-propanol and *n*-butanol. *i*-Propanol was found to be selected preferentially by the host compound for complex formation.

(a)

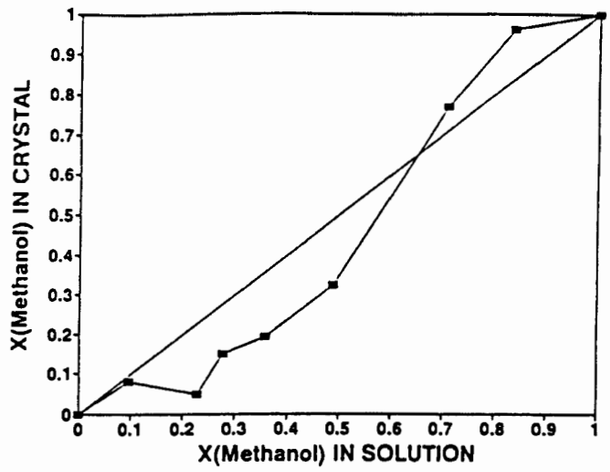

(b)

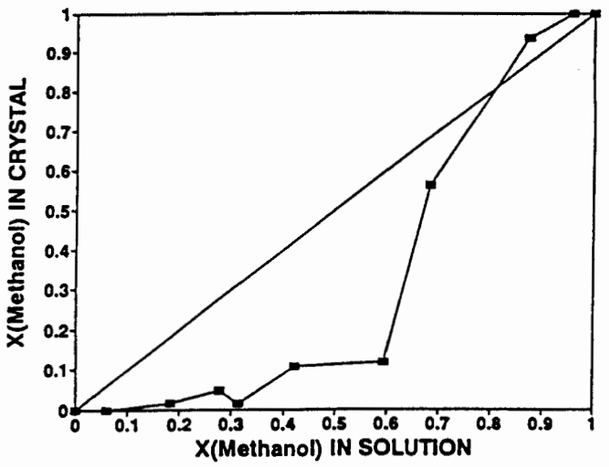

(c)

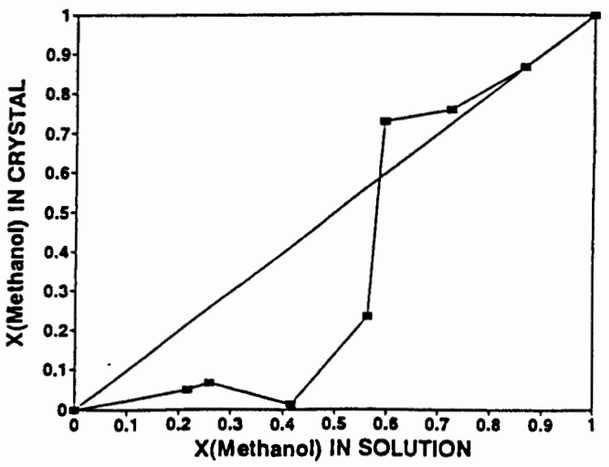

Figure 32: Results of the competition experiments carried out between (a) methanol and ethanol, (b) methanol and *i*-propanol and (c) methanol and *n*-butanol

(a)

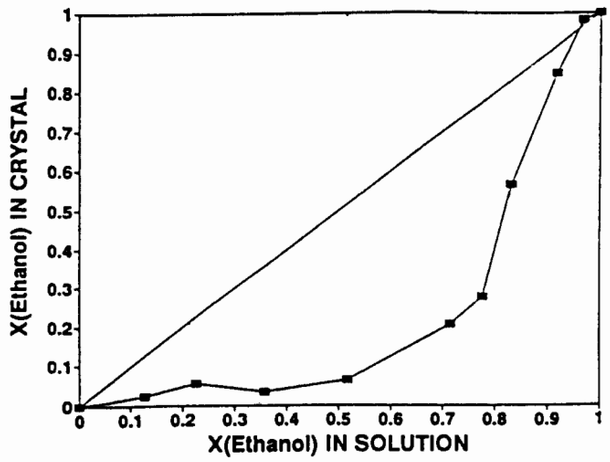

(b)

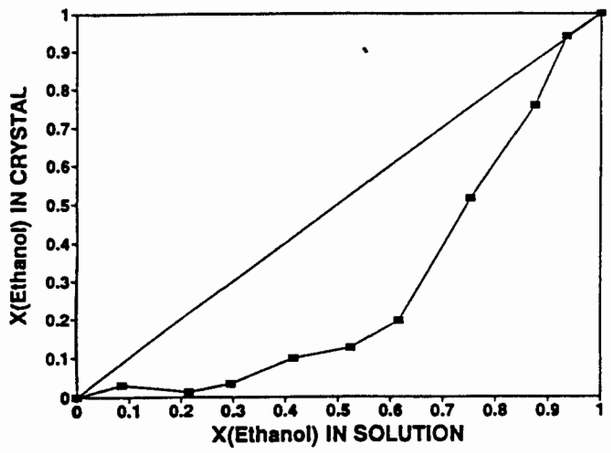

(c)

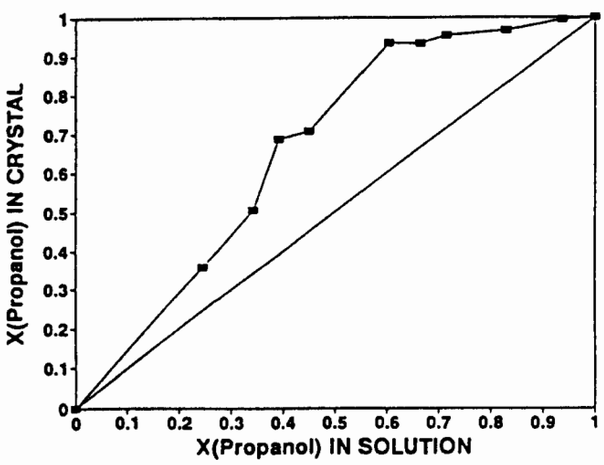

Figure 33: Results of the competition experiments carried out between (a) ethanol and *i*-propanol, (b) ethanol and *n*-butanol, and (c) *i*-propanol and *n*-butanol

7.6.2 4-Component

The competition experiments were extended to include all four alcohols simultaneously. The host compound was added to the various mixtures, and crystals of the preferred inclusion complexes were allowed to form. The crystals were removed from the mother liquors and blotted dry on filter paper. The crystals were placed in glass vials fitted with rubber septa under their screw-on lids. The vials were heated to 150°C, at which temperature complete desorption of the included guest mixtures occurred. Since the vials were airtight, the vapours of the desorbed guests were contained in the vials. On cooling the vials to room temperature, the alcohol vapours condensed on the upper sides of the vials, and these drops were analysed by GC to determine the ratios of the alcohols in the crystals.

A tetrahedron was chosen to represent the relative concentrations of the four alcohols. Each alcohol investigated was assigned a vertex of the tetrahedron, so that each vertex represents 100% of the corresponding alcohol, as measured perpendicularly from the opposite face. An icosahedron was placed in the centre of the tetrahedron, as illustrated in Figure 34. The defining points of the icosahedron were chosen to represent the initial alcohol mixtures. Figure 35 illustrates the shape of an icosahedron in greater detail.

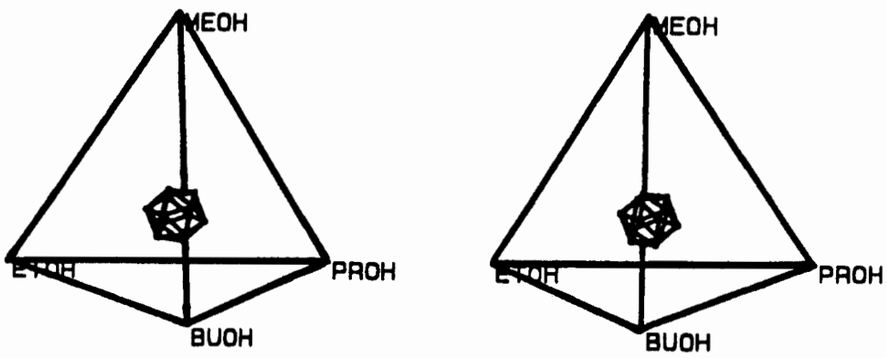

Figure 34: The icosahedron in the centre of the tetrahedron representing the four alcohols

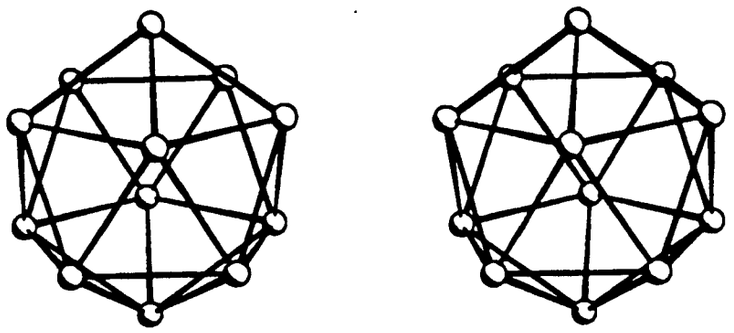

Figure 35: An icosahedron with its defining points illustrated as spheres

The relative amounts of each alcohol represented by the points of the icosahedron were calculated as follows:

The distance from each point of the icosahedron to each of the four planes of the tetrahedron was calculated[4]. These distances were converted to fractions of the total distance from a vertex to a plane, and in this manner the percentages of the alcohols in the starting solutions were determined. This calculation is represented graphically in Figure 35, and a detailed explanation is given in Appendix 2.

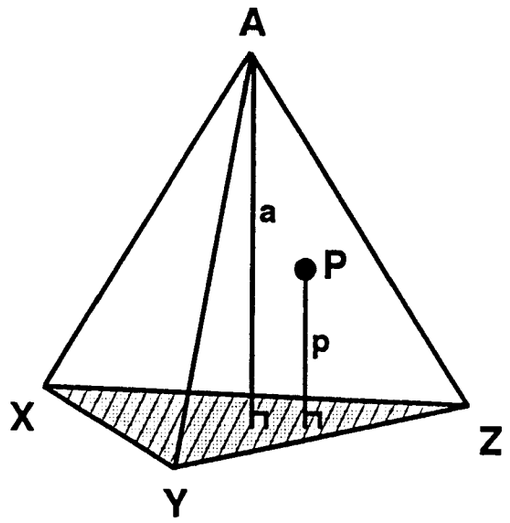

$\therefore$ (p÷a) x 100 = %(component A) represented by point P

Figure 35: Graphical representation of the calculations performed in order to determine the starting concentrations of the alcohols

The ratios of the four alcohols in the starting mixtures used during the 4-component competition experiment are listed in Appendix 1.

After the competition experiments were performed, the percentages of each alcohol included by the host was obtained by GC analysis. These percentages were converted to distances for the planes, and a series of final co-ordinates were obtained. The results of the competition experiment are represented graphically in Figures 36(a) and 36(b).

(a)

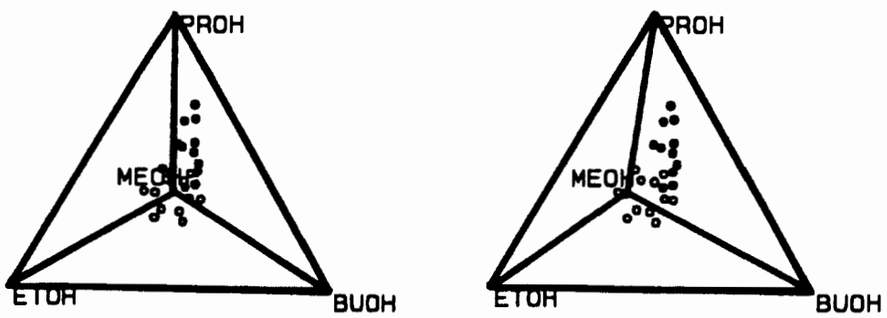

(b)

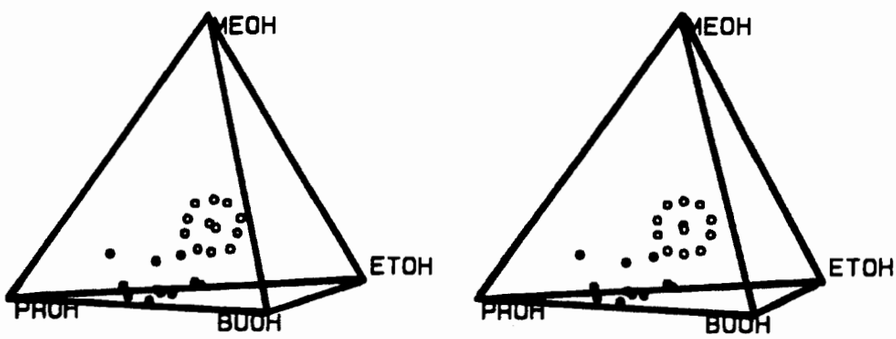

Figure 36: Results of the 4-component competition experiments carried out on the alcohol system

Figure 36(a) is a view of the tetrahedron perpendicular to the ethanol/propanol/*n*-butanol plane, and illustrates the migration of the icosahedron towards propanol. Figure 36(b) illustrates the migration of the icosahedron away from the methanol vertex. These results indicate that the host compound selectively enclathrates *i*-propanol above the other alcohols, in mixtures initially containing all four alcohols.

7.7 DISCUSSION

Inclusion compounds were formed between the host and the following alcohols: methanol, ethanol, *i*-propanol and *n*-butanol. The crystal structures of these complexes were analysed, and were found to be similar. Hydrogen bonding results in the formation of layers of host molecules which run parallel to the *b* axis in all structures. The packing of the host molecules in the four crystal structures is very similar, and this consistency is reflected in the small variation of the unit cell parameter *a* (from 6.276 Å to 6.3207 Å) and the cell parameter *b* (from 10.784 Å to 10.895 Å). However, a significant increase of the cell parameter *c* occurs: from 12.887 Å in **MEOH** to 13.420 Å in **ETOH**, to 14.301 Å in **PROH**, and finally to 14.789 Å in **BUOH**. This variation in the unit cell parameter *c* occurs since the 'layers' of host molecules along *c* are stabilised mainly by weak van der Waals forces, and therefore their periodicity may be relatively easily increased. This increase in the spacing between the layers occurs in order to accommodate the larger guest molecules between the layers.

The complexes **ETOH** and **MEOH** display a degree of isostructuraility. The structures have similar unit cell dimensions and packing motifs. Also, their lattice energies are essentially equal.

The calculated lattice energies of the four structures indicate that the **PROH** complex (-268 kJ mol^{-1}) is most stable, followed by **BUOH** (-258.3 kJ mol^{-1}). The **ETOH** (-215.2 kJ mol^{-1}) and **MEOH** (-215.9 kJ mol^{-1}) have similar lattice energies, and therefore are of similar stability. The relative stabilities of the complexes were reflected by the results obtained from the competition experiments. The 2-component guest competition experiments revealed that the host compound revealed the following complexation selectivity trend: *i*-propanol > *n*-butanol > ethanol ≈ methanol. This trend agrees with the lattice energy values, with the most stable complexes forming preferentially.

The competition experiment carried out with all four alcohols present simultaneously agree with the results obtained from the 2-component experiments. A migration of the starting icosahedron occurs away from the vertices representing methanol and ethanol, and towards the vertex representing *i*-propanol. A less pronounced migration occurs away from the *n*-butanol vertex toward the *i*-propanol vertex. This result is expected, since the lattice energy of **PROH** is only ~10kJ mol^{-1} lower than that of the **BUOH** complex.

1 I. Olovsson and P. Jönsson, *The Hydrogen Bond - Structure and Spectroscopy*, P. Schuster, G. Zundel and C. Sarderfy (eds.), North-Holland Publishing Company, Amsterdam, 1976.

2 F. H. Allen, O. Kennard, D. G. Watson, L. Brammer, A. G. Orpen and R. Taylor, *J. Chem. Soc. Perkin Trans* 2, 1987, S1 - S19.

3 A. R. West, *Solid State Chemistry and its Applications*, Wiley, Chichester, 1984.

4 E. W. Swokowski, *Calculus with Analytic Geometry*, Third Edition, PWS Publishers, 1979.

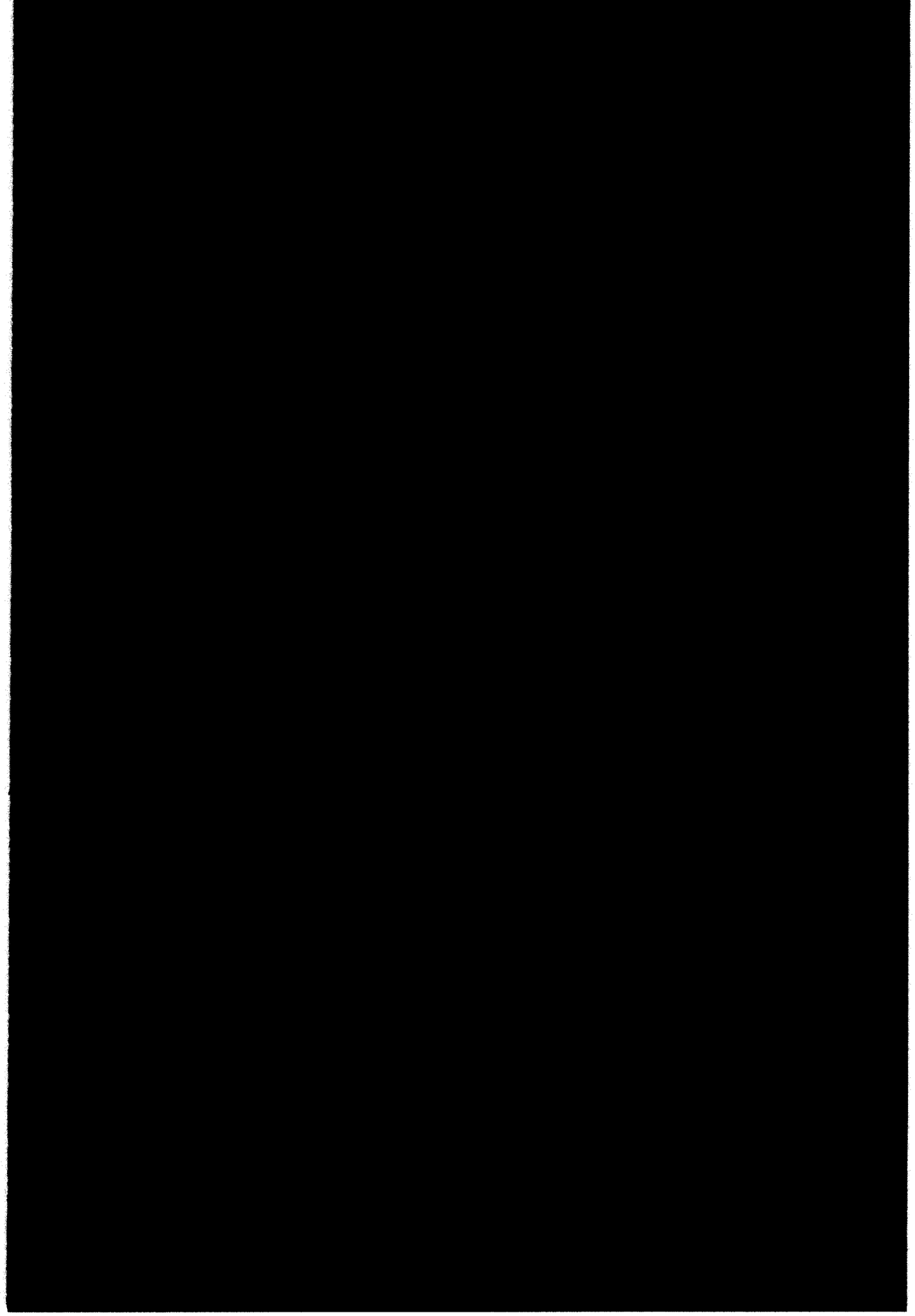

8. TERNARY INCLUSION COMPLEXES, AND CONFORMATION OF HOST COMPOUNDS

Three ternary inclusion complexes were investigated during the course of this study. They are the complexes **H**•H_2O•½Dioxane (**DIOXW**), **H**•H_2O•½Ethyl acetate (**EAW**) and **H**•H_2O•2-picoline (**2PIC**). These complexes were formed by recrystallising the host compound from solutions of 1,4-dioxane, ethyl acetate and 2-picoline respectively. Inclusion of water occurred from the atmosphere. The complex **2PIC** has been discussed in Chapter 5, and the structures of **DIOXW** and **EAW** will be discussed in this chapter.

The host conformations in the inclusion complexes whose structures have been elucidated in this study (see Chapters 3 to 7) will be discussed collectively in Section 8.3 of this chapter.

Preliminary photography determined the unit cell parameters and the space groups of the **DIOXW** and **EAW** complexes. Crystallographic experimental and refinement details for the structures are contained in Table 1, while lists of final atomic co-ordinates, temperature factors, tables of bond lengths and bond angles are to be found in Appendix 3. Tables of observed and calculated structure factors are presented in Appendix 4.

Table 1: Crystal data, experimental and refinement parameters.

	DIOXW	**EAW**
Molecular formula	$C_{18}H_{20}O_2 \bullet H_2O \bullet ½C_4H_8O_2$	$C_{18}H_{20}O_2 \cdot H_2O \cdot ½C_4H_8O_2$
M_r /g.mol^{-1}	330.41	330.41
Space Group	P $\bar{1}$	P $\bar{1}$
a /Å	6.327(2)	6.380(1)
b /Å	10.820(2)	10.892(2)
c /Å	13.593(2)	13.823(2)
α /°	100.66(1)	102.24(1)
β /°	97.33(2)	96.99(2)
γ /°	103.95(2)	101.04(2)
V /Å^3	872.9(3)	908.2(3)
Z	2	2
D_c /g.cm^{-3}	1.26	1.21
D_c /g.cm^{-3}	1.24(3)	1.19(3)
μ(Mo-K_α) /cm^{-1}	0.86	0.83
F(000)	356	356
Crystal size /mm	0.4 x 0.4 x 0.4	0.35 x 0.4 x 0.4
Range scanned θ /°	1 - 25	1 - 25
Range of indices	*h*: ±7; *k*: ±12; *l*: ±16	*h*: ±7 ; *k*: ±12 ; *l*: 0,16
Crystal decay /%	-0.5	+5.8
No. reflections collected	6130	3338
No. reflections observed	4253	3192
No. parameters	237	215
R_1	0.0412	0.1002
wR_2	0.1061	0.2857
S	1.042	1.098
$\Delta\rho$ excursions /eÅ^{-3}	0.313; -0.244	0.540; -0.532

8.1 DIOXW

8.1.1 Structure Solution

Preliminary X-ray photography indicated that **DIOXW** belonged to the triclinic crystal system. The centrosymmetric space group P $\bar{1}$ was chosen based on the $|E^2-1|$ values for the zonal and general reflections, which were in the range 0.967 to 1.043. TG experiments confirmed the host:water:dioxane ratio in this complex to be 1:1:½.

The atomic numbering scheme used for the host molecule is as before (see Chapter 3, Figure 1), while that used for the dioxane and water guest molecules is illustrated in Figure 1.

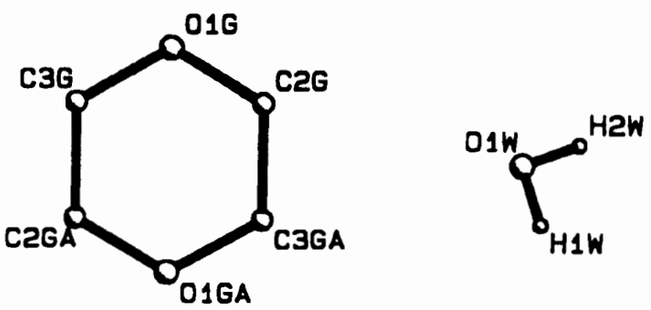

Figure 1: Atomic numbering used for dioxane and water

The positions of all the host non-hydrogen atoms in the asymmetric unit were obtained from direct methods. One host molecule was placed in a general position in the unit cell, with Z=2. The positions of the water and dioxane guest atoms were located in the difference electron density maps upon subsequent refinement. The water oxygen atom was placed in a general position in the unit cell. The dioxane molecule was found to lie on a centre of inversion, at Wyckoff position *b*, and therefore one half of the dioxane molecule was placed in the asymmetric unit. The dioxane molecule was therefore in the chair conformation. The oxygen atom of the dioxane molecule was placed at the location of the peak with the higher electron density in the map for this guest

molecule. The non-hydrogen atoms of both host and guest molecules were treated anisotropically.

The host and dioxane hydrogen atoms were located in difference electron density maps, but were placed in the model in geometrically constrained positions and refined with common temperature factors for atoms of the same type. The hydroxyl hydrogens of the host, and the water molecule hydrogen atoms were located in a difference map, and were entered independently and refined with simple bond length constraints according to a function of O-H versus O--O distances[1]. The structure refined successfully to R_1 = 0.0412.

8.1.2 Structure Analysis

Bond lengths and bond angles of the molecules were all in acceptable ranges for structures of this type[2], and will be discussed in more detail in section 8.3. of this chapter. The crystal structure of **DIOXW** is illustrated in Figures 2 and 3, viewed down [100] and [010]. The host molecules pack to form channels parallel to [100] in which the guest molecules are located. These channels are unconstricted, and have approximately circular cross sections with diameters of ~6Å. Figure 4 is a MOLMAP plot illustrating the shapes of the channels.

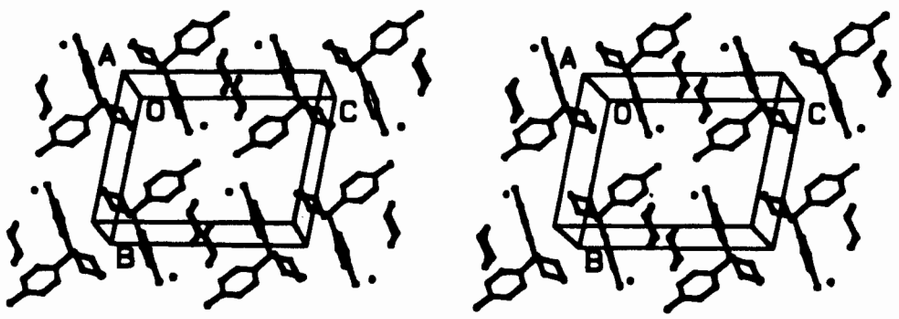

Figure 2: Stereo view of the crystal packing of **DIOXW** down [100]

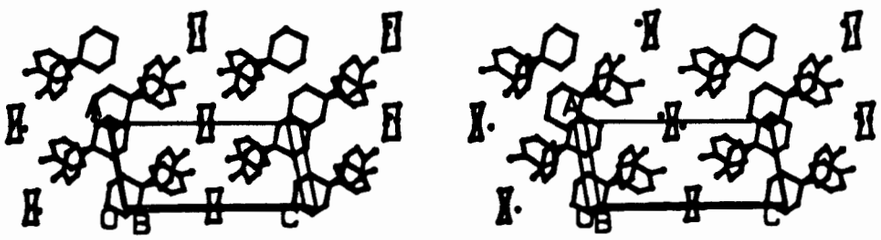

Figure 3: Stereo view of the crystal packing of **DIOXW**, down [010]

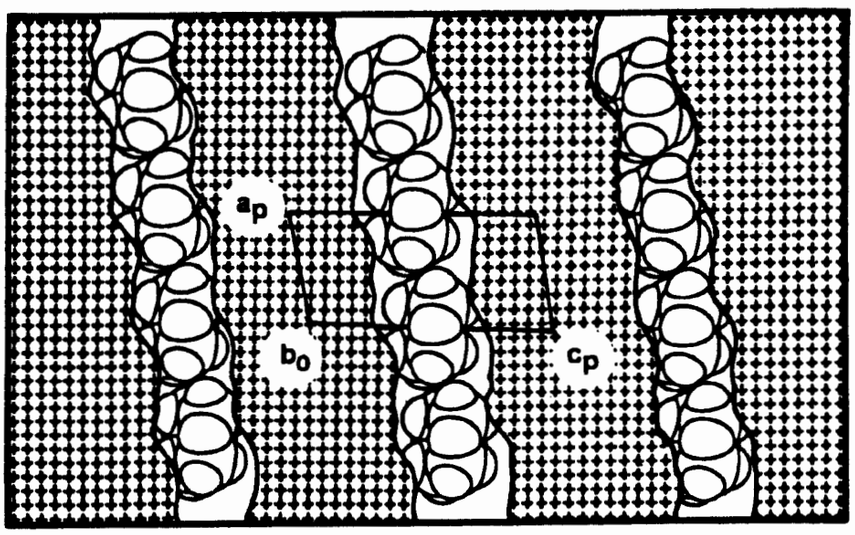

Figure 4: MOLMAP plot of **DIOXW** viewed down [010], and sectioned at y = 0. The host structure is represented by the hatched area, and the guest molecules are depicted with van der Waals radii.

Host molecules related by translation along *b* hydrogen bond with each other via their hydroxyl groups. Ribbons of host molecules parallel to *b* are formed in this manner. Each host-host site is hydrogen bonded to two water molecules, one from above and one from below, when viewing the crystal packing down

[100]. In one of these host–water hydrogen bonds, the water molecule acts as a proton donor. The water molecule utilises its second proton in forming a hydrogen bond to the dioxane molecule. Thus the dioxane molecules do not interact directly with the host structure, but are linked to it via the water molecules. The intermolecular interactions which occur in **DIOXW** are illustrated in Figure 5, while geometric details are listed in Table 2.

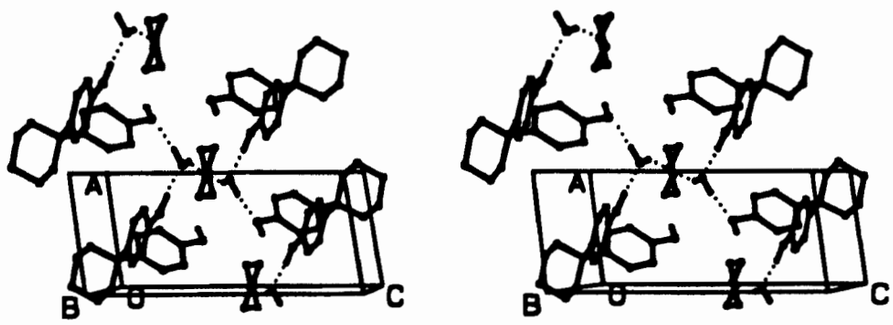

Figure 5: Intermolecular interactions in **DIOXW**

Table 2: Details of hydrogen bonding in **DIOXW**.

Donor	Acceptor	D-H /Å*	D–A /Å*	D-H–A /°*
O13	O1W	0.94(3)	2.630(2)	175(3)
O1W	O1G	0.87(3)	2.780(3)	157(3)
O1W	O20[a]	0.89(3)	2.820(2)	172(3)
O20	O13[b]	0.96(3)	2.719(2)	171(3)

Symmetry code: (a) x+1, y+1, z (b) x, y-1, z

* **D** = Donor ; **A** = Acceptor

8.1.3 Thermal Analysis

8.1.3.1 TG and DSC

Samples of **DIOXW** were heated over the temperature range 50 to 200°C at a rate of 10 °C min^{-1}. The resulting TG and DSC traces are shown in Figure 6. A mass loss step of 18.0% was observed in the TG trace. The calculated mass losses for the release of water and dioxane from the **H**•H_2O•½dioxane complex are 5.5% and 13.3% respectively. The sum of the two calculated mass losses (18.8%) is in good agreement with the experimental result.

Three endotherms, labelled "A", "B" and "C", were observed in the DSC trace. These occurred at onset temperatures of 114.8°C, 183.6°C and 189.1°C. Endotherm A corresponds to the desolvation of the water and dioxane. Repeating the DSC trace at a heating rate of 2°C min^{-1} did not result in the resolution of endotherm A into two endotherms representing the individual desolvation of water and dioxane. Endotherm B is due to a polymorphic rearrangement of the host compound shortly before its melt (endotherm C).

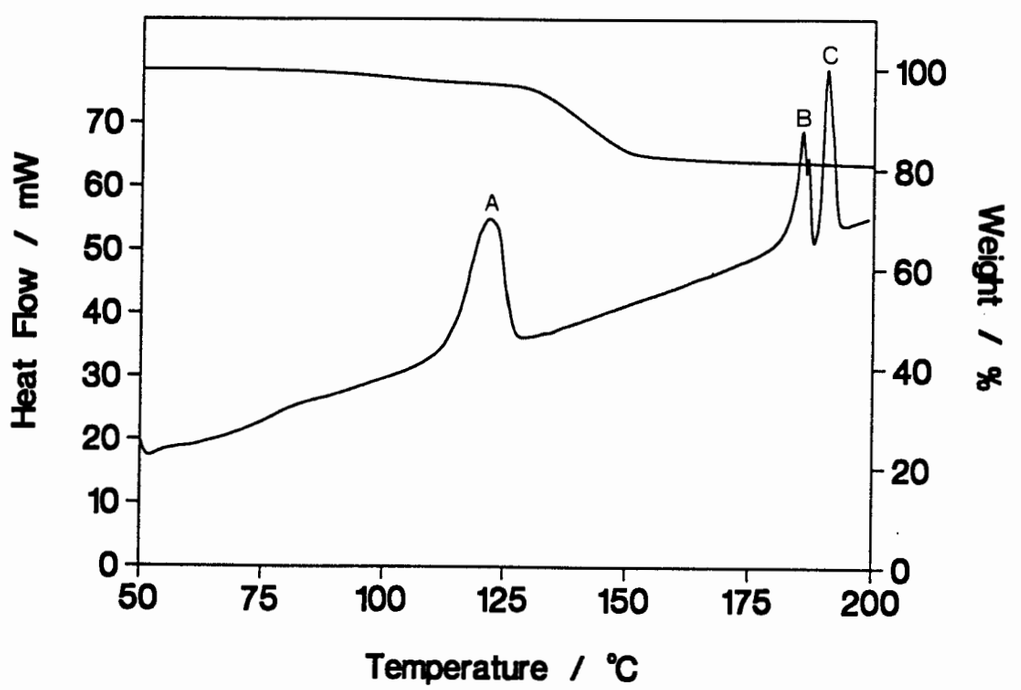

Figure 6: TG and DSC traces of **DIOXW**

8.1.3.2 Hot Stage Microscopy

A single crystal of **DIOXW** was heated on a hot stage over the temperature range 20 to 200°C, and photographs were taken of any physical changes to the crystal. The photographs are shown in Figure 7. The physical changes observed during the hot stage experiment occurred at different temperatures from the thermal events indicated by TG and DSC experiments. This is due to the fact that the hot stage apparatus has a different geometry from that of the DSC apparatus. Also, samples of very different particle sizes were used in the different experiments. In TG and DSC experiments, powdered samples were used (10 - 100μm), while in the hot stage experiment large crystals with dimensions between 0.2mm and 0.4mm were used.

The edges of the crystal started becoming opaque at 103°C, indicating the beginning of the desolvation reaction. With further heating, cracks appeared in the crystal (Figure 7(c)), and recrystallisation at the edges of the crystal was observed. By 125°C, the crystal had become completely opaque. The crystal melted at 195°C.

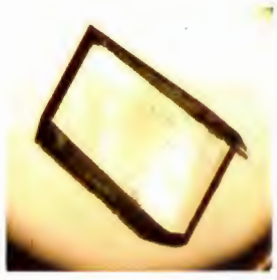

(a) 20°C

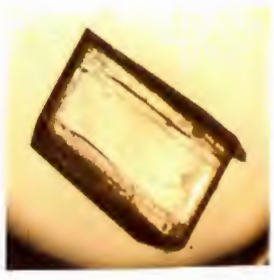

(b) 103°C

(c) 121°C

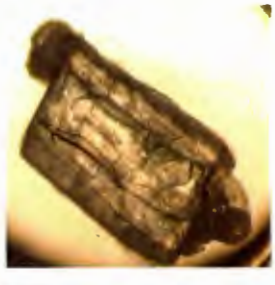

(d) 121°C, after 30 seconds

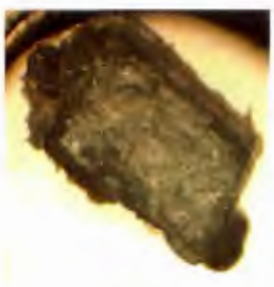

(e) 125°C

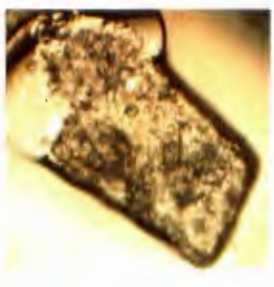

(f) 195°C

Figure 7: Hot stage microscope photographs of **DIOXW** (25X enlarged)

8.2 EAW

8.2.1 Structure Solution

A single crystal of **EAW** was subjected to X-ray photography to determine its cell dimensions and space group. The centrosymmetric space group P $\bar{1}$ was chosen from the two possible triclinic space groups, P1 and P $\bar{1}$, based on the $|E^2-1|$ statistics of zonal and other reflections.

The **H**:H_2O:ethyl acetate ratio of 1:1:½ in **EAW** was confirmed by TG analysis. Direct methods yielded the positions of all the non-hydrogen host atoms, and these were placed at a general position in the cell, with Z=2. The non-hydrogen atoms of the host were treated anisotropically. The host hydrogen atoms were located in the maps, but were geometrically constrained in the model at *d*(C-H) = 1Å, and similar hydrogen atoms were assigned common isotropic temperature factors. The two host hydroxyl hydrogen atoms were located in difference electron density maps and were entered into the model with independent isotropic temperature factors. These hydrogen atoms were constrained with simple bond lengths relating O-H distances to O⋯O distances[1].

The oxygen atom of the water molecule was located in a difference electron density map, and this atom was refined with anisotropic temperature factors. One of the water hydrogen atoms was located in an electron density map, and was constrained at *d*(O-H) = 0.98Å in the model. The second water hydrogen could not be located and therefore was omitted from the model.

The ethyl acetate guest molecule was found to be disordered, and was positioned in such a manner that an apparent centre of symmetry was located between the ester oxygen and the methylenic carbon was invoked, as illustrated in Figure 8.

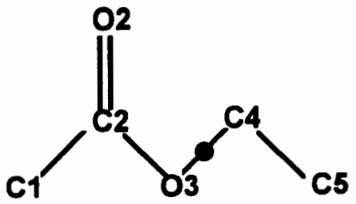

Figure 8: Positioning of the ethyl acetate guest molecule on a centre of inversion (•)

This has the effect of doubling the site occupancies of these atoms such that they are filled by both O and C at the same positions, as shown in Figure 9.

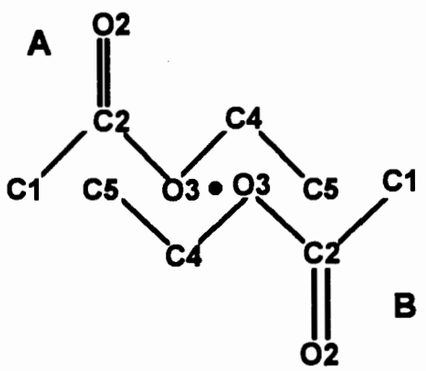

Figure 9: The two positions of the ethyl acetate guest molecule

The two molecules labelled A and B were inserted into the structure factor calculation with s.o.f. of 0.5 for each atom, ensuring that identical positions were kept by atoms C2A and C5B, O3A and C4B, C4A and O3B, and C5A and C2B. The molecule was refined using free variable parameters incorporated into the SHELX93 program[3]. The ethyl acetate atoms were all refined using isotropic temperature factors, which were all in an acceptable range ($0.13Å^2 < U < 0.19Å^2$). Hydrogen atoms of the ethyl acetate molecule were omitted from the final model.

8.2.2 Structure Analysis

The crystal packing in **EAW** is illustrated in Figures 9 and 10, viewed down [100] and [010] respectively. The host molecules pack to form double ribbons parallel to [010]. The layers formed in this manner are separated by ribbons of water and ethyl acetate molecules. The channels formed by the packing of the host molecules are unconstricted and run parallel to [100]. The channels have circular cross sections with diameters of ~4.5Å, and are depicted in Figure 11.

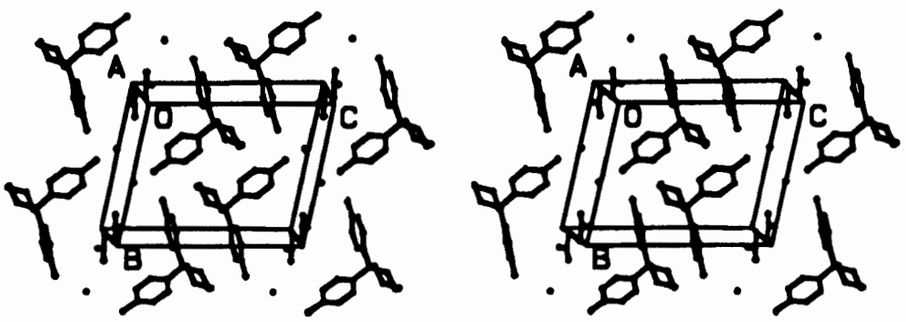

Figure 9: Stereo view of the crystal packing of **EAW**

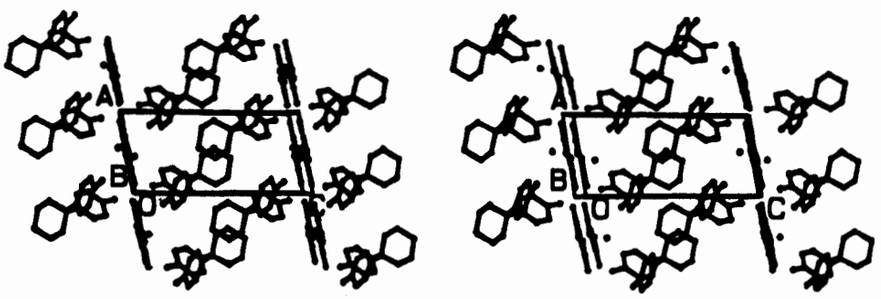

Figure 10: Stereo view of the crystal packing of **EAW** down [010]

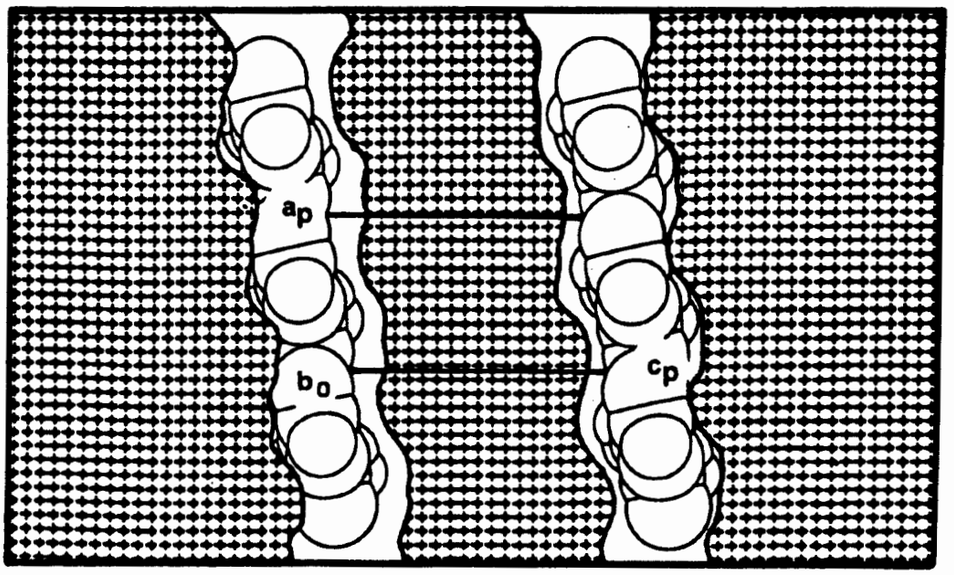

Figure 11: MOLMAP plot of **EAW** viewed down [010], and sectioned at y = 0. The host framework is represented by the hatched area, while the water and ethyl acetate molecules are depicted with van der Waals radii.

Adjacent host molecules interact with each other by means of the hydrogen bonding of their hydroxyl groups. Each host molecule also forms a hydrogen bond with a water molecule, which in turn interacts with an ethyl acetate molecule. Thus the ethyl acetate molecules do not interact directly with the host structure, but are linked to it via the water molecules. Table 3 lists geometric details of the hydrogen bonds, and Figure 12 illustrates the intermolecular interactions in **EAW**.

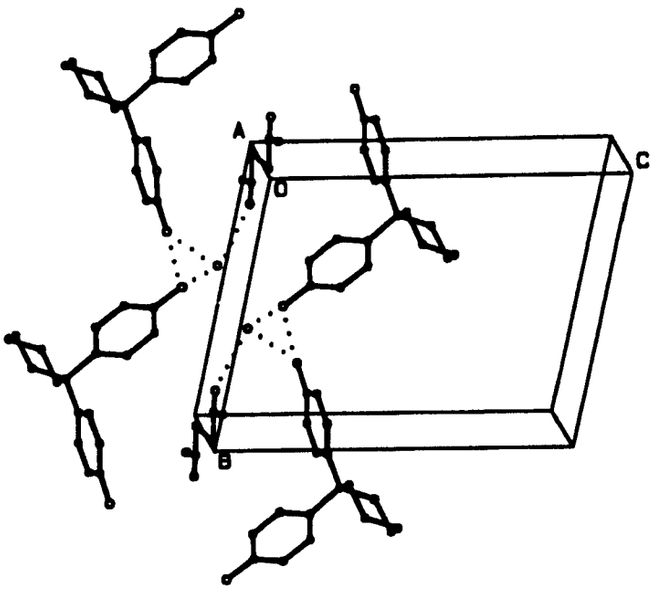

Figure 12: Hydrogen bonding interactions in **EAW**

Table 3: Details of hydrogen bonding in **EAW**.

Donor	Acceptor	D-H /Å*	D–A /Å*	D-H–A /°*
O13	O1W	0.97(6)	2.649(7)	130(5)
O20	O13[a]	0.98(6)	2.723(7)	171(5)
O1W	O20[b]	0.97(7)	2.766(7)	148(5)
O1W	O2G	-	2.729(5)[†]	-

Symmetry code: (a) x, y+1, z (b) x-1, y-1, z

* **D** = Donor ; **A** = Acceptor

[†] Geometric details could not be determined, since the water hydrogen atom could not be located in difference electron density maps.

8.2.3 Thermal Analysis

8.2.3.1 TG and DSC

TG and DSC experiments were performed on a powdered sample of **EAW** over the temperature range 50 to 200°C, and the resulting traces are illustrated in Figure 13. The TG experiment reveals a mass loss step of 18.9%. This is in agreement with the total calculated mass loss of 18.8% for the loss of one water and half an ethyl acetate molecule.

The DSC trace reflects two endotherms at onset temperatures of 72.3°C and 189.6°C. Endotherm A corresponds to the desolvation reaction of both guests, and shows complex behaviour. Endotherm B represents the melt of the desolvated compound.

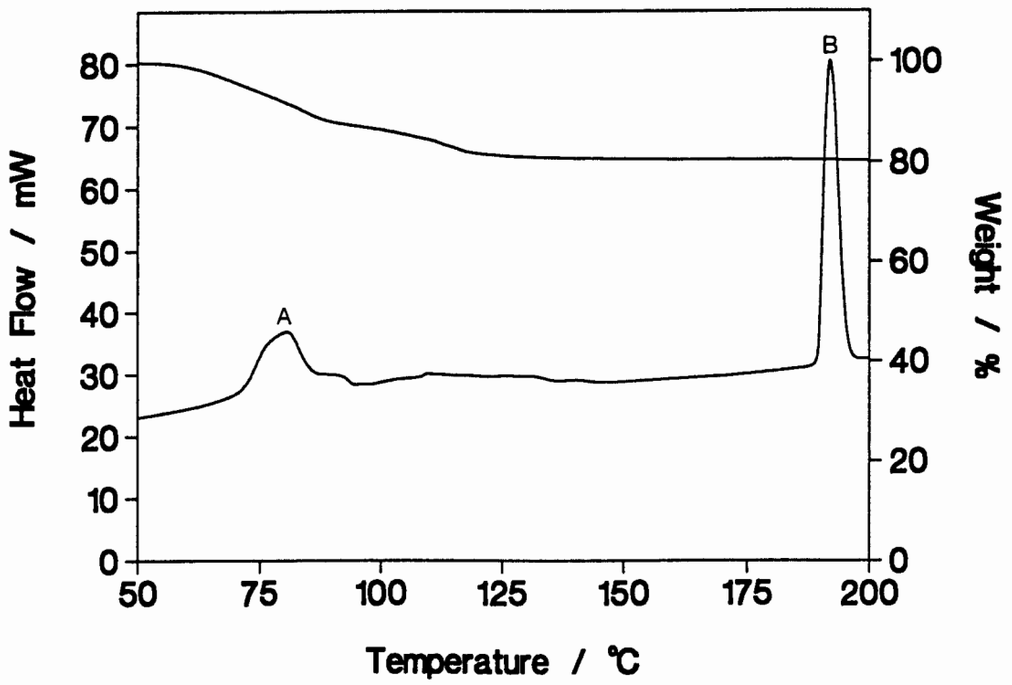

Figure 13: TG and DSC traces of **EAW**

8.2.3.2 Hot Stage Microscopy

A crystal of **EAW** was heated from 20 to 200°C on a hot stage apparatus. Photographs were taken of all physical changes occurring in the crystal, and these are shown in Figure 14. The first signs of the desolvation reaction appeared at 107°C, at which temperature bubbles of vapour were observed in the silicone oil. As guest release proceeded, more bubbles formed in the oil, and the **EAW** crystal became more opaque. By 150°C, guest desorption was complete, since the crystal was completely opaque, and no more vapour escaped from the crystal. The crystal melted at 190°C.

The complexes **DIOXW** and **EAW** display a degree of isostructurality. The two structures have similar unit cell parameters, and the host molecules pack in the same general packing motif in both cases.

(a) 20°C

(b) 107°C

(c) 111°C

(d) 122°C

Figure 14: Hot stage photographs of **EAW**, (25X enlarged)

8.3 HOST CONFORMATION

The host compound conformation in the inclusion compounds presented in this study, will be discussed. Parameters obtained from the **2PIC** complex have been omitted from the analysis due to the low precision[2] of the structure solution (*R* factor > 0.10) which resulted in mean estimated standard deviations > 0.010Å for the C-C bonds.

The atomic numbering scheme used for the host compound is illustrated in Figure 15.

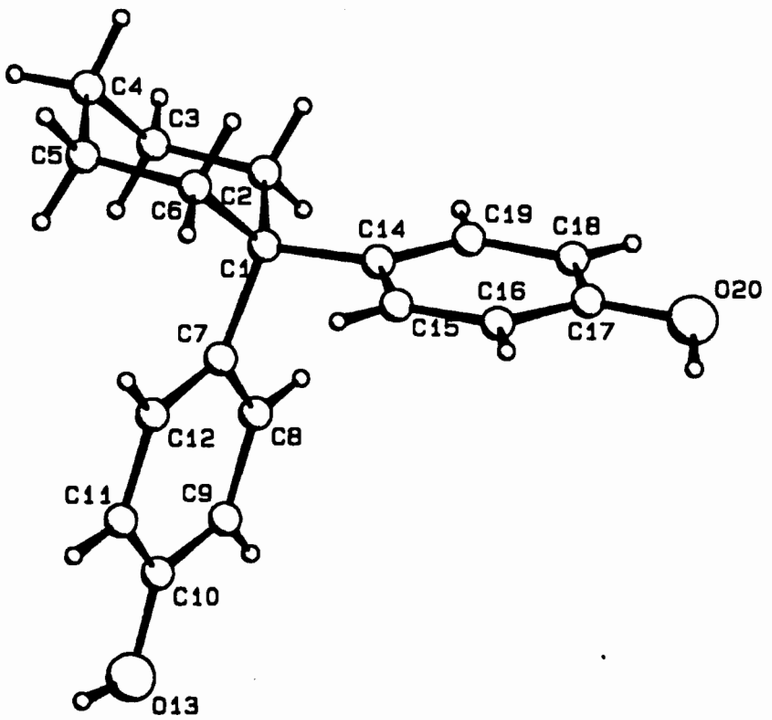

Figure 15: Atomic numbering used for **H** in all structure solutions

The general conformation of the host molecule is shown in Figure 16, which was extracted from the **OBD** structure.

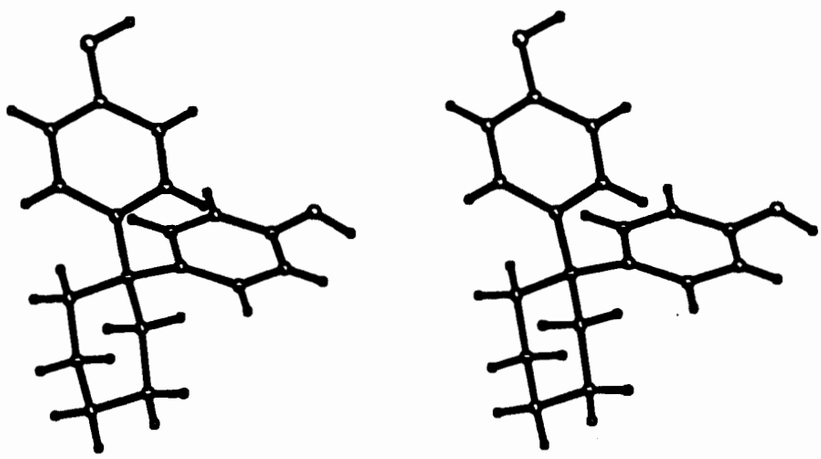

Figure 16: Stereo view of the general host conformation

The bonds of the host compound may be classified into five different types, and these are shown in Figure 17. The maximum, minimum, median and mean[4] values of these bonds are tabulated in Table 4. These bond lengths were all found to lie in acceptable ranges for similar bonds, as derived from the structures in the Cambridge Structural Database[2,5]. The distributions of the bond lengths *a* to *e* are illustrated in Figure 18.

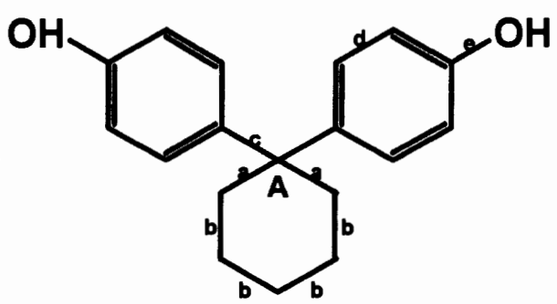

Figure 17: Classification of bonds for the host, **H**

Table 4: Cumulative host bond lengths and angle statistics for all structures solved in this thesis (excluding **2PIC**)

	Minimum /Å	Maximum /Å	Mean /Å*	Median†	n‡
a = $Csp^3 - Csp^3$	1.534(4)	1.562(7)	1.547(25)	1.548(3)	32
b = $Csp^3 - Csp^3$	1.505(5)	1.533(5)	1.519(34)	1.519(3)	64
c = Csp^3 – Car	1.529(3)	1.550(5)	1.539(20)	1.540(3)	32
d = Car ≅ Car	1.364(6)	1.401(4)	1.382(91)	1.382(5)	192
e = Car – O	1.361(6)	1.387(2)	1.373(29)	1.373(3)	32

* Calculated as described by Allen *et. al.*[2]

† The sample median, *m*, has the property that half of the observations in the sample exceed *m*, and half fall short of it.

‡ n = sample size

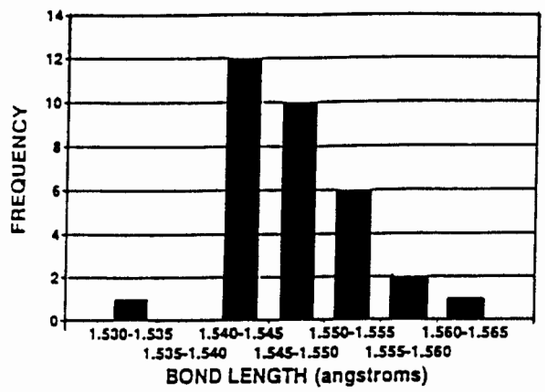

(a) Bond type *a*

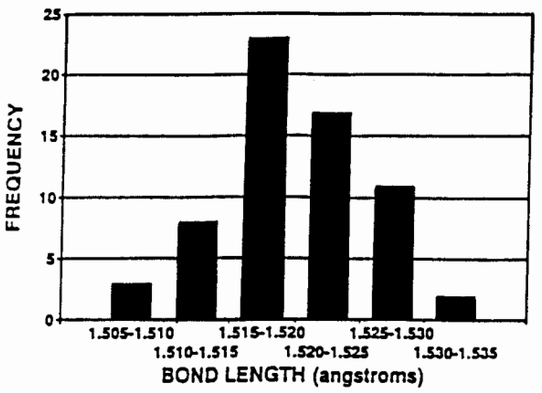

(b) Bond type *b*

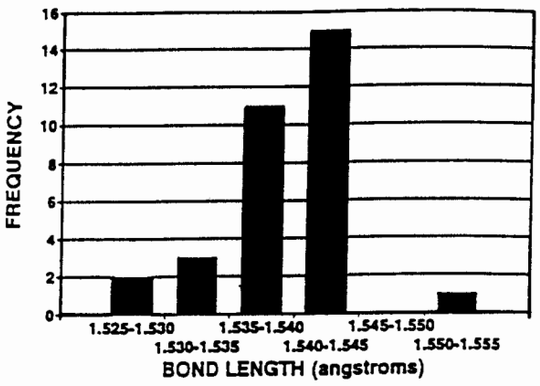

(c) Bond type *c*

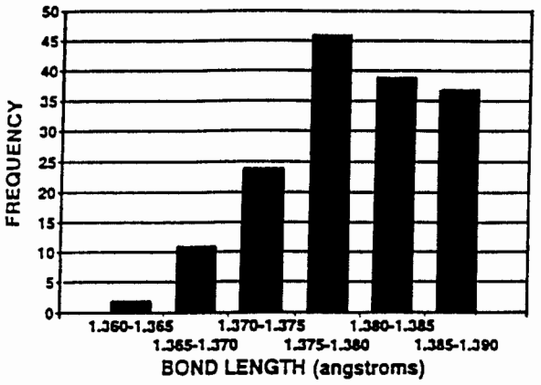

(d) Bond type *d*

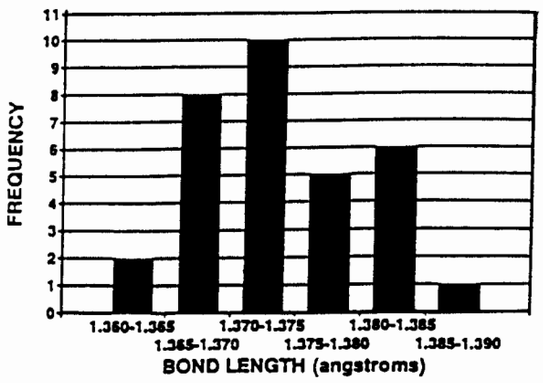

(e) Bond type *e*

Figure 18: Distribution of bond lengths *a*, *b*, *c*, *d* and *e*

The lengths of the two cyclohexyl bonds C1-C6 and C1-C2 (bond type *a* in Figure 17) were found to be longer than the remaining cyclohexyl bond lengths (bond types *b*). This is possibly due to repulsion between the C2 and C6 atoms and the aromatic rings. The distances C2 – C8 and C6 – C15 are in the range 2.880(3) – 3.876(4)Å. This repulsion also results in the compression of the angle A relative to the other cyclohexyl bond angles. Angle A varies from 105.9(2) – 106.8(1)° whereas the remaining angles of the cyclohexyl ring vary from 109.9(3) – 114.7(2)°. The cyclohexane rings are in the chair conformation in all structures studied, and the puckering parameter θ, as defined by Cremer and Pople[6], is always in the range 174(1) – 178.1(3)° or 1.4(2) – 3.6(3)°. The bond angles of the aromatic ring are in the range 115.3(2) – 122.9(2)°. The aromatic rings are all planar, and the maximum deviation of any aromatic carbon atom from its phenyl ring least-squares plane is 0.019(2)Å[7].

The conformation of the host molecule is best described by the torsion angles τ_1 and τ_2, illustrated in Figure 19, and by the dihedral angle between the planes of the two phenyl rings. Labelling of the host compounds in each structure, although following the prescribed numbering scheme, was initially done arbitrarily and thus it is not feasible to compare the various τ_i angles directly. A systematic search was performed for the combination of torsion angles which yielded the torsion angles τ_1 and τ_2 close to 45°, with $\tau_1 < \tau_2$. The torsion angles and the dihedral angles between the phenyl rings are listed in Table 5. The distributions of the two torsion angles τ_1 and τ_2 are shown in Figures 20 and 21.

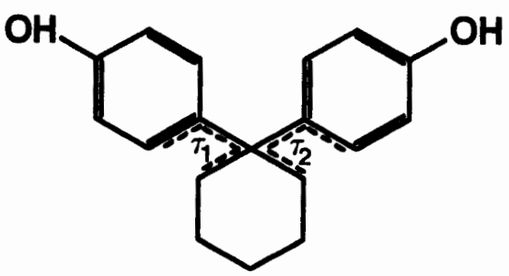

Figure 19: The torsion angles describing the host conformation

Table 5: Comparison of the overall host conformation

Complex	τ_1 / °	τ_2 / °	Dihedral angle / °
OPDA	52.8(2)	70.5(3)	88.3(1)
PPDA	45.9(2)	54.8(2)	81.95(6)
OBD	51.0(2)	66.2(2)	88.25(6)
PBD	31.7(2)	56.6(2)	86.96(7)
3PIC (a)*	41.6(3)	50.0(2)	81.12(7)
3PIC (b)*	44.3(2)	53.6(2)	82.04(7)
4PIC (a)*	37.6(3)	45.8(2)	78.73(7)
4PIC (b)*	43.7(3)	48.3(2)	80.44(8)
4LUT	34.0(3)	35.0(3)	75.16(7)
5LUT	45.7(3)	49.2(3)	84.90(8)
MEOH	50.1(2)	63.1(2)	87.29(9)
ETOH	48.8(2)	62.0(2)	85.13(6)
PROH	48.7(4)	61.9(3)	85.5(1)
BUOH	48.8(4)	61.3(3)	86.8(1)
DIOXW	48.4(2)	61.0(2)	87.47(6)
EAW	48.5(6)	65.6(6)	86.2(1)

* the two host molecules in the asymmetric unit are labelled (a) and (b)

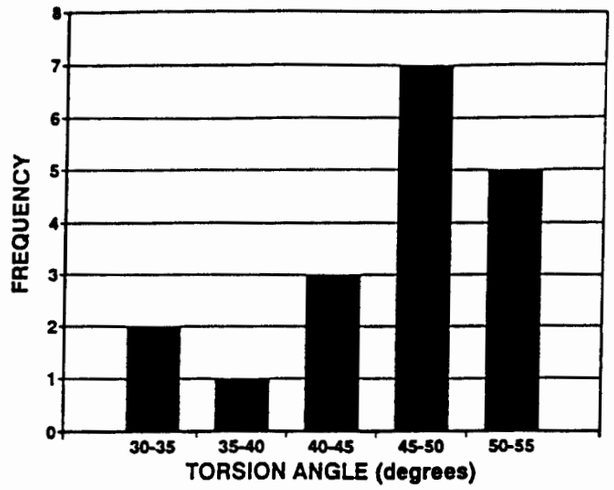

Figure 20: Distribution of the torsion angle τ_1

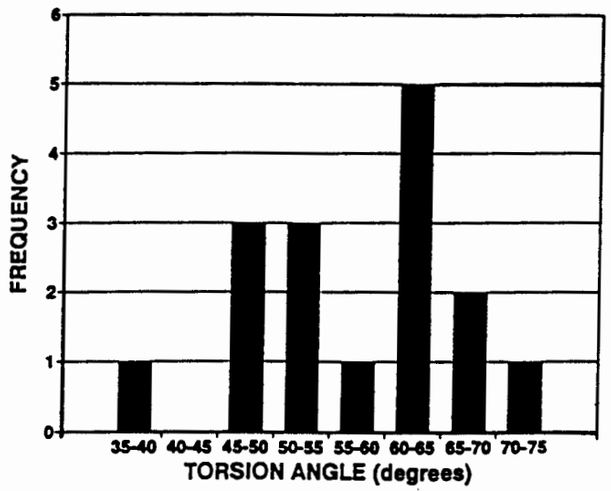

Figure 21: Distribution of torsion angle τ_2

Figures 20 and 21 illustrate that the torsion angles τ_1 and τ_2 are distributed over a fairly wide range of values. This is reminiscent of the behaviour of Werner[8] clathrates, where the ring systems of the host molecules twist in order to accommodate guest molecules of different sizes and geometries.

Table 5 indicates an increase in both torsion angles on exchanging *para*-substituted guest molecules with *ortho*- and *meta*- substituted guest molecules. For example, in **PPDA** the angle τ_1 is 45.9(2)° and τ_2 is 54.8(2)°. On changing the guest molecule from *p*-PDA to *o*-PDA, τ_1 increases to 52(8)° and τ_2 increases to 70.5(3)°. In the **DIOXW**, **EAW** and alcohol inclusion complexes, the torsion angles are remarkably constant, varying from 48.4(2) to 50.1(2)° for τ_1, and from 61.0(2) to 65.6(6)° for τ_2.

1 I. Olovsson and P. Jönsson, *The Hydrogen Bond - Structure and Spectroscopy*, P. Schuster, G. Zundel and C. Sarderfy (eds.), North-Holland Publishing Company, Amsterdam, 1976.

2 F. H. Allen, O. Kennard, D. G. Watson, L. Brammer, A. G. Orpen and R. Taylor, *J. Chem. Soc. Perkin Trans 2*, 1987, S1 - S19.

3 G. M. Sheldrick, *SHELXL-93: Programme for Crystal Structure Determination*, unpublished work.

4 G. H. Stout and L. H. Jensen, *X-ray Structure Determination. A Practical Guide*, Macmillan Publishing Co., New York, 1968.

5 Cambridge Structural Database and Cambridge Structural Database System, Cambridge Crystallographic Data Centre, University Chemical Laboratory, Cambridge, England.

6 D. Cremer and J. A. Pople, *J. Am. Chem. Soc.*, **97**, 1975, 1354.

7 V. Schomaker, J. Waser, R. E. Marsh and G. Bergman, *Acta Cryst.*, **12**, 1959, 600.

8 L. R. Nassimbeni, M. L. Niven and M. W. Taylor, *J. Chem. Soc. Dalton Trans.*, 1989, 119.

9. CONCLUSION

The ultimate goal of the structural chemist is to explain macro-phenomena such as selectivity, thermal stability and kinetic behaviour of a particular compound in terms of intermolecular forces. This study has investigated molecular recognition occurring between a particular diol host and a number of closely related guests, and has reconciled the physical properties of the crystalline inclusion compounds in terms of the structure and lattice energies of the host-guest assemblies.

This study dealt with the structure relationships of inclusion compounds formed with the host 1,1-bis(4-hydroxyphenyl)cyclohexane. The structures of the inclusion compounds were elucidated in an attempt to determine the relative stabilities of the complexes. Although the overall packing of the inclusion complex ultimately determined the stability of the structure, the degree of interaction between the host and guest species in each of the complexes was an indication of the stability of the complexes. In all the complexes, the guest molecules were hydrogen bonded to the host framework, although the number of bonds per guest molecule differed. The dual capacity of amine and hydroxyl groups for hydrogen bonding was well illustrated, with these groups acting as both proton donors and proton acceptors in most instances. In the case of the ternary complexes, **2PIC**, **EAW** and **DIOXW**, the ethyl acetate and dioxane guest molecules were not hydrogen bonded directly to the host structure, but were linked to it via water molecules.

In all the complexes studied, the host molecules were arranged in generally the same packing motif. This consisted of double ribbons of host molecules which were arranged so that channels formed between the ribbons, in which the guest molecules were located.

The shapes of the channels also provided an indication of the relative stability of the complexes. In some complexes (*e.g.* **MEOH** and **ETOH**) the channels were unconstricted. Crystals of these complexes were relatively unstable in the atmosphere, and desolvated after one to two days. In the majority of the complexes (*e.g.* **OPDA** and **4PIC**) the channels were constricted, and provided a barrier to guest desorption. In only one case, **PBD**, the channels were completely constricted, and in fact formed cavities. The *p*-benzenediol molecules were completely surrounded by host molecules, and therefore the guest molecules experienced a high physical barrier to desolvation. The stability of the complex **PBD** was indicated by the high melting point, T = 194°C of the complex. This was 50°C higher than the melt of the **OBD** complex in which the *o*-benzenediol guest molecules were located in constricted channels.

The lattice energies of all the complexes were calculated, and the relative stabilities indicated by these values agreed well with the observed selectivity trends of the host compound. In each system studied, the complex with the highest lattice energy was always formed preferentially during the competition experiments. In the case of *3*- and *4*-picoline, where the lattice energy values were equal, no selectivity of either isomer was observed.

Gavezzotti[1] recently studied the relative stabilities of pure compounds of substituted benzenes, similar to some of the guest compounds investigated during this thesis. He used melting temperatures as an indication of cohesion and thus stability of a compound. It was found that in most cases, the *para*-compounds have higher melting temperatures than their *meta*- and *ortho*-counterparts. An old rule of thumb[2] was quoted, which states that symmetrical molecules pack in a three-dimensional periodic lattice more easily than less symmetrical ones, and hence form more stable, higher-melting and less soluble crystals.

This notion may possibly be extended to inclusion compounds, since the host compound in this study always exhibited preferential inclusion of the *para*-substituted isomers, or in the case of the lutidine compounds, the more symmetrical *3,5*-lutidine isomer.

The solid-solid reactions between the host and the isomers of the solid guest compounds studied were successful in all cases except one. The inclusion complexes formed had the same structures as the corresponding complexes obtained by recrystallisation from solution. This result is very satisfactory, since obtaining inclusion compounds by grinding the host and guest components together is quicker and simpler than obtaining the complexes by recrystallisation from solution. It eliminates the need to find a suitable solvent in which both compounds are soluble, and the inclusion compounds are formed after a few minutes rather than a few days.

Activation energies of the desolvation reactions of four of the inclusion complexes, **3PIC**, **4PIC**, **24LUT** and **35LUT**, were obtained by non-isothermal and isothermal thermogravimetric methods. The activation energies were in the range 85 to 106 kJ mol^{-1}. Much controversy[3] surrounds the issue of which method yields the most reliable results. However, the values obtained using the two different methods in this study were in remarkably good agreement. A study by Coetzee[4] compared the activation energies of the decomposition reactions of inclusion compounds, similar to those studied in this thesis, with those of inorganic compounds, of *e.g.* hydrides, carbonates and oxides, surveyed by Galwey[5]. The activation energies of the inclusion compounds studied by Coetzee were in the range 35 to 150 kJ mol^{-1}. The inclusion compound desolvation energies were relatively low in comparison to the decomposition of inorganic salts, but this is expected since guest desolvation requires the breaking of hydrogen bonds and not covalent or ionic bonds.

The results obtained from this study confirm that an inclusion-type crystallisation is an excellent technique for molecular separation between species of nearly identical chemical and physical properties, but containing a small structural variation. The crystalline state represents a close-packed phase, and its relative stability is very sensitive to the degree of spatial and functional complementarity between the various constituents. The correct manipulation of these parameters can lead to successful molecular separations.

It would be valuable to develop this study to investigate mixtures of isomers resulting from industrial processes currently in operation, and to optimize the selectivity of the host compound 1,1-bis(4-hydroxyphenyl)cyclohexane to separate the constituents of the mixtures. However, industrial processes often lead to mixtures containing more than three components, and therefore the competition experiments described in this work would have to be extended to examine mixtures of higher complexity.

1 A. Gavezzotti, *J. Chem. Soc. Perkin Trans. 2*, 1995, 1399.

2 W. Hückel, *Theoretische Grundlagen der Organischen Chemie*, Akademische Verlagsgesellschaft, vol. II, Leipzig, 1931, 185.

3 M. E. Brown, *J. Thermal Anal.*, **49**, 1997, 17.

4 A. Coetzee, *Structure and Reactivity of Selected Inclusion Compounds*, PhD thesis, University of Cape Town, 1996.

5 A. K. Galwey, *J. Therm. Anal.*, **41**, 1994, 267.

APPENDIX 1: Results of the competition experiments

(1) ***p*-PDA versus *o*-PDA**

$X_{p\text{-PDA}}$ start	$X_{p\text{-PDA}}$ included
1.0	1.0
0.91	1.0
0.82	1.0
0.68	1.0
0.62	1.0
0.47	0.79
0.37	0.55
0.30	0.37
0.23	0.22
0.11	0.09
0.0	0.0

(2) ***o*-PDA versus *m*-PDA**

$X_{o\text{-PDA}}$ start	$X_{o\text{-PDA}}$ included
1.0	1.0
0.92	0.85
0.83	0.84
0.68	0.79
0.61	0.71
0.49	0.65
0.41	0.58
0.30	0.47
0.21	0.31
0.09	0.23
0.0	0.0

(3) ***p*-PDA versus *m*-PDA**

$X_{p\text{-PDA}}$ start	$X_{p\text{-PDA}}$ included
1.0	1.0
0.87	1.0
0.76	0.92
0.69	0.84
0.62	0.82
0.53	0.75
0.39	0.71
0.32	0.62
0.21	0.56
0.10	0.27
0.0	0.0

(4) ***p*-PDA versus *o*-PDA versus *m*-PDA**

Starting solutions			Included by host		
$X_{p\text{-PDA}}$	$X_{o\text{-PDA}}$	$X_{m\text{-PDA}}$	$X_{p\text{-PDA}}$	$X_{o\text{-PDA}}$	$X_{m\text{-PDA}}$
0.33	0.36	0.31	0.56	0.25	0.19
0.51	0.24	0.25	0.63	0.23	0.13
0.45	0.18	0.37	0.68	0.17	0.15
0.25	0.28	0.47	0.51	0.21	0.27
0.17	0.40	0.43	0.38	0.33	0.30
0.26	0.50	0.24	0.40	0.38	0.22
0.57	0.39	0.14	0.54	0.32	0.14

(1) *p*-BD versus *o*-BD

$X_{p\text{-BD}}$ start	$X_{p\text{-BD}}$ included
1.0	0.99
0.89	0.98
0.78	0.97
0.70	0.98
0.59	0.96
0.50	0.93
0.39	0.87
0.30	0.69
0.21	0.33
0.11	0.11
0.0	0.0

(2) *o*-BD versus *m*-BD

$X_{o\text{-BD}}$ start	$X_{o\text{-BD}}$ included
1.0	1.0
0.87	0.99
0.76	0.91
0.72	0.92
0.63	0.77
0.52	0.67
0.41	0.48
0.34	0.44
0.18	0.30
0.08	0.14
0.0	0.0

(3) *p*-BD versus *m*-BD

$X_{p\text{-BD}}$ start	$X_{p\text{-BD}}$ included
1.0	1.0
0.92	1.0
0.84	1.0
0.71	0.93
0.58	0.89
0.49	0.75
0.37	0.71
0.30	0.26
0.22	0.20
0.14	0.11
0.0	0.0

(4) *p*-BD versus *o*-BD versus *m*-BD

Starting solutions			Included by host		
$X_{p\text{-BD}}$	$X_{o\text{-BD}}$	$X_{m\text{-BD}}$	$X_{p\text{-BD}}$	$X_{o\text{-BD}}$	$X_{m\text{-BD}}$
0.32	0.32	0.36	0.36	0.34	0.30
0.53	0.26	0.21	0.60	0.20	0.20
0.44	0.19	0.37	0.56	0.13	0.31
0.27	0.25	0.48	0.28	0.27	0.45
0.19	0.43	0.47	0.20	0.41	0.39
0.23	0.52	0.25	0.27	0.45	0.28
0.54	0.35	0.11	0.57	0.28	0.15

(1) *4*-Picoline versus *3*-picoline

$X_{3\text{-PIC}}$ start	$X_{3\text{-PIC}}$ included
1.0	0.0
0.87	0.76
0.81	0.71
0.67	0.64
0.61	0.42
0.50	0.45
0.42	0.39
0.27	0.25
0.18	0.19
0.14	0.12
0.0	0.0

(2) *4*-Picoline versus *2*-picoline

$X_{4\text{-PIC}}$ start	$X_{4\text{-PIC}}$ included
1.0	1.0
0.89	0.99
0.76	0.97
0.71	0.98
0.62	0.96
0.48	0.98
0.37	0.97
0.32	0.93
0.24	0.67
0.07	0.28
0.0	0.0

(3) *3*-Picoline versus *2*-picoline

$X_{3\text{-PIC}}$ start	$X_{3\text{-PIC}}$ included
1.0	1.0
0.93	1.0
0.82	0.99
0.68	0.99
0.57	0.99
0.49	0.99
0.42	0.93
0.34	0.91
0.18	0.84
0.08	0.36
0.0	0.0

(4) *3*-Picoline versus *4*-picoline versus *2*-picoline

Starting solutions			Included by host		
$X_{3\text{-PIC}}$	$X_{4\text{-PIC}}$	$X_{2\text{-PIC}}$	$X_{3\text{-PIC}}$	$X_{4\text{-PIC}}$	$X_{2\text{-PIC}}$
0.33	0.34	0.33	0.46	0.47	0.07
0.27	0.53	0.20	0.31	0.50	0.19
0.16	0.46	0.38	0.58	0.33	0.09
0.22	0.28	0.50	0.53	0.34	0.13
0.41	0.15	0.44	0.63	0.21	0.16
0.55	0.21	0.24	0.24	0.74	0.02
0.32	0.52	0.16	0.25	0.72	0.03

(1) ***3,5*-Lutidine versus *2,4*-lutidine**

$X_{3,5\text{-LUT}}$ start	$X_{3,5\text{-LUT}}$ included
1.0	1.0
0.92	1.0
0.84	0.95
0.72	0.98
0.64	0.99
0.52	0.88
0.45	0.84
0.28	0.42
0.21	0.33
0.10	0.09
0.0	0.0

(2) ***2,4*-Lutidine versus *2,6*-lutidine**

$X_{2,4\text{-LUT}}$ start	$X_{2,4\text{-LUT}}$ included
1.0	1.0
0.96	1.0
0.85	0.99
0.71	0.99
0.63	0.97
0.54	1.0
0.38	0.96
0.29	0.95
0.22	0.89
0.14	0.6
0.0	0.0

(3) ***3,5*-Lutidine versus *2,6*-lutidine**

$X_{3,5\text{-LUT}}$ start	$X_{3,5\text{-LUT}}$ included
1.0	1.0
0.92	1.0
0.78	0.98
0.71	1.0
0.63	0.97
0.50	0.98
0.39	0.99
0.28	0.92
0.19	0.94
0.12	0.72
0.0	0.0

(4) ***3,5*-Lutidine versus *2,4*-lutidine versus *2,6*-lutidine**

Starting solutions			Included by host		
$X_{3,5\text{-LUT}}$	$X_{2,4\text{-LUT}}$	$X_{2,6\text{-LUT}}$	$X_{3,5\text{-LUT}}$	$X_{2,4\text{-LUT}}$	$X_{2,6\text{-LUT}}$
0.33	0.34	0.33	0.78	0.12	0.20
0.27	0.53	0.20	0.98	0.01	0.01
0.16	0.46	0.38	0.90	0.08	0.02
0.22	0.28	0.50	0.64	0.34	0.02
0.41	0.15	0.44	0.85	0.12	0.03
0.55	0.21	0.24	0.96	0.02	0.02
0.32	0.52	0.16	0.58	0.42	0.0

(1) **Methanol versus Ethanol**

$X_{methanol}$ start	$X_{methanol}$ included
1.0	1.0
0.83	0.96
0.71	0.77
0.48	0.32
0.35	0.19
0.27	0.15
0.22	0.04
0.09	0.08
0.0	0.0

(2) **Methanol versus *n*-Butanol**

$X_{methanol}$ start	$X_{methanol}$ included
1.0	1.0
0.86	0.86
0.72	0.75
0.59	0.72
0.56	0.23
0.41	0.01
0.26	0.06
0.21	0.05
0.0	0.0

(3) **Methanol versus *i*-Propanol**

$X_{methanol}$ start	$X_{methanol}$ included
1.0	1.0
0.95	1.0
0.87	0.93
0.68	0.56
0.59	0.12
0.42	0.10
0.31	0.02
0.27	0.04
0.21	0.04
0.18	0.02
0.0	0.0

(4) **Ethanol versus *n*-Butanol**

$X_{ethanol}$ start	$X_{ethanol}$ included
1.0	1.0
0.93	0.94
0.87	0.75
0.75	0.51
0.62	0.19
0.52	0.12
0.41	0.09
0.29	0.03
0.21	0.01
0.08	0.02
0.0	0.0

(5) **Ethanol versus *i*-Propanol**

$X_{ethanol}$ start	$X_{ethanol}$ included
1.0	1.0
0.96	0.98
0.91	0.84
0.83	0.56
0.77	0.27
0.71	0.21
0.52	0.06
0.35	0.03
0.22	0.05
0.13	0.02
0.0	0.0

(6) ***i*-Propanol versus *n*-Butanol**

$X_{i\text{-}propanol}$ start	$X_{i\text{-}propanol}$ included
1.0	1.0
0.93	0.99
0.82	0.96
0.71	0.95
0.66	0.93
0.60	0.93
0.45	0.70
0.39	0.68
0.34	0.50
0.25	0.36
0.0	0.0

(7) **Methanol versus ethanol versus *i*-propanol versus *n*-butanol**

Starting solutions				Included by Host			
$X_{methanol}$	$X_{ethanol}$	$X_{i\text{-}propanol}$	$X_{n\text{-}butanol}$	$X_{methanol}$	$X_{ethanol}$	$X_{i\text{-}propanol}$	$X_{n\text{-}butanol}$
0.34	0.23	0.16	0.27	0.15	0.16	0.38	0.31
0.34	0.16	0.27	0.23	0.11	0.17	0.51	0.20
0.16	0.27	0.34	0.23	0.0	0.19	0.55	0.25
0.23	0.34	0.27	0.16	0.03	0.16	0.52	0.29
0.27	0.16	0.23	0.34	0.03	0.17	0.46	0.33
0.16	0.34	0.23	0.27	0.06	0.25	0.35	0.34
0.27	0.23	0.34	0.16	0.02	0.13	0.65	0.19
0.23	0.27	0.16	0.34	0.04	0.19	0.32	0.34
0.34	0.27	0.23	0.16	0.06	0.13	0.55	0.26
0.16	0.23	0.27	0.34	0.03	0.13	0.57	0.26
0.23	0.16	0.34	0.27	0.0	0.12	0.69	0.18

APPENDIX 2: Calculations to determine the equation of a plane, and the distance from a point to a plane[1]

1) The equation of a plane:

The equation of a plane determined by the points X (x_1, y_1, z_1), Y (x_2, y_2, z_2) and Z (x_3, y_3, z_3) is calculated as follows:

Vectors **a** and **b** corresponding to $\vec{XY}$ and $\vec{XZ}$ are

$$\mathbf{a} = \langle x_2 - x_1, y_2 - y_1, z_2 - z_1 \rangle \text{ and } \mathbf{b} = \langle x_3 - x_1, y_3 - y_1, z_3 - z_1 \rangle$$

The cross product vector **a** x **b** is normal to the plane, and is given by

$$\mathbf{a} \times \mathbf{b} = \begin{vmatrix} \mathbf{i} & \mathbf{j} & \mathbf{k} \\ a_1 & a_2 & a_3 \\ b_1 & b_2 & b_3 \end{vmatrix} = \begin{vmatrix} a_2 & a_3 \\ b_2 & b_3 \end{vmatrix}\mathbf{i} - \begin{vmatrix} a_1 & a_3 \\ b_1 & b_3 \end{vmatrix}\mathbf{j} + \begin{vmatrix} a_1 & a_2 \\ b_1 & b_2 \end{vmatrix}\mathbf{k} = p\mathbf{i} + q\mathbf{j} + r\mathbf{k}$$

then the equation of the plane is given by the equation:

$$p(x - x_1) + q(y - y_1) + r(z - z_1) = 0$$

2) Distance from a point to a plane

Given a plane XYZ with the equation $ax + by + cz + d = 0$, then the distance, h, of a point , P (x_1, y_1, z_1) to the plane is given by the formula

$$h = \frac{|ax_1 + by_1 + cz_1 + d|}{\sqrt{a^2 + b^2 + c^2}}$$

1 E. W. Swokowski, *Calculus with Analytic Geometry*, Third edition, PWS Publishers, 1979

APPENDICES 3 and 4: Supplementary Material

The supplementary material for structures of the inclusion compounds solved in this study appear on diskette. The material is divided into two files for each structure, with the code of the structure used as the filename.

The diskette labelled "APPENDIX 3" contains the following information:

1. atomic co-ordinates and isotropic displacement parameters
2. bond lengths and angles
3. anisotropic displacement parameters
4. hydrogen co-ordinates and isotropic displacement parameters

These are found in the files with the extension "tex", *e.g.* **PPDA**.tex

The diskette labelled "Appendix 4" contains lists of the calculated and observed structure factors. These are found in the files with the extension "sft", *e.g.* **PPDA**.sft

All these files are text files and can be viewed in an editor, under any of the following operating systems:
DOS
WINDOWS 3.1
WINDOWS 95
OS/2
APPLE MAC
UNIX
VMS
Linux

Guest	Host:Guest Ratio	Code Name of Complex
o-phenylenediamine	1:1	OPDA
m-phenylenediamine	1:1	MPDA
p-phenylenediamine	1:½	PPDA
o-benzenediol	1:1	OBD
m-benzenediol	1:1	MBD
p-benzenediol	1:½	PBD
2-picoline / water	1:1:1	2PIC
3-picoline	1:1	3PIC
4-picoline	1:1	4PIC
2,4-lutidine	1:1	24LUT
2,6-lutidine	1:1	26LUT
3,5-lutidine	1:1	35LUT
methanol	1:1	MEOH
ethanol	1:1	ETOH
i-propanol	1:1	PROH
n-butanol	1:1	BUOH
1,4-dioxane / water	1:½:1	DIOXW
ethyl acetate / water	1:½:1	EAW